TECHNISCHE UNIVERSITÄT MÜNCHEN

MAX-PLANCK-INSTITUT FÜR EXTRATERRESTRISCHE PHYSIK

Simulated Observations of Galaxy Clusters for Current and Future X-ray Surveys

Martin L. Mühlegger

Vollständiger Abdruck der von der Fakultät für Physik der Technischen Universität München zur Erlangung des akademischen Grades eines

Doktors der Naturwissenschaften (Dr. rer. nat.)

genehmigten Dissertation.

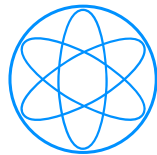|	
Vorsitzender:	Univ.-Prof. Dr. M. Ratz
Prüfer der Dissertation:	
	1. Hon.-Prof. Dr. G. Hasinger
	2. Univ.-Prof. Dr. L. Oberauer

Die Dissertation wurde am 27.07.2010 bei der Technischen Universität München eingereicht und durch die Fakultät für Physik am 02.11.2010 angenommen.

TECHNISCHE UNIVERSITÄT MÜNCHEN

Simulated Observations
of Galaxy Clusters for
Current and Future X-ray Surveys

Dissertation von

Martin L. Mühlegger

10. November 2010

MAX-PLANCK-INSTITUT
FÜR
EXTRATERRESTRISCHE PHYSIK

Abstract

Clusters of galaxies are versatile tools for both astrophysics and cosmology. In the X-ray band, clusters are clearly identifiable by their distinct extended emission from the hot Intra Cluster Medium, which qualifies X-ray search techniques as a preferred method for cluster surveys. One of the currently active X-ray cluster surveys is the XMM-Newton Distant Cluster Project (XDCP), with the main objective to identify and study high redshift ($z \gtrsim 0.8$) clusters using XMM archival data. The next generation all-sky X-ray cluster survey will be performed with eROSITA (extended ROentgen Survey with an Imaging Telescope Array), which is currently under development in a Russian-German collaboration led by the Max-Planck-Institute for Extraterrestrial Physics (MPE). Identifying clusters in X-ray surveys is a challenging task, but has the advantage that the surveys can be calibrated by simulations to fully exploit them in statistical studies.

In this thesis, I have pursued three main projects, which are all connected to the detection of galaxy clusters in X-ray surveys:

(1) As a hardware related project, I developed a new sub-pixel resolution algorithm making use of split events in X-ray CCDs. With the enhanced resolution, the measured Point Spread Function (PSF) of the first eROSITA mirror shells could be characterized with improved accuracy. A test measurement showed, that the derived half energy width of the PSF could be decreased by $18\,\%$ with respect to an analysis with standard CCD resolution.

(2) For the upcoming eROSITA mission, I developed an image simulator, which combines large-scale structure simulations of galaxy clusters with point-sources and realistic background components as well as instrumental effects, such as the PSF, the spectral response, and sub-pixel resolution. The first simulated images will be used as input for the characterization of the cluster detection capabilities of eROSITA, once a dedicated analysis software becomes available in the near future. In order to allow predictions of the eROSITA cluster yield, I followed an alternative approach using all-sky maps of exposure time and galactic neutral hydrogen, and a redshift dependent cluster luminosity function. With this, I could estimate the number of clusters being detectable in each $1° \times 1°$ sky pixel and $\mathrm{d}z = 0.01$ redshift bin based on globally defined count limits. Relying on results from earlier X-ray cluster surveys with ROSAT or XMM-Newton, I was able to confirm the feasibility of the scientific goal with the derived expectation values for the number of detectable clusters in the range from $85\,000$ to $177\,000$ based on realistic count limits from 100 to 50 photons.

(3) The largest project within this thesis was the characterization of the detection sensitivity of the XDCP. I developed an image simulator tailored to XMM-Newton as a pointing instrument, which adds β-model clusters to real XMM observations. In a large simulation run including 2.5 million model clusters, I could determine the completeness functions of 160 XDCP pointings, i.e. the detection probability depending on the core radius r_c, the number of photons N_ph, and the off-axis angle θ at which the cluster was observed. By assuming a realistic r_c distribution, I calculated the flux-dependent sky coverage of these fields. The average combined flux limit for a 50% completeness level was determined to be $f_\mathrm{lim}(0.5 - 2.0\ \mathrm{keV}) = 5.7 \times 10^{-15}\ \mathrm{erg\ cm^{-2}\ s^{-1}}$ for a maximum off-axis angle of $\theta_\mathrm{max} = 12'$. Using a more conservative $\theta_\mathrm{max} = 10'$, implying a loss of 30% of the survey area, would only marginally improve the flux limit by 3.5%.

The simulation tools developed within this thesis will allow further extensive studies on cluster detection with XMM-Newton and eROSITA and serve as a starting point for testing and improving the currently developed sophisticated data analysis algorithms, which are required to process the extensive amount of all-sky survey data to be expected from eROSITA.

Zusammenfassung

Galaxienhaufen sind vielseitige Studienobjekte, sowohl für die Astrophysik als auch für die Kosmologie. Im Röntgenlicht sind Galaxienhaufen durch ihre charakteristische ausgedehnte Emission des heißen Haufengases klar indentifizierbar. Dies qualifiziert Röntgenbeobachtungen als bevorzugte Suchmethode für Galaxienhaufen. Eine der aktuell aktiven Durchmusterungen ist das XMM-Newton Distant Cluster Project (XDCP), mit dem Ziel, Galaxienhaufen bei hoher Rotverschiebung ($z \gtrsim 0.8$) in XMM-Archivdaten zu identifizieren und zu studieren.

Die Himmelsdurchmusterung der nächsten Generation wird mit eROSITA (extended ROentgen Survey with an Imaging Telescope Array) durchgeführt werden, welches zur Zeit in einer russisch-deutschen Kollaboration unter Federführung des Max-Planck-Instituts für extraterrestrische Physik (MPE) entwickelt wird. Die Identifikation von Galaxienhaufen in Röntgendurchmusterungen ist eine Herausforderung, hat aber den Vorteil, dass die Daten mit Hilfe von Simulationen kalibriert werden können, um ihr volles Potential in statistischen Studien zu nutzen.

In dieser Arbeit habe ich hauptsächlich drei Themen bearbeitet, die alle mit dem Nachweis von Galaxienhaufen in Röntgendurchmusterungen verknüpft sind:

(1) Als Hardware-nahes Projekt entwickelte ich einen neuen Algorithmus für Sub-Pixel-Auflösung auf der Basis von Split-events in Röntgen-CCDs. Mit der verbesserten Auflösung kann die gemessene Punktbildfunktion (PSF) der ersten eROSITA-Spiegelschalen mit höherer Genauigkeit charakterisiert werden. In einer Testmessung konnte die abgeleitete halbe Energiebreite der PSF, im Vergleich zu einer Messung mit Standard-CCD-Auflösung, um $18\,\%$ gesenkt werden.

(2) Für die bevorstehende eROSITA-Mission entwickelte ich einen Bildsimulator, der Simulationen der großräumigen Struktur und Galaxienhaufen mit Punktquellen und realistischen Hintergrundkomponenten kombiniert, sowie instrumentelle Effekte, wie PSF, spektrale Empfindlichkeit und Sub-Pixel-Auflösung berücksichtigt. Die ersten simulierten Bilder werden als Grundlage für die Charakterisierung der Haufen-Nachweisfähigkeit von eROSITA verwendet werden, sobald eine dedizierte Analyse-Software in naher Zukunft zur Verfügung steht. Um Vorhersagen zum Ertrag an Galaxienhaufen mit eROSITA treffen zu können, verfolgte ich einen alternativen Ansatz unter Verwendung von Himmelskarten von Belichtungszeit und galaktischem neutralem Wasserstoff, sowie einer Rotverschiebungs-abhängigen Leuchtkraftfunktion von Galaxienhaufen. Damit konnte ich die Zahl der detektierbaren Haufen pro $1° \times 1°$ Himmelspixel und $\mathrm{d}z = 0.01$ Rotverschiebungs-Intervall auf der Basis von global definierten minimalen Photonenzahlen abschätzen. Beruhend auf Ergebnissen von früheren Röntgendurchmusterungen mit ROSAT und XMM-Newton konnte ich die Realisierbarkeit der wissenschaftlichen Zielsetzung von eROSITA bestätigen, wobei der Erwartungswert für die Zahl der detektierbaren Haufen im Bereich von $85\,000$ bis $177\,000$ liegt, bei realistischen Untergrenzen von 100 bis 50 Photonen pro Haufen.

(3) Das umfangreichste Projekt im Rahmen dieser Arbeit war die Charakterisierung der Sensitivität von XDCP. Dazu entwickelte ich einen auf XMM-Newton, als ein im pointierten Modus betriebenes Observatorium, zugeschnittenen Bildsimulator, der β-Modell-Haufen zu realen XMM-Beobachtungen hinzufügt. In einem umfassenden Simulationslauf mit 2,5 Millionen Modell-Haufen konnte ich die Vollständigkeits-Funktionen von 160 XDCP Feldern bestimmen, d.h. die Entdeckungswahrscheinlichkeit in Abhängigkeit von Core Radius r_{c}, Photonenzahl N_{ph} und Off-Axis-Winkel θ, bei welchem der Haufen beobachtet wurde. Unter Annahme einer realistischen r_{c}-Verteilung berechnete ich die flussabhängige Himmelsabdeckung dieser Felder. Das durchschnitt-

liche Flusslimit für ein Vollständigkeits-Niveau von 50% bestimmte ich zu $f_{\mathrm{lim}}(0.5 - 2.0 \text{ keV}) = 5.7 \times 10^{-15} \text{ erg cm}^{-2} \text{ s}^{-1}$ für einen maximalen Off-Axis-Winkel von $\theta_{\mathrm{max}} = 12'$. Eine konservativere Bechränkung auf $\theta_{\mathrm{max}} = 10'$, entsprechend einem um 30% reduzierten Raumwinkel der Durchmusterung, würde das Flusslimit nur marginal um 3.5% verbessern.

Die in dieser Arbeit entwickelten Simulations-Werkzeuge werden weitere umfangreiche Studien zur Galaxienhaufen-Detektierbarkeit mit XMM-Newton und eROSITA ermöglichen. Des Weiteren dienen sie als Startpunkt für das Testen und Verbessern von zur Zeit entwickelten fortschrittlichen Datenanalyse-Algorithmen, die zur Prozessierung der von eROSITA zu erwartenden erheblichen Datenmenge notwendig sind.

Table of Contents

Chapter 1

Introduction

Some of the currently strongest constraints on the energy content of the universe and cosmological parameters (e.g. Dark Energy) come from observations of clusters of galaxies. These most massive virialized objects constitute the top end of the hierarchical structure formation processes and structure formation in turn depends strongly on cosmological parameters. Galaxy clusters are therefore very well suited for cosmological studies.

Under the assumption of the gas mass fraction in clusters $f_{\mathrm{gas}} = M_{\mathrm{gas}}/M_{\mathrm{tot}}$ being constant with redshift z, Allen et al. (2008) were able to put constraints on the Dark Energy equation-of-state[1] parameter w. The measurement of f_{gas} is sensitive to the assumed angular diameter distance d_{ang} to the cluster. Therefore, only the $d_{\mathrm{ang}}(z)$ corresponding to the real underlying cosmology will lead to the required $f_{\mathrm{gas}}(z) = const.$ By measuring f_{gas} from Chandra observations of 42 clusters of galaxies spanning a redshift range of $0.05 < z < 1.1$ the study could determine $w = -1.14 \pm 0.31$ under the assumption of a flat universe with a non-evolving equation-of-state.

Vikhlinin et al. (2009) have studied the evolution of the mass function of galaxy clusters by comparing a sample of 37 high redshift ($\langle z \rangle = 0.55$) clusters serendipitously detected in ROSAT pointed observations with a sample of 49 low redshift ($z \approx 0.05$) clusters from the ROSAT All-Sky Survey (RASS). By following up those two samples with the Chandra observatory, they were able to constrain the equation-of-state parameter to $w = -1.14 \pm 0.21$ under the assumption of a flat universe and constant w. In a combined analysis together with data from observations of supernovae, the Cosmic Microwave Background (CMB) and Baryonic Acoustic Oscillations (BAO), the tight constraint of $w = -0.991 \pm 0.045\,(\mathrm{statistical}) \pm 0.039\,(\mathrm{systematic})$ could be achieved. This represents an improvement of a factor of 1.5 in the statistical and a factor of ~ 2 in the systematic uncertainties, as compared to an analysis without the results from galaxy clusters.

For making use of clusters of galaxies for cosmological studies, it is necessary to **(i)** find and identify them among the extensive diversity of celestial objects as well as **(ii)** understand their astrophysical appearance and the scaling of their various observables with cluster mass. Both tasks can be arbitrarily challenging depending not only on the minimum mass which is used in an analysis but on many other cluster properties as well. Using X-ray observations, the first prerequisite (i) is governed mainly by the spatial distribution of the X-ray emission of the galaxy cluster, i.e. its shape, concentration and brightness. Especially the latter one is tightly related to the cluster mass. The second prerequisite (ii) is equally ambitious since the observed relations between cluster tem-

---

[1]Dark Energy is commonly described by its equation-of-state which relates its density to its pressure: $p = w\rho c^2$. A cosmological constant in the sense of general relativity would imply a non-evolving $w = -1$. Departure from this model would express itself in $w \neq -1$ or a w evolving with redshift.

perature, luminosity (and other observables called "mass proxies") and the total mass of a cluster are only tested down to a lower mass limit and are furthermore functions of redshift.

Studies based on observations of clusters of galaxies have to be carefully corrected for the above mentioned effects before the data can be applied to the inference of parameters of cosmological models. Since only a small part of the objects predicted by the models can actually be observed, the connection between observations and theory can only be made by simulating observations. This thesis deals with such simulations and their analysis with the focus on two X-ray observatories. One of them is the X-ray Multi-Mirror mission (XMM-Newton), a pointing observatory which is operational since 1999. The other one is the extended ROentgen Survey with an Imaging Telescope Array (eROSITA), an X-ray telescope, which is currently under development at the Max-Planck-Institute for Extraterrestrial Physics (MPE). It is the core instrument on the Russian Spektrum-Röntgen-Gamma (SRG) mission, which is scheduled for launch in 2012 from Baikonur, Kazakhstan. For brevity, it is hereafter referred to as "eROSITA mission".

The topics treated here can be divided into three main parts. All projects are embedded within larger programs beyond the scope of the thesis. Ordered by increasing project size the individual studies are listed in the following:

- A hardware related project was performed at the X-ray testing facility PANTER which is an MPE based laboratory in the south of Munich. During the development phase of X-ray mirrors for the eROSITA mission, individual mirror shells are tested there with respect to their imaging quality. Due to the relatively short focal length of the mirrors ($f = 1600$ mm), the pixel size of the employed X-ray CCD corresponds to a relatively low angular resolution on the order of the size of the mirror's Point Spread Function (PSF). This is a limiting factor for the mirror characterization measurements. In developing a new algorithm making use of Sub-Pixel Resolution (SPR) on the basis of split events, the effective resolution could be substantially improved. When employing the SPR algorithm, the PSF core is now well resolved and also figure errors (deviations of the mirror surface from the ideal Wolter geometry) can be characterized in a better way. Sub-Pixel Resolution will also be applied to the science data from the eROSITA mission. This algorithm will therefore also be an essential part of the simulations and the science analysis software system.

- Two projects are devoted to the estimation of the cluster detection capabilities of the eROSITA mission. An eROSITA image simulator has been developed on the basis of a hydrodynamically simulated input of large-scale structure on the one hand and instrumental characteristics on the other hand. Since no dedicated analysis software for eROSITA data was available at the time of writing, the eROSITA image simulator was not applied to the estimation of cluster detection probability. It is described here for the purpose of being used in future projects and possible further development.

  The second project related to the eROSITA mission estimates the number of galaxy clusters to be expected from the eROSITA cluster survey based on pure luminosity arguments. The input data consists of a luminosity function, an all-sky exposure map, an all-sky map of galactic neutral hydrogen column density, and the instrumental spectral response. The resulting cluster number density is represented in an all-sky map and as a function of redshift.

- The XMM-Newton Distant Cluster Project (XDCP) is a serendipitous cluster survey using archival data of the XMM-Newton observatory. Its goal is the detection of high redshift galaxy clusters ($z \gtrsim 0.8$). In order to make use of the project for cosmological applications,

a crucial ingredient is the selection function of the survey, i.e. the cluster detection probability depending on various cluster parameters. For this purpose an XMM image simulator has been developed, which adds simulated clusters to real observations taking into account instrumental effects. The employed cluster model is the β-model with core radius and number of photons as model parameters and off-axis angle as an additional observational parameter. The simulated images were analyzed by the same procedure as the real data.

From a first simulation run of 2.5 months on 20 CPUs, a subsample of 160 out of the 469 XDCP fields could be characterized with respect to the cluster detection probability depending on those three parameters. With suitable assumptions on the core radius distribution at high redshifts the flux limit dependent survey sky coverage was derived for the subsample.

The thesis is organized in the following way: Chapter 2 gives an introduction to the astrophysics of clusters of galaxies and their cosmological applications. Chapter 3 provides the relevant background about the concepts of observational X-ray astronomy and introduces the XMM-Newton satellite and the eROSITA project. In chapter 4, a more detailed description of Point Spread Functions (PSFs) in general and the imaging capabilities of the XMM-Newton observatory and the eROSITA mission is given. It also describes the work on the development of the sub-pixel resolution algorithm and the mirror characterization measurements performed at the PANTER facility.

Chapters 5 deals with the principle of Monte-Carlo simulations and the development of the XMM-Newton image simulator. Its first application and the derivation of the sky coverage of a subsample of the XDCP is described in chapter 6.

Chapter 7 is dedicated to the development of the eROSITA simulator software which differs from the XMM simulator in some important aspects. The eROSITA simulator is intended for use in future projects such as studying the selection function of the mission or working out predictions on the cluster survey. A realistic estimation of the prospects of the eROSITA cluster survey in terms of the number of clusters to be detected is provided in chapter 8. Chapter 9 summarizes the thesis, compiles its main conclusions and provides an outlook on future projects[2].

---

[2]An electronic version of the thesis is available from the library of the Technical University of Munich: http://www.ub.tum.de/.

Chapter 2

Clusters of Galaxies

Galaxy Clusters are the most massive dynamically relaxed structures in the universe, containing typically 50 to 1000 individual galaxies. This chapter introduces briefly the individual components of galaxy clusters as well as the physical mechanisms going on within them and how they can be used as cosmological tools and astrophysical laboratories.

The goal is not to give a comprehensive introduction to the subject. This has been done by many good reviews and textbooks including Sarazin (1986), Voit (2005b) and Schneider (2006). The intention here is rather to review the main concepts as far as they are required for the understanding of the main part of the thesis and to provide basic equations for reference in later chapters.

2.1 Overview

Clusters of Galaxies are the largest well defined building blocks of the universe. In the framework of hierarchical structure formation, they are currently the largest objects which have had time to collapse and reach their dynamical equilibrium. Therefore, they appear only relatively late in the cosmic history which means that very massive systems exist only up to a certain lookback time corresponding to a certain distance. With increasing distance or increasing redshift, massive galaxy clusters become increasingly rare. Up to now, galaxy clusters have been found out to redshifts of $z \sim 1.5$.

Detailed studies of galaxy clusters are still a young field of research, but modern techniques allow for ever growing data sets and a better understanding of the phenomenon from both, the observational and the theoretical point of view. One of the modern observational approaches is X-ray astronomy[1]. The appearance of galaxy clusters in X-rays is described in section 2.2. One of the main theoretical approaches to the subject are simulations of Dark Matter distributions (*N-body simulations*) as well as hydrodynamical simulations of both, Dark Matter and gas particles. These simulations were able to reproduce the observed universal density profile of galaxy clusters.

Optical and infrared observations of galaxy clusters reveal the phenomenon which coined their name: an overdensity of galaxies, clustering in a small region in the sky. The first catalogue of galaxy clusters was compiled using a minimum number of galaxies within a brightness range in a specified solid angle (Abell, 1958). The left panel of figure 2.1 shows the core region of the Coma cluster (one of the nearest galaxy clusters) in the optical wavelength range. More than 60

---

[1]The first X-ray emission from galaxy clusters was detected by rocket-borne experiments as well as the Uhuru satellite in the 1960s and '70s. For the history of X-ray observations of galaxy clusters see also section 3.4.1.
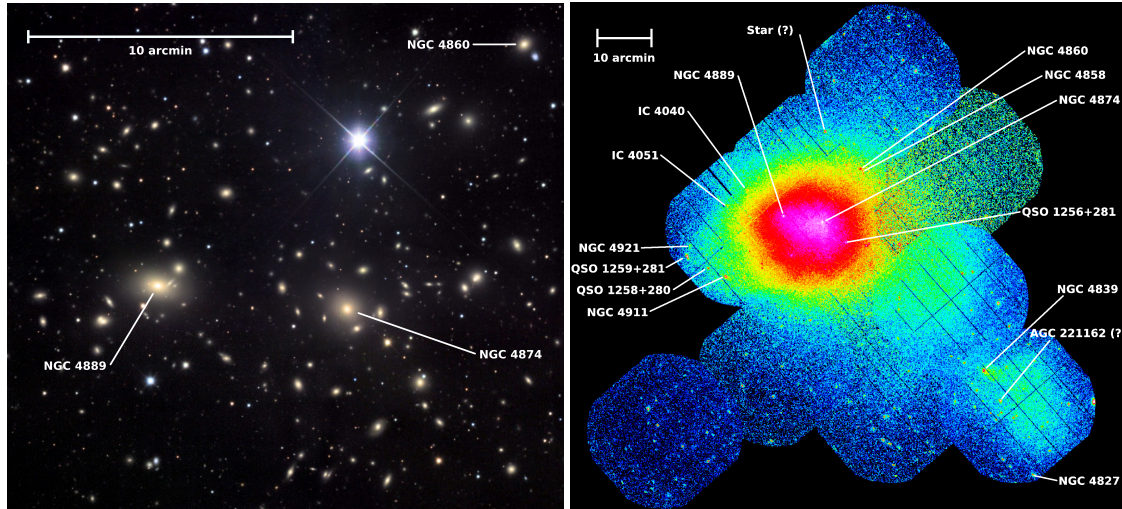
Figure 2.1: The Coma Cluster (Abell 1656) observed in two different wavebands. Note the different image scales. **Left:** The optical image of the core region shows individual galaxies. The two brightest cluster galaxies can also be identified in the X-ray image due to emission from their interstellar medium (ISM). Image credits: Jim Misti, Misti Mountain Observatory[2]. **Right:** The same cluster in X-rays ($0.3 - 2.0$ keV) with color coded intensity. X-ray emission from a merging group around NGC 4839 can be seen in the lower right. Image credits: Briel et al. (2001)

individual galaxies can be identified only in this central part of the cluster. The right panel shows an X-ray mosaic taken with XMM-Newton (with a different angular scale). The Coma Cluster was one of the first galaxy cluster detected in X-rays. The X-ray radiation originates from another main component of galaxy clusters: the Intra Cluster Medium (ICM). It consists of a hot plasma with a temperature of several 10^7 Kelvin which is bound by a gravitational potential well. It is therefore visible as one object with some additional substructure. In the case of the Coma cluster, also the two brightest cluster galaxies, NGC 4889 and NGC 4874 are visible in X-rays due to emission from their warm interstellar medium (ISM), see Vikhlinin et al. (2001).

The total mass of a cluster, and thus the depth of the gravitational potential are dominated by the Dark Matter component which contributes $\gtrsim 80\,\%$ of the mass budget. It cannot be observed directly but is inferred from many other methods, including the velocity distribution of the galaxy population, the ICM temperature or gravitational lensing of distant background galaxies.

To summarize, the total mass of a galaxy cluster (from about $10^{14}\,M_\odot$ to $10^{15}\,M_\odot$) is made up of the following components:

- the galaxies which are observable in the optical and infrared ($\lesssim 5\,\%$ of the total mass),

- the intracluster medium (ICM) which consists mainly of hot gas and can therefore be observed in X-rays ($\lesssim 15\,\%$ of the total mass),

- the Dark Matter halo which dominates the gravitational potential of the cluster ($\gtrsim 80\,\%$ of the total mass).

---

[2]http://www.mistisoftware.com/astronomy/index.htm
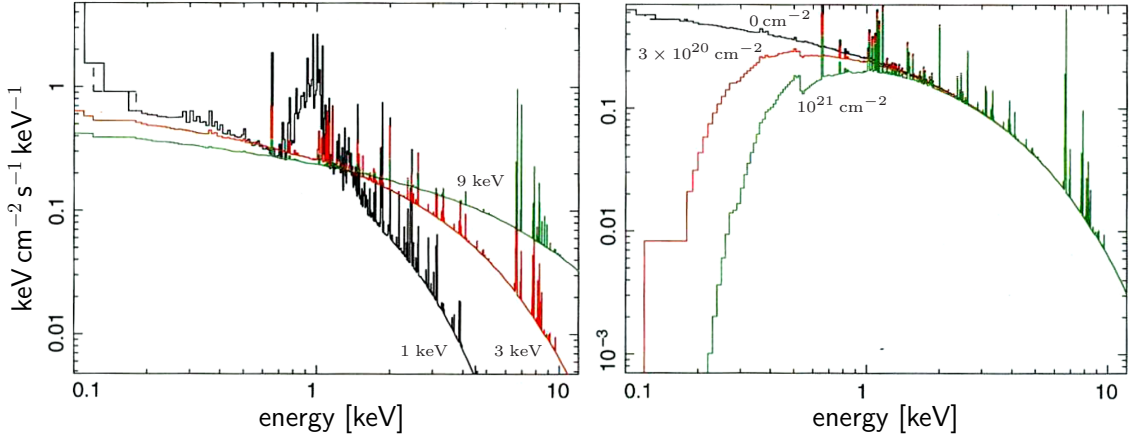
Figure 2.2: Model spectra of X-ray emission from the ICM. **Left:** Unabsorbed spectra of the continuum plus line emission with metallicity $Z = 0.4 Z_\odot$ and three different ICM temperatures. Black: $kT = 1$ keV, red: $kT = 3$ keV, green: $kT = 9$ keV. **Right:** Three spectra with $kT = 3$ keV observed through different absorbing columns of galactic hydrogen. Black: no absorption ($n_H = 0$), red: $n_H = 3 \times 10^{20}$ cm^{-2} green: $n_H = 10^{21}$ cm^{-2} Plots from Schneider (2006).

2.2 X-ray Emission from Galaxy Clusters

Besides Active Galactic Nuclei (AGN), clusters of galaxies are the brightest extragalactic X-ray sources. As opposed to AGN (which show up as point-sources), a distinct characteristic is *extended* emission.

2.2.1 Spectral Characteristics

The analysis of X-ray cluster spectra reveals an optically thin plasma emitting thermal bremsstrahlung, i.e. radiation from free-free transitions of electrons being accelerated in the coulomb potential of the nuclei (mainly hydrogen, i.e. single protons). Also free-bound emission, i.e. radiation through the capture of free electrons by ions contributes to the continuum part of the total spectrum whereas the line radiation originates from bound-bound transitions of various highly ionized chemical elements abundant in the ICM. A typical cluster metallicity (abundance of elements heavier than helium) is $30\,\%$ of the solar metallicity: $Z = 0.3\,Z_\odot$.

Figure 2.2 (left panel) shows unabsorbed model spectra with three different ICM temperatures. With increasing temperature, the spectrum extends to higher energies and less line emission due to the higher ionization state of the ICM plasma. The right panel of figure 2.2 shows a model spectrum with a typical cluster temperature of $kT = 3$ keV as it appears without absorption (black) and observed through two different galactic hydrogen absorbing columns (red and green). The realistically absorbed spectra show their maximum emission roughly in the standard X-ray band $0.5 - 2$ keV for which for example the eROSITA sensitivity has been optimized (see figure 3.5, right panel).

The main dependence of the bolometric[3] plasma emissivity $\epsilon_{\rm bol}$, measured in erg s^{-1} cm^{-3},

---

[3]The bolometric luminosity is the total luminosity integrated over all frequencies/wavelengths/energies. For practical purposes X-ray astronomers frequently use the luminosity in the band $0.1 - 100$ keV as bolometric.

on temperature and plasma density can be modelled as

$$\epsilon_{\mathrm{bol}} = \int_0^\infty \epsilon_\nu \; \mathrm{d}\nu \; \propto \; n_{\mathrm{e}}^2 \cdot \sqrt{T} \tag{2.1}$$

where ϵ_ν is the spectral emissivity, T is the ICM temperature and n_{e} is the electron density. The dependence of emissivity on density squared leads to a high contrast of the signal in the high density central regions of galaxy clusters.

2.2.2   Spatial Modelling

Galaxy clusters can exhibit a significant amount of substructure resulting in a variety of shapes that can deviate from the assumption of spherical symmetry.

The typical sound speed c_{s} in the ICM of a galaxy cluster is of the order of $c_{\mathrm{s}} \sim 1000\,\mathrm{km\,s^{-1}}$. The sound crossing time t_{s} can thus be estimated using a typical cluster radius of $R \sim 1$ Mpc as

$$t_{\mathrm{s}} = \frac{2R}{c_{\mathrm{s}}} \sim 2 \times 10^9 \, \mathrm{years} \tag{2.2}$$

which is smaller than the life time of the cluster (which can be approximated by the age of the universe). For this reason, most clusters are relaxed if there was no major disturbance (e.g. mergers) within the last few gigayears. This means that the ICM is in hydrostatic equilibrium with the overall (Dark Matter dominated) gravitational potential.

The *King model*, originally applied to the study of globular star clusters, uses the further simplifying assumption of an isothermal sphere with a truncated velocity distribution of the particles (King, 1966). If one assumes the additional relation between the gas density ρ_{gas} and the total density ρ to be $\rho_{\mathrm{gas}} \propto \rho^\beta$, the radial gas density distribution can be derived as

$$\rho_{\mathrm{gas}}(r_3) \propto \left[1 + \left(\frac{r_3}{r_{3,\mathrm{c}}} \right)^2 \right]^{-3\beta/2} \tag{2.3}$$

where $r_{3,\mathrm{c}}$ is the *core radius*[4] (Cavaliere and Fusco-Femiano, 1976).

From this three dimensional distribution, the surface brightness distribution as it appears projected on the sky can be obtained by integrating the plasma emissivity ϵ_ν along each line of sight. This calculation yields the azimuthally symmetric β-model

$$I(r) \propto \left[1 + \left(\frac{r}{r_{\mathrm{c}}} \right)^2 \right]^{-3\beta + 1/2} . \tag{2.4}$$

Measurements have shown that the average value of β is well approximated by $\beta \approx 2/3$ (e.g. Jones and Forman, 1999).

---

[4]In this equation the radius in the three dimensional distribution is denoted as r_3 in order to be distinguishable from the projected radius of the two dimensional distribution r (which is actually an angle on the sky). Throughout the rest of the thesis, r_{c} will denote the core radius of the projected distribution (measured in arcseconds).

2.3 Self Similarity and X-ray Scaling Relations

From N-body simulations of Dark Matter particles, a universal equation for the radial Dark Matter density distribution could be established which is now commonly referred to as NFW[5] profile (Navarro et al., 1997)[6]:

$$\rho_{\mathrm{DM}}(r) = \frac{\rho_{\mathrm{s}}}{\left(\frac{r}{r_{\mathrm{s}}}\right)\left(1 + \frac{r}{r_{\mathrm{s}}}\right)^2} \tag{2.5}$$

where r_{s} is a characteristic length scale and ρ_{s} is the central density. Within this formalism, Dark Matter halos can be described by only two parameters: ρ_{s} or equivalently the total mass and r_{s} or equivalently the halo concentration. They are therefore called *self-similar*, meaning that clusters with lower mass are scaled down versions of clusters with higher masses.

The ICM properties are mostly governed by the gravitational potential, dominated by the Dark Matter halo. Therefore, one can expect some degree of self-similarity also concerning the X-ray appearance of galaxy clusters, i.e. all global cluster parameters are expected to scale with mass according to power laws, which are called *scaling relations*.

Theoretical scaling relations for the most important cluster parameters (mass, temperature and X-ray luminosity) can be derived based on the following assumptions:

1. Clusters are formed by the infall of cold gas into the potential wells formed by Dark Matter halos. In the process, the gas is heated up by gravitationally driven shocks. Once an equilibrium state is reached, the virial theorem is valid:

$$2\langle E_{\mathrm{kin}}\rangle + \langle E_{\mathrm{pot}}\rangle = 0 . \tag{2.6}$$

2. Spherical symmetry is applicable.

3. The bolometric ICM emissivity scales with the square root of the ICM temperature (equation 2.1).

4. The total cluster mass scales with the characteristic cluster radius R_* like $M_{\mathrm{tot}} \propto R_*^3$.

5. The gas mass fraction is constant, i.e. $f_{\mathrm{gas}} = \frac{M_{\mathrm{gas}}}{M_{\mathrm{tot}}} = \mathrm{const.}$

6. The underlying Dark Matter halos are self-similar and follow e.g. an NFW profile (equation 2.5).

2.3.1 M-T Relation

Since the average kinetic energy of a gas particle is $\langle E_{\mathrm{kin}}\rangle = \frac{3}{2}kT$, the virial theorem (equation 2.6) can be written as

$$\frac{3kT}{\mu m_{\mathrm{p}}} - \frac{GM}{R_*} = 0 , \tag{2.7}$$

---

[5]NFW refers to the initials of the paper's authors Navarro, Frenk and White.
[6]In equation (2.5), r and r_{s} are radii in three dimensions (not projected ones).

where k is Boltzmann's constant, T is the global ICM temperature, G is the gravitational constant, μm_{p} is the average mass of the ICM particles (acting as test particles in the gravitational potential of the Dark Matter halo). From this equation, the proportionality

$$T \propto \frac{M}{R_*} \propto M^{2/3} \tag{2.8}$$

can be directly inferred where in the last step assumption (4) was applied. Solving for the total cluster mass yields the expected self-similar M-T relation:

$$M \propto T^{3/2} \ . \tag{2.9}$$

2.3.2   L-T Relation

Integrating the ICM emissivity (equation 2.1) over the cluster volume within the characteristic radius R_* yields

$$L_{\mathrm{bol}} \propto \rho_{\mathrm{gas}}^2 T^{1/2} R_*^3 \ . \tag{2.10}$$

With assumption (5), ρ_{gas} can be expressed as

$$\rho_{\mathrm{gas}} = \frac{M_{\mathrm{gas}}}{\frac{4\pi}{3}R_*^3} = \frac{f_{\mathrm{gas}}M_{\mathrm{tot}}}{\frac{4\pi}{3}R_*^3} = \mathrm{const.} \tag{2.11}$$

where assumption (4) was additionally used in the last step. This expression reduces equation (2.10) to

$$L_{\mathrm{bol}} \propto T^{1/2} R_*^3 \propto T^{1/2} M_{\mathrm{tot}} \propto T^2 \tag{2.12}$$

with the use of equation (2.9) in the last step. The self-similar L-T relation is thus in short

$$L_{\mathrm{bol}} \propto T^2 \ . \tag{2.13}$$

2.3.3   L-M Relation

Combining the above derived scaling relations equation (2.9) and (2.13) yields the self-similar L-M relation:

$$L_{\mathrm{bol}} \propto M^{4/3} \ . \tag{2.14}$$

Once calibrated on real observations (for different redshifts), the L-M relation promises to be a key mass estimator especially for X-ray cluster surveys like the upcoming eROSITA survey where no temperature measurement is feasible for the majority of the clusters due to limited photon statistics.

2.3.4   Evolution of the Scaling Relations

Since galaxy clusters do not have a sharp boundary, quantities like mass and luminosity are usually defined within a certain radius R_Δ where $\Delta = \langle\rho\rangle / \rho_{\mathrm{cr}}(z)$ (see equation B.6) is the mean overdensity within that radius with respect to the critical density ρ_{cr} of the universe at redshift z, e.g. for $\Delta = 200$:

$$\langle\rho\rangle = \frac{M_{200}}{(4\pi/3)R_{200}^3} = 200 \cdot \rho_{\mathrm{cr}}(z) \ . \tag{2.15}$$

As a consequence, the above derivation of the self-similar scaling relations is only valid at redshift zero. Going to higher redshifts, R_{200}, M_{200} and all derived quantities are expected to evolve. This can be expressed by means of the dimensionless evolution factor $E(z)$ which is defined in equation B.8. Including the redshift evolution, the scaling relations then change to (see Voit, 2005a):

$$\text{M-T relation:} \qquad M_{200} \propto E^{-1}(z) \cdot T^{3/2} \qquad\qquad (2.16)$$

$$\text{L-T relation:} \qquad L_{200} \propto E(z) \cdot T^2 \qquad\qquad (2.17)$$

$$\text{L-M relation:} \qquad L_{200} \propto E^{7/3}(z) \cdot M_{200}^{4/3} \ . \qquad\qquad (2.18)$$

Observationally, these X-ray scaling relations have been calibrated in many studies (e.g. Markevitch, 1998, Reiprich and Böhringer, 2002, Pratt et al., 2009) with partly differing power law exponents. Deviations from the self-similar scaling point to additional physics in the ICM, e.g. non-gravitationally driven heating mechanisms or cooling. The observational status of X-ray scaling relations and their evolution with redshift is currently studied in a diploma thesis at MPE (Reichert, 2010, *in prep.*).

2.4 The Scientific Significance of Galaxy Clusters

Galaxy Clusters are versatile tools for both astrophysics and cosmology. The statistical properties of the population of galaxy clusters as well as their variation with time (redshift) provide valuable information to estimate cosmological parameters in many different ways. Cosmology and the properties of galaxy clusters are related through the theory of structure formation, i.e. how galaxies, clusters and the large-scale structure formed.

2.4.1 Structure Formation in the Universe

The currently prevailing theory of structure formation is the paradigm of *hierarchical structure formation*. It states that small objects are formed first which then merge to larger objects which in turn accrete more and more matter to grow further ("bottom-up" scenario). Galaxy clusters are the largest (virialized) objects in the universe, which therefore implies that they formed most recently.

From Quantum Fluctuations to the Collapse of Dark Matter Halos

In the very early and very hot universe, quantum fluctuations in the density distribution serve as seeds for the formation of structure. They are enlarged to macroscopic scales during the epoch of inflation. After inflation, these primordial fluctuations in the matter density field further evolve according to a self-gravitating fluid in an expanding universe. The matter density field $\rho(\vec{x}, t)$ is usually described in terms of the density contrast $\delta(\vec{x}, t)$:

$$\delta(\vec{x}, t) = \frac{\rho(\vec{x}, t) - \bar{\rho}(t)}{\bar{\rho}(t)} \ , \qquad\qquad (2.19)$$

where $\bar{\rho}$ denotes the spatially averaged matter density. As long as the density contrast is small ($|\delta| \ll 1$) it evolves linearly with the scale factor[7] a.

---

[7]For a definition of the scale factor see equation B.1.

Larger density contrasts can still be analytically treated in the special case of a *top-hat collapse*: a spherical overdense region with constant overdensity can be considered independently from the background universe. Due to its gravitation it expands slower than the universe itself (= the Hubble flow). If the initial density is large enough, the expansion of the sphere stops at some maximum radius, decouples from the Hubble flow and collapses. The time at which this happens is the *turn-around time*. The collapsed objects are called Dark Matter halos.

Cluster Mass Functions

The model of spherical collapse can be used to analytically estimate the number density of Dark Matter halos of a certain mass at a certain redshift (Press and Schechter, 1974). The *Press-Schechter* formalism uses the statistics of the density fluctuations field $\delta(\vec{x}, t)$ to identify the number of density peaks above the critical collapse value after smoothing the field with a window function, where each smoothing length scale corresponds to a certain object mass. For the special assumption that the power spectrum is approximated by a power law ($P(k) \propto k^n$), the Press-Schechter mass function can be written as

$$n_{\mathrm{PS}}(M, z) = \frac{\bar{\rho}}{\sqrt{\pi}} \cdot \frac{\gamma}{M^2} \cdot \left(\frac{M}{M^*(z)}\right)^{\gamma/2} \cdot \exp\left[-\left(\frac{M}{M^*(z)}\right)^{\gamma}\right] \qquad (2.20)$$

with $\gamma = 1 + n/3$ and $M^*(z)$ is the redshift dependent mass scale above which the mass function is cut off exponentially.

An improved model which is based on the more realistic assumption of an ellipsoidal collapse was derived by Sheth et al. (2001). Jenkins et al. (2001) provides a mass function which has been calibrated with large N-body simulations and is widely used in cosmological predictions. The Jenkins mass function can be written in differential form as

$$\frac{\mathrm{d}n_{\mathrm{J}}(M, z)}{\mathrm{d}M} = 0.315 \cdot \frac{\bar{\rho}}{M^2} \cdot \frac{\mathrm{d}\ln\sigma_M^{-1}}{\mathrm{d}\ln M} \cdot \exp\left[-\left|\ln\sigma_M^{-1} + 0.61\right|^{3.8}\right] , \qquad (2.21)$$

where σ_M is the mass variance. The very good agreement of this fitting function with even the most modern simulations can be seen in figure 2.3. It shows the mass spectra as they were measured from the *Millennium Simulation* (Springel et al., 2005) for five epochs as well as the predictions from the Jenkins mass function, which was calibrated with *different* simulations. The predictions from the Press-Schechter formalism are shown for the redshifts $z = 0$ and $z = 10.07$. The redshift range from $z = 0$ to $z = 1.5$ is the currently observationally accessible cosmic epoch and is therefore of special importance. The comparison between real measurements and predictions from the Jenkins mass function or from simulations bear a large potential in constraining cosmological parameters through clusters of galaxies.

2.4.2 Cosmological Applications

The scientific potential of a large population of clusters of galaxies observed in X-rays is manifold. A general compilation is given e.g. in Fassbender (2008). This list provides a short summary with a focus on the upcoming eROSITA cluster survey.

- The cluster mass function n(M,z=0) of the local universe depends mainly on the matter density Ω_{m} and the amplitude of the primordial power spectrum, σ_8. The mass of galaxy clusters is tightly related to their X-ray luminosity (e.g. Reiprich and Böhringer, 2002). Thus the mass function can be derived directly from the luminosity function of the cluster sample.
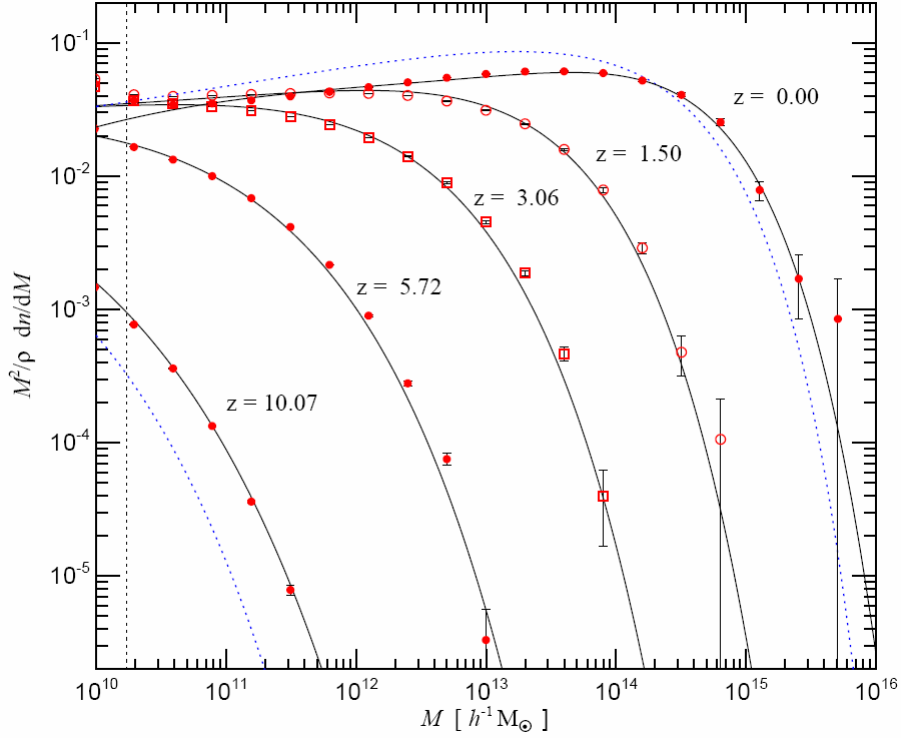
Figure 2.3: Differential number density of Dark Matter halos (represented by the halo multiplicity function $(M^2/\bar{\rho}) \cdot (\,\mathrm{d}n/\mathrm{d}M)$) as counted in the *Millennium Simulation* (red data points with black error bars). Solid black lines show the predictions from the Jenkins mass function (equation 2.21) while the dotted lines are the predictions from the Press-Schechter formalism for the two redshifts $z = 0$ and $z = 10.07$. Plot from Springel et al. (2005).

- The evolution of the cluster mass function n(M,z) depends on the growth of structure in the universe and thus contains information about Dark Energy density Ω_{DE} and the equation-of-state parameter $w(z)$.

- The spatial distribution of galaxy clusters, expressed in the power spectrum P(k) of the cluster population and its redshift evolution allows for a further determination of cosmological parameters of both Dark Matter and Dark Energy.

- With the assumption of a constant gas mass fraction in the ICM, further constraints on cosmological parameters can be derived via the redshift dependence of the angular diameter distance $d_{\mathrm{ang}}(z)$ (e.g Allen et al., 2008).

- Combining X-ray observations with the recently emerging SZ measurements bears the potential to determine absolute distances to galaxy clusters and thus constrain the geometry of the universe (e.g. Molnar et al., 2004).

- With a large cluster sample as expected from the eROSITA survey ($\sim 100\,000$ clusters of galaxies) it is possible to detect for the first time Baryonic Acoustic Oscillations (BAO) in the galaxy cluster power spectrum (Angulo et al., 2005).

2.4.3   Clusters as Astrophysical Laboratories

Cosmological studies involving galaxy clusters require a good understanding of the baryon physics of the ICM and the cluster galaxies. In turn, galaxy clusters are ideal laboratories to study the evolution of the baryonic component in the hot (ICM) and cold phase (cluster galaxies).

- With the redshift range of observed galaxy cluster populations expected from ongoing and future surveys, cluster formation paradigms can be tested and improved.

- From comparison of cluster galaxies with field galaxies, important insights can be gained about the influence of the environment on the evolution of galaxies.

- The evolution of the dynamical and thermal structure of galaxy clusters, the heating of the ICM as well as its chemical enrichment are still under investigation. This field will especially gain from high resolution X-ray studies (e.g. with Chandra).

- There have been recent studies in order to improve the calibration of scaling relations between cluster mass and observables, e.g. X-ray luminosity (e.g. Pratt et al., 2009). These results will have to be extended towards higher redshifts for the calibration of future surveys. Especially the evolution of scaling relations is to be constrained better, which will influence the accuracy of cosmological applications.

- A central point of cluster research is dealing with the phenomenon of "cool cores", i.e. a significant drop in the temperature profile of the ICM towards the cluster center due to radiative cooling. Cool core clusters have very peaked surface brightness profiles complicating their discrimination from point-sources. A subject of recent research was the incidence rate of these cool cores. (e.g. Santos et al., 2008, Vikhlinin et al., 2007)

Chapter 3

X-ray Observatories and Observing Strategies

This chapter gives an introduction to X-ray astronomy, which became feasible only during the past century by moving observatories from the ground into space, since the Earth's atmosphere is highly intransparent for photons with energies higher than a few electronvolts. Section 3.1 presents the layout of X-ray telescopes in general, along with the basic concepts required for data analysis as well as for simulations. It is intended as a first overview for people who are new in the field of X-ray astronomy, especially future students who might take over and continue the efforts started in this thesis. Sections 3.2 and 3.3 are dedicated to the introduction of the two X-ray missions being dealt with in this thesis. Section 3.4 gives an overview of current and future X-ray surveys and outlines some important observing strategies.

3.1 General Design of X-Ray Telescopes

The design of X-ray telescopes (XRTs) is in principle very similar to that of modern optical telescopes. Photons are first reflected by a paraboloid shaped mirror and then again by a hyperboloid shaped mirror before they hit the detector. The main difference is, that optical photons are reflected by the mirrors regardless of the photon's incidence angle[1], whereas X-ray photons have such a high energy that photons with a small incidence angle would penetrate the mirror rather than being reflected. Therefore, X-ray telescopes use *grazing incidence* mirrors which were invented by the German physicist Hans Wolter for the purpose of X-ray microscopy (Wolter, 1952). Since the first Wolter type telescope was flown on a satellite (HEAO-2, later renamed to Einstein Observatory, Giacconi et al., 1979), the basic principle of focussing X-rays has remained the same, whereas the detector side underwent some major steps of development.

3.1.1 Mirror Technology

This section about the principles of modern X-ray optics is a summary of the articles by Aschenbach (1985) and Friedrich (2008). More detailed calculations along with graphical representations can be found there.

---

[1]The incidence angle is usually defined as the angle between the photon path and the normal to the reflecting plane.

X-Ray Reflection

A light beam propagating from an optically thicker medium to an optically thinner one is refracted away from the axis of incidence which is perpendicular to the interface between the two media. Total reflection occurs when the emergent angle of the refracted beam becomes $90°$ or larger. The minimum incidence angle α_t for which total reflection appears can be calculated from Snell's law

$$n_1 \cdot \sin(\alpha_1) = n_2 \cdot \sin(\alpha_2) \tag{3.1}$$

(with n_1, n_2 being the real part of the complex refraction index) by setting $\alpha_2 = 90°$ and $\alpha_1 = \alpha_t$. In this case equation (3.1) becomes

$$\alpha_t = \arcsin \frac{n_2}{n_1} \ . \tag{3.2}$$

For reflection of optical light at a boundary between water ($n_1 = 1.33$) and vacuum ($n_2 = 1$) the minimum angle is $\alpha_t \approx 48.8°$. This case is called internal total reflection because the incident and reflected rays lie in the medium. External total reflection (where the rays propagate in vacuum) happens, if the medium's n is smaller than 1 (that of vacuum). At X-ray wavelengths, n follows approximately the equation

$$n = 1 - N_A \frac{Zr_e}{A \cdot 2\pi} \rho \lambda^2 \ , \tag{3.3}$$

with N_A : Avogadro's number, $N_A = 6.0221 \cdot 10^{23} \mathrm{mol}^{-1}$
      Z : atomic number
      A : atomic mass
      r_e : classical electron radius, $r_e = 2.8179 \cdot 10^{-15} \mathrm{m}$
      ρ : mass density
      λ : X-ray wavelength
      (Aschenbach, 1985).

From this equation it can already be seen that the higher the density ρ of the reflecting material, the lower n and the smaller also α_t becomes, which implies "steeper" incident angles. This is the reason for aiming at heavy elements for X-ray mirrors. For gold[2] together with a typical photon energy[3] of $E = 1$ keV, one obtains a refraction index of $n \approx 0.9968$ and thus an *incident angle* of $\alpha_t \approx 85.4°$ or a *gracing angle* of $\theta_t = 90° - \alpha_t \approx 4.6°$. Since only the real part of the refraction index was used here, this estimation is strictly speaking only valid for the ideal case of a vanishing absorption coefficient (imaginary part of the complex refraction index) but it shows the basic principle why X-rays can be focussed at all in spite of their generally high penetration power.

Wolter Geometry

In optical imaging, the surface where paraxial rays intersect with rays through the system's focal point is called *principal surface*. Abbe's sine condition of geometrical optics (Abbe, 1904) states, that an image is only similar to the object, if the principal surface is a sphere, i.e. the following equation is fulfilled:

$$\sin \theta = \frac{d}{f} \ . \tag{3.4}$$

---

[2]Gold constants: $Z = 79$, $A = 197$ g/mol, $\rho = 19.3$ g/cm^3
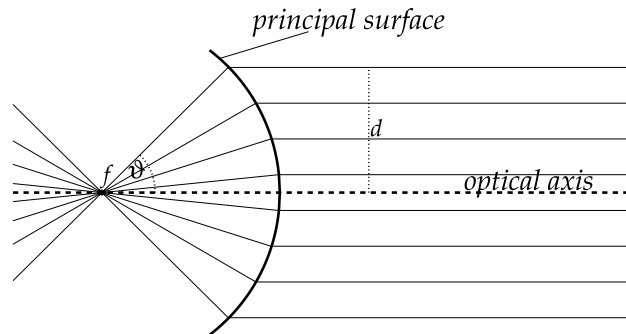[3]$\lambda = hc/E$ with $h =$ Planck's constant, $c =$ speed of light

Figure 3.1: An illustration of Abbe's sine condition (from Friedrich, 2008).

The sine condition and the principal surface are illustrated in figure 3.1. For single mirrors, the principal surface is always the mirror itself. This means that Abbe's sine condition and the condition of grazing incidence can not be fulfilled both at the same time, because in spherical mirrors the light rays going to the focal point are almost perpendicular to the mirror.

Hans Wolter solved this problem by developing a system of two mirror surfaces, the first one in the shape of a paraboloid and the second one being a hyperboloid (see figure 3.2) (Wolter, 1952). The principal surface in this case becomes a paraboloid, and therefore Abbe's sine condition is fulfilled at least approximately for beams close to the optical axis (see figure 3.3 for an illustration). The telescope's aperture (ratio of focal length over diameter) should not be chosen too small, so that incident rays stay close enough to the spherical approximation of the paraboloid and yield a good image quality. There are also mirror configurations, which fulfill Abbe's sine condition exactly (Schwarzschild, 1905), but they require more complicated figures of revolution and have thus not gained much importance in X-ray astronomy. Hans Wolter developed several other two-mirror configurations apart from the one shown in figure 3.2, which is called Wolter type 1 geometry. It is the one most widely used in X-ray astronomy due to its advantage that the individual mirror shells can be nested to increase the telescope's light collecting area.

Burrows, Burg and Giacconi have suggested a wide-field X-ray optics with an imaging quality which is much more homogeneous over a large field-of-view (Burrows et al., 1992), as opposed to the Wolter type 1 geometry which produces a sharp image on-axis but shows a rapid decrease in imaging quality towards larger off-axis angles. However, the wide-field optics has not been realized on an X-ray mission up to now.

Nesting of individual Mirror Shells

An important part of X-ray telescopes has been neglected in figure 3.2: the aperture stop. It prevents direct light from falling onto the detector in the focal plane. Each X-ray photon has to be reflected exactly twice in order to contribute to a good image quality. By nesting several mirror shells, as illustrated in figure 3.4, *single reflections* are avoided. The main purpose of nesting is however, to enhance the collecting area of the XRT (see section 3.1.2). For the innermost mirror shell, an additional plate is used as aperture stop, which can also be seen schematically in figure 3.4.
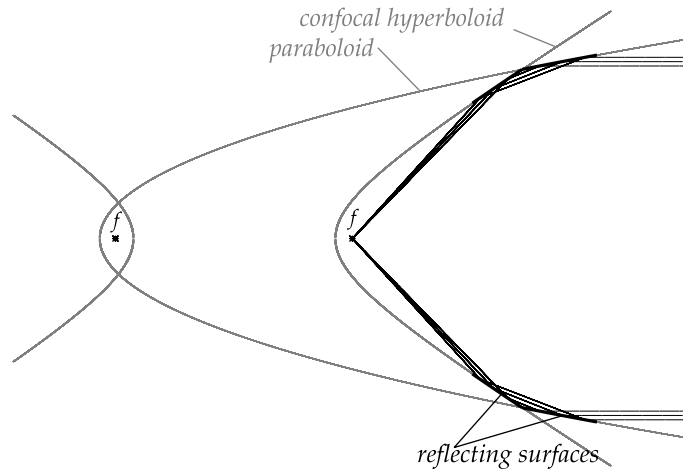
Figure 3.2: The light path of the Wolter type 1 geometry (from Friedrich, 2008).
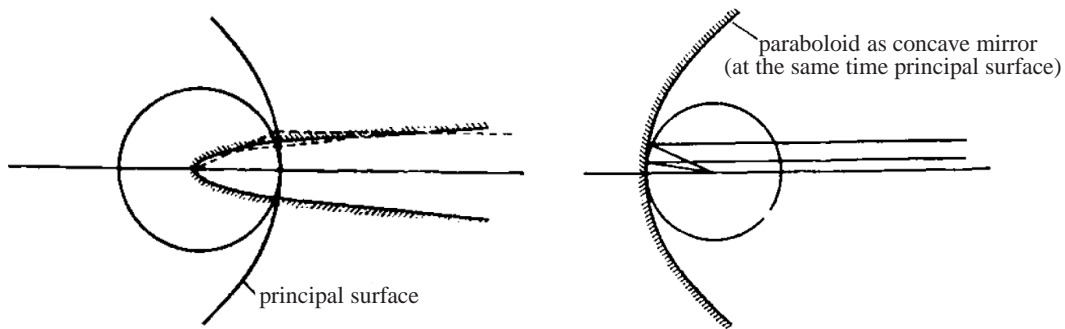
Figure 3.3: Left panel: Paraboloidal shape of the principal surface of a Wolter type 1 two-mirror system. **Right panel:** A conventional concave mirror system for comparison (from Wolter, 1952).

Industrial Realization

The first Wolter telescopes have been made from glass with low thermal expansion, which was ground and polished and finally coated with high atomic number and corrosion resistant elements like nickel, iridium or gold. Since the glass has to be rather thick, to ensure stability, only few mirror shells can be used, which results in a low effective area. Modern high throughput X-ray telescopes are manufactured by *mirror replication*: For each size of mirror shell an aluminium cylinder is ground to obtain the paraboloid-hyperboloid shape including the break where the two shapes join. This *mandrel* is then polished and coated with a thin gold surface. After the coating, it is inserted into a chemical bath where a nickel layer is electro-formed onto the gold layer. After the electro-forming process, the mirror shell cools down and thereby separates from the aluminium mandrel and takes the gold layer with it. The mirror shell thus consists of a thin nickel layer ($\sim 0.5\,$–1 mm) coated with a gold surface (~ 200 nm). This replication technique requires a long development process in order to obtain mirrors with sufficient quality. The main advantage is though, that many shells can be replicated from just one mandrel. The individual mirror shells are mounted together on a common structure which is called *spider wheel* (the white radial structures in figure 3.5, left panel).
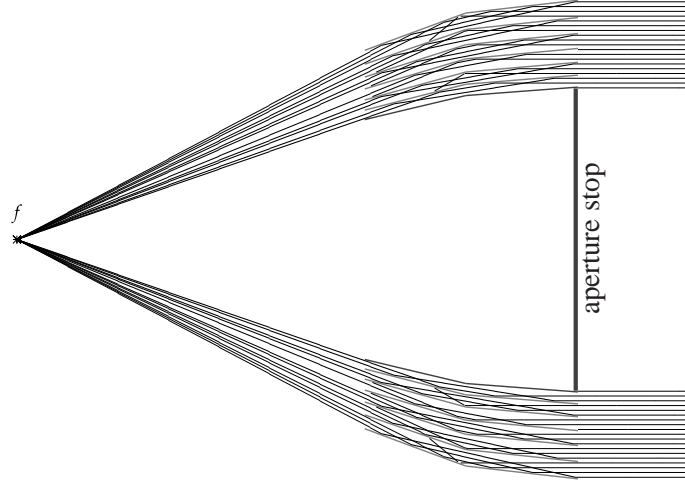
Figure 3.4: Nesting of Wolter type 1 mirror shells results in a large increase in effective area as compared to just using individual mirror shells. Furthermore, the inner shells act as beamstops for the outer ones and thus prevent singly reflected as well as direct X-rays from reaching the detector. (from Friedrich, 2008)

3.1.2 Effective Area

A key quantity which characterizes an X-ray telescope is its effective area. It is derived in the following way: The geometric area (A_g) is the area between the individual mirror shells where photons can enter the X-ray telescope, seen along the telescope's optical axis (see figure 3.5, left panel). By multiplying with the cosine of the off-axis angle θ, the collecting area (A_c) is obtained (now projected along the path of the incoming photon):

$$A_\mathrm{c}(\theta) = A_\mathrm{g} \cdot \cos(\theta) \tag{3.5}$$

This off-axis angle effect is negligible, since the maximum possible off-axis angle is usually very small. There is, however, a much larger effect of off-axis angle which is called *vignetting* (here $v(\theta)$). It is due to the fact that photons from higher off-axis angles have fewer mirror shells available to be reflected twice. The higher the off-axis angle the more photons will be singly reflected and thus stopped by the backside of the next mirror shell. Further multiplying with the intrinsic reflectivity of the mirrors' gold surface, which depends on the photon energy (here $r(E)$), yields the mirror effective area:

$$A_\mathrm{mirr}(E, \theta) = A_\mathrm{c} \cdot r(E) \cdot v(\theta). \tag{3.6}$$

The total effective area of the instrument is obtained from this, by taking into account the transmission of an optional filter (here $T(E)$) and the detector's quantum efficiency (here $\mathrm{QE}(E)$), which both depend on photon energy:

$$A_\mathrm{eff} = A_\mathrm{eff}(\theta, E) = A_\mathrm{mirr}(E, \theta) \cdot T(E) \cdot \mathrm{QE}(E). \tag{3.7}$$

3.1.3 Point Spread Function (PSF)

Strictly speaking, a point-source is defined as a source with an intensity distribution following

$$I(\alpha, \delta) = I_0 \cdot \delta_\mathrm{D}(\alpha - \alpha_\mathrm{S}, \delta - \delta_\mathrm{S}), \tag{3.8}$$
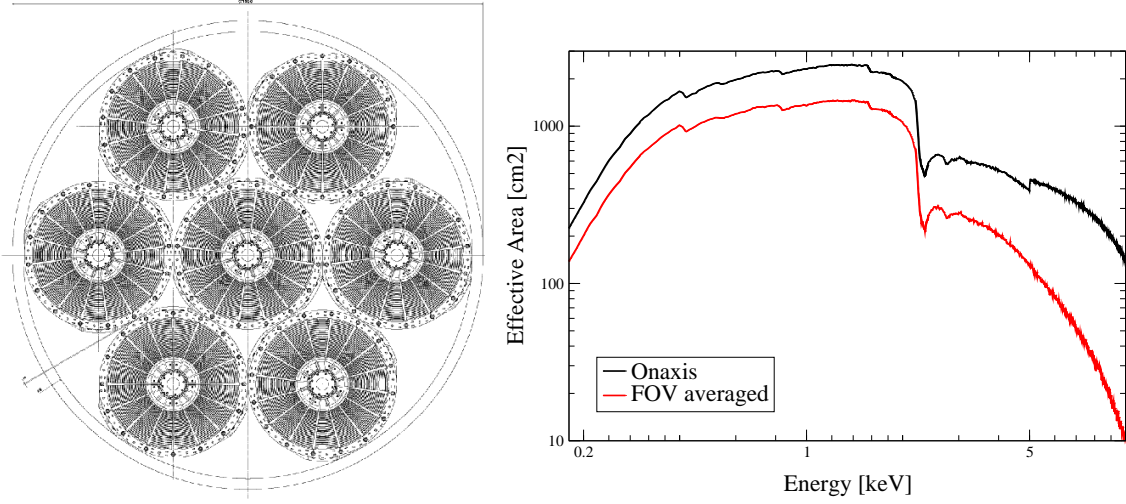
Figure 3.5: Effective area of the eROSITA instrument. **Left:** The seven X-ray telescopes seen in projection along their common optical axis. The geometric telescope area (A_{g}) is the space in between the individual mirror shells. **Right:** Total effective area of all seven telescopes plotted against photon energy for an on-axis source (black) and averaged over the field-of-view (FoV), which is needed to simulate the instrument's scanning mode (red). It can also be seen from this plot that the instrument is optimized for soft X-rays between about 0.5 keV and 2.0 keV where clusters of galaxies have their maximum emission (see figure 2.2, right panel).

where α and δ are the right ascension and the declination, respectively and α_{S} and δ_{S} are the angular coordinates of the source. δ_{D} is a two-dimensional version of the Dirac delta function with

$$\delta_{\mathrm{D}}(x,y) = \begin{cases} +\infty\,, & x = 0 \wedge y = 0 \\ 0\,, & \text{else} \end{cases}$$

and   (3.9)

$$\int\limits_{-\infty}^{\infty} \int\limits_{-\infty}^{\infty} \delta_{\mathrm{D}}(x,y)\ \mathrm{d}x\ \mathrm{d}y = 1\,.$$

The photon intensity field reaching the satellite is altered by the various components of the instrument like the X-ray mirrors and the spatial detector resolution[4]. The point spread function $\mathrm{PSF}(x,y)$ is the measured intensity distribution after the radiation field of a point-source has passed all instrument components. The transformation by an XRT can be thought of as a Fourier transformation from angular space into real space, so the PSF is usually measured in detector coordinates and normalized to one:

$$\int\limits_{-\infty}^{\infty} \int\limits_{-\infty}^{+\infty} \mathrm{PSF}(x,y)\ \mathrm{d}x\ \mathrm{d}y = 1$$ (3.10)

---

[4]In optical astronomy, the main part of the PSF is usually due to the turbulence in the Earth's atmosphere.

or in radial coordinates:

$$\int\limits_{0}^{2\pi} \int\limits_{0}^{\infty} \mathrm{PSF}(x,y)\ r\,\mathrm{d}r\,\mathrm{d}\phi = 1\ .$$ (3.11)

The modification of the radiation field by the various instrumental components can also be described by a convolution with the PSF as the convolution kernel:

$$D(x,y) = \int\limits_{-\infty}^{\infty} \int\limits_{-\infty}^{\infty} I(\alpha,\delta)\ \cdot\ \mathrm{PSF}(x - f\alpha, y - f\delta)\ \mathrm{d}\alpha\,\mathrm{d}\delta$$ (3.12)

where $D(x,y)$ is the intensity distribution on the detector, $I(\alpha,\delta)$ is the intensity distribution on the sky, and f is the instrument's focal length which relates angular sky coordinates to detector coordinates by

$$x = f \cdot \tan(\alpha) \overset{5}{\approx} f\alpha\ .$$ (3.13)

Although the term "PSF" generally refers to all causes of image distortions, it is mostly used for the part of the image distortions which is caused by the mirrors only. A detailed description of theoretical and measured shapes of mirror PSFs is provided in chapter 4. A very good guide to practical handling of PSFs and image convolution is given in the book by Berry and Burnell (2005).

3.1.4 X-Ray Detectors

The first detectors used in X-ray astronomy were scintillation counters for hard X-rays above $15\ \mathrm{keV}$ (e.g. Clark, 1965) and proportional counters for soft X-rays (e.g. Giacconi et al., 1971). In its simplest geometry, a proportional counter consists of a cylindrical volume, filled with a (noble) gas, and an anode wire in its center. A high voltage is applied between the tube which acts as a cathode and the anode wire. An X-ray photon entering the volume via a window creates pairs of electrons and positive gas ions. These drift to the anode wire and the cathode respectively and ionize further gas atoms on their way, which is called multiplication process. The high voltage can be tuned such that the charge generated by the multiplication process is proportional to the original number of electrons and thus to the energy of the incident X-ray photon. Further details can be found in Pfeffermann (2008b).

Simple proportional counters as such do not possess any spatial resolution. When focusing X-ray optics became available, it was the desire to employ not only their capability to increase the instrument's effective area but also to use their imaging capability. Detectors sensitive to the incident position of X-ray photons were developed. Such *imaging proportional counters* for X-ray astronomy were flown on only a few missions. They all have in common that they use a grid of wires in order to determine the interaction point of the X-ray photon with the counter gas. The most famous one is the Position Sensitive Proportional Counter (PSPC) which was flown on ROSAT (Trümper, 1982) and achieved a spatial resolution of $250\ \mu\mathrm{m}$ (FWHM) at $0.93\ \mathrm{keV}$ (Pfeffermann and Briel, 1986). A comparison between the four main imaging proportional counters which were used in X-ray astronomy is given in Pfeffermann (2008a).

---

[5]Small angle approximation has been used here.

X-ray CCD Detectors

Charge Coupled Devices (CCDs) were developed in 1969 at the Bell telephone company with the intended use as a computer memory (Howell, 2006). The name stems from the fact that charges are stored in small potential wells and can be transported along columns towards the edge of the device in order to be read out by an electronic circuit. It was quickly recognized that CCDs can not only *store* charges but are also sensitive to light, which leads to the *production* of charges which are then collected in the potential wells. Each of the wells is called a *pixel* ("picture cell").

A special type of X-ray CCD is the pnCCD. Its characteristic feature is the depletion from charge carriers over its full thickness, which can reach up to $500 \ \mu\mathrm{m}$. The result is a high Quantum Efficiency (QE) over a large energy range (still 90% at $11 \ \mathrm{keV}$ in the case of the eROSITA CCD, Meidinger et al., 2008). The general layout of the pnCCD is sketched in figure 3.6. Photons hit the detector from the back side ("back-illuminated") to prevent them from interacting with the electronics structure on its front. This ensures a homogeneous and high quantum efficiency. The primary interaction of photons with the silicon is the photo effect which causes the production of electron-hole-pairs in the bulk material. Although the band gap of silicon is only $E_{\mathrm{gap}} = 1.1 \ \mathrm{eV}$, the average creation energy for one electron-hole-pair is $E_{\mathrm{e}^-} = 3.7 \ \mathrm{eV}$ because the main part of the photon's energy is transformed into phonons (oscillations of the silicon's crystal lattice).
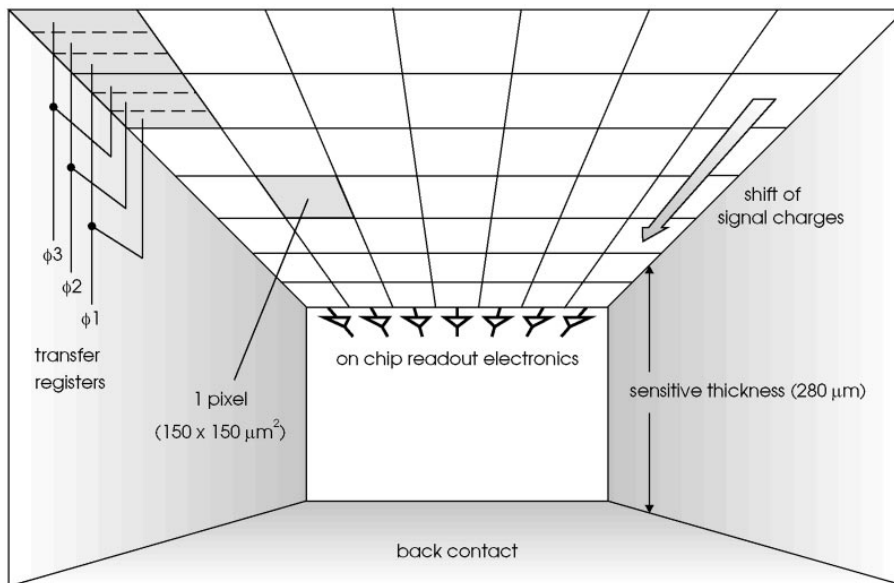
Figure 3.6: Sketch of a pnCCD: photons coming from the back side of the detector (bottom in this figure) interact with the silicon and create pairs of electrons and holes. The charges are collected in pixels. After the expiration of the exposure time, they are shifted to the readout nodes where they are amplified and digitized. (From Strüder, 2000)

By suitable doping and externally applied voltages, the potential within the detector can be shaped in such a way that the holes drift to its back contact while the electrons are collected at the detector's front, where the signal charge is collected in single pixels or can be distributed over neighboring pixels (*split events*). The pixels are formed by the potentials of the three transfer registers ϕ_1, ϕ_2 and ϕ_3 in *transfer direction* (*column direction*). In the direction perpendicular to it, the charges are kept in place by alternating n-doped *channel guides* and p-doped *channel*

stops in between them[6]. One exposure is called a *frame*. After one exposure time has expired, the charges are transferred along the columns by appropriate variation of the voltages of the three transfer registers.

Once they reach the readout node, the charges are amplified and processed in the CAMEX (CMOS Amplifier and MultiplEXer) chips and digitized by Analog-to-Digital Converters (ADCs). The x and y pixel coordinates of the events are reconstructed from the sequence of charges reaching the readout nodes. The raw images coming from the CCD have to be calibrated because charges are lost during the shift to the readout node (Charge Transfer Inefficiency, CTI) and each amplifier has a different gain so that each column appears with a different magnification factor. Furthermore, an offset map (individual bias level of each pixel) is subtracted and a common mode correction[7] is performed.

Out-of-Time Events

A typical readout of one pnCCD frame takes some milliseconds. Photons reaching the detector during the readout are assigned a wrong y-position (coordinate along the column) because they generate additional charges in pixels whose charge content has already been shifted towards the readout node. This effect leads to the occurrence of Out-of-Time (OoT) events which appear in the final image as strips in y-direction originating from each bright source[8]. With a typical exposure time of some tens of milliseconds, the fraction of OoT events can reach significant levels (e.g. 6.3% in the case of XMM-Newton's pnCCD). A technique to suppress OoT events is the *frame store* mode which is used for the seven detectors of the eROSITA cameras. It is described together with the TRoPIC CCD in section 4.4.2. More details about CCD detectors in X-ray astronomy can be found e.g. in Strüder and Meidinger (2008).

3.1.5 The Concept of Response Matrices

Unlike optical photons, an X-ray photon hitting a CCD produces several hundred electron-hole pairs in the detector. The total charge contained in the created charge cloud is to first order proportional to the energy of the incident photon. This makes it possible to perform (low resolution) X-ray spectroscopy without using any additional dispersive device[9]. The detector electronics measures the total charge contained in each CCD pixel and assigns it an individual detector channel called Pulse Height Amplitude (PHA) channel. The relation between incident photon energy and PHA channel would simply be linear in an ideal detector. Real detectors, however, have a different response to each incident photon energy. Similar to the concept of spatial PSFs (see section 3.1.3), this response can be regarded as a "spectral point spread function" which states the probability for generating a signal in a specific PHA channel for each incident photon energy. The number of counts $n(c)$ in each channel c produced by a number $p(E)$ of photons with energy E can be

---

[6]The donor atoms of the n-doped channel guides attract signal electrons, while the acceptor atoms of the p-doped channel stops repel them.

[7]The common mode is the noise picked up during the readout of one line of the CCD affecting all pixels of the line equally.

[8]The strip of OoT-events points to both sides along the readout direction, because during the readout of one frame, the next frame already "moves in", where OoT-events occur as well.

[9]A precondition for this to work is that the photons do not pile up, i.e. not more than one X-ray photon hits the same pixel during one readout cycle. In X-ray astronomy this precondition is valid most of the time due to low countrates.

written as

$$n(c) = \int\limits_{0}^{\infty} R(c,E)p(E) \ \mathrm{d}E \ . \tag{3.14}$$

Binning the continuous response function $R(c,E)$ on a discrete grid of energy bins and channels results in the response matrix:

$$R_D(c,j) = \frac{1}{E_j - E_{j-1}} \int\limits_{E_{j-1}}^{E_j} R(c,E) \ \mathrm{d}E \tag{3.15}$$

(George et al., 2007). The matrix $R_D(c,j)$ is called *response matrix* or *redistribution matrix* since it states how photons are "redistributed" onto detector channels. $R_D(c,j)$ is usually normalized to one (in channel-direction):

$$\sum_{c=0}^{c_{max}} R_D(c,j) = 1 \tag{3.16}$$

and states the probability of getting a signal in the PHA channel c from an incident photon with energy $E_{j-1} < E < E_j$. It is normally stored in a *Redistribution Matrix File* (RMF). As an example, the eROSITA RMF is illustrated in figure 3.7.

The detector's energy resolution can be estimated from the width of the main diagonal. The features below the main diagonal correspond to intrinsic effects of silicon detectors: When the primary photon activates a silicon atom in the detector material, which in turn emits a Si-K_α photon (1.74 keV), this Si-K_α photon is not always re-absorbed but can escape from the detector volume. The energy determined for the primary photon is thus reduced by 1.74 keV, which causes the *escape peak*. *Partial events* occur, when the charge produced by an event is not entirely registered by the detector. This happens especially for primary interactions close to the detector surface and leads to a continuous distribution below the main diagonal (see e.g. Popp et al., 2000).

Since the RMF is normalized to one, additional information is needed about the probability of whether a photon is detected at all. It is encoded in the effective area (see section 3.1.2) and is usually stored in the *Ancillary (or Auxiliary) Response File* (ARF). It is available for either on-axis or specific off-axis angles or averaged over the field-of-view (see e.g. figure 3.5, right panel).

In the case of eROSITA, the detector's response is available by the product of RMF and ARF and stored in a file with the extension "*.rsp*". Further literature about detector responses includes the books by Knoll (2000) and Tsoulfanidis (1995).

3.1.6   Countrate-to-Flux Conversion

A basic tool in (X-ray) astronomy is the conversion from a measured countrate to the source flux which represents the scientific product. For simulations, the opposite direction is important in order to simulate individual photons from a given source flux. The Energy Conversion Factor ECF is defined in the following way:

$$\mathrm{ECF}_{\mathrm{band/model}} = \frac{\text{instrumental countrate [counts/s]}}{\text{source flux in observer's frame [erg/cm}^2\text{/s]}} \tag{3.17}$$

Apart from the detector and filter properties (which are encoded in the response matrix), the ECF always depends on the specific model of the source spectrum and the specific energy band.
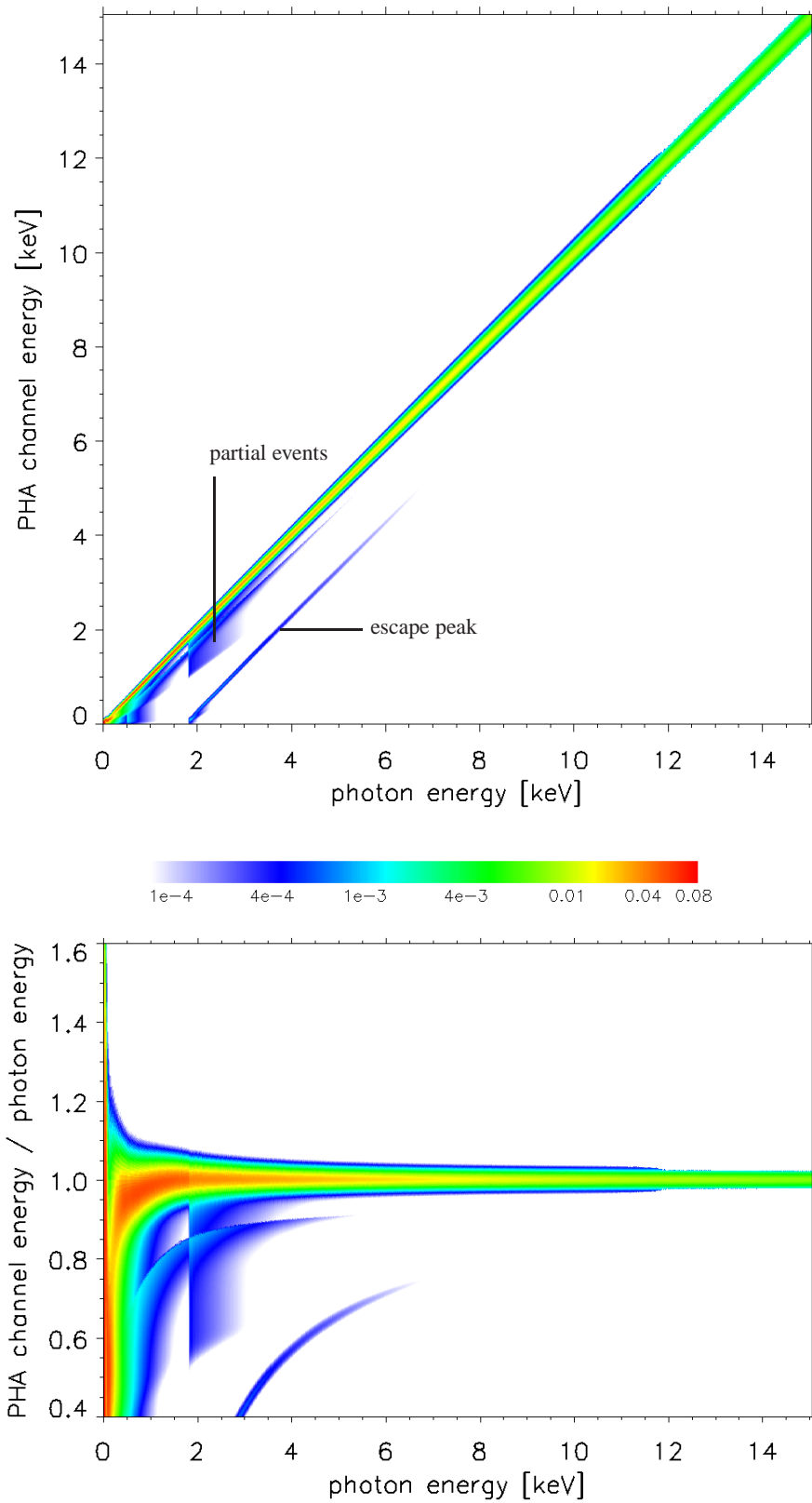
Figure 3.7: A model for eROSITA's redistribution matrix. **Upper panel:** For each photon energy, the color indicates the probability of getting a signal in the respective PHA channel. Each vertical cut through the distribution results in a spectral point spread function for the specific energy bin. **Lower panel:** For better visibility of the detector's energy resolution, the y-axis has been normalized to the photon energy. The logarithmic color scale is valid for both panels. Interesting features like *escape peak* and *partial events* are explained in the text.

The X-ray spectral fitting package Xspec[10] (Arnaud, 1996) is used to calculate ECFs for various source models.

   Some prerequisites are necessary to perform the calculation:

   EITHER

   1. (a) the redistribution matrix (see section 3.1.5) and

       (b) the ancillary response file, encoding the probability that a photon is detected at all (It takes into account the effective area of the mirror and the quantum efficiency of the detector.)

   OR

   2. a combination of the two (as in the case of the eROSITA .rsp-file used in this thesis).

Given a model spectrum $M(E)$, Xspec is then able to calculate the flux of this model within a certain Energy band $[E_{\min}, E_{\max}]$, as well as the countrate, which the instrument would observe within the same band. These can be inserted into equation (3.17) to compute the respective ECF value. Model spectra used in this thesis are for example a power law

$$M(E) \propto E^{-\Gamma} \tag{3.18}$$

or a thermal plasma model (e.g. *Mekal*[11] or *Raymond-Smith*[12]) which is a combination of bremsstrahlung and line emission from hot plasmas occurring for example in the ICM of galaxy clusters (see figure 2.2). Both can additionally be absorbed by galactic hydrogen which is modelled in Xspec as a multiplication factor to any emission model.

3.2   XMM-Newton

XMM-Newton, initially known as "High Throughput X-ray Spectroscopy" mission, was developed as the second Cornerstone Mission within the scope of the "Horizon 2000" program of the European Space Agency (ESA). The name XMM originates from the X-Ray Multi-Mirror design of this X-ray observatory. The second part of the name honors Sir Isaac Newton (1642-1727), who showed the principle of spectral analysis (with a glass prism) which is one of the main science drivers of XMM-Newton. The observatory was launched on 10th December 1999 from Kourou in French Guiana and it is the largest scientific satellite ever built in Europe[13].

   XMM-Newton is in a highly elliptical 48 hour orbit around the Earth with an apogee of $114\,000$ km and a perigee of $7\,000$ km. The satellite is designed for pointed observations, but it has been realized that the data, which taken during the slew between different targets, can make an important contribution to astronomical research in X-rays (e.g. Saxton et al., 2008).

   The satellite's payload consists of three co-aligned X-ray telescopes (XRTs) each with 58 nested mirror shells of the Wolter type 1 geometry (see section 3.1.1) with a focal length of $f_{\mathrm{XMM}} = 7493$ mm. The largest shell has a diameter of 70 cm. An additional optical/ultraviolet monitor telescope with 30 cm in diameter allows for simultaneous multiwavelength observations. Each of the XRTs is equipped with one European Photon Imaging Camera (EPIC) as focal plane

---

[10]http://heasarc.nasa.gov/xanadu/xspec/
[11]From Mewe, Kaastra and Liedahl (e.g. Mewe et al., 1985)
[12]Raymond and Smith (1977)
[13]See http://www.esa.int/esaSC/120385_index_0_m.html

detector. One of the three EPICs has been developed at MPE and it is called EPIC-PN (Strüder et al., 2001). This camera benefits from the full collection area of its XRT. It consists of twelve backside-illuminated CCDs with 200×64 pixels each and a scale of $4.1''$ per pixel. They have a high quantum efficiency of $QE_{PN} > 90\%$ over a broad energy range, but do not possess a frame store and are thus affected by out-of-time events.

The other two imaging detectors have been developed at Leicester University, UK and are called EPIC-MOS cameras (Turner et al., 2001). They share their telescope's light each with a Reflection Grating Spectrometer (RGS) which provides a much higher spectral resolution than the one intrinsic to the CCDs. Due to this light path splitting, the MOS detectors receive only about 44% of the light from their XRTs. Together with their quantum efficiency of $QE_{MOS} \approx 40 - 85\%$ this leads to the significantly lower effective area as compared to the PN detector, which is drawn in figure 3.8 (right panel). Each of the two MOS detectors consists of seven front-illuminated 600×600 pixel CCDs with a scale of $1.1''$ per pixel, which employ frame store technology. This suppresses out-of-time events (see section 3.1.4) to a large degree. PN and MOS refer to the respective semiconductor technology[14].
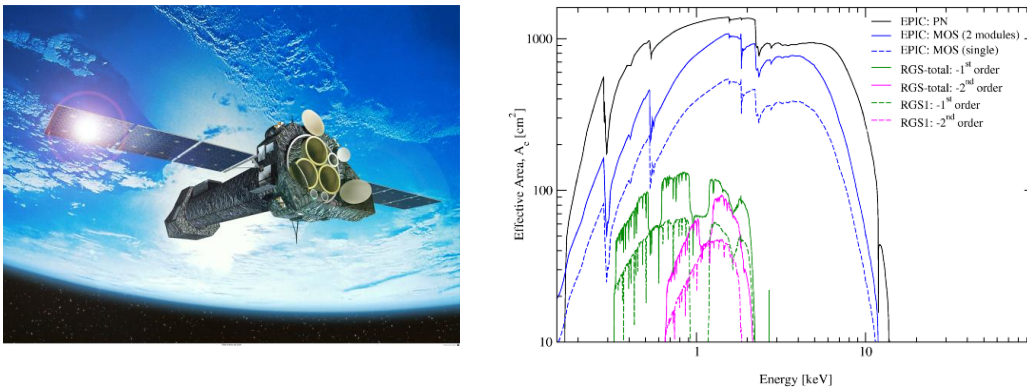
Figure 3.8: Left: Artist's impression of the XMM-Newton X-ray observatory. The three X-ray telescopes (XRTs) are well visible. Image courtesy of ESA. **Right:** On-axis effective area (see section 3.1.2) of the individual instruments of XMM-Newton. For imaging, the sum of the upper two curves is the relevant total effective area. (Plot from the XMM user handbook, Ehle et al., 2007)

XMM-Newton's field-of-view (FoV) is approximately circular with a diameter of about $30'$. The exact geometry depends on the detector. The PSF of the three X-ray telescopes is described in the chapter about point spread functions (section 4.2).

3.3 eROSITA

The eROSITA mission, the **e**xtended **RO**entgen **S**urvey with an **I**maging **T**elescope **A**rray, which is now being developed at the Max-Planck-Institute for Extraterrestrial Physics (MPE) has a long history dating back to the 1990s when ROSAT was still operating very well. The first part of this section gives an outline of these developments and the second part provides an overview of the mission's technology and its scientific goals.

---

[14]PN stands for the pn-junction in this CCD, MOS is the acronym for Metal Oxide Semiconductor.

3.3.1   Historical Development

ROSAT

The PSPC detector (Pfeffermann and Briel, 1986) on ROSAT (Trümper, 1982) had a sensitivity in the energy range between $0.1\,\mathrm{keV}$ and $2.4\,\mathrm{keV}$. Such soft X-ray radiation is strongly absorbed by dust which can be found e.g. in tori around active black holes (Active Galactic Nuclei, AGN). Therefore it was the desire to design an all-sky survey with an extended sensitivity towards harder X-rays in order to reveal the nature of those obscured black holes. XMM-Newton and Chandra (NASA's current major X-ray satellite, formerly known as AXAF, Weisskopf et al., 1996) would both be capable of observing in this extended energy range but they can only cover a small portion of the sky due to their smaller grasp[15]. See table 3.1 and figure 3.10 for a comparison of the grasps of eROSITA and XMM-Newton.

ABRIXAS

A Broad Band Imaging X-ray All-sky Survey (ABRIXAS, Hasinger et al., 1998) was planned in the energy range between $0.5\,\mathrm{keV}$ and $12\,\mathrm{keV}$ and the instrument was developed in collaboration of the Astrophysical Institute Potsdam (AIP), the Institute of Astronomy and Astrophysics Tübingen (IAAT) and the Max-Planck-Institute for Extraterrestrial Physics (MPE). ABRIXAS consisted of seven Wolter type telescopes, with 27 nested mirror shells each. The telescopes were focussed onto a common CCD (of the same type as it was used in XMM's PN camera) and therefore tilted with respect to each other by an angle of $7.25°$. This lead to a separation of the seven Fields of View (FoV) by the same angle. The FoV diameter was $40'$. ABRIXAS was launched into space on 28th April 1999. However, due to a failure in the satellite's power supply, the instrument could never be put into operation and thus the mission failed to achieve its scientific goal (see Predehl, 1999).

ROSITA

Immediately after this incident, plans were established to repeat the mission. The next attempt was started in 2002 with the plan to place an X-ray telescope on the International Space Station (ISS). It was called ROentgen Survey with an Imaging Telescope Array (ROSITA). The design was similar to that of ABRIXAS with the same 27 mirror shell telescopes. Although each of the seven telescopes this time was planned to be focused on individual CCDs, they were still tilted with respect to each other, due to the common detector housing of the seven CCDs (Predehl et al., 2003). Unfortunately, during the development phase of ROSITA, a contamination experiment showed that the space station's environment was inappropriate for the operation of an X-ray telescope (Friedrich et al., 2005).

DUO

A joint activity between the US and MPE lead to the proposal to NASA for a small explorer (SMEX) mission called Dark Universe Observatory (DUO, Griffiths et al., 2004). The instrument's design would have been a copy of ROSITA while the satellite was conceived as a free flyer in a low Earth orbit (LEO). The main scientific goal of the mission was to find clusters of galaxies in order to use them as a probe for Dark Energy studies. The mission aimed at finding 8000 galaxy

---

[15]The grasp of an instrument is the product of effective area times field-of-view and it is a measure of how efficiently the instrument can survey a portion of the sky.

clusters with redshifts up to $z < 0.7$ in a $6000 \deg^2$ wide survey and 1800 galaxy clusters in a $176 \deg^2$ deep survey with 100 clusters having redshifts larger than $z = 1$. Since NASA selected competing missions for their SMEX program, the DUO project was not followed beyond a phase A study.

Towards eROSITA

In 2005 the United States' Dark Energy Task Force (DETF[16]) announced a call for "white papers" to the experimental research community in order to get an overview of current and possible future projects on Dark Energy. One of those white papers (Haiman et al., 2005) showed that $\sim 100\,000$ clusters of galaxies would be necessary in order to constrain the Dark Energy equation-of-state reliably and distinguish it from a spatially flat ΛCDM model. Haiman et al. (2005) also stated the requirements for the feasibility of such a mission.

For being able to detect $100\,000$ clusters of galaxies, any previous design had to be upgraded to achieve a sufficient sensitivity in the soft X-ray band ($\lesssim 2 \,\mathrm{keV}$) where galaxy clusters have their strongest emission. This was accomplished by increasing the number of mirror shells for each of the seven telescopes from 27 to 54 which enlarges the collecting power at soft energies by a factor of five. For higher energies ($\gtrsim 5 \,\mathrm{keV}$), the additional 27 outer shells do not contribute much to the effective area because of the relatively large gracing angles. Due to this upgrade of the X-ray telescopes, the new project was called "*extended* ROSITA" and so eROSITA stands for

extended **RO**entgen **S**urvey with an **I**maging **T**elescope **A**rray.

Contemporaneous with the DETF activities in the US, MPE was looking for a possibility to realize a space flight for this challenging project. Negotiations between the Deutsches Zentrum für Luft- und Raumfahrt (DLR, the German space agency) and the Russian space agency Roskosmos eventually lead to the decision to join forces for a common space project called Spektrum-Röntgen-Gamma (SRG, Pavlinsky et al., 2006) which will be launched in 2012 from Baikonur, Kazakhstan. While initially further experiments were planned on the satellite platform, the only two instruments left over are now eROSITA and ART (Astronomical Roentgen Telescope), a Russian led X-ray telescope, which is optimized for the energy range between $2 \,\mathrm{keV}$ and $15 \,\mathrm{keV}$ (Arefiev et al., 2008). It is developed at the Russian Institute for Space Research (Институт Космических Исследований, say: "Institut Kosmicheskih Issledovanij", IKI).

Since March 2007, eROSITA is approved and funded by the DLR. Several German (and one international) research institutes are part of the collaboration:

- Max-Planck-Institut für extraterrestrische Physik (MPE), Garching, Germany
- Astrophysikalisches Institut Potsdam (AIP), Germany
- Institut für Astronomie und Astrophysik der Universität Tübingen (IAAT), Germany
- Hamburger Sternwarte, Universität Hamburg, Germany
- Dr. Remeis-Sternwarte, Universität Erlangen-Nürnberg, Bamberg, Germany
- Space Research Institute, IKI, Moskau, Russia
- Max-Planck-Institut für Astrophysik (MPA), Garching, Germany
- Argelander-Institut für Astronomie, Universität Bonn, Germany
- Universitäts-Sternwarte der Ludwig-Maximilians-Universität, München, Germany.

---

[16]The DETF is a joint sub-committee established by the Astronomy and Astrophysics Advisory Committee (AAAC) and the High Energy Physics Advisory Panel (HEPAP) in order to advise the Department of Energy (DOE), the National Aeronautics and Space Administration (NASA), and the National Science Foundation (NSF) on the future of Dark Energy research (See DETF report by Albrecht et al., 2006).
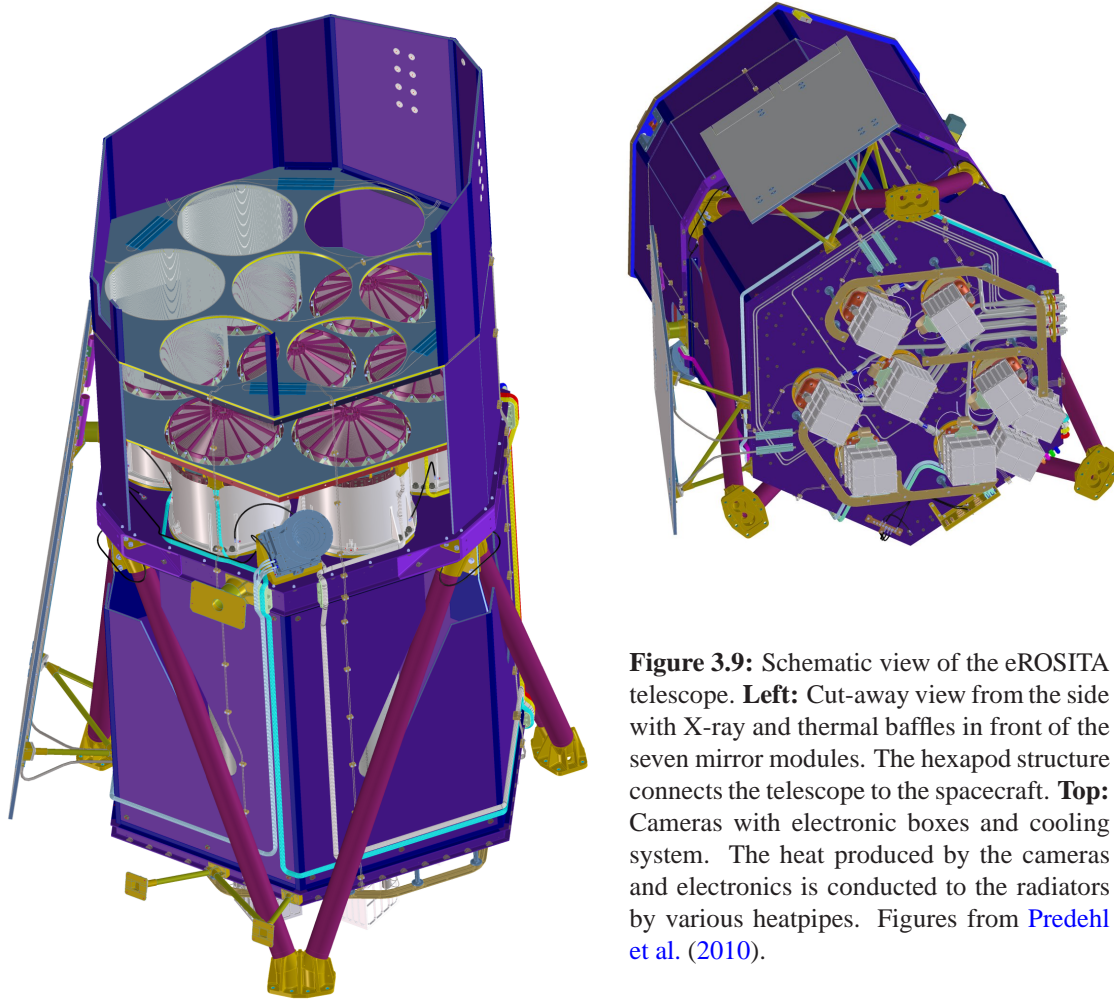
Figure 3.9: Schematic view of the eROSITA telescope. **Left:** Cut-away view from the side with X-ray and thermal baffles in front of the seven mirror modules. The hexapod structure connects the telescope to the spacecraft. **Top:** Cameras with electronic boxes and cooling system. The heat produced by the cameras and electronics is conducted to the radiators by various heatpipes. Figures from Predehl et al. (2010).

Figure 3.9 shows a schematic view of the eROSITA instrument (the satellite bus is omitted here). As opposed to ABRIXAS and ROSITA, the telescopes are now co-aligned and thus always observe the same field on the sky. Having seven individual XRTs is still an advantage for several reasons: (i) margin is allowed for the case of an instrumental failure, (ii) the X-ray flux of bright sources is shared among the telescopes which decreases the effects of pile-up (see section 3.3.2), (iii) the manufacturing of seven small telescopes is easier than making a big one with the same effective area, and (iv) the required diameter of one big telescope would decrease the effective area at high energies, due to the large gracing angles of the outer mirror shells.

3.3.2   Instrumental Concept

Since its beginnings the eROSITA project underwent some major design changes. The two most significant ones are the change of the detector size and the change of the spacecraft's orbit: While in 2006 the mission design still envisioned a detector size of 256×256 pixels (Predehl et al., 2006), by 2007 it was enlarged to 384×384 pixels (Predehl et al., 2007) which also meant an increase in the field-of-view from a square with $41.3' \times 41.3'$ to a circle with $61.8'$ diameter. The four corners of the CCD are now available for monitoring the high energy particle radiation in the spacecraft's environment.

The second major modification concerns the orbit of Spektrum-RG. Initially, it was planned to fly in a Low Earth Orbit (LEO). Due to technical constraints this had to be changed to an orbit around the second Lagrangian point of the Sun-Earth system (L2). The advantages and disadvantages of this orbit are briefly discussed in section 3.4.4. During its orbit, the instrument will be scanning over the sky with a constant angular velocity of about 4 to 6 hours per revolution, while permanently collecting X-ray photons.

The eROSITA instrument[17] consists of seven Wolter type 1 telescopes with 54 nested mirror shells each and a focal length of $f = 1600$ mm. The resolution of each X-ray telescope is required to be such that the on-axis PSF has a half energy width of better than HEW $< 15''$. Friedrich et al. (2008) give an overview of the status of the mirror fabrication. The telescopes are co-aligned and thus observe the same field-of-view. Each of them is focussed onto an individual CCD mounted in its dedicated detector housing. Every CCD has 384×384 pixels with a size of 75 μm $\times$ 75 μm corresponding to $9.67'' \times 9.67''$ on the sky. In addition, the CCDs possess a frame store with a pixel size of 51 μm $\times$ 75 μm in order to suppress out-of-time events. The frame store area is covered with 1 mm of boron carbide (B_4C) and thus insensitive to X-rays. It is only used as an image buffer. The CCD cycle time is 20 Hz so that the exposure time of one frame is approximately 50 ms. After each exposure, the image is shifted into the frame store area within about 200 μs. Once the image is kept in the frame store, it can be read out by the CAMEX chips (CMOS Amplifier and MultiplEXer) at lower pace while the imaging area is already back to collecting new X-ray photons. The readout takes ~ 5 ms. During the remaining ~ 45 ms the CAMEX chips are switched to standby mode in order to minimize the heat load onto the CCDs (Meidinger et al., 2008).

The short exposure time is chosen for two reasons. On the one hand, the scanning of the instrument broadens the effective PSF in scan direction: Attitude[18] information is only available for each CCD frame and not for each individual photon since the exact arrival time of a photon within one exposure time is not available. This effect can be minimized by choosing a sufficiently short exposure time. The more important reason is on the other hand, that photon pile-up has to be avoided: The CCD electronics assumes, that there is always only one photon per pixel per CCD frame. If two (or more) photons arrive in the same pixel within one exposure time they will be treated as one and the event will be recorded having an energy equal to the sum of the two photon energies. Therefore the frame rate has to be chosen high enough so that even for bright sources pile-up occurs very rarely. Pile-up is also suppressed by the sharing of the X-ray flux of strong sources among the seven telescopes and thus the seven CCDs.

Table 3.1 provides a comparison between the instrumental parameters of eROSITA and XMM-Newton. The observing strategy of eROSITA is described in section 3.4.4. Chapter 4 puts the focus on the instrument's point spread function.

3.3.3   Scientific Mission Goals

While the scientific focus of ABRIXAS and ROSITA was still on revealing the nature of obscured black holes, the enlarged effective area at soft X-ray energies of eROSITA reflects the change of the primary mission goal towards clusters of galaxies (compare the typical emission spectra of galaxy clusters in figure 2.2 with eROSITA's effective area plot in figure 3.5, right panel).

---

[17]Design criteria are specified in the document eRO-MPE-RS-13-04_3 "System Requirements".

[18]Attitude is the current orientation of a spacecraft or the pointing direction in the case of a spaceborne observatory.

Instrumental parameter	eROSITA value	XMM value	
spacecraft orbit	orbit around L2	highly elliptical Earth orbit	
observing mode	survey & pointing	pointing	
number of XRTs	7	3	
FoV diameter	$61.8'$	$\sim 30'$	
total on-axis eff. area at 1 keV	~ 2300 cm^2	~ 2500 cm^2	
grasp at 1 keV	~ 1100 cm$^2 \cdot$ deg^2	~ 250 cm$^2 \cdot$ deg^2	
on-axis HEW	$\leqslant 15''$	$13''$-$15''$	
average HEW in scanning mode	$\sim 30''$	not applicable	
focal length	1600 mm	7493 mm	
		EPIC-PN	EPIC-MOS
number of pixels per detector	384×384	$12 \times 200 \times 64$	$7 \times 600 \times 600$
pixel size	75 μm	150 μm	40 μm
pixel scale	$9.67''$	$4.1''$	$1.1''$
frame store	yes	no	yes

Table 3.1: Comparison between the instrumental parameters of XMM-Newton and the specifications of eROSITA.

Cosmology and Galaxy Cluster Science

Galaxy clusters can be observed most efficiently in X-rays. Optical surveys suffer from projection effects where e.g. a filament of the large-scale structure (LSS) seen along its major axis could be mistaken as a cluster of galaxies. Surveys relying on the Sunyaev-Zel'dovich (SZ) effects (Sunyaev and Zel'dovich, 1972, 1980) are still in the development phase or are slowly emerging and starting to produce first results. The large cluster sample expected from eROSITA will be exploited in many different ways. For a list of cosmological applications see section 2.4.2. If everything works out according to plan, eROSITA will be the first dedicated Dark Energy mission in space more than ten years after the first convincing evidence of Dark Energy (Riess et al., 1998).

Also research on the astrophysics of galaxy clusters can gain a lot from a large data set as it is expected from eROSITA. A list of astrophysical applications is provided in section 2.4.3.

AGN Science

The primary goal of the ABRIXAS and ROSITA missions was the detection of all Active Galactic Nuclei (AGN) in the local universe. This is still kept as a secondary goal for the eROSITA mission and addresses several scientific issues:

- The logN-logS relations of the extragalactic point-source population has been determined by pencil beam observations of the Lockman Hole (LH) and the Chandra Deep Fields (CDF-N and CDF-S) and especially by the COSMOS survey. For a summary of these projects see e.g. Brandt and Hasinger (2005) and Cappelluti et al. (2009b), respectively. However, the bright end of the logN-logS relation is still poorly determined and shows large error bars especially at high energies which were not observable with ROSAT. The all-sky survey of eROSITA with its sensitivity up to 10 keV will ideally be suited to fill this observational gap.
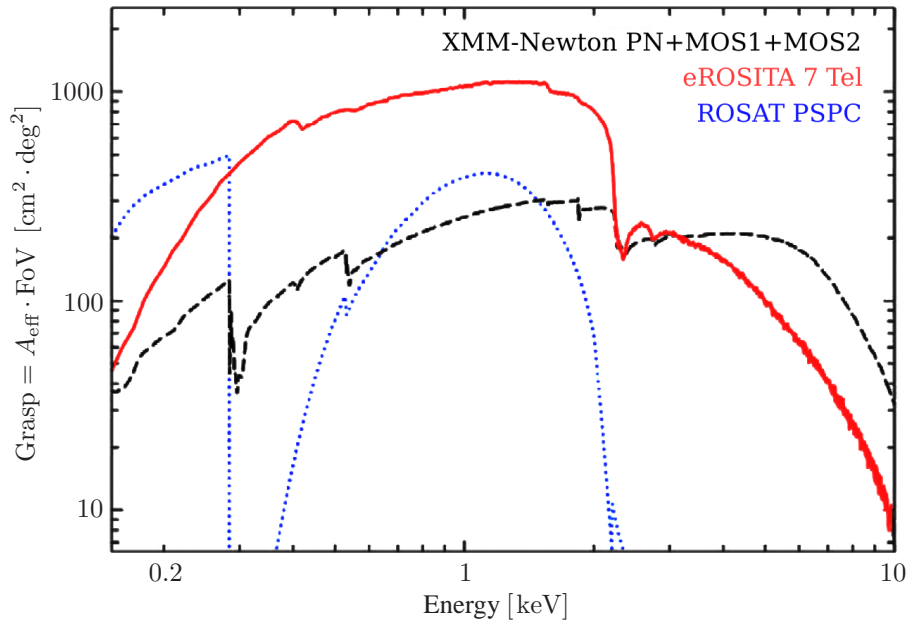
Figure 3.10: Grasp (product of effective area times field-of-view) of the eROSITA telescope in comparison with XMM-Newton and the ROSAT PSPC. The vignetting effect is properly taken into account. Plot from Predehl et al. (2010).

- The various types of AGN have been united in a *unified model* (e.g. Antonucci, 1993), which is still subject to debates among specialists in the field. Due to its enlarged energy range as compared to ROSAT, eROSITA will identify also AGN which are obscured by dust tori. This large sample will help to improve our understanding of the physical mechanisms going on in AGN and thus verify the unified picture of AGN physics. Additionally it will be possible to test general relativity in the high gravitational field environment of supermassive black holes.

- It has been realized that not only galaxy clusters but also AGN show some spatial correlation with the Large Scale Structure (LSS) of the universe. Small surveys like the COSMOS field are strongly affected by cosmic variance and low number statistics. eROSITA will overcome this problem with its all-sky survey. For an overview of the recent status of this research field see e.g. Cappelluti (2007).

Other Scientific Goals

There has been a debate among scientists about the scientific output of classical telescopes versus that of dedicated Dark Energy missions (White, 2007). Although Dark Energy research is one of the main science drivers of eROSITA, many other fields of high energy astronomy will benefit from this X-ray all-sky survey as well. Apart from the already mentioned AGN research, some further examples are

- Supersoft sources and classical novae (e.g Henze et al., 2009, Pietsch et al., 2005)

- Events of tidal disruption of stars by black holes (e.g. Cappelluti et al., 2009a, Komossa et al., 2009)

- Neutron Stars (for prospects of neutron star science with eROSITA see e.g. Grünecker, 2008, (in German))

- Cataclysmic variables

- Gamma-ray bursts and other transient events

- Stellar coronae

3.4 X-Ray Cluster Surveys

This section gives an overview of the known X-ray cluster population in the era *before* the two large X-ray observatories Chandra and XMM-Newton, i.e. including samples from the ROSAT All-Sky Survey (RASS) and its sub-samples. Then it introduces the XMM-Newton Distant Cluster Project (XDCP) and other current X-ray surveys based on XMM data before it describes the observing strategy of the eROSITA survey.

3.4.1 X-Ray detected Galaxy Clusters before Chandra and XMM-Newton

The eROSITA project aims at the detection of $\sim 100\,000$ X-ray galaxy clusters up to a redshift of $z \approx 1.5$. This is a huge advancement if one compares to the numbers of X-ray selected clusters known today and also a large extension of the redshift space of the known cluster population of the ROSAT era.

The first X-ray flux connected to galaxy clusters was identified from M87 in the Virgo Cluster (Byram et al., 1966) and the Perseus Cluster (Fritz et al., 1971) with rocket-borne experiments. With the Uhuru satellite (Giacconi et al., 1971), it was possible to detect the Coma Cluster (Gursky et al., 1971) and to reveal the extended nature of the X-ray emission from galaxy clusters (Kellogg et al., 1972). A few hundred X-ray clusters were detected with the first High Energy Astronomy Observatory (HEAO-1, e.g. Johnson et al., 1983) and the Einstein Observatory (Giacconi et al., 1979), for example by the Einstein Extended Medium Sensitivity Survey (EMSS, Gioia et al., 1990). Abound 200 to 300 X-ray clusters are known from Einstein. A more concise overview on X-ray detections of galaxy clusters in the pre-ROSAT era can be found in Sarazin (1986).

A major step forward in the size of X-ray galaxy cluster samples was done with the analysis of the ROSAT data. The ROSAT-ESO Flux-Limited X-ray cluster survey (REFLEX Böhringer et al., 2004) and the NOrthern ROSAT All-Sky Survey (NORAS Böhringer et al., 2000) are derived from the RASS data and currently the largest statistically complete X-ray cluster samples. Together with their successor catalogues REFLEX II and NORAS II (in preparation) from reanalysis of ROSAT data, they include a total of approximately 1800 galaxy clusters up to redshifts of $z \lesssim 0.5$.

Deep ROSAT surveys like the North Ecliptic Pole survey (NEP survey, Henry et al., 2006), the $400 \deg^2$ large area survey (400d survey, Burenin et al., 2007) and the ROSAT Deep Cluster Survey (RDCS, Rosati et al., 1998)[19] contain in total about 400 X-ray clusters. The redshift record among these has been achieved with the RDCS at $z = 1.27$. From the same survey, ~ 10 clusters with $z \geq 0.8$ and ~ 5 clusters with $z \geq 1.0$ are known (Rosati et al., 2000).

---

[19]The 400d survey and the RDCS are based on serendipitous cluster searches in ROSAT pointed observations.

3.4.2 The XMM-Newton Distant Cluster Project (XDCP)

With the launch of the large X-ray observatories Chandra and XMM-Newton, it was possible to extend some observational parameter spaces. With Chandra's high resolution mirror assembly[20], it became possible to resolve the cores of distant clusters and study their structural properties in unprecedented detail. With XMM-Newton and its large effective area on the other hand, the observable redshift range was increased as compared to previous missions. Chandra and XMM-Newton were designed as pointing instruments and can therefore only observe small regions of the sky (see e.g. XMM's grasp in table 3.1 and figure 3.10).

However, all data which has been collected by XMM-Newton is stored in the XMM-Newton Science Archive[21] (XSA, see also Arviset et al., 2002). After a proprietary phase of one year, all collected data become publically available. Some research groups are utilizing this fact by re-analyzing archival data and looking for galaxy clusters which have not been found in the data before. One of these activities is the XMM-Newton Distant Cluster Project (XDCP) which is conducted in the galaxy cluster group at MPE (Fassbender, 2008, Böhringer et al., 2005, Mullis et al., 2005).

Each pointing in the archive usually contains its scientific target object in the center of the field-of-view. In most cases there is a large area at higher off-axis angles which has never been looked at in detail. The XDCP is looking for galaxy clusters in suitable pointings from the XMM-Newton Science Archive (XSA) with a focus on distant clusters, i.e. clusters with a redshift around $z \approx 0.8$ or larger. Such a survey is called a serendipitous survey because clusters were observed by chance although the initial science objective had been a different one. As of the current status the XDCP has found 25 spectroscopically confirmed galaxy clusters with redshifts beyond $z > 0.8$.

The XDCP works in several steps:

Field selection: The XSA is screened for suitable pointings. If a pointing is for example 'contaminated' by foreground objects like a Magellanic Cloud or the Andromeda Galaxy M31 or attributed to another dedicated cluster survey program, it is rejected. Other requirements are a minimum exposure time of at least 10 ks, a high galactic latitude of $|b| \geq 20°$ and that the field is accessible by the ESO VLT (field declination $\mathrm{DEC} \leq +20°$).

Field analysis: The selected fields are scanned for serendipitous extended sources by a dedicated analysis pipeline. This is a very efficient method since in X-rays most extended sources are clusters of galaxies.

Candidate selection: The positions of the detected extended sources are checked for an optical counterpart in archived optical data. The candidates with no optical counterpart are classified as potentially distant because their redshift is high enough for not being seen in the shallow optical images.

Photometric follow-up: The distant candidates are followed-up with an imaging instrument at a ground-based optical telescope (at least four-meter-class) in two or more suitable optical/infrared filter bands. The cluster can be identified based on the colors of the individual

---

[20]Chandra's total PSF (including mirror shells and detector) is very sharp: $\mathrm{HEW_{tot}} < 1''$. This was possible because of the special fabrication of the telescope. It consists of only four Wolter type 1 shells made from precision figured and super-polished Zerodur glass with iridium coating. The payoff for this high accuracy is a rather low effective area of about $650 \mathrm{~cm}^2$ at 1 keV (see e.g. Weisskopf et al., 2002).

[21]The XSA can be found at the following url: http://xmm.esac.esa.int/xsa/index.shtml

cluster galaxies. Its redshift is determined by a red sequence technique relying on the color-magnitude diagram (see Fassbender, 2008).

Spectroscopic follow-up: Candidates with a photometric redshift of $z \gtrsim 0.8$ are spectroscopically followed up by an eight-meter-class telescope for final confirmation and exact redshift determination.

Scientific Goals of the XDCP

The main goals of the XMM-Newton Distant Cluster Project are:

- Determine the evolution of the cluster number density out to redshift $z \sim 1.5$.

- Provide a statistically complete sample of high-redshift clusters for cosmological studies.

- Study in detail the high redshift cluster properties and their statistics.

- Make high redshift clusters available for follow-up in all wavelengths and detailed astrophysical studies.

- Test observational and data analysis strategies of high-redshift clusters and thus clear the way for the upcoming larger surveys like eROSITA.

Cluster Number Density and the Need for Simulations

In order to compute the (comoving) cluster number density $\frac{\mathrm{d}^2 N}{\mathrm{d}M \, \mathrm{d}V_{\mathrm{com}}}$, an accurate determination of all three components (mass, comoving search volume and cluster number) is an important prerequisite. In flux limited surveys with a limiting flux much higher than the sensitivity of the lowest exposure ($f_{\mathrm{lim}}(\mathrm{survey}) \gg f_{\mathrm{lim}}(\mathrm{lowest\ exposure})$), it is clear that all clusters have in principle been detected. However, going as deep as possible in flux limit is of course the desire of any ambitious project. At borderline fluxes, not all clusters are detected any more because they might have a too large core radius and thus disappear in the background or they might be "hidden" behind a bright AGN. The quantity which describes this effect is called *completeness*. It is defined as the percentage of galaxy clusters which are discovered down to a certain flux f:

$$c(f) = \frac{\text{number of discovered clusters}(f)}{\text{number of real clusters}(f)} \ . \tag{3.19}$$

Since the real underlying cluster population is unknown, the survey completeness can only be calibrated by simulations. These simulations and the computation of the survey volume are described in detail in chapters 5 and 6.

3.4.3   Other XMM-Newton based Cluster Surveys

The XDCP is not the only cluster survey making use of the good sensitivity of XMM-Newton. Another serendipitous survey is the XMM Cluster Survey (XCS) which is not particularly focussed on high redshift clusters. Initial estimates predicted the discovery of 8000 X-ray clusters from the XMM Science Archive with about 750 clusters with $z > 1$ (Romer et al., 2001). These predictions were based on a cosmological model with large cluster abundances and observational conditions facilitating cluster detection which both turned out to be too optimistic. In the current status of the

project, 30 cluster candidates with redshifts $0.8 < z < 1$ and 14 cluster candidates with redshifts $z > 1$ have been detected[22].

Among the serendipitous surveys, it is also worth mentioning the "XMM-Newton Serendipitous Survey" which is performed by the XMM-Newton Survey Science Centre (SSC) and is a general survey without a focus on any specific object class. The SSC is a consortium of ten institutes within Europe, including MPE, with the tasks to compile and follow-up the XMM-Newton Serendipitous Source Catalogue, and to participate in the pipeline processing of all XMM observations and further development of the analysis software (Watson et al., 2001). The most recent catalogue from the SSC is the Second XMM-Newton serendipitous source catalogue (2XMM, Watson et al., 2009). One of the most luminous high redshift clusters was identified in 2XMM by Lamer et al. (2008).

Also dedicated cluster surveys (as opposed to serendipitous ones) are being performed with XMM-Newton. Among them is the XMM Large-scale Structure Survey (XMM-LSS, Pierre et al., 2004) planning to cover a contiguous field of $64 \deg^2$ and the X-ray part of the multi-wavelength Blanco Cosmology Survey (XMM-BCS, for first results see Suhada et al., 2010) covering $14 \deg^2$. The deep multi-wavelength Cosmic Evolution Survey (COSMOS), aiming to study the formation and evolution of galaxies, identified 72 galaxy clusters with a maximum redshift of $z = 1.25$ in a field of $2 \deg^2$ (COSMOS, e.g. Finoguenov et al., 2007).

3.4.4 Observing Strategy of the eROSITA Mission

As already mentioned in section 3.3.2, Spektrum-Röntgen-Gamma will be launched into an orbit around the second Lagrangian point of the Sun-Earth-system (L2). This special location is defined as the point where the centrifugal force on a spacecraft orbiting the Sun (!) is exactly balanced by the gravity of Sun and Earth, acting as centripetal force. L2 is located at a distance of 1.5 million kilometers from the Earth in the direction away from the Sun and the point is in a solar orbit moving along with the Earth.

The launch of Spektrum-Röntgen-Gamma is scheduled for 2012 from the Baikonur cosmodrome in Kazakhstan. Soon after the launch, eROSITA will begin its checkout phase with the opening of the telescope cover. During the ~ 110 days of cruise time to L2, the instrumental calibration and commissioning phase is planned. This includes for example the cool-down of the cameras and some pointed observations of selected calibration targets.

During its orbit around L2, the spacecraft describes an ellipse with L2 at its center (not its focus). The orbit will be inclined by $\sim 65°$, i.e. the semi-minor axis, measuring $250\,000 \text{ km}$, encloses an angle of $65°$ with the ecliptic plane. The semi-major axis is oriented along a tangent to the Earth's orbit around the Sun and measures $300\,000 \text{ km}$. The orbital period will be ~ 180 days.

In principle independent from the spacecraft's orbit is the movement of the instruments' scan over the sky. There are however three major constraints which the spacecraft has to obey: (i) the solar panels have to be directed towards the Sun with some degrees of tolerance, (ii) the heat radiator should never be irradiated by the Sun, and (iii) the spacecraft's antenna always has to point towards the Earth. Since the antenna cone angle is only $2°$, and a continuous re-orientation of the antenna should be avoided, the latter one is a very tight constraint and therefore determines the spacecraft's scan-axis. The duration of one revolution of the spacecraft around itself is to be

---

[22]According to a recent presentation on the conference "Galaxy Clusters in the Early Universe" in Pucón, Chile: http://www.eso.org/sci/meetings/GCEU2009/Talks/K_Romer.pdf
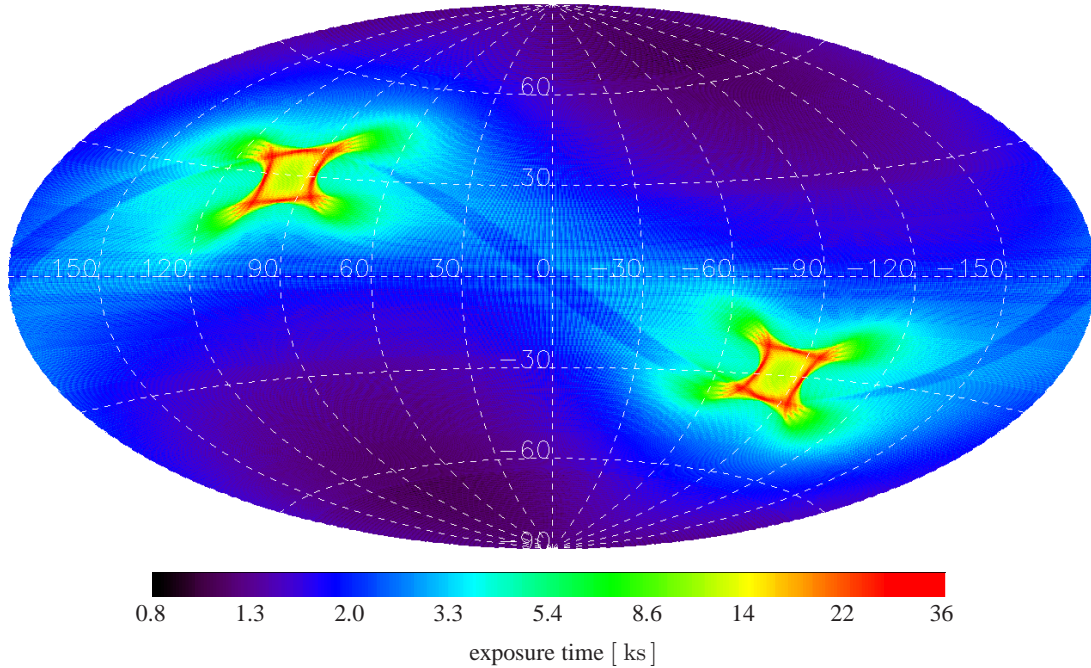
Figure 3.11: Aitoff projection of the exposure map of the eROSITA all-sky survey in galactic coordinates and logarithmic scale. The assumed survey parameters are: mission duration = 4 years, scanning rate = 4 hours per revolution, scan axis pointing towards the Earth and observing efficiency = 80%. Image courtesy of Maria Fürmetz (MPE).

determined and will be around 4 to 6 hours, i.e. the scan velocity will be around $1.5\,\mathrm{arcmin/s}$ to $1\,\mathrm{arcmin/s}$. A source crossing the FoV through its center is therefore visible for $40\,\mathrm{s}$ to $60\,\mathrm{s}$.

Adding all constraints and parameters together this leads to an all-sky survey which has its deepest exposures at the ecliptic poles. The orientation of the scan-axis will change during the course of the 180 days orbit. This leads to a smearing of the survey poles, which is absolutely desired in order to provide an extended and more homogeneous deep survey area of $\sim 2 \times 100 \deg^2$. A further smearing could be achieved by variation of the scan velocity during the scanning over the survey poles. This option has to be investigated by simulations outside the scope of this thesis.

Figure 3.11 shows a simulation of the expected all-sky exposure map after four years of mission duration with a scan velocity of $1.5\,\mathrm{arcmin/s}$ ($\,\widehat{=}\,4\,\mathrm{h}$ per revolution). An observing efficiency of 80% was assumed. This fraction of the 4 year all-sky survey, in which the instrument will be observing, is a conservative estimate based on experience with ROSAT. While ROSAT was regularly switched off during passages of the South Atlantic Anomaly (SAA), eROSITA's efficiency will mostly be limited by times of high particle radiation due to solar flares. This exposure map is used for the estimation of the cluster yield discussed in chapter 8.

Mission Phases

The scheduled seven years of mission lifetime are divided into the following phases:

- Checkout- and commissioning phase: This will be performed during the ~ 110 days of cruise time to L2.

- All-sky survey: Four years with constant rotation of the spacecraft around the scan-axis. One all-sky scan takes half a year and thus the sky will be scanned in total eight times during this mission phase.

- Deep survey: This is included in the all-sky survey through the deeper scan of the ecliptic poles. Further deep surveys might be achieved through variations of the scan velocity. This option is still under investigation.

- Pointing phase: After the all-sky survey, a series of individual observations with long exposures and fixed spacecraft attitude is planned. This includes for example some follow-up observations of interesting targets which are discovered during the survey phase.

Comparison of the Low Earth Orbit with the Orbit around L2

One major change during the design phase of eROSITA was the modification of the orbit. Due to space flight related reasons it was decided in 2008 that the mission will not be in a low Earth orbit (LEO) but in an orbit around L2.

The major disadvantage of the L2 orbit is the expected higher background radiation which will also have consequences on cluster detection. Another problem is, that the spacecraft is now outside the Van Allen radiation belts, which protect low Earth orbit missions from cosmic rays. Therefore the electronics has to be specially designed to survive in the high radiation space environment. On the other hand, in this respect eROSITA can serve as a pathfinder mission for the upcoming "International X-Ray Observatory" (IXO, see e.g. White and Hornschemeier, 2009) which will also be in an L2 orbit. Furthermore, there are also positive aspects of being far away from the radiation belts because in low Earth orbit, the instrument would suffer from high radiation impact during passages of the South Atlantic Anomaly (SAA).

The major advantage of the new eROSITA orbit is the increased flexibility in terms of mission planning. Continuous observing time in all directions without occultations by the Earth is now possible. This leads to an easier navigation concept with fewer maneuvers during the all-sky survey and ensures the possibility of performing very long observations during the pointing phase. A technical advantage are the stable thermal conditions as compared to the complicated situation in low Earth orbit with the Earth as largest heat radiator and the spacecraft regularly passing the Earth's shadow.

Chapter 4

Models and Measurements of Point Spread Functions

The concept of the Point Spread Function (PSF) was introduced in section 3.1.3. It is defined as the instrumental response to a point-source. In realistic instrument simulations, this effect is taken into account properly by regarding the PSF as a probability distribution. In this case, it states the probability that a photon is scattered to a certain position within the PSF.

The representation of a PSF for utilization in a simulator can be an analytical formula or a digitized dataset, i.e. a *sampled* PSF. There are mainly two different origins of such a dataset: it can either be from a real observation and the analysis of point sources in the image, or it can be simulated by ray-tracing codes of varying complexity. In either case, the dataset is called a "PSF model".

This chapter introduces several concepts concerning point spread functions (section 4.1) and gives an overview of the PSF models being dealt with in this thesis (section 4.2 for XMM-Newton and section 4.3 for a ray-tracing model of eROSITA's PSF). The second intention of this chapter is to summarize the work on Sub-Pixel Resolution (SPR) which has been performed within the scope of the thesis (section 4.4). The last section (4.5) reports on first applications of the developed SPR algorithm for the purpose of X-ray measurements of individual eROSITA mirror shells. This gives an idea of what the real PSFs of the seven eROSITA telescopes might look like.

4.1 General Considerations about Point Spread Functions

There are various means of describing a PSF in general. Three of them shall be described here in order to provide the reader with the necessary concepts and terminology for the following sections.

Analytic Descriptions

The only case in which the full information is given, is when the function is given in analytic form. For example in quicklook image simulations, a PSF is often approximated as a Gaussian although it is only a rough approximation to a realistic PSF of X-ray telescopes (see figure 4.1). The shape can be described either as a one dimensional radial distribution which is being rotated about the center (equation 4.1, centered around $r = 0$) or as a two dimensional Gaussian on a Cartesian
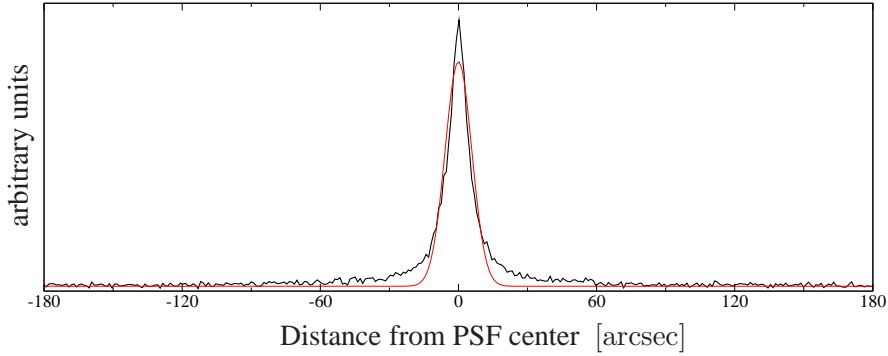
Figure 4.1: Comparison of two PSF projections: The black curve is the projection of a real PSF created from a point-source image taken with the MOS1 detector onboard XMM-Newton (figure 4.2, left panel). The red curve is a Gaussian fitted to the distribution. It can be seen that a Gaussian is only a rough approximation to a realistic PSF: the PSF is more peaked in the center and has broader wings than the Gaussian.

coordinate system (equation 4.2, centered around $x, y = 0, 0$) [1]:

$$\text{PSF}(r) = \frac{1}{2\pi\sigma^2} \exp\left[-\frac{1}{2}\left(\frac{r}{\sigma}\right)^2\right] \tag{4.1}$$

$$\text{PSF}(x, y) = \frac{1}{2\pi\sigma_x\sigma_y} \exp\left[-\frac{x^2}{2\sigma_x^2} - \frac{y^2}{2\sigma_y^2}\right] \quad . \tag{4.2}$$

PSF Images

Realistic point spread functions are often too complicated to be expressed as analytic functions. A further way of describing a PSF is to represent it in an image. The image can be derived e.g. from real observations of point-sources or from ray-tracing simulations (in principle also from sampling of analytic functions). In either way, an image can never be as accurate as an analytic description although it usually takes much more memory to store it. The image has however the advantage that it is much more flexible in storing any kinds of PSFs, especially when it comes to azimuthally *asymmetric* shapes (see e.g. figure 4.3) which is important for off-axis sources.

FWHM and HEW

The most compressed form of describing a PSF is when only one number is given. There are mainly two figures used to characterize the distributions: The **Full Width at Half Maximum (FWHM)** is the diameter of the distribution at the probability level of half the maximum (peak-) probability. In the case of the radial description (e.g. equation 4.1), this can be written as:

$$\text{PSF}(r = \text{FWHM}/2) = \frac{1}{2}\text{PSF}(r = 0) , \tag{4.3}$$

whereas in the case of an elliptical PSF (e.g. with $\sigma_x\sigma_y$ in equation 4.2) the FWHM depends on the azimuthal angle at which it is measured.

---

[1]Note that the normalization constant is different from that of the one-dimensional normal distribution ($\frac{1}{\sigma\sqrt{2\pi}}$) because the *volume* under the function has to be equal to one rather than the *area*.

The **Half Energy Width (HEW)** is the diameter of a circle around the center of the distribution, which contains half of the total amount of energy (or photons) in the distribution. Since the PSF is normalized to one (equations 3.10 and 3.11) this can be expressed by equating the two-dimensional integral over the distribution to $\frac{1}{2}$:

$$\int_{0}^{2\pi} \int_{0}^{\text{HEW}/2} \text{PSF}(r)\; r\,\mathrm{d}r\,\mathrm{d}\phi = \frac{1}{2} \;. \tag{4.4}$$

In special cases, also modifications of the HEW are used with a different fraction of encircled energy ξ:

$$\int_{0}^{2\pi} \int_{0}^{W_{\xi*100}/2} \text{PSF}(r)\; r\,\mathrm{d}r\,\mathrm{d}\phi = \xi \;. \tag{4.5}$$

For example, W_{90} is commonly used to describe the scattering halo of a PSF of an X-ray mirror.

As an illustration, the HEW and FWHM values of a Gaussian distribution depending on its standard deviation are calculated here. Using the PSF definition of equation (4.1), equation (4.3) reads:

$$\frac{1}{2\pi\sigma^2} \exp\left[-\frac{1}{2}\left(\frac{\text{FWHM}}{2\sigma}\right)^2\right] = \frac{1}{4\pi\sigma^2} \;. \tag{4.6}$$

Solving this for FWHM yields

$$\text{FWHM} = \sigma\sqrt{8\ln 2} \approx 2.3548\sigma \;. \tag{4.7}$$

To calculate the HEW of a Gaussian, equation (4.1) is inserted into equation (4.4):

$$\int_{0}^{2\pi} \int_{0}^{\text{HEW}/2} \frac{1}{2\pi\sigma^2} \exp\left[-\frac{1}{2}\left(\frac{r}{\sigma}\right)^2\right] r\,\mathrm{d}r\,\mathrm{d}\phi = \frac{1}{2} \;. \tag{4.8}$$

Thanks to the Jacobian r, this integration is straightforward and leads to

$$\text{HEW} = \sigma\sqrt{8\ln 2} \approx 2.3548\sigma \;. \tag{4.9}$$

Thus, HEW and FWHM are equal for two-dimensional Gaussian distributions. For all other shapes, they can have any relation with respect to each other. While the FWHM describes the sharpness of the PSF's core, the HEW is a measure of the intensity in the wings with respect to the core.

4.2 XMM-Newton's PSFs and their Models

4.2.1 The Real PSFs

The fabrication of high quality X-ray mirrors (see section 3.1.1) is not an easy task. XMM-Newton has three X-ray telescopes (XRTs), with each of them consisting of 58 nested mirror shells. All of them have to be in a sufficiently precise shape and all of them have to be aligned with respect to each other in order to achieve a point spread function of reasonable quality. Any deviation
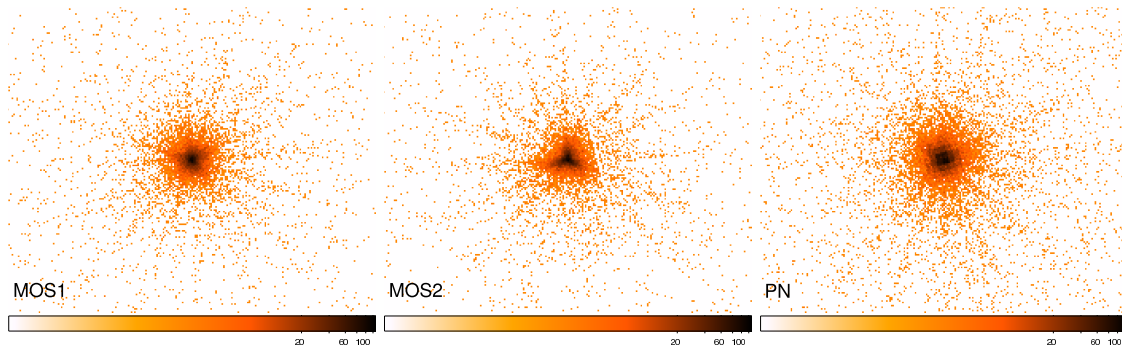
Figure 4.2: Real images of a bright point-source taken with the three EPIC instruments. Figure errors can be recognized here. The 16 radial spikes are due to the spider wheel, which carries the mirror shells. The color represents the number of photons in an image pixel (log scale).

from the perfect Wolter shape will lead to figure errors while non-perfect mirror surfaces cause straylight which broadens the PSF. Furthermore, a perfect PSF can in principle be only achieved on the optical axis, while off-axis sources are subject to the so called off-axis blurring. This is due to the non-perfect optical imaging, which is an intrinsic property of the Wolter geometry. The on-axis PSFs of the three XRTs of XMM-Newton (marked by their corresponding EPIC detector) are shown in figure 4.2. These are images of a real point-source close to the optical axis. Figure errors can easily be recognized here, especially the triangular shape of the MOS2 PSF. The binning in all three images is on $1.1''$ pixels, corresponding to the physical pixel size of the MOS detectors. In the PN image, the physical pixels (of size $4.1''$) are visible in the center of the point-source.

4.2.2 The Ray-tracing PSF Model

Figure 4.3 shows a PSF model which was created by a ray-tracing simulation using the ideal mir-ror shape. Thus, the figure errors are not included in this model. The off-axis blurring however is very well visible here. It increases with larger off-axis angles. This effect is equally prominent in real images and hampers the distinction between point-sources and extended sources at large off-axis angles significantly. This PSF model is used for image convolution in the newly devel-oped XMM simulator (xmm_sim) as well as for the analysis of XMM images by emldetect (which are described in sections 5.1 and 5.2, respectively). The ray-tracing model is also called the "MEDIUM accuracy model".

PSF File Format

The XMM PSF models are stored in the form of images of 512×512 pixels with $1.1'' \times 1.1''$, corresponding to the physical pixel size of the MOS detectors. The images are provided by the XMM-SAS as three FITS[2] files[3]. Each FITS file corresponds to one of the three XRTs. The three files are currently identical. However, by looking at the real point-source in figure 4.2 it is easy to see that three different models taking care of the individual properties of each XRT would be a vast improvement.

---

[2]FITS: Flexible Image Transport System. A file format for all kinds of astronomical data. The definition of the FITS format can be found in Hanisch et al. (2001).

[3]In SAS terminology they are part of a large collection of Current Calibration Files (CCF). Other CCFs contain for example the response matrix or alignment parameters, etc.
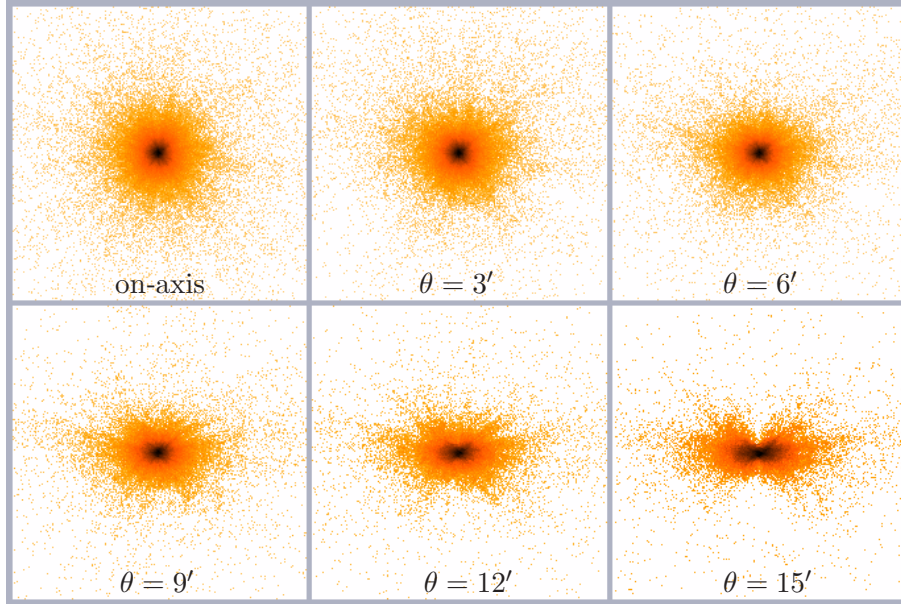
Figure 4.3: PSF ray-tracing model from the XMM-SAS calibration database, shown for different off-axis angles θ. The images illustrate the PSF shape variations over the field-of-view which makes the characterization of extended sources at large off-axis angles increasingly difficult. The ray-tracing model is the same for all three XRTs.

A still ongoing project is to create such an improved PSF model from real point-sources ("in-flight calibration"). An elliptical β-model (plus a Gaussian core for the MOS XRTs) is fit to stacked images of point-sources, sorted by energy and off-axis angle. The model is therefore called "*ellbeta*"-model. It also takes into account the azimuthal variation of the PSF core and the spokes from the mirror mounting. A first version of this model is already included in the latest SAS version but it is not activated by default because it still needs to be tested extensively. Throughout the thesis, only the ray-tracing model has been used because it was the best one available at the time of starting the simulation run.

A PSF calibration file is technically a FITS file with many extensions. Each extension contains an image[4] corresponding to one out of 11 photon energies (100 eV and 1.5 keV, 3.0 keV, 4.5 keV, ..., 15.0 keV) and a specific off-axis angle ($0'$, $3'$, $6'$, ..., $15'$).

4.3 A Ray-tracing Model for eROSITA's PSF

Since eROSITA is not in orbit yet, real images of point-sources can of course not be provided at the moment. However, first measurements of individual mirror shells have been performed at MPE's PANTER X-ray test facility (see sections 4.4.1 and 4.5). For the eROSITA image simulator, a ray-tracing PSF has been produced by P. Friedrich (priv. comm.), which is described in the following.

For ray-tracing through eROSITA's X-ray Mirrors, the ideal Wolter type 1 geometry was assumed. This mirror geometry was then "illuminated" by randomly generated photons. In order to produce a point spread function, a point-source would have to be simulated, i.e. all photons should come from the same off-axis angle but enter the mirror's sensitive area at different incident points.

---

[4]Additional extensions consist of fit parameters only. They are required for the LOW, EXTENDED and HIGH accuracy models, which were not used in this work.
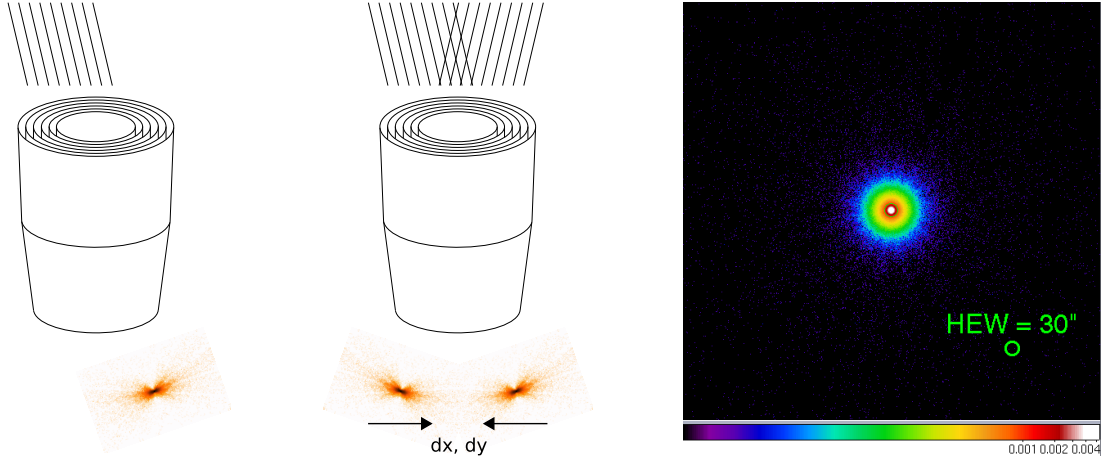
Figure 4.4: Ray-tracing through the eROSITA telescope. **Left:** Photons coming from a point-source hit the telescope at a single off-axis angle but many different incident points. They produce a butterfly-shaped PSF. This effect is known as *off-axis blurring*. **Center:** For the scanning mode PSF, photons coming from all possible angles were cast onto the telescope. Each off-axis angle in x and y direction was kept in memory. After the ray-tracing, every single photon was moved back accordingly (**dx**, **dy**). **Right:** The scanning PSF as it was used in the eROSITA simulator (log-scale). The green circle is also visible in the center and contains half of the photons.

This parallel photon beam is sketched in figure 4.4 (left panel). However, the eROSITA telescope is a survey instrument, which means that the seven telescopes are scanning over the sky, or, said the other way round, a source moves with respect to the telescopes. Photons from that source hit the telescopes at many different off-axis angles. The source image is reconstructed afterwards by sorting the photons onto a sky grid according to attitude data of the satellite. The scanning PSF is constructed in just the same way. Photons from all possible off-axis angles are traced through the telescope (see figure 4.4, center). This produces an overlay of many PSFs. However, for each photon the off-axis angles θ_x and θ_y are kept in memory. Therefore it becomes possible to move the individual photons back (along the detector plane) in order to reconstruct the average survey PSF:

$$\mathrm{d}x = f \cdot \tan\theta_x \tag{4.10}$$

$$\mathrm{d}y = f \cdot \tan\theta_y \tag{4.11}$$

where $f = 1600$ mm is eROSITA's focal length.

This approach is only valid for a *perfect* Wolter type 1 telescope. By construction, an on-axis point-source seen in pointing mode would be imaged as a perfect 2D-delta-function. In order to also include the imperfections of a real telescope (where also on-axis point-sources are broadened[5]), the on-axis PSF was modelled as a 2D-Gaussian distribution. The final equations for correcting the individual photon positions then look like this:

$$\mathrm{d}x = f \cdot \tan\theta_x + g_x(\mathrm{HEW}) \tag{4.12}$$

$$\mathrm{d}y = f \cdot \tan\theta_y + g_y(\mathrm{HEW}) \tag{4.13}$$

___
[5]Not only mirror imperfections contribute to the on-axis broadening but also e.g. the accuracy of the attitude reconstruction as well as thermal and mechanical effects.

where $g_x(\text{HEW})$ and $g_y(\text{HEW})$ are random numbers drawn from a single two-dimensional Gaussian distribution with a standard deviation calculated from equation (4.9) for the desired HEW. The specifications for the eROSITA mirrors require that the on-axis HEW is better than $15''$ (see table 3.1). For being able to investigate how source detection properties would change if this goal would not be achieved, models with larger on-axis-HEW ($15''$, $20''$ and $25''$) were also created for use with the simulator. Figure 4.4 (right panel) shows the final average survey PSF with an on-axis Gaussian of HEW=$15''$. In this case, the total HEW adds up to $30''$ due to *off-axis* blurring.

4.4 Sub-Pixel Resolution

In the course of this PhD thesis the development of Wolter mirror shells for eROSITA had already started. For being able to judge the imaging quality of the resulting X-ray telescope, individual mirror shells were measured in the PANTER X-ray test facility. In order to analyze these measurements with better quality than it was possible before, a Sub-Pixel Resolution (SPR) algorithm was developed within the scope of this thesis. After a description of the PANTER facility (section 4.4.1) and the CCD camera used for the measurements (section 4.4.2), this section introduces the mechanism of split events (section 4.4.3) and then focuses on the algorithm developed for sub-pixel analysis. Sub-Pixel Resolution will also be used later during the flight phase of eROSITA. Detailed measurements concerning split events and a thorough description of X-ray CCDs in general can be found in Kimmel (2008).

4.4.1 The PANTER X-Ray Test Facility

PANTER is an X-ray test facility operated by MPE and situated in Neuried, a township to the south of Munich. It was built in the years 1977 to 1980 for the purpose of development and verification of the mirror system of the German X-ray satellite ROSAT (Trümper, 1982) and subsequently adapted to the experimental needs (Döhring et al., 1997). The main part of PANTER is the cylindrical instrument chamber with a diameter of 3.5 m and a length of 12 m. It is connected to an X-ray source, which is accommodated in a separate building, via a tube of 1 m diameter and 120 m length. This length is necessary to mimic the paraxiality of star light from distant sources as closely as possible. The whole setup can be evacuated by several pumps, which are attached to the main tank (turbo- and cryogenic pumps) as well as to the 120 m-tube in auxiliary pumping stations (turbopumps) and to the X-ray source (smaller turbopumps). A stable vacuum of 10^{-5} - 10^{-6} mbar is routinely achieved. Figure 4.5 shows an aerial view of the research facility while figure 4.6 provides a cross-section through the main test chamber.

Several types of X-ray sources with different radiation characteristics are available. They produce radiation with energies ranging from 0.18 keV up to 50 keV. The large distance between the X-ray source and the test setup causes a loss of light due to the $1/r^2$-law on the one hand, but it ensures a very homogeneous and nearly parallel X-ray beam of ≈ 1 m in the test chamber. Countrates of up to ~ 3000 cts/s/cm^2 can be reached in the test chamber. For most purposes however, a low countrate is required in order to prevent pile-up in the detector (e.g. for PSF measurements < 1 cts/s in the PSF core).

The test chamber contains a monitor counter at the entrance of the 120 m-tube. It serves for verification of the beam homogeneity as well as for monitoring of the temporal stability of the X-ray flux. All kinds of X-ray optics can be mounted on different telescope manipulators carrying weights of up to a few hundred kilograms. Test-optics include for example individual mirror

Figure 4.5: Aerial view of the PANTER X-ray test facility in Neuried (to the south of Munich). The small shed on the right contains several X-ray sources. The building on the left is the main building, which houses the test chamber and the control room, among others. In between the two buildings, the 120 m long, 1 m diameter vacuum tube with the two auxiliary pumping stations are visible.
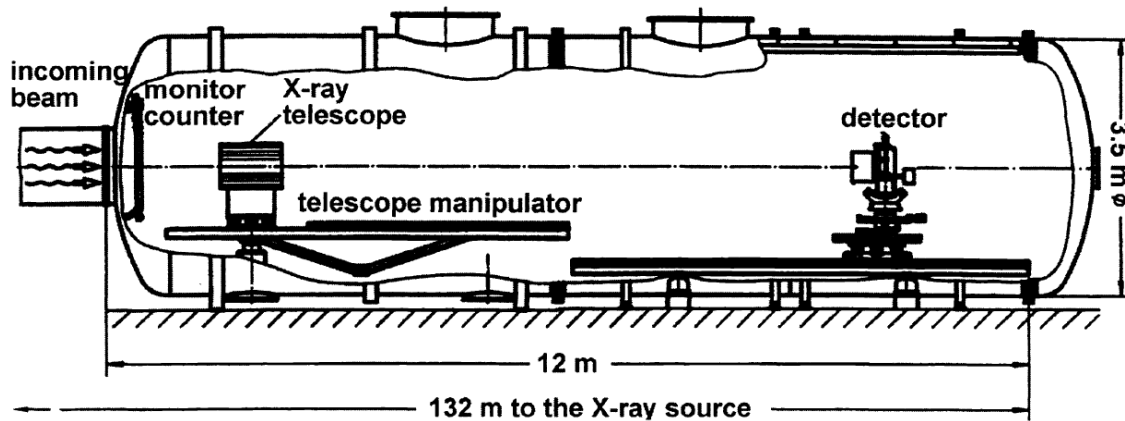
Figure 4.6: Cross-section through the main test chamber of the PANTER facility with schematic setup of the individual instruments. This view is horizontally inverted with respect to the one in figure 4.5. From Döhring et al. (1997)

shells and integrated X-ray telescopes as well as test pieces of modern light weight X-ray optics for future missions. Three different X-ray detectors are available for the measurements:

- A flight spare of the ROSAT PSPC (see section 3.1.4), which among the three detectors has the largest field-of-view (circular with a diameter of 80 mm).

- A flight spare of the EPIC-PN (see section 3.2) with a field-of-view of 60 mm × 60 mm.

- A DUO CCD which serves as a prototype for the eROSITA detector. It has a field-of-view of 19.2 mm × 19.2 mm and is described in detail in section 4.4.2.

Via a full-diameter door, the tank is accessible for mounting and adjusting the experimental setup. The door is situated in a clean room environment.

Figure 4.7: Layout of the TRoPIC CCD: The frames are shifted from the image area to the frame store area. From there they are read out by the CAMEX chips. Drawing from Meidinger et al. (2005).

4.4.2 The TRoPIC CCD - a Precursor of the eROSITA Detector

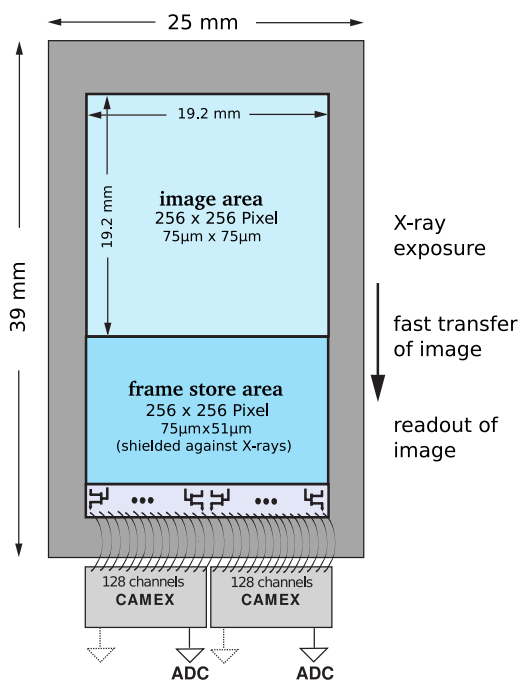TRoPIC is the Third Röntgen Photon Imaging Camera operated at the PANTER facility. It was constructed from a CCD which was developed for DUO (see section 3.3.1) at the semiconductor laboratory of the Max-Planck Society. The functional principle of a CCD was described in section 3.1.4. This section describes the special properties of the TRoPIC CCD which can be considered a precursor of the eROSITA CCD despite the smaller number of pixels. The sub-pixel resolution algorithm has been developed for the TRoPIC, which is frequently used for mirror characterization measurements of eROSITA mirrors. However, sub-pixel resolution will also be used for the analysis of the scientific data from the eROSITA telescope.

The TRoPIC CCD is a *frame store* CCD. This means, the imaging area of the TRoPIC CCD has 256×256 pixels, $75~\mu m \times 75~\mu m$ each, and the same number of pixels is repeated in the frame store directly attached to the imaging area (see figure 4.7). The frame store pixels have the same width but a shortened length (in transfer direction) of $51~\mu m$. The frame store area is protected from illumination by a layer of boron carbide (B_4C) of $1~mm$ thickness plus an additional copper shielding. The purpose of the frame store is to store the image during its read-out by the detector electronics: after an exposure time of $50~ms$, the image is shifted to the frame store within a time of less than $100~\mu s$ (Meidinger et al., 2005). While the next frame is already illuminated, the image in the frame store is not altered by any additional photons. The readout takes approximately $5~ms$ and is thus finished well before the end of the exposure time of the next frame. This technique reduces the fraction of out-of-time events significantly with respect to non frame store CCDs. The readout itself is also significantly quicker than with a conventional CCD because the CAMEX chips amplify and process the signals from each column in parallel, before they are serialized and transfered to the Analog-to-Digital Converters (ADC). The readout process is optimized for low noise and high energy resolution (FWHM ≈ 130 eV at 5.9 keV).

4.4.3 Split Events

When a photon hits a CCD, a charge cloud is produced in the semiconductor bulk material. During the drift of the charge cloud towards the potential minimum (close to the front side), its size increases due to diffusion and electrostatic repulsion. The final shape of the charge cloud is approximately a 3D Gaussian distribution. The size of the charge cloud depends on the energy of the photon. Details about the behavior of charges in the CCD can be found in Kimmel (2008).

When the charge cloud reaches the potential minimum, its charge is divided among adjacent pixels depending on position and size of the cloud. If the charge collected in a neighboring pixel (next to the one in which the charge cloud was initially produced) exceeds a certain threshold, the event is called a "split event". Otherwise it is called a "single event". The event type depends on the photon's incident position as well as on the setup of the thresholds.

Data Treatment by the DSP

The data coming from the ADCs are further investigated by a Digital Signal Processor (DSP). Two different thresholds are implemented in the code running on the DSP: **The event threshold** (or "trigger threshold") T_{evt} is stored individually for each CCD pixel. Its value is a constant factor n of the standard deviation of the noise in each pixel:

$$T_{\mathrm{evt}} = n \cdot \sigma_{\mathrm{noise}} . \tag{4.14}$$

Every pixel with a signal larger than its event threshold is handed over to the next step of the DSP code, which is the split threshold analysis: The environment (3 by 3 pixels) of each pixel having passed the first test is examined for possible neighbors.
The split threshold T_{split} (given in ADU) is constant over the whole CCD and usually lower than the event threshold. If any of the eight neighboring pixels show an amplitude exceeding the split threshold, this information is stored along with the amplitude of the main pixel. Otherwise, the event is defined to be a single event.

An offline analysis checks each split event whether it fits to one of the patterns shown in figure 4.8. Also patterns rotationally symmetric to the ones shown are valid patterns, i.e. probably caused by photons. Invalid patterns would be for example three or more pixels in one line. Those can be caused e.g. by pattern pile-up or by cosmic ray particles. Typical values for the two thresholds are: $T_{\mathrm{evt}} = 10.0 \cdot \sigma_{\mathrm{noise}}$ (corresponding to ~ 98.8 eV) and $T_{\mathrm{split}} = 32\,\mathrm{ADU}$ (corresponding to ~ 28.4 eV).

Figure 4.9 (left panel) shows a sketch of the charge clouds of three example events. It becomes clear from the figure that (for monochromatic energies) there are regions where incident photons produce certain types of events. The inner squared region is the single region, the rectangular marginal regions are the double regions. Photons hitting in the corners can produce either triple or quadruple events, depending on the split threshold of the neighboring pixels and on their exact incident position (compare the sub-division of the corners in the right panel of figure 4.9).

4.4.4 The Sub-Pixel Resolution Algorithm

The SPR code was developed in the programming language IDL[6]. The purpose of the code is to reconstruct the initial incident points of photons that produce split events, based on information from their charge distribution. During the development phase, it has been realized that a crucial

---
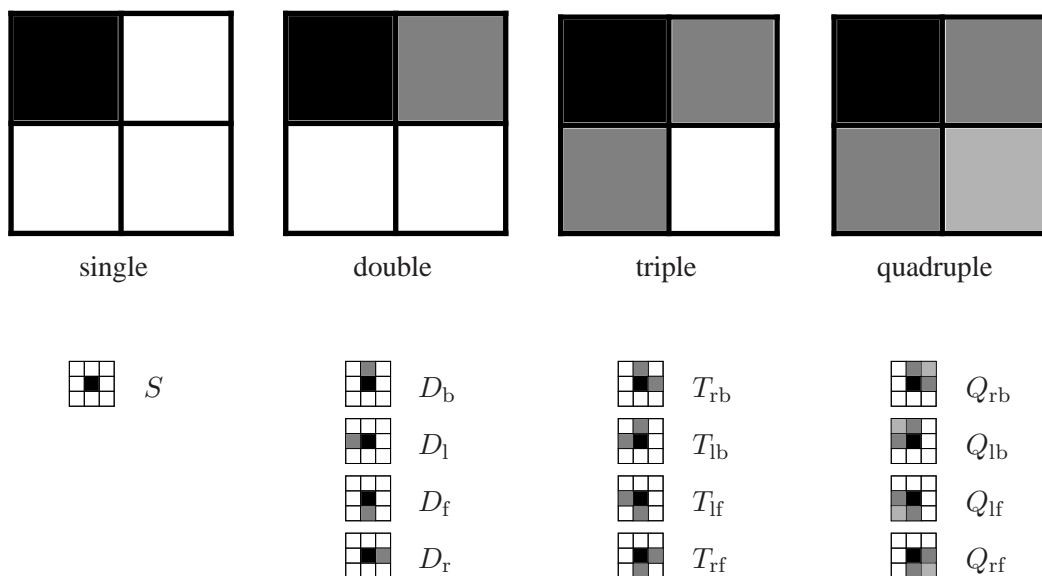
[6]IDL = Interactive Data Language

Figure 4.8: Upper panels: Valid pattern types. Different shadings indicate the different relative charge content in each pixel. Black: maximum charge, dark grey: intermediate charge, light grey: minimum charge, white: no charge exceeding any threshold. **Lower panels:** Possible split directions together with their identifiers, which are used as variables denoting the pattern abundance. The indices l and r stand for left and right, b and f for backward and forward (with respect to the readout direction).

ingredient for each SPR measurement is an associated flatfield. Therefore it was introduced as a standard procedure to perform a flatfield exposure contemporary to the actual measurement to make sure that the setup parameters from both match as exactly as possible. The newly introduced flatfield analysis is described in the following.

Flatfields

Due to the size of the charge cloud varying with the photon energy, also the marginal regions where split events occur vary in width. In order to calibrate this behavior, each SPR measurement is accompanied by a flatfield measurement: The TRoPIC CCD is illuminated by monochromatic X-rays with a spatially homogeneous intensity distribution. The flatfield image is analyzed with respect to the occurring abundance of the four valid pattern types and their split directions (see figure 4.8).

From the pattern fractions, the widths of the margins of an average pixel can be calculated for the current photon energy. Figure 4.10 shows an example of a postscript page which is automatically produced by the flatfield analysis tool. The lower panels show the sizes of average pixels graphically and as percentages of the physical pixel size. The average pixels of the two halfs of the CCD are displayed separately in case there is a difference between the two CAMEX chips[7]. The margins are labelled x_l, x, x_r, and y_b, y, y_f.

---

[7]A split behavior different for the two halfs of the CCD has occurred during the commissioning phase of the TRoPIC due to a non-perfect setup of the back-end electronics.
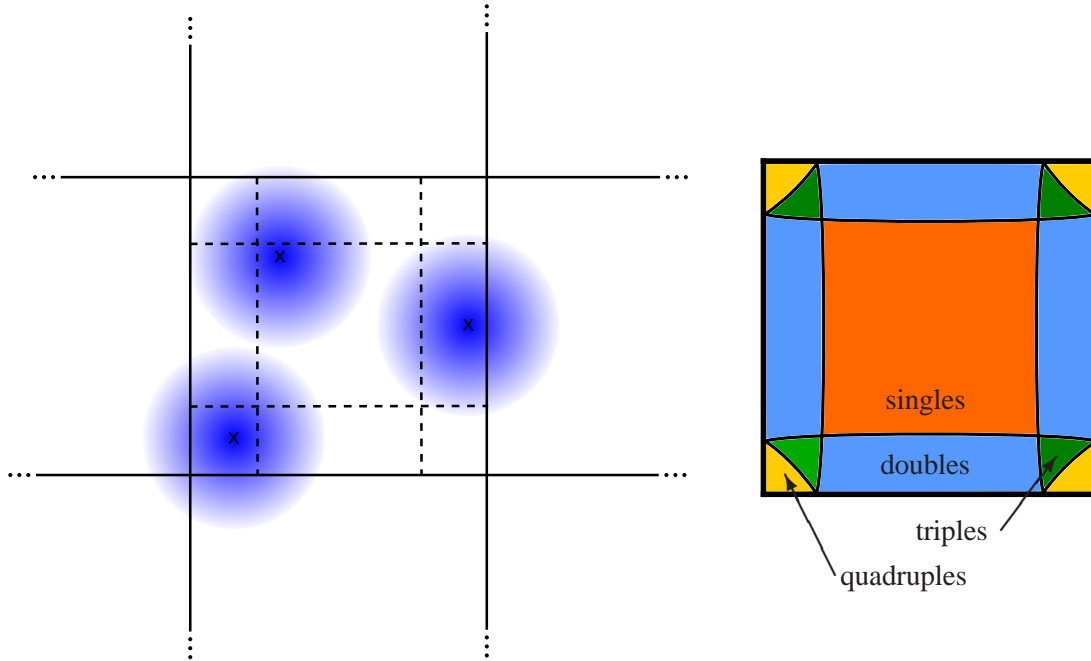
Figure 4.9: Left: A CCD pixel with three photons. The X marks the respective incident point of the photon, the blue shaded area illustrates the charge cloud. The dashed lines mark the borders of marginal regions where incident photons produce different patterns. **Right:** The approximate realistic shape of the marginal regions and their corresponding pattern types. Due to statistical fluctuations, in reality the borders are not as sharp as drawn here. Compare e.g. the measurements in Kimmel (2008) or Kimmel et al. (2006).

Because the margins' area is proportional to the pattern abundance, the following four equations could be derived (for variable definition see figure 4.8):

$$\frac{x}{x_{\mathrm{l}}} = \frac{S + D_{\mathrm{b}} + D_{\mathrm{f}}}{D_{\mathrm{l}} + T_{\mathrm{lb}} + T_{\mathrm{lf}} + Q_{\mathrm{lb}} + Q_{\mathrm{lf}}} \tag{4.15}$$

$$\frac{x}{x_{\mathrm{r}}} = \frac{S + D_{\mathrm{b}} + D_{\mathrm{f}}}{D_{\mathrm{r}} + T_{\mathrm{rb}} + T_{\mathrm{rf}} + Q_{\mathrm{rb}} + Q_{\mathrm{rf}}} \tag{4.16}$$

$$\frac{y}{y_{\mathrm{b}}} = \frac{S + D_{\mathrm{l}} + D_{\mathrm{r}}}{D_{\mathrm{b}} + T_{\mathrm{lb}} + T_{\mathrm{rb}} + Q_{\mathrm{lb}} + Q_{\mathrm{rb}}} \tag{4.17}$$

$$\frac{y}{y_{\mathrm{f}}} = \frac{S + D_{\mathrm{l}} + D_{\mathrm{r}}}{D_{\mathrm{f}} + T_{\mathrm{lf}} + T_{\mathrm{rf}} + Q_{\mathrm{lf}} + Q_{\mathrm{rf}}} \tag{4.18}$$

These equations can be solved for the geometry of the average pixels.

Image Creation

There are different levels of accuracy with which the reconstruction of photon positions can be implemented. The most straightforward method is to look at each event and decide (upon its pattern) which marginal region it has to be assigned to (see figure 4.9, right panel). In order to avoid aliasing effects, the final photon position has to be uniformly randomized within the
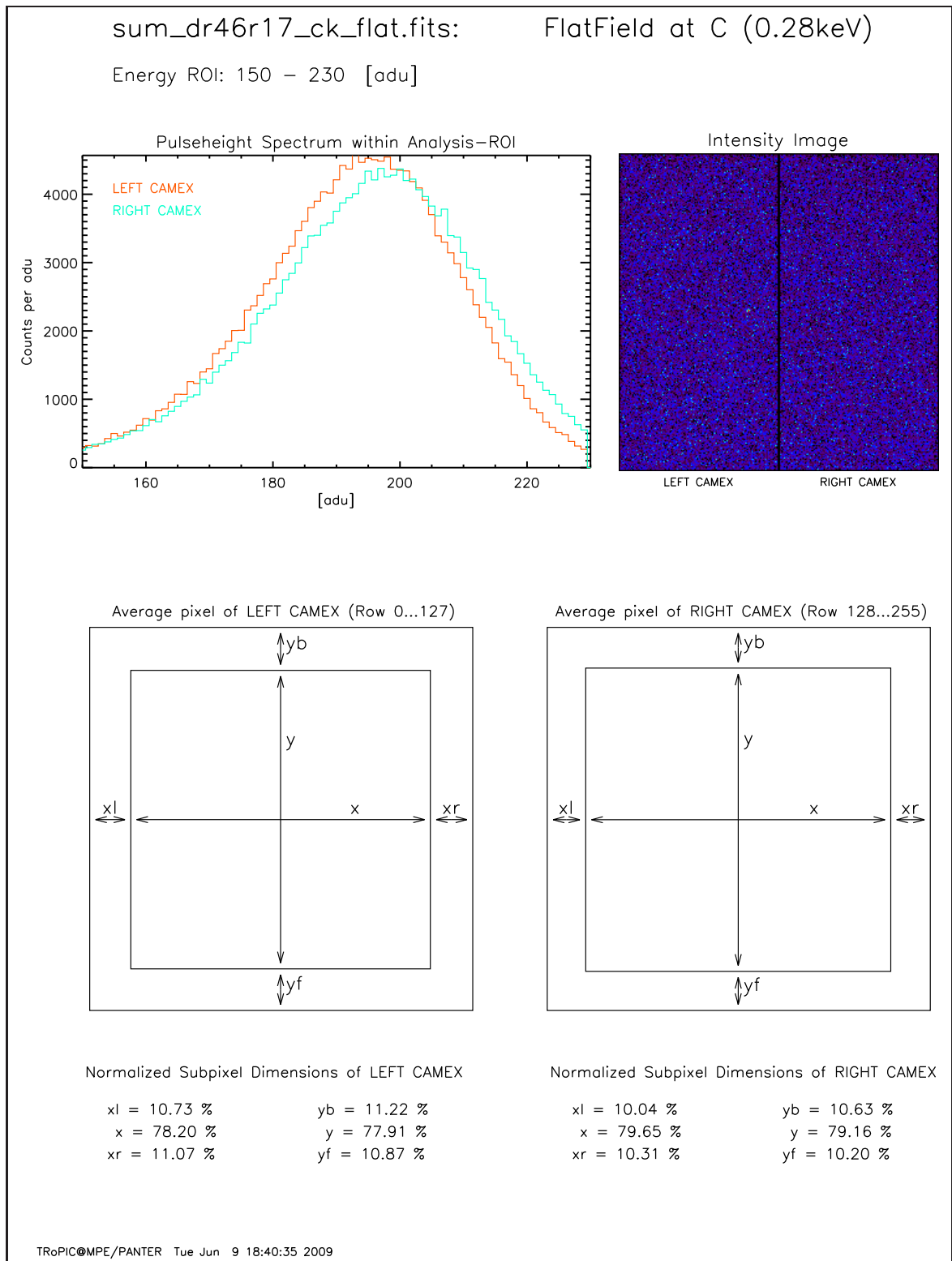
Figure 4.10: A typical postscript page as it is produced by the flatfield analysis tool. **Top left:** Spectral energy distribution in the selected region of interest (ROI), separately displayed for left and right CAMEX. **Top right:** Spatial photon distribution (image) on the TRoPIC chip. This is important to be able to judge the flatness of the flatfield measurement. **Bottom:** Pixel display for both CAMEX. Here the sizes of the split margins are given graphically as well as in numbers.

respective region. This is the method which is currently implemented in the SPR code. The final image is then created by binning the final photon positions onto a grid (image pixels). The image pixel size has to be chosen not too large, or otherwise the resolution gain from SPR would be lost, but large enough to have a sufficiently high photon statistics in the pixels. The ratio of CCD pixel size (75 μm × 75 μm) to image pixel size has been called *magnification*:

$$\text{mag} = \frac{75 \ \mu\text{m}}{\text{image pixel size}} \tag{4.19}$$

The current implementation of the SPR code produces four images with 1024×1024 image pixels with the following properties:

mag	image pixel size	image size
5	15 μm × 15 μm	15.3 mm × 15.3 mm
15	5 μm × 5 μm	5.12 mm × 5.12 mm
25	3 μm × 3 μm	3.072 mm × 3.072 mm
75	1 μm × 1 μm	1.024 mm × 1.024 mm

The position of the SPR image with respect to the full CCD area (19.2 mm × 19.2 mm) can be chosen via mouse click from a preview image.

It is planned to also write the reconstructed photon positions back to the initial data file (into an additional column) for further processing. The split events consist of more than one participating CCD pixel, so the reconstructed event will be written next to the main charge (maximum charge of the event).

More Exact Reconstruction of Photon Positions

Assigning photons just to their correct marginal regions does not make full use of the available information. By additionally looking at the ratio of the charges, a more exact photon position can be reconstructed for split events. Together with N. Kimmel from the semiconductor laboratory of the Max-Planck-Society a more sophisticated method has been worked out, which is not implemented yet.

First consider a double event. Let the split direction (line connecting the centers of the two participating CCD pixels) be the x-axis. The charge cloud has approximately the shape of a 3D Gaussian. Projected onto the x-axis this is again a Gaussian (with standard deviation σ). The charge collection function is defined as the amount of charge collected in a pixel depending on the photon's incident point. This is just the integral over the projected Gaussian along the x-direction from one pixel border to the other one. The charge collected in one pixel can therefore be expressed by the error function:

$$q(x) = \text{erf}(\sigma, x) \tag{4.20}$$

where x is the photon incident position. The details about the charge collection function in CCD pixels are described e.g. in Kimmel (2008) and Kimmel et al. (2006). Since the error function is not analytically invertible, it has to be tabulated for a large number of σ and x values. The algorithm can then look up x when $q(x)$ and σ is known. In two dimensions (for triple and quadruple events) x, σ_x and y, σ_y would be involved.

The applicable σ, σ_x and σ_y can be determined in the following way: A measurement with a sharp edge (realized e.g. by a razor blade) casting a well defined shadow onto the CCD is reconstructed by this technique, trying many different combinations of σ, σ_x, σ_y. The best fit values are the ones where the edge is best reproduced. It is planned to implement this method in a future project.

4.5 Mirror Characterization Measurements for eROSITA

As a first application of the newly developed SPR code, individual mirror shells of the eROSITA telescope have been measured at PANTER in order to test whether they meet the specifications.

4.5.1 Pixel Scans

A good eROSITA PSF has a half energy width of HEW $\leq 15''$. The size of a CCD pixel is 75 μm which translates to $9.55''$ at PANTER due to the finite source distance[8]. This means that the very core of the PSF is quite small compared to a CCD pixel. In order to exclude effects from the PSF shining always onto one region of a pixel[9], a *pixel scan* is performed:

The CCD is moved in steps of 3.75 μm on a grid of 20×20 positions by means of the manipulator inside PANTER's test chamber. Each position is illuminated for an exposure time of 75 s in order to achieve a fair sampling of a CCD pixel. It is not necessary to know the absolute location of each of the 400 measurement positions with respect to the CCD pixels. The SPR code automatically re-shifts the derived photon positions according to the recorded relative manipulator offsets during the image reconstruction process.

Figure 4.11 shows the inner regions of a PSF measurement evaluated without (left) and with (right) sub-pixel resolution analysis. It is well visible that the PSF core shrinks and image structures emerge much more clearly when switching from normal resolution to SPR. A measurement of a mirror shell with figure errors has been deliberately chosen here so that the effects of SPR are much better visible than in an ideal case. The measured half energy width of this mirror shell decreased from $26.5''$ in the standard resolution case to $24.4''$ in the SPR case.

4.5.2 HEW Measurement

Another feature implemented in the SPR code is the measurement of the half energy width of the PSF photon distribution. Based on the SPR-reconstructed photon event list, this is possible in a quick way: An initial guess for the distribution's center is determined from its centroid. The distance (=radius) from this center is calculated for each photon. The median of the radius distribution is the half energy *radius*, since half of the photons have a radius smaller and the other half larger than the median. The HEW is just double the half energy *radius*. This HEW measurement is repeated for 41×41 center positions around the initial guess. The minimal HEW is taken as the final measured value.

The most recent measurement analyzed with the SPR algorithm was carried out with an eROSITA mirror model containing five out of the total 54 mirror shells, illuminated in the light of Al-K_α (Aluminium, 1.49 keV). The result of this measurement is shown in figure 4.12 in a different representation: the encircled energy fraction $E(< r)$ is the fraction of the total number of photons enclosed in a circle of radius r. From this plot, one can read of the HEW as well as all other fractions of the PSF, e.g. W_{90}. The measured HEW decreased by 18%, from $18.6''$ in the standard analysis to $15.3''$ with SPR analysis.

---

[8]Note the difference to the value with infinite source distance: pixel scale = $9.67''$ (see table 3.1).

[9]E.g. shining always onto the single region would produce mostly single events and therefore be of minor use for SPR analysis.
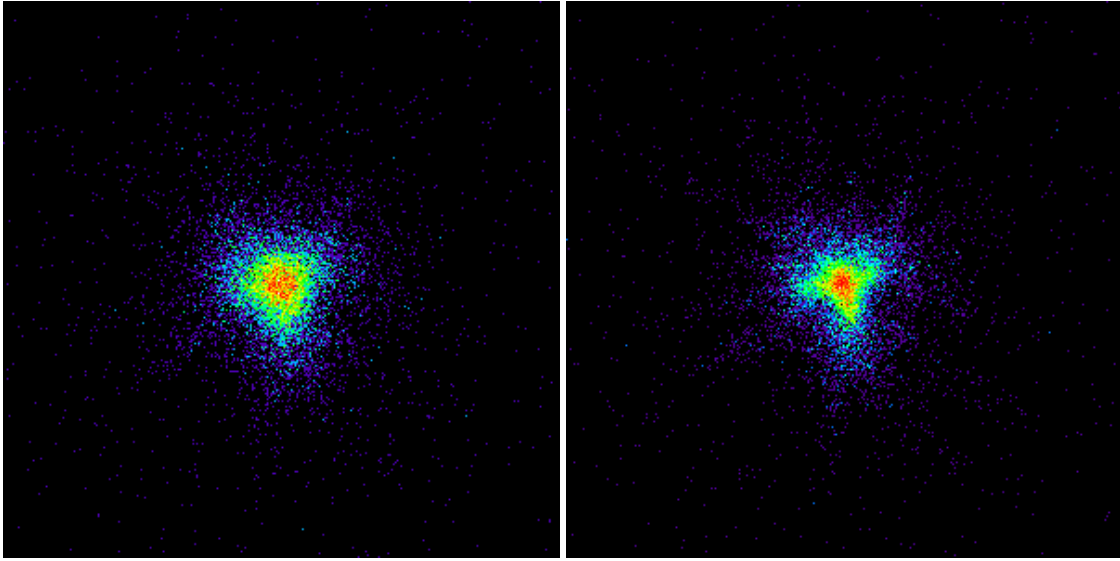
Figure 4.11: Comparison of PSF measurements in the light of the W-M_α line (tungsten, 1.78 keV) using normal detector resolution and sub-pixel resolution. **Left:** PSF of mirror shell 27-4 reconstructed from a pixel-scan measurement. **Right:** The same measurement evaluated with the newly developed algorithm for sub-pixel resolution. Not only the spikes from the mirror mounting (spider wheel) are visible much more clearly in the SPR image, but also irregularities due to figure errors of the mirror shell are enhanced. In both images the magnification factor is $\mathrm{mag} = 15$, i.e. one image pixel is 15 times smaller than a CCD pixel: $5\ \mu\mathrm{m} \times 5\ \mu\mathrm{m}$.
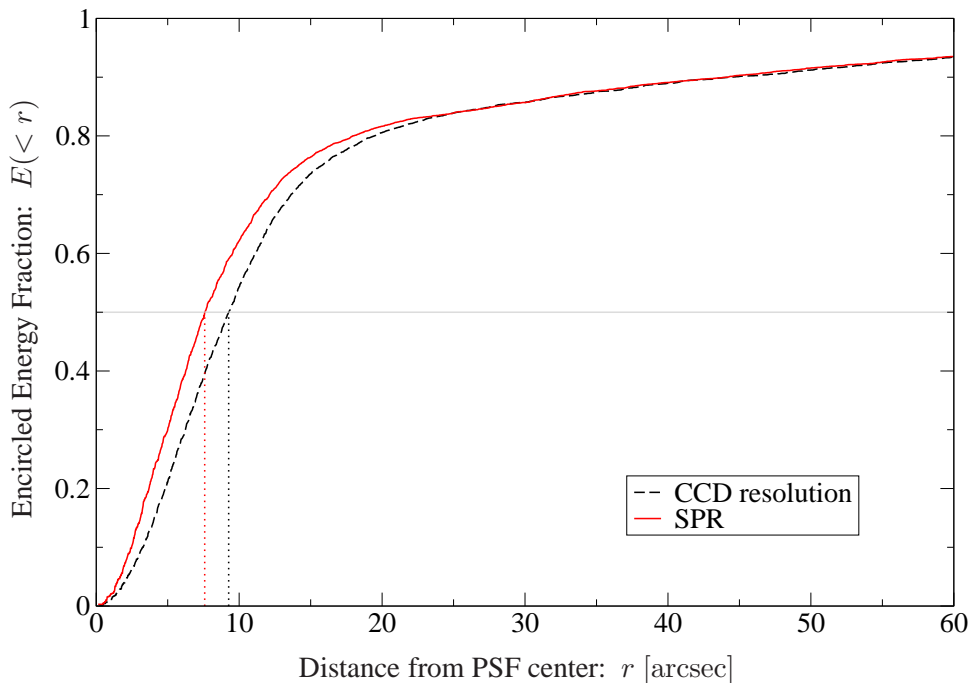
Figure 4.12: Encircled energy fraction of the measured eROSITA mirror model evaluated with normal CCD resolution as well as with sub-pixel resolution. At the horizontal grey line, one can read off the half energy radius which decreases by 18% when switching from normal resolution to SPR.

Chapter 5

XMM-Newton Simulations

The XMM-Newton Distant Cluster Project (XDCP) was introduced in section 3.4.2. It is very important that the statistics of the source detection and classification is calibrated by suitable simulations, in order to use the sample for high redshift cluster cosmology. For this purpose an XMM-Newton simulator was developed, which directly produces images (rather than event lists). These images are then analyzed with the same methods and parameter settings that have also been used for the analysis of the real data.

Cluster detection depends not only on the properties of the source, like shape, size, and brightness of a cluster, but also on various observational effects. Due to the PSF degradation towards the edge of the field-of-view, the discrimination between point-like and extended sources becomes more difficult at larger off-axis angles. A bright point-source in the vicinity of a cluster can reduce the cluster's detectability or influence the derived cluster parameters. Additionally, the galactic, extragalactic, and instrumental background as well as the exposure map and the galactic hydrogen column density of the observed XMM field play an important role in characterizing cluster detectability (see section 7.2 of Vikhlinin et al. (1998)). All these effects are realistically taken into account by the simulator code. This chapter describes in detail the characteristics of the XMM-Newton image simulator and summarizes the various steps of the analysis pipeline.

5.1 The XMM-Newton Image Simulator

The XMM-Newton simulator program is called xmm_sim and it has been developed within the programming language C, using the CFITSIO library (Pence, 1999)[1] for reading data and writing simulated images to hard disk. It relies on the Monte Carlo principle, which will be introduced briefly in section 5.1.1. Section 5.1.2 explains the "transformation method", a special Monte Carlo technique which is crucial for the high computational efficiency of xmm_sim. The simulator code is capable of dealing with the X-ray background and point-sources as well as extended sources and does a sophisticated PSF convolution according to the MEDIUM accuracy PSF model (see section 4.2.2). Finally, it performs a binning of the calculated photon events onto a sky image, taking into account the realistic structure of the chip-gaps. The image is written out as a FITS file. The components of the program are discussed in sections 5.1.3 to 5.1.7.

All XMM simulations are carried out on squared images of 648×648 image pixels of size $4'' \times 4''$. These are also the parameters used by the XDCP pipeline[2]. The XDCP has introduced

---

[1] http://heasarc.gsfc.nasa.gov/fitsio/

[2] This pixel size is a natural choice due to the physical pixel size of EPIC-PN, which is the most sensitive detector of XMM-Newton (see table 3.1).

a non-standard detection band, which is optimized for high redshift galaxy cluster search (see Fassbender, 2008 and Scharf, 2002). This $0.35 - 2.4$ keV energy band is used throughout the simulations.

5.1.1 The Monte Carlo Principle

Monte Carlo is a technique, which is widely used in simulations and relies on pseudo-random numbers[3]. It has been developed in parallel with the emergence of the first automatic computers during the first half of the 20th century. The name is related to the gambling in the casino of Monte Carlo, Monaco. Metropolis (1987) reports on the details of the history of the Monte Carlo method.

Monte Carlo simulations are frequently used in many physical sciences, whenever a set of particles and their positions has to be followed through time according to certain decisions. Every decision is based on an appropriate probability distribution which describes the physical process to be studied. One of the method's first applications was the study of the behavior of neutron diffusion in fissionable materials. It is also perfectly suited for simulating the production, scattering and detection of photons in (X-ray) astronomy.

Pseudo-random numbers are generated in a computer based on one number which is called "seed" and has to be given by the user. With the seed at hand, exactly the same series of pseudo-random numbers can be reproduced whenever running the random number generator again. This property can be very useful for the testing, development and comparison of algorithms.

The natural random distribution for a computer is the uniform distribution, i.e. every number between an upper and a lower bound occurs at the same probability. A list of algorithms producing uniformly distributed pseudo-random numbers between zero and one is given in Press (2002).

5.1.2 The Monte Carlo Transformation Method

Since random number generators only produce uniform distributions, a method is needed to transform the uniform distribution into an arbitrary random distribution. Examples for random distributions needed in astronomy include e.g. the logN-logS of AGN, models of extended sources and especially point spread functions[4]. In the latter two cases, the associated random number is the photon's position in the source model or the PSF, respectively.

The following argumentation is based on Press (2002). Consider a probability density $p(x)$, which obeys a uniform probability distribution. The probability $p(x)\,\mathrm{d}x$ of finding a number between x and $x + \mathrm{d}x$ is constant on the interval $[0, 1]$:

$$p(x)\,\mathrm{d}x = \left\{ \begin{array}{ll} \mathrm{d}x \,, & 0 \leq x \leq 1 \\ 0 \,, & \text{otherwise} \,. \end{array} \right. \tag{5.1}$$

By definition, the integral over the probability density $p(x)$ is equal to one:

$$\int_{-\infty}^{\infty} p(x)\,\mathrm{d}x = 1 \,. \tag{5.2}$$

---

[3]Pseudo-random numbers are distributed statistically but generated by an entirely deterministic process from an initial seed. Sequences of pseudo-random numbers have the advantage that they are exactly reproduced when using the same seed again. This can be useful for the development and testing of software.

[4]PSFs can be taken as probability distributions since they describe the probability of finding a photon at a certain image position.
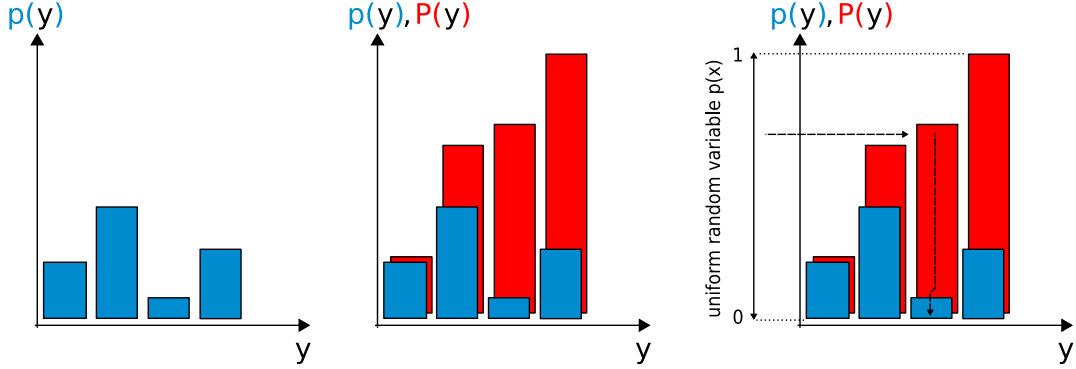
Figure 5.1: Monte Carlo simulation of a random number following an arbitrary discrete probability distribution. y is the random variable to be distributed according to $p(y)$. The three steps from left to right are described in the text.

In order to obtain a random number from an arbitrary desired probability distribution, x is transformed by a function $y = y(x)$. The probability of finding y in the interval $[y, y + \mathrm{d}y]$ has to be equal to the probability of finding x in the interval $[x, x + \mathrm{d}x]$:

$$p(y)\,\mathrm{d}y = p(x)\,\mathrm{d}x \qquad \text{or} \qquad p(y) = p(x)\frac{\mathrm{d}x}{\mathrm{d}y}\ . \tag{5.3}$$

For the case $0 \leq x \leq 1$ this reduces to

$$p(y) = \frac{\mathrm{d}x}{\mathrm{d}y}\ , \tag{5.4}$$

the solution of which is just

$$x = P(y)\ , \tag{5.5}$$

with $P(y)$ being the anti-derivative of $p(y)$. Solving equation (5.5) for y leads to

$$y(x) = P^{-1}(x)\ , \tag{5.6}$$

where P^{-1} is the inverse function of P. With this expression for the demanded function $y(x)$, one can now construct random numbers following any distribution whose integral is invertible. With a uniformly distributed input for $p(x)$, the transformation will then be distributed according to the desired $p(y)$.

Visualization of the Transformation Method for the Discrete Case

The algorithm described above can be directly applied whenever the integral of the desired distribution can be analytically calculated and inverted. This is the case e.g. for the logN-logS distributed flux of a point-source sample (see section 5.1.4). Non-analytic distributions[5] have to be treated slightly different although the principle is the same. The left panel of figure 5.1 shows a simple example of a probability distribution $p(y)$ with only four bins.

The first step is to compute the cumulative distribution $P(y) = \int_{-\infty}^{y} p(\tilde{y})\,\mathrm{d}\tilde{y}$, which is shown in red in the central panel. Seen from the left side, each element of the cumulative distribution

---

[5]A ray-tracing simulated PSF model like the one in section 4.2.2 can be taken as an example for a non-analytic probability distribution.

which is not "covered" by the previous bin is proportional to the probability of that bin in the original distribution. A random number x (from a uniform distribution $p(x)$) is then generated by the computer's random number generator and transformed by the recipe according to equation (5.6) to find the corresponding y. This is indicated in the right panel of figure 5.1 by the two arrows.

In a computer program, the distribution $P(y)$ can be calculated once in the beginning and then be stored in an array. The remaining issue is to find the correct location in this array according to the generated random number x. This has been solved by nested intervals for which an appropriate bisection algorithm can be found in Press (2002).

5.1.3 X-Ray Background Modelling

The first source component taken into account by the simulator xmm_sim is the X-ray background. It is generated on the basis of background models obtained from real observations.

In the analysis pipeline for real XDCP data (see section 5.2), the X-ray background is estimated for each of the 469 XDCP fields by fitting a model to the X-ray image with excised sources (point-like as well as extended ones), the *cheese image*. The model is a linear combination of a constant component and a vignetted[6] component. Figure 5.6, panel (a) shows an example of a background model. A detailed description of the creation of the background models is given in Fassbender (2008).

In order to simulate photons from a background template, the image value in each pixel is interpreted as the expectation value of a Poisson distribution. A random number is then drawn from this distribution (in the case of the Poisson distribution, this is always an integer) and the result is the number of background photons to be stored in the respective pixel. This process is called *poissonization* and the appropriate algorithm is known as *poidev* in Press (2002).

Instead of the background modelling described above, the simulator xmm_sim is also capable of using a real observation as background for the simulated galaxy clusters.

5.1.4 Point-Sources (AGN)

In the X-ray band, the major part of the point-source population at high galactic latitudes are Active Galactic Nuclei (AGN), i.e. accreting black holes sitting in the centers of galaxies which shine brightly in X-rays. Regardless of the type of AGN, all point-sources impose a strong impediment to the detection of extended sources (galaxy clusters). For example, two point-sources close to each other can be mistaken as an extended source (due to the PSF blurring) and thus result in a false positive detection. Also the opposite can happen: a bright point-source located "on top" of a galaxy cluster can hide the cluster, resulting in a lower overall detection efficiency. It is therefore very important to include the point-source population into the simulations with a realistic flux distribution.

The flux distribution used here follows the logN-logS measured in the COSMOS field by Cappelluti et al. (2007) and is assumed to be representative for observations outside the galactic disk at latitudes $b \geq 20°$. The data from Cappelluti et al. (2007) is parameterized by the following differential distribution (broken power law):

$$n(S) = \frac{\mathrm{d}N}{\mathrm{d}S} = \begin{cases} AS^{-\alpha_1}, & S > S_b \\ BS^{-\alpha_2}, & S \leq S_b \end{cases} \qquad (5.7)$$

---

[6]Vignetting: see section 3.1.2

with S : flux in units of $10^{-14}\ \mathrm{erg\ cm^{-2}\ s^{-1}}$
    $n(S)$: Number of sources per square degree (deg^2) in a certain flux bin $\mathrm{d}S$
    $N(>S)$: Number of sources per deg^2 above a certain flux S (cumulative distribution)
    A,B : Normalization constants with the boundary condition $AS_b^{-\alpha_1} = BS_b^{-\alpha_2}$
    α_1 : Bright end slope
    α_2 : Faint end slope
    S_b : Break flux.

The input parameters for the simulator are taken from the best fit values of the more updated paper by Cappelluti et al. (2009b): $\alpha_1 = 2.40 \pm 0.05$, $\alpha_2 = 1.60^{+0.04}_{-0.10}$, $S_b = 1.00^{+0.21}_{-0.26} \times 10^{-14}\ \mathrm{erg\ cm^{-2}\ s^{-1}}$ and $A = 141\,\mathrm{deg}^{-2}$.

The AGN population has to be simulated down to the lowest flux value which can still be detected. This flux limit varies from field to field depending on the background and exposure time of each pointing as well as with off-axis angle[7]. The flux of AGN below the detection limit will be contained in the background model due to the way it has been constructed (see section 5.1.3). If the flux limit is given by S_{lim}, the total number of AGN in the image is given by the equation

$$\langle N_{\mathrm{AGN,tot}} \rangle = \int_{S_{lim}}^{\infty} n(S)\ \mathrm{d}S \ \times (648 \cdot 4'')^2 \,, \tag{5.8}$$

where the last term expresses the sky area covered by the image[8]. The result is the expectation value of the number of AGN. It has to be poissonized (see also appendix A) to obtain the actual number of AGN to be simulated. Once the total number of AGN is fixed, $N_{\mathrm{AGN,tot}}$ random numbers are drawn from the flux distribution according to $n(S)$ to determine the flux of each source by applying equation (5.6) (with $P(y) \equiv N(>S)$). The image positions of the sources are generated from two independent uniform random distributions. Although AGN in reality show some spatial clustering (e.g. Yang et al., 2006), the homogeneous distribution is a good approximation for the purpose of the simulations.

Flux-to-Countrate Conversion

In order to convert the simulated flux of each source to a countrate, an energy conversion factor (ECF) is required (see section 3.1.6). As a model spectrum to compute the ECFs, a power law (equation (3.18)) with $\Gamma = 2.0$ is assumed, following Cappelluti et al. (2009b). In the simulations described here, the non-standard band $0.35 - 2.4$ keV is used instead of the $0.5 - 2.0$ keV band, leading to an ECF that is different from the one used in the paper. Furthermore, X-rays are absorbed by the galactic interstellar medium (ISM) before they reach the observatory. The ISM's absorption is expressed in terms of the galactic neutral hydrogen column density (n_H). The n_H value differs from field to field, which has to be considered in the model to calculate the ECF value.

---

[7]The procedure described here assumes a flux limit being constant over the field-of-view. At a further development stage the point-source population will be created on rings with constant off-axis angle and thus an off-axis angle dependent flux limit $S_{\mathrm{lim}}(\theta)$ can be used.

[8]Point-sources are distributed randomly over the whole image, regardless of whether the position is covered by a detector or not. The decision about whether a source is seen in the final image is taken at a later step (see section 5.1.7).

The expectation value of the number of photons in each point-source i is obtained by multiplying the countrate by the respective exposure value taken from the exposure map's value at the source position:

$$\langle c_i \rangle = r_i \times \exp_{x(i),y(i)} \tag{5.9}$$

with $\langle c_i \rangle$: expected number of counts (photons) in source number i,
         r_i : countrate of source number i,
         $\exp_{x,y}$: exposure value at position x, y
         $x(i), y(i)$: position of source number i.

Analogously to the background photons, also here the expectation value is poissonized (see appendix A and section 5.1.3) to get the final number of photons in each source. Since the AGN are point-sources, each of them occupies only a single pixel before PSF convolution.

The same as in the case of the X-ray background is also true for the point-source population: if a real observation is used as background for the simulated galaxy clusters, the point-sources are not simulated additionally. This simulator mode has two advantages: **(i)** the spatial distribution of the point-sources is real as opposed to the idealized uniform distribution of the simulated AGN population and **(ii)** the flux distribution (logN-logS) for each field is already set by nature.

5.1.5   Galaxy Clusters

Galaxy clusters, as the most important source component to be simulated, are realized as β-models (see section 2.2.2). Equation (2.4) together with the appropriate normalization constant (for a fixed $\beta = 2/3$) reads:

$$\langle n_{\mathrm{ph}}(r) \rangle = \frac{N_{\mathrm{ph}}}{2\pi r_{\mathrm{c}}{}^2} \left[1 + \left(\frac{r}{r_{\mathrm{c}}} \right)^2 \right]^{-3\beta + 1/2} \tag{5.10}$$

with $\langle n_{\mathrm{ph}}(r) \rangle$: Expectation value of the number of photons in each pixel
         r : Radius
         N_{ph} : Total number of photons contained in the cluster model
         r_{c} : Core radius of the beta model
         β : β-parameter, in this case fixed to $\beta = \frac{2}{3}$.

The choice of a fixed β-parameter is justified by the result of Vikhlinin et al. (1998), who found that the detection probability has very little dependence on β. This simplifies the technical feasibility of a large simulation run, since each additional parameter variation causes a large increase of points in the parameter space to be probed.

N_{ph} and r_{c} are input parameters for `xmm_sim`. This means that the flux is not derived from a distribution like in the case of point-sources (section 5.1.4). It is rather determined by N_{ph} which is set from outside the program. The choice of various values for the input parameters N_{ph} & r_{c} is described in section 6.2.1.

The β-model clusters are generated in large boxes of 150×150 pixels, corresponding to $10' \times 10'$, to make sure that edge effects are negligible. Figure 5.2 shows two examples of β-models and their realizations with $10\,000$ photons. This large number has been chosen to enhance the image details. As can be seen in the figure, the model drops significantly at large radii: panel **(a)** shows a β-model with a core radius $r_{\mathrm{c}} = 128''$. This is the largest core radius used in the simulation, which in reality is beyond the expected values at high redshifts. The 150×150 pixel
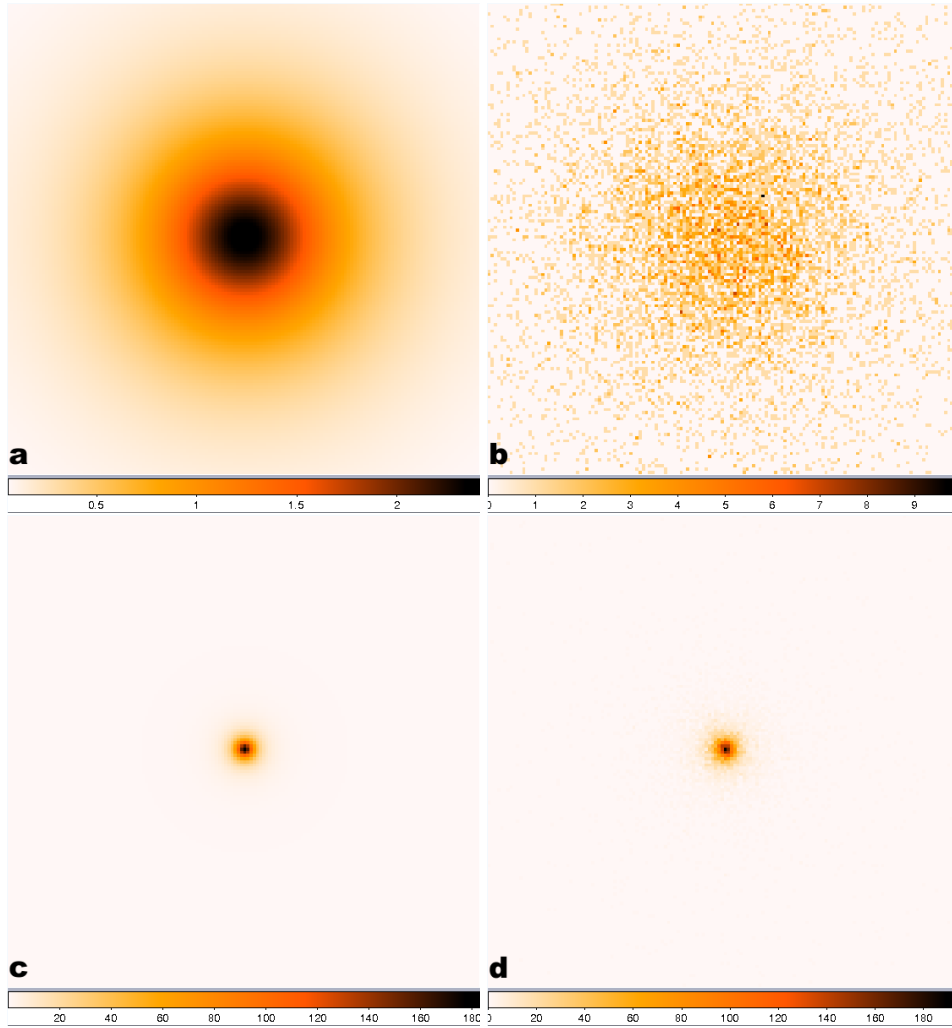
Figure 5.2: Examples of β-model clusters (before PSF convolution): width of the box = $150 \, \text{pixels} = 10'$. **a)** Model with $r_{\text{c}} = 32 \, \text{pixels} = 128''$ **b)** Realization of model (a) with $10\,000$ photons **c)** Model with $r_{\text{c}} = 3 \, \text{pixels} = 12''$ **d)** Realization of model (c) with $10\,000$ photons.

box contains in this case 64.2% of the model when integrated out to infinity. Panel **(c)** shows a very common example with $r_{\text{c}} = 12''$ containing 96.4% of the total counts. Nevertheless, in both cases the realization of the cluster (panels **(b)** and **(d)**, respectively) contains *exactly* $10\,000$ photons within the box so that the flux generation is exact. This is achieved by means of the Monte-Carlo transformation method: As a first step, the image of the β-model is linearized, i.e. each line of the image is put next to the previous one, as shown in figure 5.3 for the case of a 7×7 pixels cluster model. The resulting one-dimensional array can then be integrated according to figure 5.1, to obtain the cumulative array. This enables the simulator to apply the Monte-Carlo transformation method to distribute exactly the required number of photons over the cluster box.
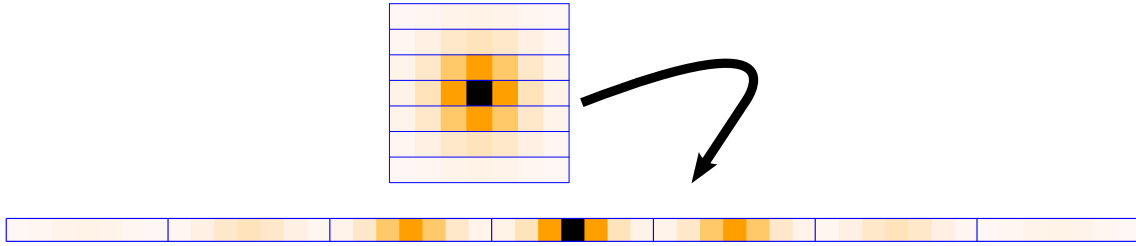
Figure 5.3: A squared image is transformed to a linear array. The color indicates image intensity. This is a necessary preparation for applying the Monte-Carlo transformation method to a 2D-array (image).

Distribution of Photons among the Three XRTs

After each source component (background, point-sources and galaxy clusters) has been added, the complete sky image, sampled on 648×648 $4''$-pixels, is available in the computer memory. The next step is to distribute the photons among the three X-ray telescopes of XMM-Newton. This is done according to the approximate relative sensitivity of the three EPIC instruments MOS1, MOS2, and PN. The exact sensitivity ratios depend on the ECFs, calculated with each detector's response individually. For simplicity it has been decided to implement the following approximated sensitivity ratio:

$$\mathrm{MOS1} \div \mathrm{MOS2} \div \mathrm{PN} = 1 \div 1 \div 3.2 \quad . \tag{5.11}$$

The photon assignment is done again via Monte-Carlo transformation by assuming equation (5.11) to be a probability distribution. Each photon is randomly assigned to an XRT according to this distribution.

The XDCP field selection (see section 3.4.2) works with the criterion that at least one EPIC instrument has to work in full frame imaging mode in order for a pointing to be selected as XDCP field. In cases where the instrumental mode could not be used for cluster detection, these images are missing in the survey. This fact is considered by the simulator: for pointings where one or two cameras are missing, the corresponding photons are discarded rather than distributing them among the remaining detectors.

5.1.6 PSF Convolution

The central part of the simulator is dealing with the PSF convolution. It involves the convolution itself which can be done in different ways and, as a second step, a rotation according to the azimuthal angle of the source. PSF rotation is very important in the case of XMM-Newton since the PSF is not rotationally symmetric. For image convolution in xmm_sim, the 1.5 keV template of the MEDIUM accuracy PSF model is used (see section 4.2.2).

The images of the six off-axis angles avaiable at 1.5 keV in the MEDIUM model ($0' \dots 15'$ in $3'$-steps, see figure 4.3) are interpolated to 61 images ($0' \dots 15'$ in $0.25'$-steps). These are saved in a separate PSF file. To save computation time, no further interpolation takes place during the runtime of xmm_sim. The appropriate PSF is chosen from these 61 images according to the off-axis angle at which the convolution currently takes place.

Image convolution is mathematically described by equation (3.12). There are different algorithms to implement it in a program. The two which have been considered in this thesis are described below.
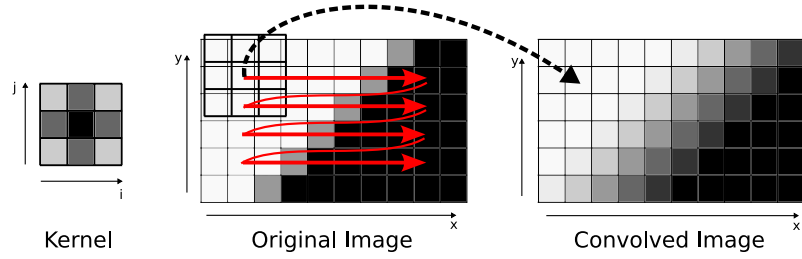
Figure 5.4: Illustration of conventional convolution according to equation (5.12): The kernel (in this case 3x3 pixels) sweeps over the image and collects values from neighboring pixels, multiplies them with the corresponding kernel pixel and sums the products. The shades of grey correspond to different image intensities. Drawing adapted from Berry and Burnell (2005).

Conventional Convolution

In the discrete case of pixelized images, equation (3.12) can be re-interpreted as

$$\tilde{I}(x,y) = \sum_{j=-r}^{r} \sum_{i=-r}^{r} I(x+i, y+j) \cdot K(i,j) \tag{5.12}$$

with I : Unconvolved image
$\tilde{I}$: Convolved image
K : Convolution Kernel = PSF
x, y : Image coordinates
i, j : Kernel coordinates
r : Half size of the kernel.

This equation is visualized in figure 5.4. The Kernel (PSF) calculates the convolved image pixelwise: for each image pixel, as many products as pixels in the kernel ($= i \cdot j$) have to be computed and summed up to get the new image value. Due to the two required for-loops, the runtime of the image convolution scales with (number of image pixels)^2. In the case of xmm_sim, $648^2 \cdot 512^2 \approx 1.1 \times 10^{11}$ calculations are thus required for one image convolution. Depending on the CPU type, this leads to a total runtime of a few minutes (see figure 5.5).

Convolution by Monte Carlo Transformation

Image convolution in the X-ray regime can profit a lot from the fact that there are fewer photons the higher the energy of the observed radiation. In the deepest exposures of the XDCP, there are at most some 10^5 photons per field. In this case, simulating positions for each photon is much quicker than conventional convolution. To do this, all 61 PSF models are linearized analogously to the linearization of the β-model described in section 5.1.5 (see figure 5.3). These linear arrays are integrated and the cumulative arrays are stored in a FITS file. With these cumulative distributions, the Monte-Carlo transformation method as described in section 5.1.2 can immediately be applied for each individual photon.

PSF rotation

Since the applied PSF model is not azimuthally symmetric, but shows an orientation (especially at large off-axis angles, see figure 4.3), a final rotation is required depending on the azimuth angle of the source within the field. PSF convolution by Monte-Carlo transformation was the
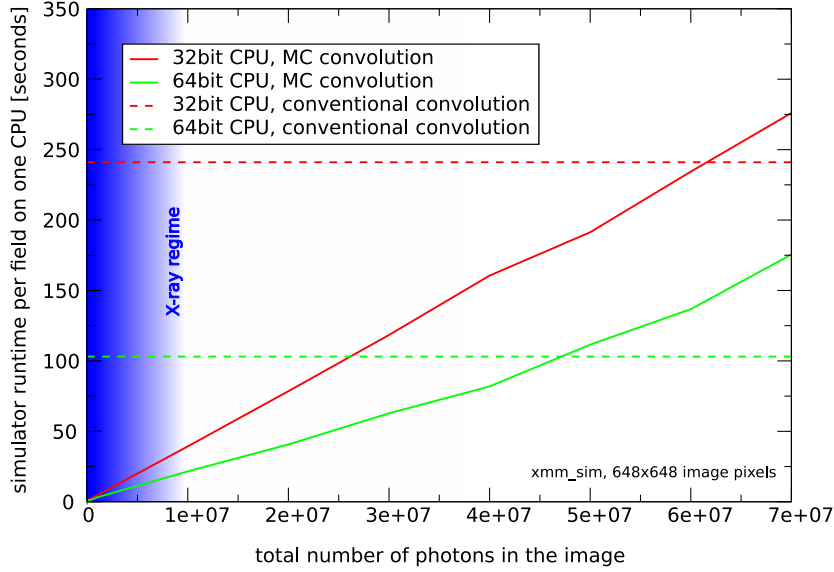
Figure 5.5: Runtime comparison of the two PSF convolution methods on two different CPUs.

only convolution algorithm which was implemented in the final simulator program. Therefore PSF rotation is described here for this algorithm only: after the new position $\tilde{x}$ due to the PSF convolution is known for a source photon, it is transformed again by a rotation matrix M:

$$x_{rot} = M \cdot \tilde{x}$$

$$\text{with}$$

$$M = \begin{pmatrix} \cos\phi & -\sin\phi \\ \sin\phi & \cos\phi \end{pmatrix}$$

(5.13)

where x_{rot} is the final photon position after rotation and ϕ is the azimuth angle at which the convolution currently takes place.

Runtime comparison

In order to verify the gain in runtime by applying the Monte-Carlo convolution algorithm, a series of tests has been performed with different implementations of xmm_sim and on two different CPUs. The result of the measurement is displayed in figure 5.5: while the runtime of the program that uses conventional convolution is independent of the number of photons, the runtime of the Monte-Carlo version is roughly proportional to the number of photons. In contrast to optical wavelengths, observations in the X-ray regime (marked in blue) usually deal with few photons where Monte-Carlo convolution is much faster than conventional convolution.

An additional advantage of the Monte-Carlo convolution is that the number of photons per source (e.g. galaxy cluster) is unchanged during the calculation. Conventional convolution can only deal with expectation values which have to be poissonized afterwards to get realizations. This introduces some noise, i.e. the number of photons varies from source to source and also from simulation to simulation if different seeds are used.

Binning of Photons onto the Final Image

During PSF convolution, the photon positions are kept in the computer memory as double precision floating point numbers. However, the resolution is limited by the $1.1''$-binning of the PSF models. In order to achieve a fair distribution of PSF convolved photons among the $4''$-pixels, each photon is shuffled within its respective target-$1.1''$-pixel after PSF convolution according to a uniform distribution. It is then assigned to the final $4''$-imagepixel according to its final double precision value. In this way, alias effects from the PSF rotation are eliminated.

5.1.7 Photon Detection and Example Images

The final step of the program simulates the detection of photons on the EPIC CCDs. Since the quantum efficiency is already included in the ECF (see section 5.1.4), the only task left at this stage is taking into account the insensitive chip-gaps and dead columns[9], i.e. to decide, whether a photon is detected or not. This has been realized by putting photons into the final FITS file only at positions where the exposure value according to the exposure map is larger than one second. Figure 5.6 shows the photon distribution before and after the chip-gap simulation and the exposure map. For comparison, other intermediate simulator products and one real XMM observation are shown as well. The detailed description of the six panels follows here:

a) Background model of EPIC-PN, as described in section 5.1.3. The large variation over the field-of-view is due to the vignetting effect. The chip-gaps and dead columns can be identified. The diameter of the sensitive detector area is approximately $30'$.

b) Exposure map of EPIC-PN. The vignetting effect and the chip-gaps and dead columns are visible here as well. The highest exposure marks the telescope's optical axis (boresight). The boresight was deliberately designed to have a little offset from the chip center since it would otherwise fall on a chip-gap.

c) Simulated photon field *before* PSF convolution. For illustration purpose, the image has been slightly smoothed, otherwise the point-sources would be hardly visible because they occupy only single pixels. Ten β-model clusters have been added with parameters $N_{\mathrm{ph}} = 1000$, $r_{\mathrm{c}} = 3\,\mathrm{pixels} = 12''$.

d) Simulated photon field after PSF convolution, but before the final cleaning of the chip-gaps. Some photons from point-sources were scattered into the chip-gaps by the convolution from sources lying just next to the gap. Also clusters outside the actual field-of-view are still visible here. Note the increasing PSF elongation with increasing off-axis angle.

e) Final simulated EPIC-PN observation of the photon field of panel (d) with photons removed from the chipgaps. The generated clusters are marked with circles. The $\otimes$ marks the boresight. Clusters outside the field are generated, but will not be detectable in the PN exposure. They might be covered by the MOS1 or MOS2 detectors.

f) *Real* observation of the XDCP field LBQS 2212-1759 ($\sim 51.7\,\mathrm{ks}$ clean effective exposure time, see equation 6.1). Real galaxy clusters are marked with circles. The source populations (clusters and point-sources) are different from the ones in panels c, d, and e because the simulation was done with the artificially generated populations.

---

[9]Dead columns can occur on a CCD due to partial damage of the electronics or the chip itself, e.g. through high energy radiation in the space environment.

The output of xmm_sim are three FITS files, one for each EPIC detector, along with a list of simulated point-sources in the case of the artificial AGN field, and a list of simulated galaxy clusters.

5.2 Pipeline Analysis of the simulated XMM Fields

Just as in the case of the 469 XDCP fields, every simulated observation as well is analyzed by the Science Analysis System for the XMM-Newton observatory (XMM-SAS[10]). The XDCP analysis of the 469 fields is based on SAS version 6.5.0, which was the latest released version at the time of running the analysis. For consistency, the same version is also used for the analysis of simulated images. Throughout the thesis, the term *XDCP pipeline* is used for the pipeline that has been used to analyze the 469 real pointings of XDCP while the one analyzing the simulated pointings is referred to as *simulation pipeline*.

The XDCP pipeline is a dedicated development based on a bash script which calls the various tasks of the XMM-SAS ("SAS-tasks[11]"). The details of the pipeline are described extensively in Fassbender (2008). The simulation pipeline is an offspring from the XDCP pipeline with some adaptations. It is described in the following.

5.2.1 The appropriate Background Model

The XDCP pipeline performs preparatory steps, such as the removal of out-of-time events, flare cleaning (i.e. removal of time periods during solar flares) and image creation from the photon events. The first task working on images is the source detection by eboxdetect. For this first detection step, eboxdetect is run in the *local mode*, i.e. the background is estimated from the surrounding of the detection box.

Sources are then cut out circularly with a radius depending on the estimated source flux. After the detected sources have been removed, the image contains to first order only background (including unresolved sources). This image is called *cheese image* and it is used for fitting the background model (linear combination of constant and vignetted part, see section 5.1.3). The production of the cheese image and the model fit are performed by the SAS-task esplinemap.

For the simulation run, 10 β-model clusters are artificially inserted into each simulated pointing (see section 6.2.1). Therefore the cheese images of the simulations would be not as filled as the ones of the real pointings (more "holes"). This means that the background fit is not as stable and definitely different as compared to the background models from real pointings. Although the treatment of the data would be more realistic when implementing the background fitting, it has been decided to not do a re-fit for the above mentioned reason. Instead, the background model from the respective real pointing is adopted as input for the second run of eboxdetect.

---

[10]http://xmm.esac.esa.int/sas/
[11]The manuals for each task of SAS version 6.5.0 can be found online at
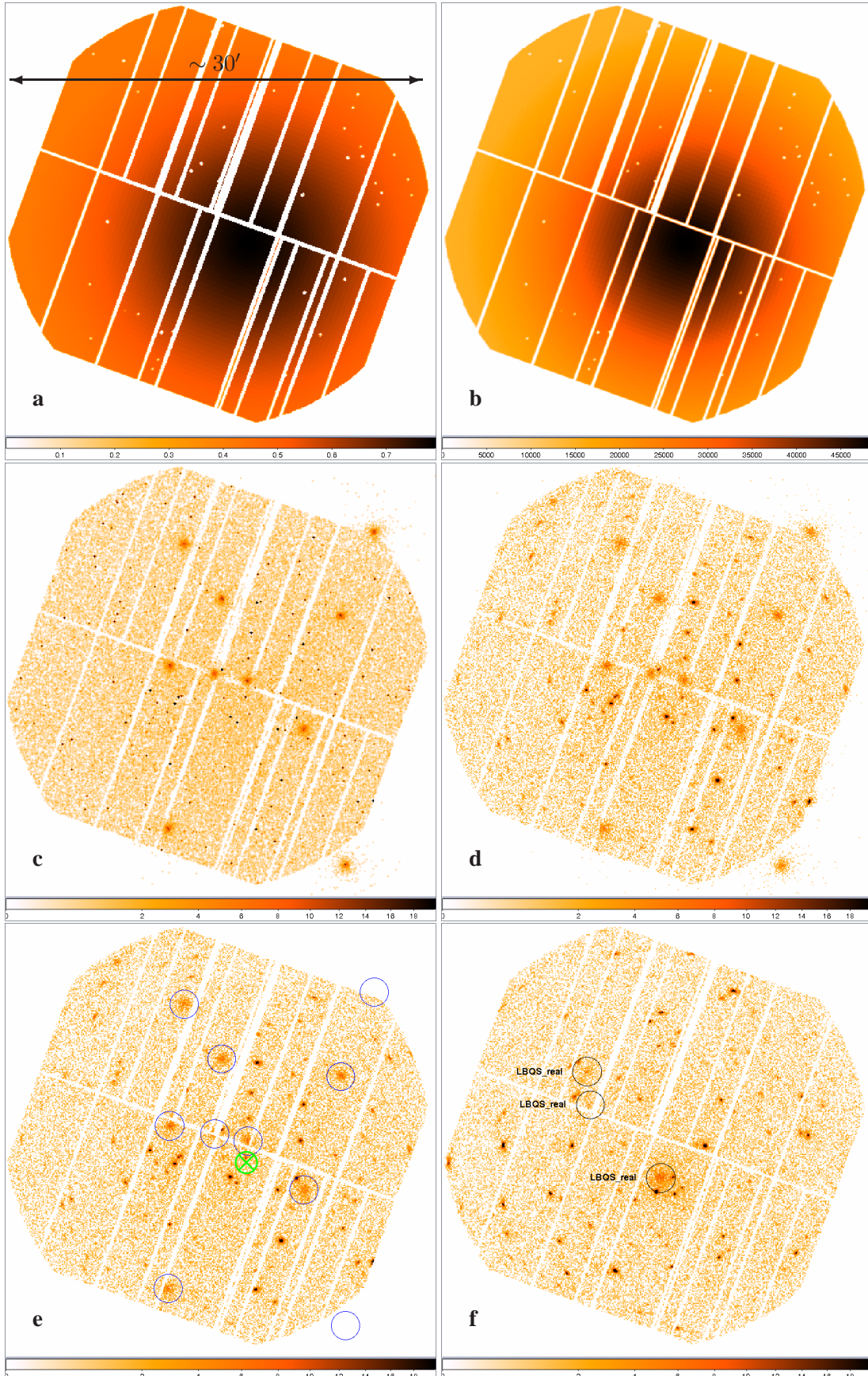   http://xmm.vilspa.esa.es/sas/6.5.0/doc/packages.All.html.

Figure 5.6: Images of various intermediate and final steps of the simulator. **a)** Background model, **b)** exposure map, **c)** unconvolved photon field, **d)** PSF-convolved photon field, **e)** final simulated EPIC-PN observation and **f)** real XMM-Newton observation. For symbol definitions, see text.

5.2.2   Sliding Box Source Detection

The task eboxdetect has a second mode of operation, called *map mode*. In this case, the background is taken directly from the background map at the current position of the detection box. Once the signal-to-noise ratio exceeds a certain threshold, the corresponding source information is written out to the source list including source position, estimated number of photons, estimated countrate (determined by use of the exposure map), estimated flux, and detection likelihood.

5.2.3   Maximum Likelihood Source Fitting

The final SAS-task used in the simulation pipeline is emldetect. It steps through the source list produced by eboxdetect and looks at each source separately. The goal of the task is to characterize each source as either point-like or extended and determine the respective parameters of each model, i.e. source position in the image (X_IMA and Y_IMA), source countrate RATE, and, in the case of an extended source, additionally the extent parameter EXT. Two different extent models are implemented in emldetect: in the case of a Gaussian profile, EXT is the standard deviation σ, whereas in the case of a β-model profile, EXT is the core radius r_{c} (see equation (2.4) with fixed $\beta = \frac{2}{3}$). The XDCP pipeline and the simulation pipeline both use the latter extent model.

The algorithm is based on an earlier implementation that has been used for the analysis of ROSAT data (Cruddace et al., 1988). Details can be found there as well as on the webpage of the emldetect manual. Here, the intention is only to describe qualitatively how the algorithm works.

The statistical significance for the detection (or the extent) of a source is expressed as a likelihood $L = -\ln p_{\mathrm{poi}}$, with p_{poi} being the probability that a random Poissonian background fluctuation has caused the source to appear (or to be extended). Therefore, it is the goal to determine source parameters, for which the source probability $p_{\mathrm{sou}} = 1 - p_{\mathrm{poi}}$ is maximized, i.e. to maximize the likelihood function.

For each source in the input source list (coming from eboxdetect), two likelihood functions are constructed (for all three EPIC images simultaneously): one for the point-source model and one for the extended source model (β-model). By differentiating the likelihood function with respect to the different source parameters, their best fit values are determined. Since the extended source model has an additional fit parameter, all likelihoods are transformed to normalized likelihoods, corresponding to two fit parameters, in order to allow for comparison between models with different numbers of fit parameters.

If the maximum likelihood value of the extended source model exceeds that of the point-source model by less than a fixed value $\Delta L_{\min} = 5$, the point-source parameters are written out to the final source list. If $\Delta L \geq 5$ the likelihood of a third model of two superimposed point-sources (which might imitate an extended source) is determined. Only if the likelihood of the extended model fit exceeds the two point-sources model fit, the source is written out to the final source list as extended together with its best fit parameters including the extent parameter EXT. All uncertainties of the fit parameters are written out as well. The most important parameters of the final source list are listed in table 5.1. DET_ML is the difference between the normalized likelihood of having a source and the normalized likelihood of having no source (random background fluctuation). EXT_ML is the difference between the normalized likelihood of having an extended source and the normalized likelihood of having a point-source.

emldetect parameter	explanation
`ML_ID_SRC`	`emldetect` source number
`BOX_ID_SRC`	corresponding `eboxdetect` input source number
`SCTS`	number of source counts
`X_IMA`	source image pixel X coordinate
`Y_IMA`	source image pixel Y coordinate
`EXT`	source extent, in this case core radius r_c of the β-model [imagepixels]
`DET_ML`	likelihood of detection
`EXT_ML`	likelihood of extent
`BG_MAP`	background at source location [counts/pixel]
`EXP_MAP`	exposure at source location (vignetting corrected) [s]
`RATE`	source count rate [counts/s]
`FLUX`	fiducial source flux (for an assumed ECF) [erg cm^{-2} s^{-1}]
`RA`	source right ascension [degrees]
`DEC`	source declination [degrees]

Table 5.1: Selection of important output parameters written to the final source list by `emldetect` together with their explanation. The primary fit parameters are shaded in grey.

5.2.4 The Final Extended Source List

After the source characterization by `emldetect` is finished, all sources with a non-zero core radius (implemented as `EXT` ≥ 0.1 pixels) are written to an ascii-file with their parameters r_c, N_{ph}, x, and y [12]. These sources are now called *reconstructed clusters*. The simulator `xmm_sim` writes the same parameters for the simulated clusters also to an ascii-file. These sources are now called *generated clusters*. The two ascii-files are merged into one for comparison of generated versus reconstructed clusters. A *gen-vs-rec* file is saved on disk for each simulation of an XDCP field.

Figure 5.7 shows an example of such a gen-vs-rec ascii-file. In its four columns, it lists the parameters r_c [pixels], N_{ph}, x, and y. In this case, the simulator was run in the mode where it uses a real XMM observation as background and does neither produce an artificial background nor an artificial point-source population. The real observation already contained four galaxy clusters, which are marked in the file as *fiducial* clusters by setting $r_c = 1.0$ and $N_{ph} = 0$ (first four generated clusters). The next ten lines are the parameters of ten simulated β-model clusters at ten different off-axis angles with randomly selected azimuth. Among the reconstructed clusters, the four fiducial clusters can be identified (by comparing coordinates) in lines 1, 2, 13, and 16. Two spurious sources are also among the reconstructed clusters, i.e. they have been detected although there were no real or generated sources at the respective position[13]. Thus, the number of reconstructed clusters adds up to 16.

---

[12]These are the primary source parameters which were used for the analysis in this thesis. The next step would be to investigate also the likelihood parameters `DET_ML` and `EXT_ML`.

[13]Of course one can in principle never be sure whether there is a real cluster contained in the underlying XMM observation at the position of the spurious source. However, it should have been detected in the analysis by the XDCP pipeline, if it was there.

```
-------------------------------------------------------
Comparison:  Generated versus Reconstructed Clusters
-------------------------------------------------------

Generated Clusters:
1.00 0 307.0 376.5
1.00 0 136.1 300.6
1.00 0 215.1 527.7
1.00 0 352.5 374.6
3.36 269 331.6 341.6
3.36 269 309.8 316.4
3.36 269 378.6 394.0
3.36 269 411.9 264.9
3.36 269 246.8 371.9
3.36 269 472.1 393.6
3.36 269 396.8 483.0
3.36 269 433.4 171.5
3.36 269 350.7 534.5
3.36 269 178.3 189.0

Reconstructed Clusters:
8.08291 974.209 307.032 376.494
1.80850 175.684 136.094 300.628
3.05502 285.185 351.153 534.537
6.09045 542.142 381.167 392.072
2.34062 214.157 332.122 341.854
2.49782 197.882 452.837 513.711
2.73489 229.839 411.631 263.507
4.41654 256.115 277.310 364.218
2.60915 211.976 246.984 372.623
2.20598 151.700 433.343 170.451
4.99246 318.972 397.542 482.968
6.75577 403.278 308.938 317.716
2.52246 121.416 215.166 527.771
3.79360 136.820 289.501 464.179
2.28641 122.126 471.679 393.432
4.10314 180.143 352.468 374.420
```

Figure 5.7: Example of a gen-vs-rec ascii-file. The columns are from left to right: r_c [pixels], N_ph, x, y. For a detailed description see text.

Chapter 6

First Results from XMM-Simulations

As a first application of the newly developed XMM simulator, 160 out of the 469 XDCP pointings have been simulated in a run of 2.5 months on 20 CPUs[1]. The purpose and the selection criteria of this subsample are described in section 6.1. Section 6.2 explains how the simulator xmm_sim and the simulation pipeline were used to compute a selection function depending on several cluster parameters. These results are then post-processed (section 6.3) to yield the sky coverage of the survey (section 6.4). Section 6.5 shows how to calculate the corresponding survey volume, while section 6.6 lists opportunities for possible further improvements in future projects.

6.1   The Chandra Extended Cluster Cosmology Sample

The Chandra extended Cluster Cosmology Sample (CheCCS) is a sub-sample of the 469 XDCP pointings. In 2009, the idea emerged to follow-up XDCP clusters with $z > 0.8$ with NASA's Chandra observatory. With their high spatial resolution, Chandra observations are capable of excising point-sources from the extended cluster emission more efficiently than XMM-Newton observations and determine the cluster shapes more accurately. Therefore, the subtraction of point-source contributions to X-ray spectra and fluxes as well as the modeling of the cluster density profiles can be performed more thoroughly. This leads to a better determination of cluster parameters like X-ray luminosity, temperature and gas mass. Since these parameters can be used as mass proxies, also the mass determination for the followed-up clusters is more precise, which is very valuable for cosmological studies with any cluster sample.

The CheCCS has been designed to meet several goals:

- Establish a well understood sample with a relatively simple selection function, at flux levels well above the detection limits.

- Define a sample size feasible for Chandra follow-up.

- Extend existing samples[2] to redshifts beyond $z > 0.8$.

The criteria following from these requirements can be subdivided into field selection criteria

---

[1]The computation was performed on a Sun Fire X4600 M2 with 8 Quad-Core processors based at MPE.

[2]The most famous distant cluster sample from Chandra is currently the $400 \deg^2$ survey by Vikhlinin et al. (2008) with a redshift range of $0.35 < z < 0.9$ It was constructed by following up a sample of clusters detected by ROSAT.

and additional source selection criteria. The clean[3] effective exposure time t_{exp} is defined by weighting the individual exposure times of the three EPIC instruments with their sensitivity:

$$t_{\mathrm{exp}} = \frac{1}{5.2}(3.2 \cdot t_{\mathrm{exp,PN}} + t_{\mathrm{exp,MOS1}} + t_{\mathrm{exp,MOS2}}) \, . \qquad (6.1)$$

Field selection criteria:

- Galactic neutral hydrogen column density $n_{\mathrm{H}} < 6 \cdot 10^{20}\,\mathrm{cm}^{-2}$.

- Clean effective exposure time $t_{\mathrm{exp}} > 10$ ks with at least two EPIC instruments in imaging mode[4].

- No sources in the field that significantly contaminate selection.

- Low background level.

Applying the field selection criteria leaves 160 out of the 469 XDCP pointings.

Source selection criteria:

- Source detected in the $0.35 - 2.4$ keV single band detection mode.

- Off-axis angle $\theta_{\mathrm{source}} \leq 12'$.

- No objects associated with original target.

- Flux $f_{0.35-2.4} \geq 1.5 \cdot 10^{-14}$ erg cm^{-2} s^{-1}.

- Conservative screening to remove obvious non-clusters and low-z clusters.

6.2   Simulated Observations of β-Model Clusters

A large simulation run was carried out in autumn 2009 to determine the sky coverage for the 160 fields of the CheCCS. For this purpose, xmm_sim was run in the real-background mode, i.e. the real XMM-observation of the field to be simulated served as background image and clusters were just added to it. No artificial background and no point-source population was added.

   For computing the *completeness*, this is the operation mode of choice because the point-source population and background are exactly as in the real observation. The determination of *contamination* requires the other operation mode which uses an artificial background and an artificial point-source population. Only in this case, the complete "truth" about the contained point-sources and galaxy clusters is known. With it, the fraction of falsely reconstructed sources can be calculated. In real observations, one could never be sure whether a spurious source is really not associated with extended X-ray emission.

---

[3]"Clean" refers to exposure times after having excluded times with high background level. This flare cleaning process is described in detail in Fassbender (2008).

[4]The EPIC cameras can be operated in several modes of data acquisition. E.g. the timing mode allows for improved time resolution with imaging only in one dimension.

6.2.1 The Choice of Cluster Parameters and Locations

Ten β-model clusters ($\beta = \frac{2}{3}$, see section 5.1.5), all with the same core radius r_c and number of photons N_ph, were added to each single field to be characterized. They were distributed over the field according to the following rules:

- The ten clusters were assigned different off-axis angles, ranging from $\theta_\mathrm{min} = 1.5'$ to $\theta_\mathrm{max} = 15'$ in steps of $1.5'$.

- The boresight ($\theta = 0$) was determined from the exposure map of the PN detector. For observations where it was not available, the boresight of the MOS1 detector was taken instead.

- The azimuth of each cluster is assigned randomly from a uniform distribution, which guarantees a fair treatment of azimuth angles.

- In order to prevent overlap of galaxy clusters, an anti-coincidence radius of $2'$ was introduced as a spacer of β-models from each other as well as from real clusters contained in the real observation: The position of each new cluster is tested for the spacer criterion. A new azimuth is chosen until a position fulfilling the criterion with all other clusters is found.

- For crowded fields, a "timeout" has been implemented: after 1000 trials, the program gives up and the current off-axis angle is not occupied by a cluster. This is important for the two innermost off-axis angles ($1.5'$ and $3.0'$), where the solid angle available for simulated clusters is very limited.

- Within the CheCCS, 21 out of 160 fields contain an exclusion region in their centers in order to mask bright central targets. 8 fields have exclusion regions at higher off-axis angles. The placement of β-models is performed regardless of any exclusion regions. The masks with possible exclusion regions are taken into account in the post-processing (section 6.3.4) and in the computation of the final sky coverage (section 6.4.1).

Each of the 160 XDCP fields was simulated five times with different seeds to increase the statistics. The above population scheme was applied for 25 values of r_c, each with 25 values of N_ph:

$$
\begin{aligned}
r_\mathrm{c} &= 2'' \dots 128'' \ \text{ in 25 logarithmic bins} \\
&\text{and} \\
N_\mathrm{ph} &= 20 \dots 1280 \ \text{ in 25 logarithmicbins.}
\end{aligned}
\tag{6.2}
$$

This leads to a total number of

$$
5 \,\text{realizations} \ \times \ 25 \ r_\mathrm{c} \text{ bins} \ \times \ 25 \ N_\mathrm{ph} \text{ bins} = 3125 \text{ simulations,} \tag{6.3}
$$

containing 31250 β-model clusters per XDCP field. This would lead to a total of five million β-model clusters for the CheCCS simulation run. However, due to the compression scheme, introduced in section 6.2.4, this number is reduced to $\sim 2.5 \times 10^6$.

6.2.2   The Matcher

After the run, a gen-vs-rec file for each of the 3125 simulations per XMM field is available which summarizes the generated and the reconstructed cluster parameters (see figure 5.7). The reconstructed and the generated clusters now have to be matched with each other. For this purpose, a program has been written which compares the two sets and looks for pairs with a distance of

$$\Delta x_{gen-rec} \leq 40'' \ . \tag{6.4}$$

In test runs, 90% of the pairs had a matching radius satisfying this criterion. Thanks to the introduced anti-coincidence radius of $2'$ (see section 6.2.1), the assignment of a reconstructed cluster to a generated one is unique. The matcher code then assigns one out of three available flags to each entry in the gen-vs-rec file:

Flag	Meaning
d	generated and **d**etected
n	generated but **n**ot detected
f	**f**alsely reconstructed (=spurious).

Detection Probability

With the assigned flags at hand for the five different realizations of one fixed set of parameters $r_{\rm c}$, $N_{\rm ph}$, and θ, the detection rates can now be calculated. The rates are regarded as probabilities and they are computed by counting the number of d-flags ($\#d$) and n-flags ($\#n$) and inserting them into the following equation:

$$p_{\rm det}(r_{\rm c}, N_{\rm ph}, \theta) = \frac{\#d}{\#d + \#n} \ . \tag{6.5}$$

The sum $\#d + \#n$ is equal to the total number of generated clusters. The detection probability $p_{\rm det}$ has to be calculated for each of the 6250 parameter combinations per pointing.

6.2.3   Representation of Detection Probability in Datacubes

The detection probability, derived in the previous section can be represented in a datacube. This means, for each simulated off-axis angle θ, a grid of $r_{\rm c}$ and $N_{\rm ph}$ is drawn with the calculated detection probability colorcoded in the 625 bins. Figure 6.1 shows two such datacubes for a deep and a shallow[5] field. These two fields were processed in a test simulation run at an early development stage. The names **LBQS** and **SCSA** are not official identifiers but only used as working titles throughout the thesis. With its 8.8 ks exposure time, SCSA is not part of the CheCCS (see field selection criteria, section 6.1). The green lines and the grey shaded area overlaid on the first slices of the cubes represent a compression scheme of the parameter space which is explained in section 6.2.4.

The transition line from low to high detection rate on the left is nearly perpendicular to the $N_{\rm ph}$-axis. This transition is due to the discrimination between point-sources and extended sources. β-models with $r_{\rm c} \lesssim 4''$ cannot be spatially resolved and are thus missing in the total number of detected clusters (see equation 6.5). The fact that the transition line is slightly inclined can be explained by the photon statistics: with more counts available, the β-model fit performed by `emldetect` works better and is thus able to discriminate extended sources from point-sources

---

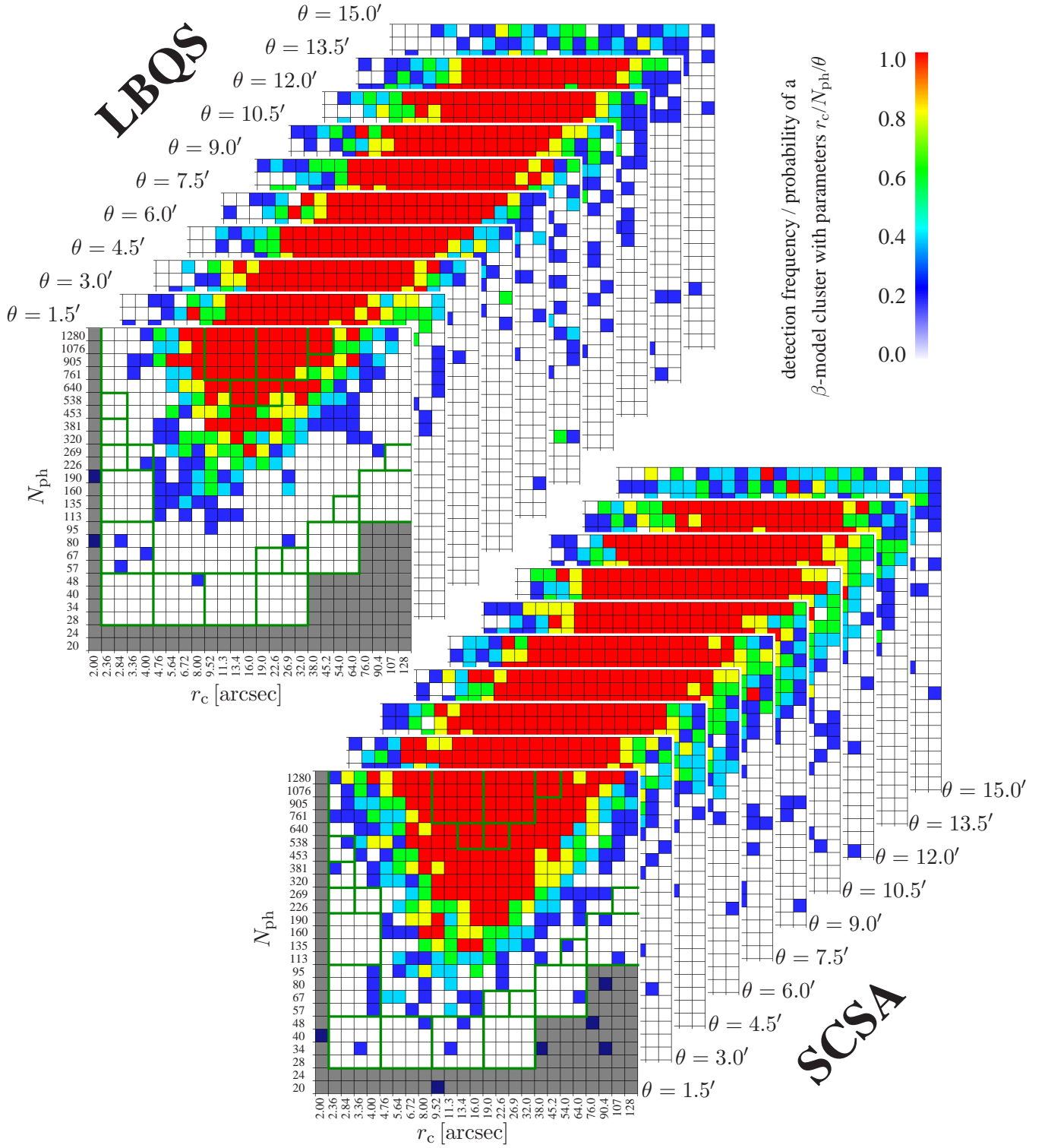[5]"Deep" and "shallow" refer to a long and short exposure time, respectively.

Figure 6.1: Probability cubes of the two XDCP test fields "LBQS" (52 ks) and "SCSA" (8.8 ks). The three considered parameters are: core radius r_c, number of photons N_ph (β-model parameters) and the off-axis angle θ (observational parameter). The green lines indicate areas where only the central point in the r_c-N_ph-plane (all θ) was simulated. The grey shaded regions were not simulated at all in the final run.

down to lower core radii. Thanks to the logarithmic r_{c}-scale, this transition region is resolved well enough to see this effect.

The other transition line at the right side of the probability distribution can be attributed to a surface brightness effect: Regarding only photons within the core of the β-model, the signal-to-noise ratio (SNR) is defined as

$$\mathrm{SNR} = \frac{S}{N} = \frac{f_{\mathrm{c}} \cdot N_{\mathrm{ph}}}{\sqrt{B}} = \frac{f_{\mathrm{c}} \cdot N_{\mathrm{ph}}}{\sqrt{\pi r_{\mathrm{c}}^2 \cdot \rho_B}} \tag{6.6}$$

with B being the number of background counts within a circle of radius r_{c}; f_{c} denotes the fraction of cluster photons encircled by r_{c}, which is independent of r_{c} for a given β-value[6]. ρ_B is the surface density of background photons at the cluster position (in photons per square arcseconds). Solving equation (6.6) for N_{ph} yields

$$N_{\mathrm{ph}} \propto r_{\mathrm{c}} \tag{6.7}$$

for a constant minimum SNR required by the source detection algorithm. The right edge of the probability distribution shows just this behavior. Clusters to the lower right of the transition line are too low in surface brightness to be detected; they disappear in the background.

Regarding the slice at $\theta = 15'$, one can see that the detection rate shows a sharp drop towards the edge of the field-of-view, even at intermediate core radii and large numbers of photons. The reason for this effect becomes clear by looking at the boresight position in figure 5.6 (e): rings at large off-axis angles are not fully covered by all detectors. The $15'$-ring is covered by the PN only at 1/3 of its perimeter and not at all by the MOS detectors (which is not seen in figure 5.6). Nevertheless, this off-axis angle was included in the simulations in order to cover the full detector area.

6.2.4 Running 160 XDCP Pointings

The production of a simulated pointing by the XMM simulator `xmm_sim` takes only a few seconds (see figure 5.5). On the other hand, the β-model fit performed by `emldetect` is computationally expensive and can take up to ten minutes for the processing of the source list of one pointing. With the layout of the first test fields, the complete simulation of one XDCP pointing (25 r_{c}-values $\times$ 25 N_{ph}-values $\times$ 5 realizations) took 5 days on 5 simultaneously running CPUs. The computation time for 160 fields would therefore have been 800 days. The required amount of storage space for the FITS files containing simulated pointings, source lists, etc. would have been approximately 13 Terabytes.

Several optimization steps were taken to save computation time as well as disk space. First of all, the storage space management of the simulation pipeline was improved with respect to the XDCP pipeline. While the latter keeps some metadata (e.g. the image sum of the two MOS detectors), the simulation pipeline regularly deletes all files which are not needed any more. Only the image sum of all three EPIC detectors is kept (for possible later diagnostics) and of course the final source list products.

A second improvement was the compression of the parameter space to be simulated. By looking at figure 6.1 it can be seen that some regions of the probability distribution are very homogeneous. This fact was utilized for saving resources. The grey shaded regions on the $r_{\mathrm{c}}/N_{\mathrm{ph}}$-plane were excluded completely from the simulations since even in the shallowest fields (SCSA)

---

[6]For the canonical value $\beta = \frac{2}{3}$, this fraction can be analytically calculated by integrating equation (5.10), which results in $f_{\mathrm{c}} \approx 29.3\%$.

those parameter combinations did not show significant cluster detections during the test runs. For each of the 2×2 and 4×4 boxes overlaid on the first slices in figure 6.1, only the central value was taken as the $r_\mathrm{c}/N_\mathrm{ph}$-combination to be simulated. The detection rates were assumed homogeneous within those regions. This measure reduced the number of simulated $r_\mathrm{c}/N_\mathrm{ph}$-combinations from 625 to 321 (each with ten off-axis angles θ).

The third improvement came with a new workstation with 32 CPU cores, 20 of which were reserved for the XDCP simulations. After a runtime of about 2.5 months, the simulation of 160 fields was completed in November 2009. The improved storage space management together with the compression of the parameter space reduced the hard disk requirement for 160 pointings to 800 Gigabytes.

6.3 Post-processing of the Datacubes

6.3.1 Conversion from Counts to Flux

In a first step of post-processing, the number-of-photons scale of the 160 data cubes (see equation 6.2) has to be converted into a flux scale. Due to the effective exposure time varying with off-axis angle, this has to be done individually for each θ-slice of the data cubes according to equation (3.17):

$$f(N_\mathrm{ph}, \theta_\mathrm{slice}) = \frac{N_\mathrm{ph,det}/t_\mathrm{exp,det}}{\mathrm{ECF}(\mathrm{det}, \mathrm{filter}, n_\mathrm{H}, T, z)} \; . \qquad (6.8)$$

In this case, $t_\mathrm{exp,det}$ is the exposure time which has been derived from the exposure map of the respective detector (det) for the correct off-axis angle θ_slice by taking the median of all pixels fulfilling the condition to lie in a ring with $\theta_\mathrm{slice} - 1\,\mathrm{pixel} < \theta_\mathrm{pixel} < \theta_\mathrm{slice} + 1\,\mathrm{pixel}$. In this way, the influence of the chip-gaps on the exposure time calculation is eliminated. The ECF in the denominator depends on instrumental parameters (detector det and the used filter) as well as on astrophysical ones (galactic hydrogen n_H and the temperature T and redshift z of the galaxy cluster). The parameters det, filter and n_H are fixed for each pointing. The n_H value has been taken from a radio astronomical survey by Dickey and Lockman (1990).

Equation (6.8) is always evaluated for one detector (det) only: for the PN where it is available and for MOS1 in cases where the PN was not in an operation mode usable for cluster detection. At least one of those two is always available in the simulated sample of 160 fields. $N_\mathrm{ph,det}$ is the expectation value of the number of photons simulated in one detector: $N_\mathrm{ph,PN} = N_\mathrm{ph} \cdot \frac{3.2}{5.2}$ and $N_\mathrm{ph,MOS1} = N_\mathrm{ph} \cdot \frac{1}{5.2}$ respectively (see equation 5.11).

Figure 6.2 shows how the ECF depends on the cluster parameters temperature T and redshift z. It varies only by approximately 6% over the redshift and temperature range which is important for XDCP. It has therefore been decided to fix the fiducial[7] values at $kT = 5\ \mathrm{keV}$ and $z = 1$ (marked by the circle).

After having transformed the N_ph scale into ten flux scales, the 160 cubes are now available in the form $p_\mathrm{det}(r_\mathrm{c}, f, \theta)$. However, their shape is not exactly cubic any more because the θ-slices are shifted with respect to each other, due to the different flux scales originating from vignetting. See figure 6.4 for a view of the relative positions of the ten flux scales.

---

[7]The term "fiducial" indicates the fact that some parameter setting has to be selected as a reference point, which is chosen to be an average representative value.
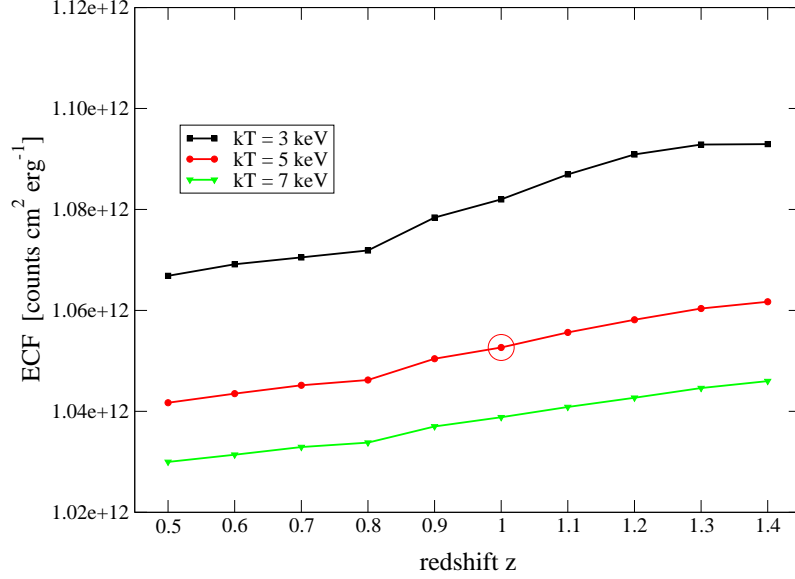
Figure 6.2: XDCP's energy conversion factors (ECF) against the cluster parameters T and z. The following assumptions have been made in this example: the countrate is the sum of the countrates of all three EPIC instruments with thin filters and the flux is taken in the $0.35 - 2.4\,\mathrm{keV}$ energy band. An absorbed mekal model (see section 3.1.6) was used with galactic hydrogen $n_\mathrm{H} = 2.36 \times 10^{20}\,\mathrm{cm}^{-2}$ and cluster metallicity $Z = 0.3\,Z_\odot$. The circle marks the fiducial values of kT and z which are used for the flux calculation in the probability cubes.

6.3.2   Interpolation of Detection Probability in the $r_\mathrm{c} - f$ Plane

Because of the reduction of the number of support points in the $r_\mathrm{c} - N_\mathrm{ph}$ plane, which was described in section 6.2.4, the parameter space is now sampled inhomogeneously. Important regions are sampled with finer resolution, while regions, where the detection probability is expected to change only marginally, are sampled on a coarser grid. For the purpose of further processing of this inhomogeneous data set, the function $p(r_\mathrm{c}, f)$ is interpolated linearly (for each of the ten θ-slices separately) on a triangular grid, which is shown in figure 6.3 (left panel).

In order to eliminate artefacts from the interpolation, the resulting image is smoothed with a boxcar average of a width corresponding to four linear bins. The smoothing is a legitimate operation because it is performed on a well understood and well behaved function (no local extrema to be expected) of the two parameters r_c and f. As an example, the resulting $p_\mathrm{det}(r_\mathrm{c}, f)$ map of the first slice ($\theta = 1.5'$) of the LBQS datacube is shown in figure 6.3 (right panel).

6.3.3   Extrapolation in Flux-Direction

Figure 6.4 shows an example of the "side view" of a probability cube. The flux scales, indicated by horizontal bars differ from each other, despite the common N_ph-range, due to the vignetting effect (decreasing effective exposure time with increasing off-axis angle). The green shaded area marks the target flux range onto which all flux scales were projected.

At the lower end, the derived detection probability has been extrapolated towards the lowest target flux $f_\mathrm{min} = 10^{-16}\,\mathrm{erg\,cm^{-2}\,s^{-1}}$ (marked in the figure by dots). When going from the lowest simulated flux towards lower fluxes, in most cases the function p_det becomes zero well before the lowest target flux is reached. This operation therefore has little influence on the results, but it is necessary to be able to further process the data.
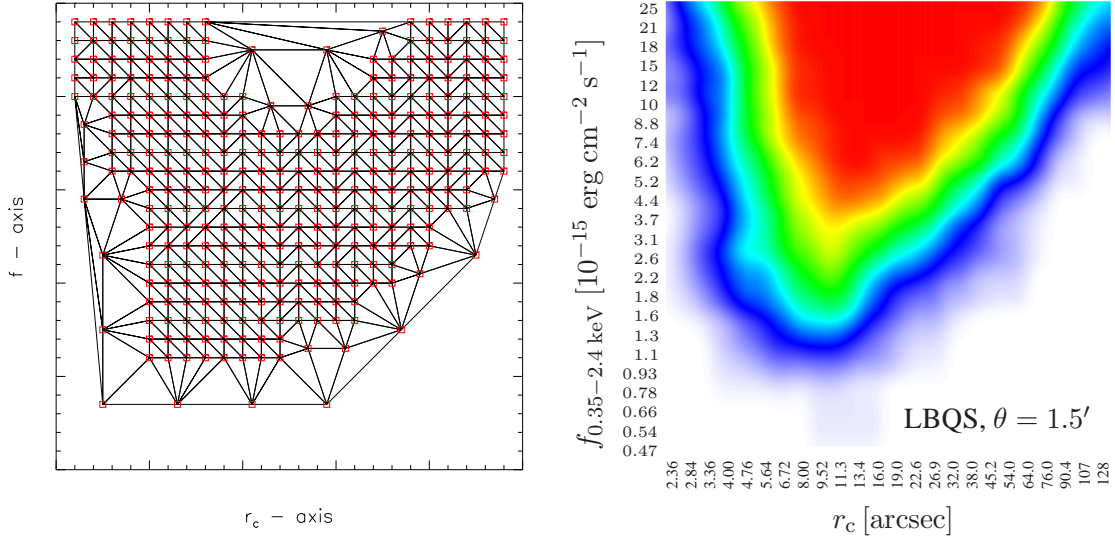
Figure 6.3: Left: The 321 support points in the $r_{\rm c}$ - f plane where the detection probability has been simulated and the lines, along which the linear interpolation of the function $p_{\rm det}(r_{\rm c}, f)$ is performed. **Right:** Interpolated and smoothed function $p_{\rm det}(r_{\rm c}, f)$ of the slice $\theta = 1.5'$ of the LBQS testfield (see figure 6.1). The colorbar is the same as in figure 6.1.

At the upper end, $p_{\rm det}$ was extrapolated out to $f_{\max} = 2 \times 10^{-13}$ erg cm^{-2} s^{-1}. This is necessary in order to estimate the sky coverage for high completeness levels. Especially for extremely small or extremely large core radii, the function $p_{\rm det}(f)$ reaches only intermediate levels at the highest *simulated* flux. These regions can have a large influence, depending on which $r_{\rm c}$-distribution is assumed for the weighting process (see section 6.3.5). Without extrapolation, some $p_{\rm det}(f)$ curves would never reach, for example, the 90 % level and the corresponding pixels would therefore be missing in the sky coverage curve for $c = 0.9$. At fluxes where the extrapolation yields numbers larger than one, the probability was fixed at $p_{\rm det} = 1$.

6.3.4 Expansion in θ-Direction

For each of the 160 simulated XMM-pointings, ten slices of the datacube at different off-axis angles θ are now available on equalized flux scales. The final sky coverage is obtained by counting pixels, depending on their individual sensitivity. Therefore, the available information has to be expanded in θ-direction as well as re-binned onto a finer grid so that for each pixel, the corresponding $p_{\rm det}(r_{\rm c}, f)$ can be chosen according to its individual θ value.

This re-binning procedure involves extrapolation and interpolation steps. There are several cases to be considered which are illustrated in figure 6.5 and described in the following.

Missing data due to too many real clusters in the image: In XDCP fields that are "crowded" by real clusters, it was often not possible to put artificial clusters at small off-axis angles, because the matching between reconstructed and generated clusters would have been distorted by the real ones, which would lead to a wrong estimation of detection probability. To prevent this effect, a timeout was implemented in xmm_sim for the positioning of β-model clusters (see positioning rules in section 6.2.1). The drawback is, that no probability estimation is available for those θ slices. Out of the 1600 simulated θ slices, this occurred 32 times at $\theta = 1.5'$ and 5 times at $\theta = 3.0'$. In these cases, $p_{\rm det}$ was extrapolated from the inner three remaining $p_{\rm det}(\theta)$ (in the
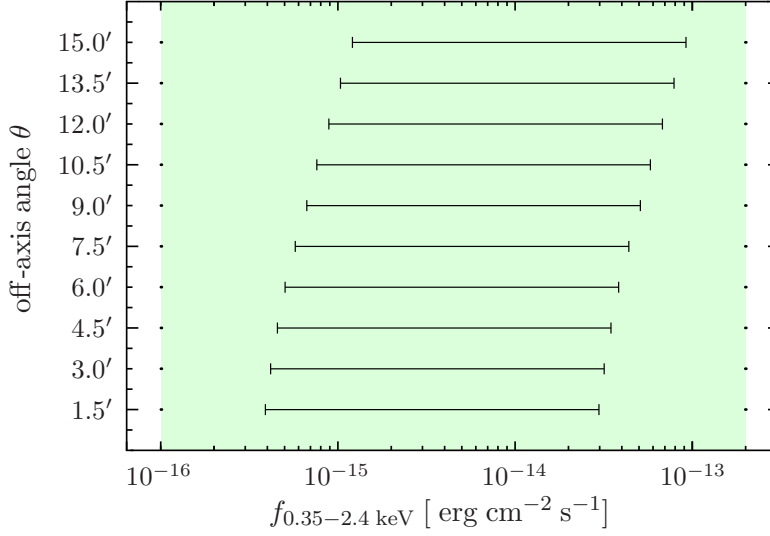
Figure 6.4: "Side view" of a probability cube (in this case LBQS data). The bars show the ranges of the flux scales for each simulated off-axis angle, derived from the common N_{ph} scale. They are shifted with respect to each other due to the decreasing exposure time with increasing θ (see equation 6.8). The shaded region marks the range of the final flux scale.

case of missing $1.5'$ value) or interpolated (in the case of missing $3.0'$ value). The latter case is illustrated in figure 6.5, where the support point at $\theta = 3.0'$ (red $*$) is not simulated and was therefore set to zero and not considered further. Note, that the point at $\theta = 1.5'$ in this case was actually simulated. Its low p_{det} value is caused by a bright central object in the field. This case is described in the next paragraph.

Low detection probability due to a bright central object: A bright central object does not prevent xmm_sim from placing β-model clusters on top of it. However, it is difficult for the analysis pipeline to detect such clusters, which are outshined by the bright object. This leads to a very low detection probability close to the bright source, in some cases reaching zero for the whole parameter space r_{c} & N_{ph}. This is also the case in the example in figure 6.5, which can be seen clearly in all panels **a** to **f**. In most cases, these regions are not counted in the final sky coverage because they are excluded by the detection mask and thus do not contribute to the XDCP survey anyway. It is however important to treat this case correctly, in order to achieve a good estimation of p_{det} just at the border outside the exclusion region where the PSF wings from the bright central target might still affect cluster detectability.

Estimation of the central detection probability: The on-axis detection probability has not been simulated since this point ($\theta = 0$) is negligible when weighted with the detector area. Furthermore, there is only one point to put a cluster and no variation of azimuth is possible to enlarge the statistics. The on-axis detection probability was therefore extrapolated from the other support points as well.

Interpolation between the support points: For the re-binning of the now available 11 support points (for fixed r_{c} and f), a spline fit was used to expand the θ scale to 101 final bins, corresponding to a bin width of $9''$. The sometimes strong variation of p_{det} with θ is real and originates
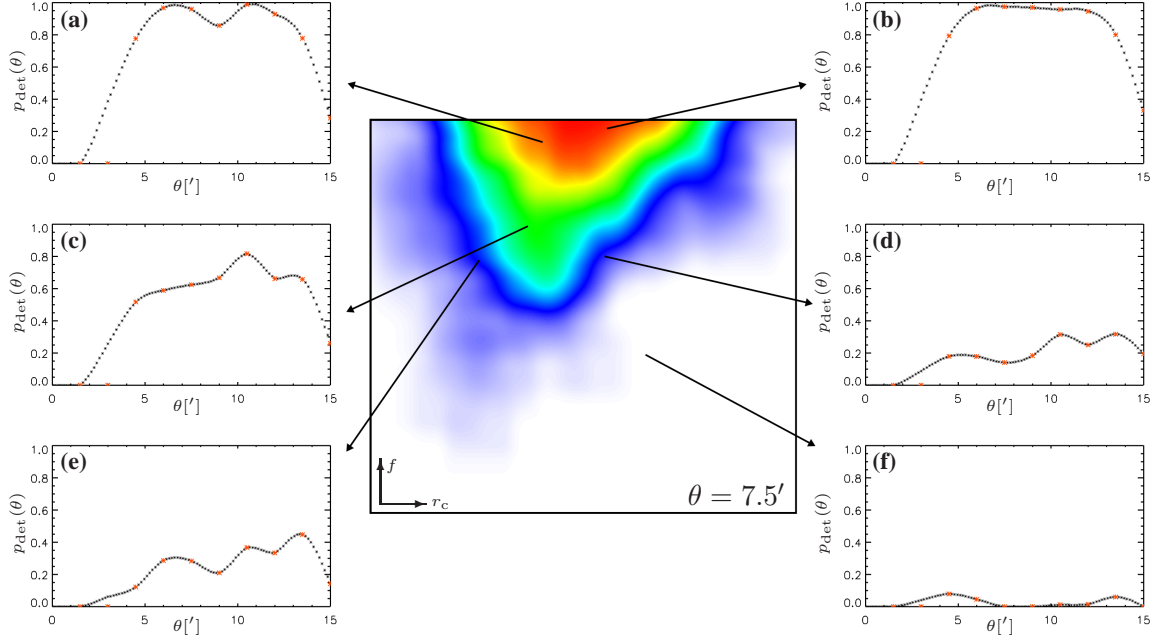
Figure 6.5: Example of a field with missing simulated data at $\theta = 3.0'$ and a bright central object, which leads to a sharp drop in p_{det} towards the center of the field. Shown in the middle is the slice at $\theta = 7.5'$ in the parameter plane f and r_{c}. The panels **a-f** show the third dimension (θ) of the the "data cube" for six example points of the $f - r_{\text{c}}$-plane. They illustrate the re-binning algorithm in θ direction: The red $*$ mark the ten simulated off-axis angles, the smaller black $*$ are the 101 finer gridpoints obtained by extra-/interpolation and a final spline fit (see text).

from the peculiarities of the fields. For example, clustering of point-sources at a specific off-axis angle can sometimes lead to a systematically reduced or enhanced p_{det} at the respective θ. Not all points in the r_{c}-f-parameter space are affected, because different seeds have been used for each run, leading to different azimuths of cluster positions. However, from a statistical point of view, the effect is present and should be taken into account. Therefore, linear interpolation between the support points plus smoothing the data or just fitting a polynomial are not considered the best approaches here. The spline fit, which preserves the peculiarities of the functions, seems to be an adequate solution.

6.3.5 Weighting of Detection Probability with a Core-Radius Distribution

The final product from the simulations is a sky coverage depending only on flux. Therefore, a suitable averaging over the parameter r_{c} is required. This is achieved by weighting $p_{\text{det}}(r_c, f)$ with an r_{c}-distribution, which should be as realistic as possible. Several attempts have been made to measure such a distribution from galaxy cluster surveys by the Einstein Observatory (e.g. Jones and Forman, 1999) and ROSAT (e.g. Vikhlinin et al., 1998).

Such measurements are likely to be affected by incompleteness, which implies that the r_{c}-distribution should be corrected for missing objects by simulating a detection probability $p_{\text{det}}(r_{\text{c}})$. In principle, the simulation run described here could be used to obtain such a function by averaging $p_{\text{det}}(r_c, f)$ over flux, assuming a suitable flux distribution, which in turn is affected by selection effects as well. Such problems can possibly be solved in an iterative way but this investigation is not performed here.

Pacaud et al. (2006) have assumed a constant *physical* core radius of $r_c = 180$ kpc. The approach followed here is to consider two extremes and an intermediate r_c-distribution (scenarios **a**, **b** and **c**, see figure 6.6, right panel) and to check how the results are influenced by the choice of the r_c-distribution.

Derivation of the r_c-Distribution

The catalog of Vikhlinin et al. (1998) contains 223 measured *angular* r_c values where in 200 cases the redshift z of the cluster is known as well. Note, that the core radii in the catalog were determined by assuming a fixed $\beta = 0.67$ which is close to the value $\beta = 2/3$ used in this thesis. The *physical* r_c values can be derived for the 200 clusters with known redshift by applying equation (B.11). The clusters are then rescaled (first without assuming any evolution) to the fiducial redshift of $z = 1$ and the resulting *angular* r_c-distribution is the one applied to the weighting of the detection probability function. This distribution is roughly Gaussian in $\log(r_c)$, see figure 6.6 (left panel). In order to use it for the averaging procedure, it has been fitted by a log-normal function, normalized to fulfill the condition $\int_{-\infty}^{\infty} n(r_c) = 1$. This yields a most frequent core radius of $\mu_{r_c} = 14.05''$ (scenario **a**). The extremes are obtained by moving the mean of the fitting function to the two values $\mu_{hi} = 2 \cdot \mu_{r_c}$ (scenario **b**) and $\mu_{lo} = \frac{1}{2}\mu_{r_c}$ (scenario **c**).

The right panel of figure 6.6 shows the three applied versions of r_c-distributions overlaid on the colorcoded $p_{det}(r_c, f)$ at $\theta = 7.0'$. In this way, it can be seen which parts of the simulated parameter space contribute most to the final sensitivity curve.

The justification for the lower extreme (scenario **c**) is given by assuming an evolution of the core radius with redshift like $r_c \propto \frac{1}{1+z}$. Since the original cluster population has a rather low redshift (with a peak of the redshift distribution around $z \approx 0.2$), this leads to a shift of the core radii by a factor of ~ 2 to lower values. The width of the Gaussian does not change on a logarithmic scale. The case of higher r_c values (scenario **b**) has been considered mostly for completeness. A possible astrophysical reason could be, that there are more cluster mergers taking place at high redshifts, which may appear as single clusters with a larger core radius when fitted with a β-model.

The weighting algorithm steps through the 101 fine θ-bins and computes the function $p_{det}(f, \theta)$ according to the equation

$$p_{det}(f, \theta) = \sum_{r_c} p_{det}(r_c, f, \theta) \cdot n(r_c) \ . \tag{6.9}$$

To exemplify, the resulting $p_{det}(f, \theta)$ for $\theta = 7.0'$ is shown in figure 6.6 (right panel) as well. Due to occasional outliers, this curve is not always strictly monotonic. Section 6.4 describes, how this artefact is dealt with. The data available at this stage consists of the functions $p_{det}(f, \theta)$ for all simulated 160 fields, which are stored as images in FITS format. In the following these datasets are called pft-maps ("**p** of **f** and **t**heta").

6.4   Sky Coverage of the 160 CheCCS Fields

The sky coverage $S_c(< f)$ of a survey states the survey area (solid angle in square degrees) which is complete to a certain percentage down to a given flux. For example, $S_c(f_{lim} < f_0) = S_{50}(< f_0) = 10 \deg^2$ means, that on $10 \deg^2$, sources of flux f_0 are detected with 50% probability, sources with higher flux have a higher detection probability. In other words, $S_c(f_{lim} < f_0)$ states the survey area with a detection sensitivity (flux limit f_{lim}) of at least $f_{lim} = f_0$ or better ($f_{lim} < f_0$).

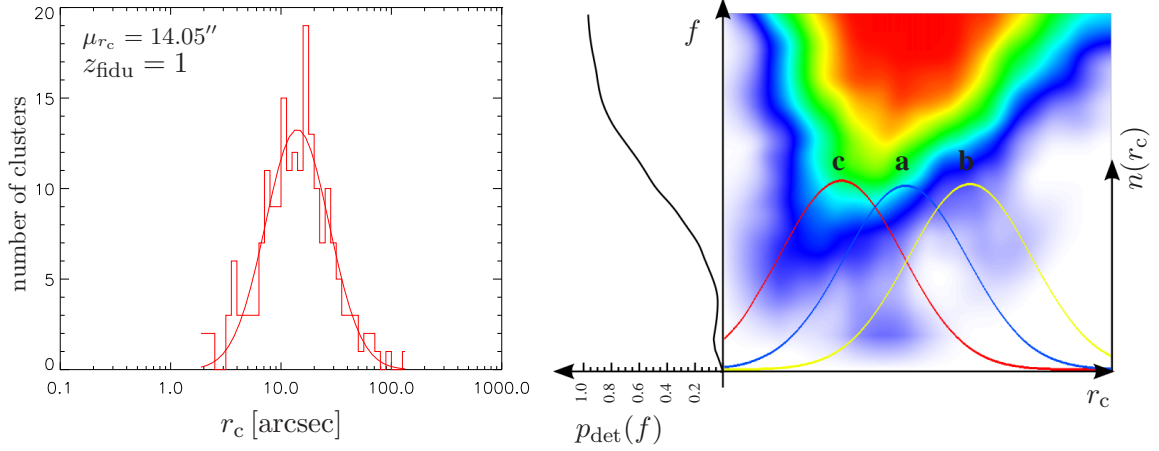**Figure 6.6: Left:** Histogram of core radii of the 200 galaxy clusters with redshift information from the survey by Vikhlinin et al. (1998) and the log-normal fit. Note, that the clusters are just *moved* geometrically to $z = 1$ and not evolved in any way. **Right:** Illustration of the weighting process (equation 6.9). Shown are the three applied distributions $n(r_c)$ overlaid on the $p_{det}(r_c, f)$ slice at $\theta = 7.0'$, and the $p_{det}(f)$ for $\theta = 7.0'$ resulting from the weighting with the central $n(r_c)$ (blue curve). The r_c-distributions are marked by labels a, b, c for identification with the corresponding resulting sky coverage plot in figure 6.8. Example field: LBQS.

6.4.1   Calculation Method

There are two equivalent methods to construct the final sky coverage curve of the simulated XDCP sample. Both rely on counting pixels with certain properties and summing them up. Each pixel then contributes to the sky coverage with $(4'')^2$.

   The first approach follows this procedure:

1. Choose a completeness level for which the sky coverage is to be constructed.

2. For each pixel, choose the corresponding function $p_{det}(f)$ according to its off-axis angle.

3. From this function, read the flux limit $f_{lim,c}$ down to which $p_{det}(f) \geq c$, so that $p_{det}(f_{lim,c}) = c$ for the chosen completeness c.

4. Step through the full flux range. For each flux f, sum up the pixels where the flux limit is below the current flux: $f_{lim,c} < f$.

This method works only for monotonic functions $p_{det}(f)$. Otherwise the flux limit $f_{lim,c}$ is not defined uniquely, i.e. there is more than one solution to the equation $p_{det}(f_{lim,c}) = c$. As described in section 6.3.5, the $p_{det}(f)$ derived from the simulations are not always monotonic. Therefore, a second approach was pursued:

1. Choose a completeness level for which the sky coverage is to be constructed.

2. For each pixel, choose the corresponding function $p_{det}(f)$ according to its off-axis angle (up to here, the tasks are identical to the ones in the first method).

3. Step through the full flux range. For each flux f, count the current pixel, if the detection probability at the current flux is larger than the currently chosen completeness level: $p_{det}(f, \theta(i,j)) \geq c$.

Mathematically, this method can be written as

$$S_c(< f) = \sum_{i,j\,|\,cond.} (4'')^2 \tag{6.10}$$

where i, j are pixel indices defined uniquely within the 160 pointings and fulfilling the condition
cond.:

$$cond. = i, j \in M \;\; \land \;\; p_{\text{det}}(f, \theta(i,j)) \geq c \;\; . \tag{6.11}$$

M is the mask, which defines the pixels that are to be considered as part of the survey. The mask is
constructed from the exposure maps by excising the exclusion regions, such as regions with bright
central sources. Note that the loop runs over all pixels in all 160 XDCP fields.

   This method works also for non-monotonic functions $p_{\text{det}}(f)$. At first sight, this might seem
unphysical. Why should a source with a certain flux f_1 be detected, but a second source with a
larger flux $f_2 > f_1$ not be detected? This is actually an artefact due to low statistics. For example
a cluster (with fixed core radius r_c) could be detected at a certain flux, but disappear behind a
bright point-source at a higher flux due to a different position in the field. This is possible because
different seeds were used for all simulated parameters. However, with the second approach, each
detection is treated statistically correct and the artefacts are averaged out in the final sky coverage
for a whole field (or even more for all 160 fields) due to the much larger statistics.

6.4.2 Treatment of overlapping Fields

Because XDCP is a serendipitous survey, all suitable XMM fields from the Science Archive (XSA)
have been considered. Thus, the chosen XMM pointings are neither placed on the sky in a special
pattern, nor distributed homogeneously. It is therefore possible that some fields overlap, especially
in regions of high astronomical interest, where e.g. the original observing purpose required to look
at one object several times or to do mosaics of a larger sky patch.

   To obtain the unique non-overlapping area on the sky, duplicate pixels must be counted only
once. Calculating WCS[8] coordinates for each pixel, sorting them in right ascension and declina-
tion and calculating their distance is a computationally very intensive task for $\mathcal{O}(2 \times 10^7)$ pixels.
Therefore, a different approach was implemented to treat the overlapping regions: All fields (in-
stead of all *pixels*) were tested for pairwise overlap by calculating their boresight distances (on
great circles on the sky). Out of the 160 CheCCS fields, 42 are close enough that they can overlap.
They can be arranged in 16 groups. For each group, a mosaic has been created using the SAS-task
`emosaic`. Each mosaic consists of the detector masks of the member fields, scaled by a unique
binary code which identifies the mask with its OBS_ID through a lookup table. An example is
shown in table 6.1 with the resulting mask mosaic in figure 6.7.

   For each pixel, it is now possible to identify unambiguously which fields overlap at the current
position. Since also the boresight coordinates are stored in the lookup table (transformed from the
single masks to the mosaic pixel coordinates), the corresponding off-axis angles are determined
and the correct $p_{\text{det}}(f)$ functions can be chosen from the pft-maps (see section 6.3.5).

6.4.3 Discussion

Figure 6.8 presents the sky coverage curves resulting from the weighting with three different r_c-
distributions. Panel **a** is valid under the assumption that the raw distribution from Vikhlinin et al.

---
[8]WCS: World Coordinate System

code	OBS_ID	boresight coordinates x / y
1	0112680101	501.5 / 632.5
2	0112680301	1100.4 / 633.5
4	0112680401	352.0 / 336.0
8	0112680501	123.3 / 347.7
16	0112681001	948.6 / 334.2
32	0112681301	632.2 / 345.9

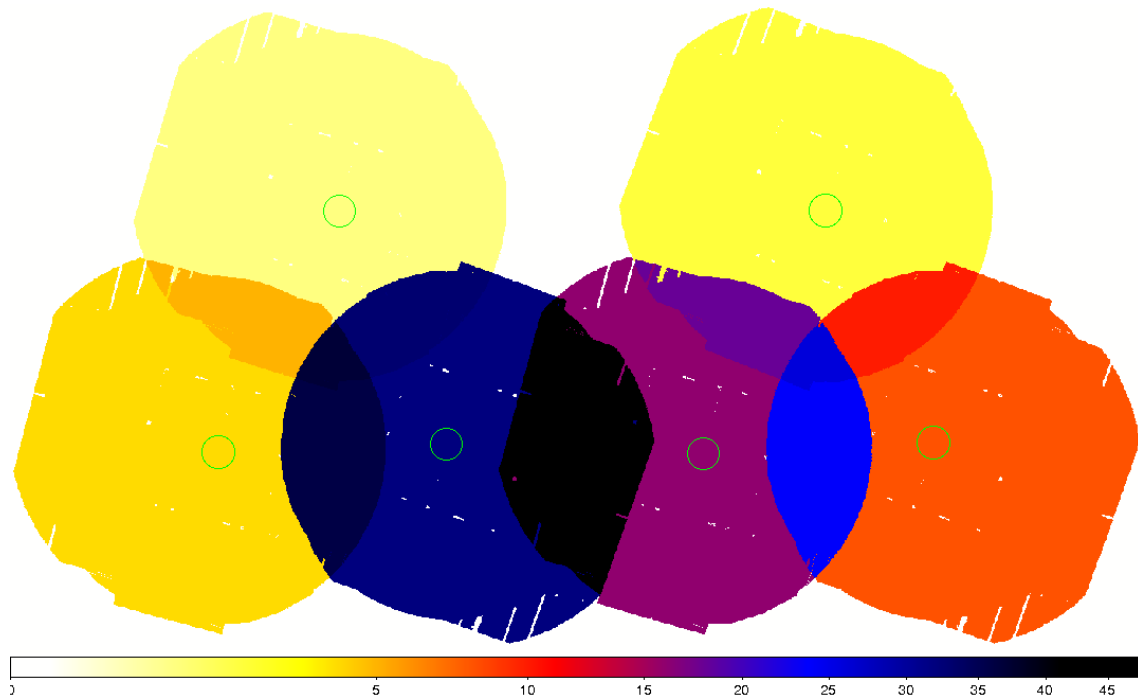**Table 6.1:** Example of a mosaic lookup table. The corresponding mosaic image is shown in figure 6.7.

Figure 6.7: One example of the 16 groups where fields overlap. The colors show the decimal values of the binary numbers which encode the field's OBS_ID (see table 6.1). Boresights are marked by green circles.
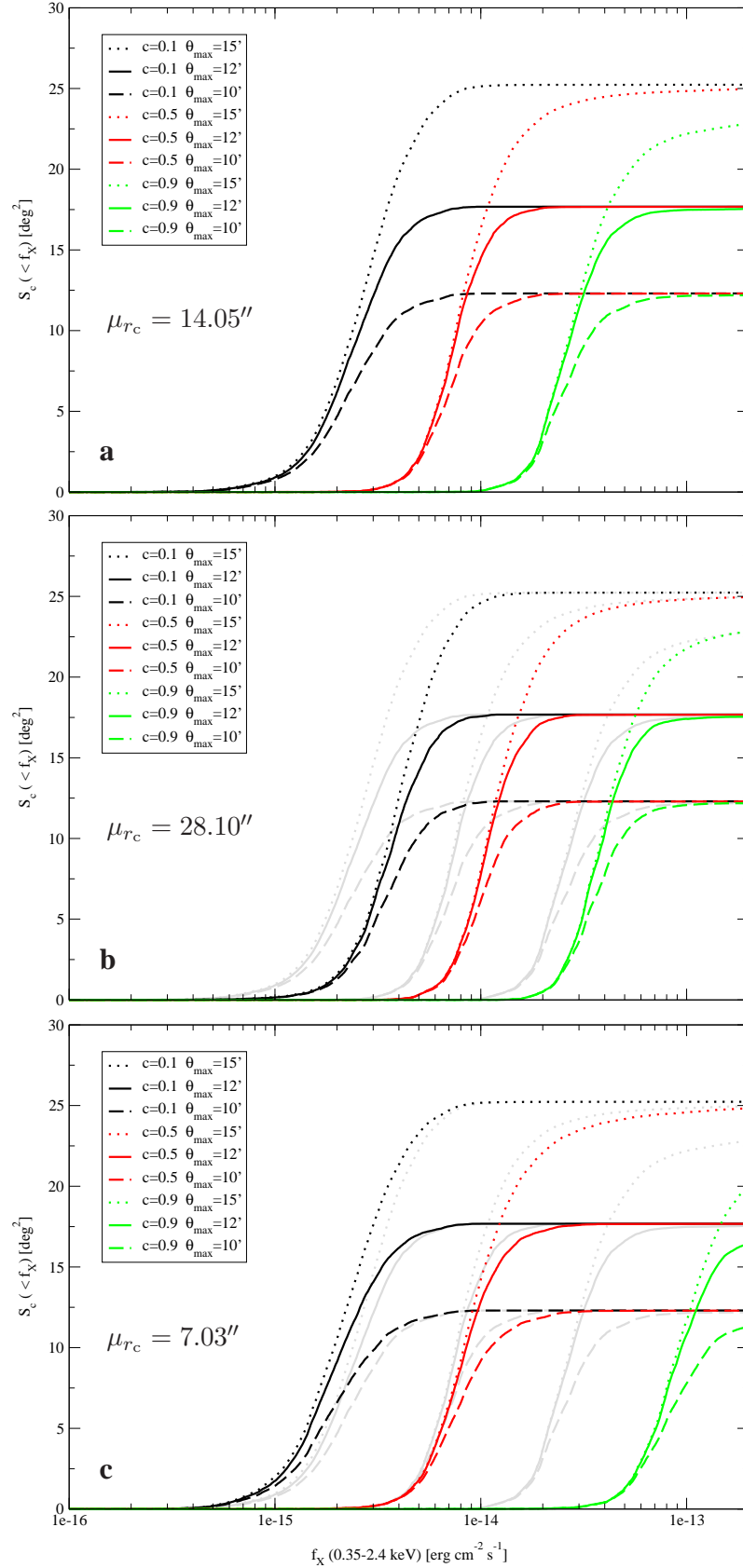
Figure 6.8: Final sky coverage of the 160 XDCP fields from the CheCCS subsample, plotted for different completeness levels, different maximum off-axis angles, and three different r_c-distributions. The flux scale is the same on all panels. For further description, see text.

(1998) represents the real cluster population with a most common core radius of $\mu_{r_c} = 14.05''$. Panels **b** and **c** result from scaling the r_c-distribution to larger ($\mu_{r_c} = 28.10''$) and smaller ($\mu_{r_c} = 7.03''$) core radii, respectively. Each panel displays the curves for three different completeness levels $c = 0.1,\ 0.5,\ \text{and}\ 0.9$ and three different maximum off-axis angles out to which pixels have been considered: $\theta_{\max} = 10',\ 12',\ 15'$.

The total area of the 160 fields included within the detection masks is $27.113\ \deg^2$. The maximum occurring off-axis angle of any mask pixel is $18.0'$. As already mentioned in section 6.2.3, already circles at $15'$ are not fully covered by the CCDs any more, i.e. the field becomes very inhomogeneous at these off-axis angles. When the sky coverage is evaluated for $\theta_{\max} = 15'$, the corresponding (dotted) curves converge to a value of $25.2\ \deg^2$. Reducing the maximum considered off-axis angle to the "standard" XDCP value of $\theta_{\max,\text{XDCP}} = 12'$ reduces the survey area to $17.7\ \deg^2$. A further constraint of $\theta_{\max} = 10'$ decreases the area by another $\sim 30\,\%$ to $12.3\ \deg^2$ with only a marginal difference in the resulting sensitivity (see figure 6.9 and table 6.2).

At arbitrarily high flux levels, the sky coverage should in principle always converge to the total survey area. However, due to the mentioned inhomogeneity at large θ, the detection probability does not always reach 50%, and even less the 90% level. Also in the case of bright central sources, the detection probability drops significantly towards the center, even for very bright cluster models. These pixels are therefore missing in the budget of the sky coverage, making a difference in total area when considering different completeness levels. This can be seen for example in figure 6.8 (top panel) when comparing the curves for $\theta_{\max} = 15'$.

For comparison, in panels **b** and **c**, the curves from panel **a** are overlayed in grey color. From the applied r_c-distributions in comparison with the $p_{\text{det}}(r_c, f)$-map (figure 6.6, right panel), it is evident that upon rescaling the r_c-distribution to higher values, the survey sensitivity decreases and all sky coverage curves are scaled to higher fluxes (panel **b**).

This effect is less pronounced, when considering the more likely scenario of decreasing core radii evolution with higher redshifts (panel **c**). The curves for completeness level $c = 0.1$ are then even shifted to the left. To understand this effect, one has to regard the completeness levels as quantiles of the core radii distribution: Recovering only $10\,\%$ of the clusters ($c = 0.1$) is easiest, if the central $10\,\%$ lie just at the tip of the $p_{\text{det}}(r_c, f)$-map. This most sensitive region is roughly situated around $r_{c,\text{tip}} \approx 10''$. This value is closer to the mean core radius of scenario **c** ($7.03''$) than to the one of scenario **b** ($14.05''$).

The curves for $c = 0.5$ are almost insensitive with respect to scaling the r_c-distribution from scenario **a** to the physically motivated evolution scenario **c**. When requesting a completeness level as high as $90\,\%$, the required fluxes increase by a factor of ~ 3.4 (green curves), because a large part of the corresponding r_c-distribution lies in regions, where it becomes increasingly harder for the detection algorithm to discriminate clusters from point-sources (see the red r_c-distribution in figure 6.6).

The flux scale of the sky coverage plots is defined for the band $0.35 - 2.4$ keV. By assuming a fiducial cluster at redshift $z = 1$ with a temperature of $kT = 5$ keV observed in a field with a hydrogen density of $n_{\text{H}} = 2.8 \times 10^{20}\ \text{cm}^{-2}$ (median of all CheCCS fields), the fluxes can be transformed to the standard band (e.g. by using Xspec[9]):

$$f_{0.5-2.0\ \text{keV}} = 0.78 \cdot f_{0.35-2.4\ \text{keV}}\ . \tag{6.12}$$

This conversion factor changes by only $1.5\,\%$ over the relevant redshift range ($0.8 < z < 1.5$) and temperature interval ($3\ \text{keV} < kT < 7\ \text{keV}$). The change to the standard $0.5 - 2.0$ keV energy
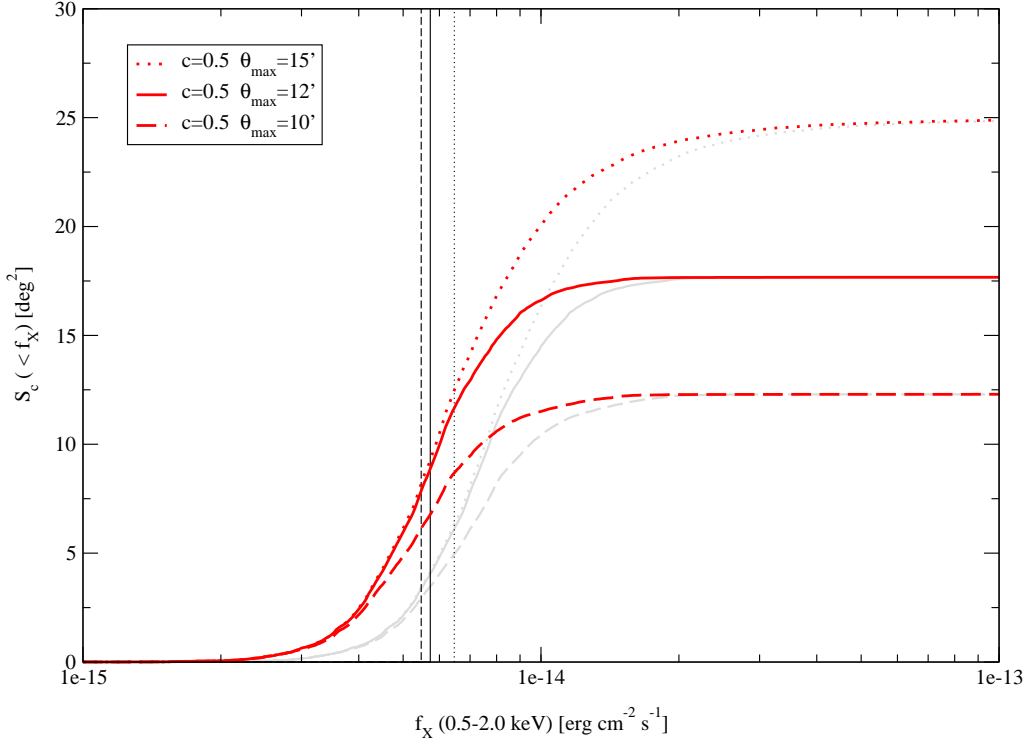
---

[9]http://heasarc.nasa.gov/xanadu/xspec/

Figure 6.9: Flux conversion from the XDCP band $(0.35 - 2.4\,\mathrm{keV})$ to the standard soft X-ray band $0.5 - 2.0\,\mathrm{keV}$ for a fiducial cluster with $kT = 5\,\mathrm{keV}$ at redshift $z = 1$. Only the curves for $c = 0.5$ and r_c-distribution **a** $(\mu_{r_\mathrm{c}} = 14.05'')$ are shown here. Vertical lines indicate the fluxes reached at half the total area for each $\theta_{\max}$.

band is illustrated in figure 6.9, which shows scenario **a** with a zoomed flux scale, now defined in the standard band from 0.5 to 2.0 keV with the original curves defined in the $0.35 - 2.4\,\mathrm{keV}$ band shaded in grey. The vertical lines mark the flux limit levels reached at half the total respective survey area. All numbers characterizing the sky coverage plots are summarized in table 6.2, which states the total survey area out to three maximum off-axis angles and the flux limits f_lim defined at half the respective area for both, the $0.35 - 2.4\,\mathrm{keV}$ XDCP band and the $0.5 - 2.0\,\mathrm{keV}$ standard band.

Note, that the flux considered here is the one *generated* for the β-models. It is the total flux within a squared box of $10'$ edge length (see section 5.1.5). In real observations, the cluster flux is usually measured within r_{200}. This influences the flux scale by another $7 - 10\%$, in the same direction as going from the XDCP band to the standard band, i.e. towards an increased sensitivity or lower flux limits, respectively.

As a final result, the detector area which is best suited for cluster detection can be evaluated: as mentioned above, the sensitivity for completeness level $c = 0.5$ changes only marginally ($\sim$ 3.5 %), when constraining the maximum off-axis angle to $\theta_{\max} = 10'$ instead of $12'$; on the other hand about 30% of the available detector area is lost. When put the other way round, more than 40% of the detector area (and therefore survey area) are gained with only a marginal loss in survey sensitivity when using the definition $\theta_{\max} = 12'$. The use of the "standard" XDCP value of $\theta_{\max,\mathrm{XDCP}} = 12'$ is therefore a suitable choice, confirming the preliminary tests of Fassbender (2008).

$\theta_{\max}$ [arcmin]	Total survey area $\deg^2$
–	27.113
15.0	25.232
12.0	17.679
10.0	12.304

r_c distr.	c	$\theta_{\max}$ [arcmin]	$f_{\lim}(0.35-2.4\text{ keV})$ [erg cm^{-2} s^{-1}]	$f_{\lim}(0.5-2.0\text{ keV})$ [erg cm^{-2} s^{-1}]
(a) $\mu_{r_c}=14.05''$	0.1	15.0	2.7×10^{-15}	2.1×10^{-15}
	0.1	12.0	2.4×10^{-15}	1.9×10^{-15}
	0.1	10.0	2.3×10^{-15}	1.8×10^{-15}
	0.5	15.0	8.3×10^{-15}	6.5×10^{-15}
	0.5	**12.0**	**7.3×10^{-15}**	**5.7×10^{-15}**
	0.5	10.0	7.0×10^{-15}	5.5×10^{-15}
	0.9	15.0	3.1×10^{-14}	2.4×10^{-14}
	0.9	12.0	2.6×10^{-14}	2.1×10^{-14}
	0.9	10.0	2.5×10^{-14}	2.0×10^{-14}
(b) $\mu_{r_c}=28.10''$	0.1	15.0	4.0×10^{-15}	3.1×10^{-15}
	0.1	12.0	3.6×10^{-15}	2.8×10^{-15}
	0.1	10.0	3.4×10^{-15}	2.7×10^{-15}
	0.5	15.0	1.2×10^{-14}	9.3×10^{-15}
	0.5	12.0	1.0×10^{-14}	8.2×10^{-15}
	0.5	10.0	1.0×10^{-14}	7.8×10^{-15}
	0.9	15.0	4.3×10^{-14}	3.3×10^{-14}
	0.9	12.0	3.7×10^{-14}	2.9×10^{-14}
	0.9	10.0	3.5×10^{-14}	2.8×10^{-14}
(c) $\mu_{r_c}=7.03''$	0.1	15.0	2.2×10^{-15}	1.8×10^{-15}
	0.1	12.0	2.0×10^{-15}	1.5×10^{-15}
	0.1	10.0	1.9×10^{-15}	1.5×10^{-15}
	0.5	15.0	9.3×10^{-15}	7.2×10^{-15}
	0.5	12.0	8.0×10^{-15}	6.3×10^{-15}
	0.5	10.0	7.7×10^{-15}	6.0×10^{-15}
	0.9	15.0	1.1×10^{-13}	8.2×10^{-14}
	0.9	12.0	8.8×10^{-14}	6.9×10^{-14}
	0.9	10.0	8.5×10^{-14}	6.6×10^{-14}

Table 6.2: Summary of the characteristic figures of the sky coverage plots. The flux limit values $f_{\lim}$ are defined as the fluxes reached at half the total area for each $\theta_{\max}$. They are stated for two different energy bands. The "standard" values are shaded in grey.

6.5   Calculation of the Survey Volume

For relating observations to theoretical predictions of cluster number density, the comoving survey volume has to be known in addition to the total number of clusters in a given redshift and mass interval. The predicted number density can then be compared to observed histograms of certain cluster properties, e.g. cluster mass or luminosity. The final goal of the complete survey will be a reconstruction of the high-z luminosity and mass functions. To compute a luminosity function of a source population, the established V_{max}-approach is commonly used, which was introduced by Schmidt (1968):

$$\Phi(L) = \frac{1}{\Delta L} \sum_{i=1}^{N_{\mathrm{S}}} \frac{1}{V_{\mathrm{max},i}} \tag{6.13}$$

with L : luminosity [erg/s]
  Φ : number density of objects with a luminosity between L and $L + \Delta L$
          $\left[(\frac{\mathrm{erg}}{\mathrm{s}})^{-1} h^5 \, \mathrm{Mpc}^{-3} \right]$
  ΔL : size of the luminosity bins [erg/s]
  i : source index
  N_{S} : number of sources in the sample
  $V_{\mathrm{max},i}$: maximum volume of the ith source.

For each source (with index i), the maximum redshift is computed, at which it would still be observable according to the (local) flux limit of the survey f_{lim}. This redshift $z_{\mathrm{max},i}$ (together with the survey area) defines the maximum volume $V_{\mathrm{max},i}$ for each source. The maximum redshift $z_{\mathrm{max},i}$ is calculated from the luminosity distance $d_{\mathrm{lum}}(z) = \sqrt{L/(4\pi f_{\mathrm{lim}})}$ by solving equation (B.10) for z, which is the desired $z_{\mathrm{max},i}$. Since the universe is expanding, a simple formula for the cone volume (like $V = \frac{1}{3} A \cdot h$) does not suffice. The maximum volume is therefore obtained by integrating over the shell elements along the lightcone[10]:

$$V_{\mathrm{max},i}(L) = V_{\mathrm{com}}[z_{\mathrm{max},i}(f_{\mathrm{lim}}, L)] = \int_0^{z_{\mathrm{max},i}} S_{\mathrm{sky}} \left(\frac{d_{\mathrm{lum}}(z)}{1+z} \right)^2 \frac{c \ \mathrm{d}z}{H(z)} \tag{6.14}$$

where S_{sky} is the sky coverage, i.e. the detection area of the survey. However, most surveys, especially serendipitous ones, do not exhibit a homogeneous coverage, because each pointing has a different exposure time and background, which leads to an individual flux limit for each pointing, or even for each image pixel. The sky coverage in this case becomes a function of the flux: $S_{\mathrm{sky}}(f_{\mathrm{lim}})$ (see figure 6.8). While usually only a very small fraction of the geometrical survey area has a small f_{lim} (i.e. high sensitivity), the sky coverage will increase for larger f_{lim}, since every piece with low f_{lim} also contributes to the sky coverage at regions with high f_{lim}. In order to properly account for this variation, a further integration over the flux is required:

$$V_{\mathrm{max}}(L) = \int_{f_{\mathrm{low}}}^{f_{\mathrm{high}}} \frac{dV_{\mathrm{com}}[z_{\mathrm{max}}(f, L)]}{\mathrm{d}f} \ \mathrm{d}f =$$

$$\int_{f_{\mathrm{low}}}^{f_{\mathrm{high}}} \int_0^{z_{\mathrm{max}}(f)} \frac{\mathrm{d}S_{\mathrm{sky}}(f)}{\mathrm{d}f} \left(\frac{d_{\mathrm{lum}}(z)}{1+z} \right)^2 \frac{c \ \mathrm{d}z}{H(z)} \ \mathrm{d}f. \tag{6.15}$$

---

[10]In equations (6.14) and (6.15), c is the speed of light and not the completeness level.

6.6 Possible Future Improvements for the XDCP Simulations

The experience gained during the project has led to several suggestions for improving the XDCP simulation and survey characterization work:

Minor Improvements

- Galaxy clusters have only been simulated at positions with fixed off-axis angles ($1.5'$-$15.0'$ in steps of $1.5'$) with random azimuth. In order to capture the full characteristics of the individual pointings, it could be worthwhile to also vary the off-axis angle within the limits of the respective θ-bin. However, this would require an increased number of realizations per field and cluster parameter set.

- As mentioned in the discussion in section 6.4.3, the flux calibration of the simulations is not yet done on a safe basis. In order to compare with real data and also with other surveys, the post-processing of the detection probability data cubes should be repeated with ECFs for the standard band of $0.5 - 2.0$ keV. Due to the different n_{H} and filter settings of each pointing, the assumption of a global flux correction (equation 6.12) can lead to minor deviations. More important is the calculation of the flux fraction integrated out to r_{200} instead to $10'$ as it is implemented at the moment (see section 5.1.5). This effect becomes increasingly prominent at larger core radii and therefore depends strongly on the applied r_{c}-distribution with which the probability data cubes are weighted.

Further Projects

- The completeness of the XDCP survey has been determined in this study. The second part is the contamination, i.e. how many false detections are expected for certain cluster and field parameters. It is important to quantify for a complete characterization of a survey. However, every distant cluster candidate (in real observations) is followed up by optical and/or infrared imaging for confirmation and possibly by spectroscopy in order to determine its accurate redshift. In most cases, the imaging step already allows for a classification of whether the source was real or spurious. Simulations of the contamination can nevertheless be helpful for the optimization of the detection software parameters.

  Simulations of the contamination rate require the second mode of xmm_sim, in which an artificial point-source population is generated and the background is poissonized from the background model of the original pointing. Simulating NO clusters at all and analyzing those images will yield an estimation of the falsely detected clusters (false positives) and their statistical properties. It is also possible to gain insight on the mechanisms leading to spurious detections and to improve the detection algorithm and the used parameters with respect to a low contamination rate. The lessons learned from this study will also influence the development of detection software for the eROSITA project, for which follow-up observations become a major challenge, regarding the expected amount of clusters to be detected in the all-sky survey.

- The main challenge in every source detection algorithm is to find the right trade-off between high completeness and low contamination. The standard analysis for XMM data has two main parameters defining the significance of the detected sources: the detection likelihood DET_ML and the extent likelihood EXT_ML (see section 5.2.3). The present study

has examined the detection efficiency with the current set of cuts on those parameters. An optimization of the cuts for the purpose of detecting extended sources could lead to further improvements in detection efficiency. In the current version of emldetect however, the parameter EXT_ML is only written out to the final source list in cases where the source has been identified as extended. In order to perform the suggested study, a modified version of emldetect is required.

Towards more realistic Models

- In the current version of xmm_sim, the ray-tracing PSF model is implemented for the image convolution. Efforts are on the way (e.g. at AIP[11]) to calibrate XMM-Newton's PSF by means of real observed point-sources. The difference between the real and the ray-tracing simulated PSF can be estimated by comparing figures 4.2 and 4.3 ("on-axis"). This improved PSF model (tentatively called "*ellbeta*"-model, see also section 4.2.2) is included in the latest version of XMM-SAS and can also be implemented in xmm_sim. At this point, it is not clear how this more realistic PSF model would influence the detection probability and contamination.

- Simulated observations of β-model clusters are based on only few parameters and thus well controlled. However, they are azimuthally symmetric by design and thus do not represent the diverse sub-structure of real clusters. Furthermore, recent comparisons to real observations have shown, that a single β-model does often not accurately reproduce the cluster profile over the full cluster radius (e.g. Croston et al., 2008).

  Therefore, an additional track of xmm_sim has been developed for the purpose of ingesting single hydrodynamically simulated clusters. Their advantage is that their mass and luminosity are accurately known from the hydro-simulation. These are the parameters linked to cosmological models of cluster formation. Completeness estimations based on simulated observations of hydro-simulated clusters can therefore be used to directly correct observations and then compare them to cosmological predictions. Furthermore, the density profile of hydro-simulated clusters is known from the simulation and thus quantities like r_{200} and f_{200} are well defined (unlike in the case of β-models). However, these parameters depend sensitively on the implemented input physics of the hydro-simulation. Hydro-simulated clusters are also the basis of the eROSITA image simulator which is described in chapter 7.

Within the scope of the present work, a large number of useful simulation and analysis tools have been developed, which are now available for further development and integration into future projects. The simulator code xmm_sim is capable of reading different PSF models and also prepared for the implementation of different cluster models. Hydrodynamic cluster simulations by Yang et al. (2009) have already been included experimentally. More development work is thus to be done in order to quantify the limits of galaxy cluster science with XMM-Newton and to gain experience for the future large efforts in doing cosmology with increasingly large cluster samples, as expected from the upcoming eROSITA survey.

---

[11]AIP: Astrophysikalisches Institut Potsdam, Germany

Chapter 7

A fast eROSITA Image Simulator

For any data analysis project, being able to simulate data is a crucial ingredient. There are two main reasons for this: Firstly, for an analysis software which is still in the development phase it is important to have mock data available to check the performance of the software and test whether the output parameters of the analysis follow as closely as possible the input parameters of the simulation. Secondly, also for well established software packages, observers sometimes have difficulties to understand their data. In this case it can be very helpful to analyze simulated data in parallel to the observed data because with the input parameters of the mock data at hand it is known exactly what the analysis software should produce. In this way one can draw conclusions about the observed data. An example of this approach is the correction of XDCP data through the selection function which was described in chapter 6.

This chapter describes in detail the eROSITA image simulator with the simulated celestial sources, flux-to-countrate conversion, image convolution and simulation of sub-pixel resolution relying on split events. The simulated images were not yet analyzed because no dedicated eROSITA analysis software was available at the time of writing. Experiments with provisionally adapting the XMM-SAS to analyze eROSITA data were given up due to technical problems. However, the first pieces of the eROSITA Science Analysis Software System (eROSITA-SASS) are currently close to being available for test runs and so the eROSITA simulator will serve as a testbed for the software developers.

7.1 The eROSITA Image Simulator

In parallel to the development of the real instrument, an eROSITA image simulator has been developed using the programming language C. The aims of the simulations are:

- Test and develop object detection algorithms of the dedicated analysis software (eROSITA-SASS) once it is available,

- Compare cluster parameters derived from a simulated survey to the respective input parameters in order to assess the integrity of the data processing chain,

- Assess, how well the eROSITA mission can detect and characterize clusters of galaxies,

- Provide a simulation tool for future analyses,

- Predict the scientific outcome of the survey and thus support the design of a sophisticated follow-up strategy.

Two different approaches to simulate mock data are followed within the eROSITA collaboration which are partly complementary to each other:

Simulating Photon Events

An important part of the eROSITA data analysis software is the Near Real Time Analysis (NRTA) which is being developed at the Dr. Remeis-Sternwarte Bamberg[1]. The NRTA is a software package which will be responsible for monitoring data directly after they are downlinked from the spacecraft. These are house keeping data of the instrument (like e.g. CCD temperatures, voltages, currents, etc.) as well as science data. Photon events are screened to detect possible errors already at this early stage. However, the main scientific purpose of the NRTA is, to analyze the science data as soon as possible and thus identify astrophysical objects immediately after their first observation. This is especially important for transient objects like novae, supernovae or gamma-ray-bursts. In these cases it is crucial to alert the astronomical community in order to trigger timely follow-up observations. Kreykenbohm et al. (2009) describes the NRTA in more detail.

In order to test this software package during the development phase and well in advance of the mission's launch, a photon event simulator is being developed which is designed to resemble the real measurement process as closely as possible and to produce the same data format as the real data. It consists of various subprograms, e.g. a program which generates photons from astrophysical source models, an orbit and attitude[2] simulator which takes care of the scanning of the telescope over the sky, and a telescope simulator which distorts the photons following a probability distribution according to the telescope's PSF. At the end, each simulated photon event carries information about its incident point on the eROSITA CCD (x and y), its photon energy, and its time of arrival.

The main drawback of this approach is that it takes a very long time to simulate even a small patch of the sky on up-to-date standard CPUs. On the other hand, the event simulator produces the most realistic data as it follows each step of the real measurement process. In order to get images from these photon event data, the photons have to be sorted into sky pixels by additional software. Furthermore, also light curves and spectra can be generated from the event data, which is a crucial precondition for the testing of the NRTA software. A comprehensive description of this project can be found in Schmid (2008).

Simulating Sky Images

Another simulation approach, which produces mock data much faster but also relies on various approximations and assumptions, is the eROSITA image simulator which was developed within the scope of this thesis. The idea is to neglect the information about the time of arrival of each photon and also its spectral information (photon energy) to some extent. The image simulator only cares about the energy band in which a photon energy lies but not about the exact energy. Up to now it is operating in the standard X-ray band from $0.5\,\mathrm{keV}$ to $2.0\,\mathrm{keV}$. The spatial information is nevertheless kept and also PSF convolution is done on an event by event basis. The data product of

---

[1] http://www.sternwarte.uni-erlangen.de/

[2] Attitude is the combination of the pointing direction and the (azimuthal) roll angle of an astronomical satellite. An attitude file contains attitude information for all times of an observation.

the image simulator are sky images in the format of FITS files. Unlike the event simulator, where images have to be produced from the events by the NRTA or the SASS, it immediately sorts every single photon into sky pixels. The high computational speed of the image simulator is needed to produce many images with a large amount of different instrumental characteristics as well as astrophysical properties, e.g. cluster parameters. In this way, many different mission scenarios in terms of hardware and software can be tested with respect to their scientific outcome. The field size of the output images of the eROSITA simulator is $3.77° \times 3.77°$ on the sky or 4096×4096 image pixels, which is a legacy of the cluster lightcone described in section 7.2.3.

The details of the eROSITA image simulator are described in the following in the order in which an X-ray photon coming from the sky would encounter the individual parts of the instrument. The emphasis is on aspects which differ from the XMM simulator. For features which are common among the two programs, a reference to the corresponding section in chapter 5 is given.

7.2 Simulated Celestial X-Ray Sources

The eROSITA image simulator is capable of generating X-ray photons from various types of sources. First of all it has to consider the diffuse extragalactic X-ray radiation. A second component which also hampers the detection of galaxy clusters are point-sources, in this case mainly Active Galactic Nuclei (AGN). Concerning the topic of this thesis, the leading characters in the eROSITA simulations are of course the galaxy clusters themselves. These three source components are described in the following sections.

7.2.1 Estimation of the expected Background Countrate

Since no experience or data about the X-ray background at eROSITA's orbit around the Lagrangian point L2 is available at present, the background radiation can not just be generated from a background model fitted to real data as it has been done for the XMM-Newton simulations as described in section 5.1.3.

The components of the background model used in the eROSITA image simulator are described here and their relative contributions are estimated by suitable assumptions. For simplicity, the eROSITA image simulator uses a constant background countrate for the whole $3.77° \times 3.77°$ image. The total background countrate resulting from the sum of the model components in the band 0.5–$2.0 \,\mathrm{keV}$ is an input parameter of the simulator program. The individual sub-components are modelled with the spectral analysis software Xspec (Arnaud, 1996):

- **Local Bubble + Solar Wind Charge Exchange:** The "local bubble" is a cavity in the interstellar medium (ISM) with an unusually low gas density and a size of $\approx 200 \,\mathrm{pc}$ in which the solar system resides. The thin gas has a temperature of some million K and therefore emits in the X-ray band. The origin of this phenomenon is still highly debated (see e.g. Welsh and Shelton, 2009). The term "Solar Wind Charge Exchange" (SWCX) in this case refers to the effect of ions in the solar wind interacting with interstellar neutral H and He atoms which produces X-ray radiation (Cravens, 2000). Both components together are modelled with a "mekal" model (Mewe et al., 1985) with temperature $kT = 8.2 \times 10^{-2} \,\mathrm{keV}$, redshift $z = 0$, and metallicity $Z = Z_\odot$.

- **Interstellar medium of the Milky Way:** The hot plasma in the Milky Way itself emits X-Rays via thermal bremsstrahlung (free-free transitions), as well as via line transitions.

Background component	xspec model	model parameters			
		n_H(wabs)	kT	Γ	norm.
Local Bubble + SWCX	mekal	–	8.2×10^{-2}	–	2.0×10^{-3}
Milky Way ISM	wabs*mekal	2×10^{20}	8.08×10^{-2}	–	1.12×10^{-2}
Supernova Remnant	wabs*mekal	3×10^{20}	12.7×10^{-2}	–	3.6×10^{-3}
Cosmic Particle Background	unfolded PL	–	–	0	0.2911

Table 7.1: The models for the individual background components used to calculate the background countrate for the eROSITA image simulator and the preliminary parameter values: n_H(wabs) is the absorbing hydrogen column density in cm^{-2}, kT is the temperature of the mekal plasma in keV, Γ is the power law index of the unfolded power law (PL). The redshift is $z = 0$, the metal abundance is $Z = Z_\odot$ and $n_H(\mathrm{mekal}) = 1\,\mathrm{cm}^{-3}$ in all components.

This component is modelled by an absorbed Mekal model with $n_H = 2 \times 10^{20}\,\mathrm{cm}^{-2}$, $kT = 8.08 \times 10^{-2}\,\mathrm{keV}$, $z = 0$, $Z = Z_\odot$.

- **Supernova remnant:** A prominent feature on the X-ray sky is the North Polar Spur, which is very well visible in the ROSAT all-sky survey. It extends over $\approx 120°$ and its origin is not fully understood (see e.g. Wolleben, 2007). Since this component appears not everywhere on the sky, an *optional* absorbed mekal model can be assumed here with model parameters $n_H = 3 \times 10^{20}$, $kT = 12.7 \times 10^{-2}\,\mathrm{keV}$, $z = 0$, $Z = Z_\odot$.

- **Cosmic particle background:** The ubiquitous ultra high energy cosmic rays (UHECR) penetrate the whole eROSITA instrument and thus contribute to the background by directly interacting with the seven CCDs. This component is modelled by a power law model which is not folded with the detector's response matrix.

The relative weights of the above components are listed in table 7.1 together with the other model parameters. In this case, all components together amount to a total eROSITA countrate of $2.7\,\mathrm{counts/s/deg^2}$ in the $0.5 - 2.0\,\mathrm{keV}$ energy band. Not included in this value is the unresolved Cosmic X-ray Background (CXB) because it is taken into account by simulating the point-source population to very deep fluxes. This is described in the next section.

7.2.2 The AGN Content

The point-source population to be observed with the image simulator was modelled following the logN-logS distribution in the 0.5-2.0 keV band as observed in the COSMOS field (Cappelluti et al., 2007). The flux generating algorithm works in the same way as the one written for the XMM simulator as described in section 5.1.4.

Rather than modelling some spatial clustering of the AGNs, their positions were chosen from a random distribution uniform over the whole simulation field. The AGNs are simulated down to a flux of $10^{-17}\,\mathrm{erg/cm^2/s}$ which is about two magnitudes deeper than eROSITA's flux limit for point-sources in its deepest exposures. This is done in order to also include the unresolved X-ray background into the simulations which was deliberately left out in the diffuse background model (see section 7.2.1). The positions and fluxes of each AGN are stored in the computer memory with double precision and can optionally be written out to disk.
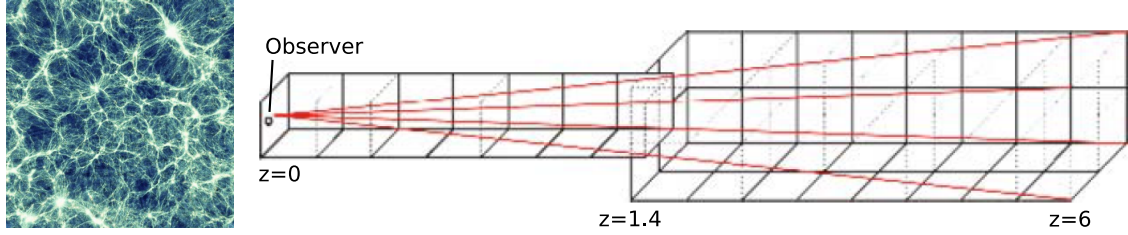
Figure 7.1: Construction of the input lightcone. **Left:** Simulation box of $192\,\mathrm{Mpc/h}$ comoving size (Borgani et al., 2004). **Right:** Several comoving volumes stacked together to form the lightcone (Roncarelli et al., 2006).

7.2.3 The Cluster Content

For simulating the X-ray emission from galaxy clusters, the program uses a surface brightness map produced by Roncarelli et al. (2006) as input data. It takes into account not only galaxy clusters but also emission from the universe's large-scale structure like filaments and galaxy groups. These dimmer components will only be observable for eROSITA in the very nearby universe. The surface brightness map was produced in the following way:

The parent simulation is a cosmological hydrodynamical simulation by Borgani et al. (2004). It was performed in a cubic volume of $192\,\mathrm{Mpc/h}$ comoving edge length. The content of the simulation box are 480^3 Dark Matter particles of mass $6.6 \cdot 10^9\,\mathrm{M_\odot}$ plus 480^3 gas particles of mass $9.9 \cdot 10^8\,\mathrm{M_\odot}$. The output of the running simulations was written to disk at many time steps corresponding to different ages of the universe or lookback times. Several such outputs of the simulation box were then attached to each other by Roncarelli et al. (2006) at simulation times corresponding to the respective redshifts. See figure 7.1 for an illustration.

In this configuration, each gas particle is given a luminosity according to its emission measure using the plasma emission model by Raymond and Smith (1977). The luminosities are converted to fluxes using the respective luminosity distances. The resulting flux field is then sampled onto a map of $3.77° \times 3.77°$ or 4096×4096 pixels, respectively. Figure 7.2 shows an image of the resulting surface brightness map. Altogether twenty such maps are available for the simulations, adding up to a total solid angle of $\approx 284\,\mathrm{deg}^2$. The surface brightness $[\,\mathrm{erg/cm^2/s/deg^2}\,]$ is converted to a flux $[\,\mathrm{erg/cm^2/s}\,]$ in each pixel by multiplying with the pixel area.

7.3 Flux-to-Counts Conversion

Once the flux of each point-source (or in each pixel, respectively) is known, it is first converted to an eROSITA countrate and then to counts, using an exposure time.

ECF Determination

The Energy Conversion Factor (ECF) is defined in equation (3.17). eROSITA's preliminary response is available in the format of a *.rsp*-file, i.e. the redistribution matrix is already multiplied by the instrument's total effective area. In this case, the effective area averaged over the field-of-view is used in order to simulate the scanning mode of the eROSITA survey. Since statistically each source crosses the field-of-view at different off-axis angles with equal probability, this automatically accounts for the vignetting effect.
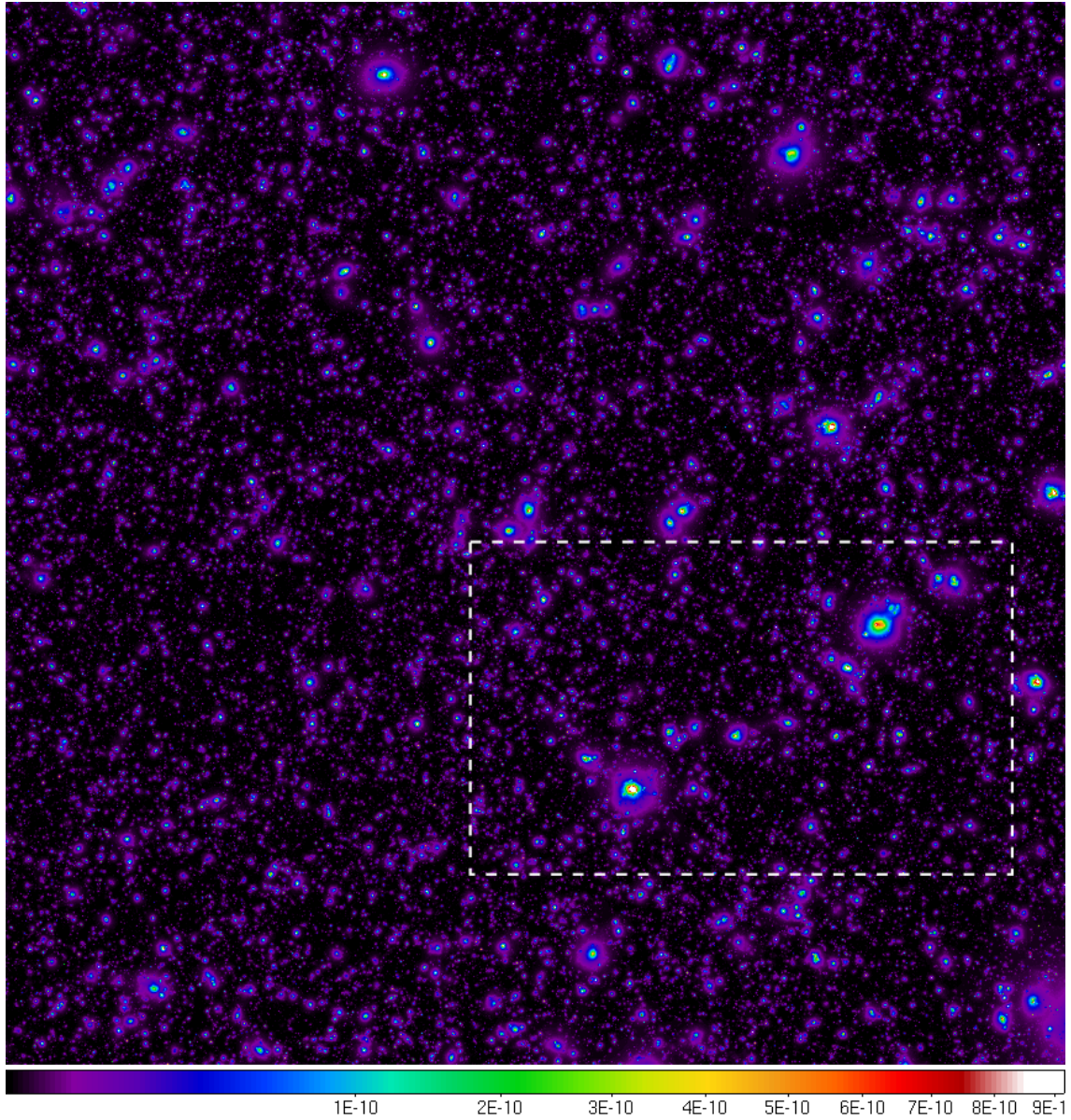
Figure 7.2: The surface brightness map resulting from observation of the lightcone by a hypothetical ideal instrument. The units are $\mathrm{erg/s/cm^2/deg^2}$ in the $0.5 - 2.0\ \mathrm{keV}$ band and the representation is on a square root scale here. The dashed frame marks the area corresponding to the observed region of figure 7.5.

With the response matrix at hand, Xspec[3] (Arnaud, 1996) can be used to calculate Energy Conversion Factors for different source models. For the point-source population, an absorbed power law has been assumed (following Cappelluti et al. (2007)) with a power law index of $\Gamma = 2$ and an absorption of $n_H = 2.6 \cdot 10^{20}$ cm^{-2}. This model does not depend on the redshift of the source and leads to an eROSITA specific energy conversion factor of

$$\text{ECF}_{\text{pointsources, } 0.5-2.0 \text{ keV}} = 7.8 \cdot 10^{11} \text{ counts} \cdot \text{cm}^2/\text{erg} . \tag{7.1}$$

For the galaxy clusters, the determination of the ECF is a little more complicated since the appropriate model, the absorbed mekal model (Mewe et al., 1985) depends on the redshift and the temperature of the source. Although from the construction of the lightcone, the redshift of each individual cluster is known, it is not possible to spatially disentangle different sources in the surface brightness map and to apply different ECFs to them. Furthermore, the temperature of each source is not known exactly but can only be derived from the cluster mass by application of an empirically calibrated Mass-Luminosity relation. It is planned to include the flux-to-countrate conversion into the construction process of the light cones and thus tailor them for eROSITA applications. The data product would in this case be a eROSITA countrate map instead of a surface brightness map.

For the moment, ECFs for a range of redshifts and temperatures have been calculated. From
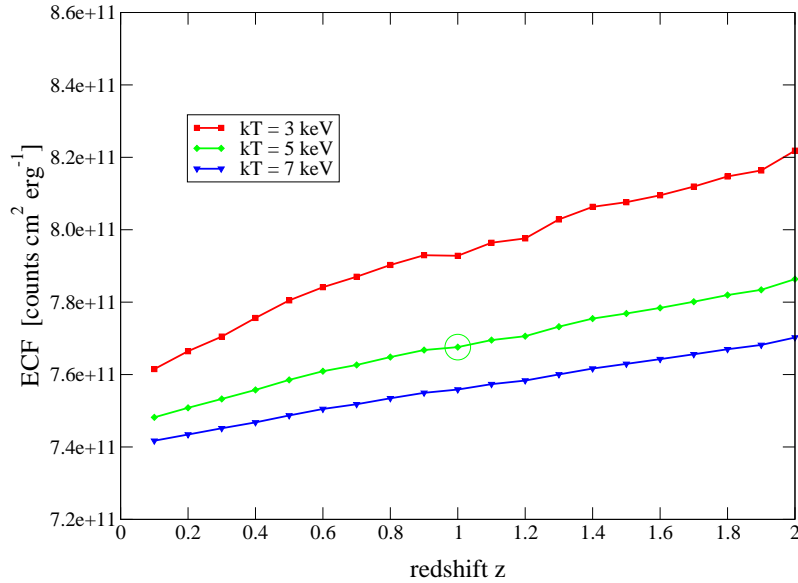
Figure 7.3: Energy conversion factors for different temperatures and redshifts of the mekal model. For the eROSITA simulations, a fiducial point at $z = 1$ and $kT = 5$ keV has been chosen.

the plot in figure 7.3 it can be seen that the ECFs do not vary by more than 10% over the parameter range which is relevant for eROSITA from $z = 0$, $kT = 7$ keV to $z = 2$, $kT = 3$ keV. Therefore, a fiducial point at $z = 1, kT = 5$ keV has been chosen for the simulations which leads to an eROSITA specific energy conversion factor of

$$\text{ECF}_{\text{clusters, } 0.5-2.0 \text{ keV}} = 7.67 \cdot 10^{11} \text{ counts} \cdot \text{cm}^2/\text{erg} . \tag{7.2}$$

The expected countrates for each point-source and for each pixel in the surface brightness map of galaxy clusters can now be calculated according to equation (3.17).

---

[3]http://heasarc.nasa.gov/xanadu/xspec/

Event List Generation

Once the countrate of each source (or pixel, respectively) is known, the expected number of photons is calculated by multiplying the countrate with the exposure time:

$$\langle n_{\mathrm{ph}} \rangle = \text{countrate} \cdot \text{exposure time} \tag{7.3}$$

In order to get realistic counts, the expectation value has to be poissonized by

$$n_{\mathrm{ph}} = \text{poidev}(\langle n_{\mathrm{ph}} \rangle) \tag{7.4}$$

where the function $\text{poidev}(\langle n_{\mathrm{ph}} \rangle)$ chooses a value according to a Poisson distribution with the expectation value n_{ph} (Press, 2002). For each source or pixel, n_{ph} events are stored in the event list with double precision image coordinates (x and y). No time or energy information is conserved. The event list is only kept internally in the computer memory and can be written out for debugging purposes. From now on, the event list stays in the memory and only the positions of the individual photons are changed by redistribution due to the telescope's Point Spread Function (PSF) and the CCD's Sub-Pixel Resolution (SPR), which are described in the following sections.

7.4   PSF Convolution

The Point Spread Function (PSF) is the probability distribution of the photon incident position on the detector when looking at a point-source. Of course not only point-sources, but the whole image (including extended sources) has to be convolved with the PSF in order to obtain a proper image simulation.

The conservative way of convolving an image with a kernel (in this case the PSF) scales with the number of PSF pixels times the number of image pixels, because each image value has to be multiplied by each PSF value. This method very quickly becomes very time consuming for large images, even on fast computers. For high-energy astronomy, where usually rather few photons are contained in an image, it is a big advantage to do the convolution on a photon by photon base (see also the runtime comparison for XMM simulations in section 5.1.6).

The construction of the PSF model used for the eROSITA simulations is described in section 4.3. The PSF convolution of the eROSITA image is done via the Monte Carlo algorithm described in section 5.1.6. Due to the scanning of the eROSITA telescope over the sky, the PSF becomes elongated in scan-direction. The magnitude of this effect can be estimated from the scan velocity (see section 3.4.4): Assuming a scanning rate of 6 hours per revolution, the telescope moves an angle of $1'$ per second. The eROSITA cameras operate with a frame rate of 20 Hz, i.e. each frame is exposed for 50 ms. During that time, the telescope advances by $3''$. Since there is no information about the time-of-arrival of a photon during these 50 ms, the $3''$ add to the positional uncertainty in scan-direction. A scanning rate of 4 hours per revolution would result in an additional error of $4.5''$ due to this effect.

The eROSITA image simulator does not use any attitude information but rather produces images of an average sky-survey. Therefore, also the smearing in scan-direction affects all directions in the final image. This can be taken into account by choosing a larger PSF model for the image simulations.

When the convolution process is finished, the event list represents the photon field as it appears between the X-ray telescopes and the CCD detectors.

7.5 Sub-Pixel Resolution and Image Creation

According to the Nyquist-Shannon sampling theorem, a function with a maximum frequency $f_{\max}$ has to be sampled with a frequency of at least $f \geq 2f_{\max}$ in order to conserve its full information content (e.g. Shannon, 1949). This means on the other hand, that the spatial binning of the photon field measured in the detector must be smaller than one half of the smallest feature to be resolved. The spatial binning is done by the pixels of the CCD detector and the smallest feature is determined by the width of the instruments PSF, because smaller features are smoothed out by the PSF convolution. eROSITA's CCD pixels have a physical size of $d = 75$ μm which translates into an angle on the sky of $\alpha = 9.66''$ by applying the formula

$$\alpha \approx \tan \alpha = \frac{d}{f} \tag{7.5}$$

where $f = 1600$ mm is the instrument's focal length. In the pointing mode, the on-axis PSF of eROSITA is specified[4] to have a half energy width of $\mathrm{HEW} = 15''$. Thus the physical CCD pixels "undersample" the image created by the X-ray telescopes.

Split Events

A lucky fact of semiconductor physics makes it possible to sample the X-ray image with better resolution. A photon falling onto the CCD produces a charge cloud in the bulk material of the chip. Due to diffusion as well as electrostatic repulsion, the charge cloud is enlarged during its travel time to the front side of the chip. The shape of the charge cloud is Gaussian and its width depends on the energy of the incident photon.

Depending on the photon's incident point, the produced charge can either be collected in one pixel or distributed among neighboring pixels and produce split events ("doubles", "triples" and "quadruples"). This mechanism is described in more detail in section 4.4.3.

Sub-Pixel Resolution

By using information about the charge distribution of an event, the incident point of the photon can be constrained much better than to the accuracy of one CCD pixel. This approach is called Sub-Pixel Resolution (SPR). Two methods with different levels of accuracy are described in section 4.4.4. One of them has been implemented for mirror characterization measurements with the TRoPIC CCD, which is a prototype of the eROSITA CCD.

Implementation in the Simulator

Although in the scanning mode the (field-of-view averaged) PSF has a Half Energy Width of $\mathrm{HEW} \approx 30''$ and is thus larger than twice the pixelsize, sub-pixel resolution has been included in the eROSITA simulator anyway, in order to design it as realistically as possible. The plan for the eROSITA mission is to use a split threshold (see section 4.4.3) which depends on the photon energy. According to a model by K. Dennerl (priv. comm.), the width of the marginal regions on a pixel and thus also the abundances of the various pattern types are constant in this case. For a threshold of 2% of the photon energy, the distribution of pattern types is as stated in table 7.2 and the width of the single region is 54% of the pixel width. These are the numbers which are also used in the simulator.

---

[4]Design criteria are specified in the document eRO-MPE-RS-13-04_3 "System Requirements".

Pattern Type	Abundance
singles	27%
doubles	53%
triples	12%
quadruples	8%

Table 7.2: Distribution of pattern types for a split threshold of 2% of the photon energy.

FOR each event DO		
decide on pattern type		
$p(S) = 27\%$	$p(D) = 53\%$	$p(T/Q) = 20\%$
choose azimuth angle $\alpha = \text{random}$ $\beta = \alpha - 90°$	choose azimuth angle $\alpha = \text{random}$	do not displace the event at all
displace event within ± 0.27 pixels in α and β direction	displace event within ± 0.27 pixels in α direction	

Figure 7.4: The simulator algorithm for the treatment of split events and sub-pixel resolution. $p(S)$, $p(D)$ and $p(T/Q)$ denote the probability of single events, double events and "corner events" (triples and quadruples).

In the eROSITA event simulator developed at the Sternwarte Bamberg, the photons are written out to the event list after this step. Using an additional attitude file, the event list can then be projected onto a grid of sky pixels to obtain an image. Unlike Bamberg's event simulator, the MPE based image simulator does not use any attitude information. Therefore, the sorting of the photons into the sky pixels has to be done in a statistical way. The image creation algorithm is summarized in figure 7.4.

For each event, the pattern type is decided in a randomly according to the pattern distribution in table 7.2. For corner events (triples and quadruples), the position of the photon in the event list is not changed at all because it is assumed that it can be exactly reconstructed by the offline analysis by using information about the charge distribution in the pixels. For double events, the position is displaced by $\pm 0.27 = \frac{1}{2} \cdot 0.54$ of a pixel because 0.54 is the height of the marginal region (measured in the direction perpendicular to the split direction) in the case of a 2% event threshold. The other direction again can be reconstructed from the distribution of the charges among the two pixels. Due to the lack of attitude information, the azimuth angle in which the event is displaced is chosen randomly. For single events, the position is displaced by the same amount, this time in two directions: one is chosen randomly and the other one is perpendicular to the first one.

With the finish of the SPR algorithm, the processing of the event list is completed and the photons are now binned into sky pixels. The size of the sky pixels can be chosen by the command line user interface. The final image is then written out to the hard disk in the FITS file format.
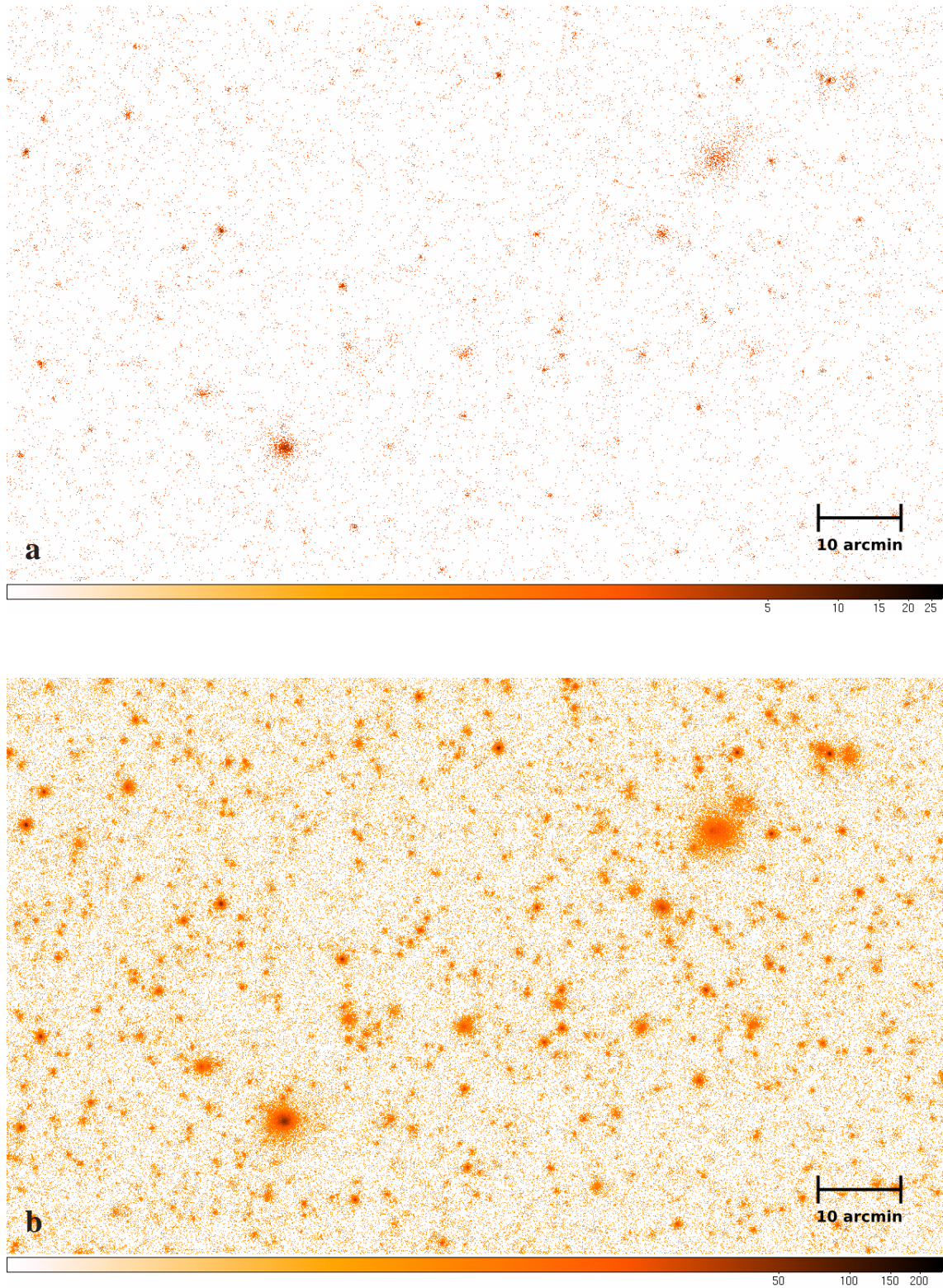
Figure 7.5: Simulated eROSITA observations including galaxy clusters and large-scale structure, point-sources and all background components. The observed region is marked in the surface brightness map of the applied lightcone in figure 7.2. Panel **a** represents an intermediate field with eROSITA's average exposure time of $2.2\,\mathrm{ks}$, panel **b** shows the same region exposed for $30\,\mathrm{ks}$.

7.6   Possible Applications of the eROSITA Image Simulator

The strength of the eROSITA image simulator is its calculation speed. The runtime of the program scales linearly with the number of photons in the image and is similar to the one of the XMM simulator (see figure 5.5). Due to the images being much larger than XMM pointings, one run can take up to a half a minute for deep exposures ($\sim$ 100 ks, while the maximum exposure of the eROSITA all-sky survey will be $\sim$ 36 ks) [5].

A first comparison by eye of the outputs produced by Bamberg's event simulator and MPE's image simulator showed a promising agreement. Further quantitative comparison studies are planned in order to ensure that the approximations made by the image simulator (like no spectral information, field-of-view averaged PSF and response) are justified for the purpose of image simulations. When this qualification step has been performed, the image simulator can serve as a reliable and fast tool to produce arbitrary amounts of simulated data with different simulation parameters which can be used for a number of tests:

- Assess the importance of sub-pixel resolution for the analysis of all-sky survey data.

- Determine eROSITA's source detection sensitivity assuming different scenarios concerning e.g. PSF quality or background radiation. For this purpose, an analysis similar to the one for XMM-Newton (see chapter 6) can be performed, with e.g. mass and redshift as cluster parameters instead of core radius and flux. It is also possible to include β-model clusters for a better control of the cluster input parameters. At a later stage, even the production of lightcones with different cosmological parameters is conceivable.

- Test different source detection algorithms, optimize their detection parameters and determine their individual selection functions.

For these applications, image simulations are the preferred approach because they show enough detail for characterizing sources as extended or point-like (spectral- or timing information is not needed in this case) but they are quick enough to be able to cover a large parameter space concerning source parameters as well as instrumental ones. The most time consuming task in this case will always be the detection algorithm.

Detection algorithms to be evaluated with respect to their applicability to eROSITA data include:

- Maximum likelihood fitting (`emldetect`, see section 5.2.3)

- Wavelet detection (e.g. Vikhlinin et al., 1998)

- Background-source separation with Bayesian probability theory (Guglielmetti et al., 2009).

Various source detection methods with a focus on XMM data are compared in Valtchanov et al. (2001). The detection of $\sim$ 100 000 clusters (see chapter 8) in the eROSITA all-sky survey will be a very challenging task which requires a lot of development and optimization work well ahead of the mission start. The development of the image simulator described in this thesis presents one of the first steps in this ambitious project.

---

[5]With fields of $3.77° \times 3.77°$ and a pixel size of $4'' \times 4''$, the writing of the simulated data to the hard disk becomes a significant time consumer. The image FITS file in this case takes about 45 MB of disk space.

Chapter 8

Predictions for the eROSITA Cluster Survey

The science goal of eROSITA is to observe a cluster sample comprising (of the order of) $100\,000$ clusters of galaxies, in order to quantify the growth of structure in the universe and test cosmological models with high precision. The prospects of a survey with the approximate scope of eROSITA have e.g. been worked out by Haiman et al. (2005). In order to test the feasibility of this goal in the special case of the eROSITA survey parameters, a simulation tool has been created, which computes the number of detectable clusters based on simplifying assumptions. This tool was given the name "cluster counter".

Up to now, there is no dedicated source detection software available for eROSITA and the hardware development for its X-ray telescopes and their characterization is ongoing. For these two reasons, the cluster detection performance of the mission could not yet be worked out in detail. This work is still in progress and first results will come in the near future.

Therefore, the cluster counter works with brightness arguments only, i.e. it does not consider sizes of galaxy clusters as it has been done in the XMM-Newton simulations (chapters 5 and 6). Instead, a minimum number of photons for a galaxy cluster to be detected (count limit c_{lim}) is given as an input parameter to the program, which can be varied arbitrarily. Plausible assumptions about the count limit are based on experience with ROSAT, XDCP and early simplified simulations.

8.1   The Input Cluster Luminosity Function

The luminosity function used for these calculations was provided by H. Böhringer (priv. comm.). Its construction is briefly summarized here.

The assumed cosmological parameter set is that of the concordance cosmological model: $h \equiv H_0/(100\,\mathrm{km\ s^{-1}\,Mpc^{-1}}) = 0.7$, $\sigma_8 = 0.79$, $\Omega_\Lambda = 0.7$, $\Omega_m = 0.3$ and $\Omega_b = 0.04$. Note, that in contrast to many earlier papers (e.g. Romer et al., 2001), where a too high value of σ_8 resulted in an over-prediction of the number of expected clusters, this study uses a realistic σ_8, which is consistent with both, cluster observations and the most recent results from WMAP (Komatsu et al., 2010).

The mass function, on which the luminosity function is based, was created following the procedure of Evrard et al. (2002). The matter power spectrum entering in the computation is calculated from

$$P(k) = T^2(k) \cdot P_{\mathrm{ini}}(k) \,, \tag{8.1}$$

107

where $P_{\mathrm{ini}}(k)$ is the initial power spectrum, modelled as a Harrison-Zel'dovich spectrum ($P_{\mathrm{ini}}(k) \propto k$), and $T(k)$ is the transfer function, which follows from Eisenstein and Hu (1998). For a given power spectrum, a mass function can be derived, following the formalism by Press and Schechter (1974). See also section 2.4.1. Evrard et al. (2002) calibrated their mass function with the *Hubble Volume* N-body simulation. Effectively, the resulting mass function is identical to a Jenkins mass function (see equation 2.21), but the Evrard mass function was preferred here for practical reasons. The mass bins are defined on a range from $M_{\mathrm{min}} = 10^{13}\,\mathrm{h}^{-1}\,\mathrm{M}_{\odot}$ to $M_{\mathrm{max}} = 3.16 \times 10^{15}\,\mathrm{h}^{-1}\,\mathrm{M}_{\odot}$.

Given the mass function, a luminosity function was derived, by applying an $L_{\mathrm{X}} - M$ scaling relation following Reiprich and Böhringer (2002). The behavior of this $L_{\mathrm{X}} - M$ relation was modelled relying on the following additional assumptions: the $M - T$ relation shows self-similar redshift evolution (according to equation 2.16, with an observationally adapted power-law exponent). This assumption is observationally justified by recent studies (e.g. Kotov and Vikhlinin, 2006). The $L_{\mathrm{X}} - T$ relation however was assumed non-evolving (equation 2.13, with observationally adapted power-law exponent). This scenario is supported by recent high redshift studies which are consistent with little or no evolution in the $L_{\mathrm{X}} - T$ relation (e.g. O'Hara et al., 2007), or show even negative trends with redshift (Ettori et al., 2004). The construction of the luminosity function used in this study agrees therefore quite well with the current knowledge about the scaling laws of X-ray properties of the ICM.

The resulting data contain information about how many clusters are expected to be found from the above modelling in a certain luminosity and redshift range per solid angle (steradian)[1]: $\tilde{\Phi}(L, z)\,[\Delta L^{-1}\,\Delta z^{-1}\,\mathrm{sr}^{-1}]$.

8.2 Further Input Data and Assumptions

Apart from the cluster luminosity function, the cluster counter is based on the following input data and parameters:

- **An exposure map.** The all-sky exposure map was calculated by Maria Fürmetz (MPE) with a simulation tool considering the special geometry of the L2 halo orbit, assuming the following survey parameters: 4 years of all-sky survey with 80% efficiency. The remaining time is assumed to be lost due to orbital maneuvers and solar flares. The exposure map is shown in figure 3.11.

- **An all-sky map of galactic neutral hydrogen.** The Milky Way's Interstellar Medium (ISM) absorbs X-rays and therefore has to be taken into account when calculating the detectable flux of a galaxy cluster. The absorption is expressed in terms of the galactic neutral hydrogen column density $n_{\mathrm{H}}[\mathrm{cm}^{-2}]$. Several n_{H} surveys are available performed by mapping the 21 cm emission of neutral hydrogen. This work uses a composite map from the survey of Hartmann and Burton (1997) and Dickey and Lockman (1990)[2].

- **A constant count limit.** This is the minimum number of photons required for being able to identify a cluster as an extended object. This number is assumed to be constant over the

---

[1]The symbol Φ usually refers to a volume number density in units of clusters per cubic Megaparsec. Here, we use the modified $\tilde{\Phi}$, to denote the surface number density of galaxy clusters.

[2]The n_{H} all-sky map is available from this URL:
http://lambda.gsfc.nasa.gov/product/foreground/f_images.cfm

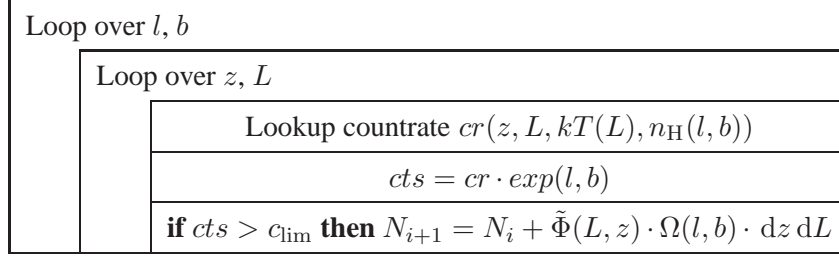| Loop over l, b		
	Loop over z, L	
		Lookup countrate $cr(z, L, kT(L), n_{\mathrm{H}}(l, b))$
		$cts = cr \cdot exp(l, b)$
		if $cts > c_{\lim}$ **then** $N_{i+1} = N_i + \tilde{\Phi}(L, z) \cdot \Omega(l, b) \cdot \mathrm{d}z\, \mathrm{d}L$

Figure 8.1: The cluster counter algorithm. See text for a detailed description.

whole sky and is an input parameter based on experience with the numerous cluster studies with ROSAT and XMM-Newton, where typical count limits range from 30 counts with ROSAT to 100 counts with XMM (compare figure 6.1). Early estimations for eROSITA proposed $c_{\lim} \sim 100$ counts. Since the count limit is strongly dependent on the background as well as on the cluster core radius, scenarios for different count limits are investigated in this study.

8.3 The Computation Algorithm

The cluster counter algorithm is summarized in figure 8.1. Its main structure is a loop over galactic longitude l and latitude b. Each map is represented by an array of 360 l-bins and 180 b-bins. The calculation is therefore performed on 64 800 points on the sky. The solid angle of each sky bin has to be corrected by multiplying with the cosine of galactic latitude:

$$\Omega(l, b) = 1 \deg^2 \cdot \cos(b) \tag{8.2}$$

In this way, the correct value of the total solid angle of the sky (4π steradian $\approx 41\,253\ \deg^2$) is maintained. The poles have been excluded from the calculation: the 180 latitude bins range from $-89.5°$ to $+89.5°$ in steps of $1°$.

Within each sky bin, a further loop runs over 200 redshift bins in the range $0 < z < 2$. Within each redshift bin, in turn, the 250 bins of the input luminosity function are probed for cluster detectability.

At each point in the parameter space l, b, z, L, the following calculation determines the number of photon counts expected from a cluster with the respective properties: The galactic hydrogen value is read from the n_{H}-map for the current sky position: $n_{\mathrm{H}} = n_{\mathrm{H}}(l, b)$. The cluster temperature is estimated from applying an L-T scaling relation (Markevitch, 1998), assuming self-similar evolution (according to equation 2.17, but with a power-law index adapted to observations).

With the parameters z, L, kT, and n_{H} at hand (and furthermore setting the ICM metallicity to $Z = 0.3\, Z_\odot$), an absorbed mekal model is fully defined and the expected eROSITA countrate $cr(z, L, kT(L), n_{\mathrm{H}}(l, b))$ for the $0.5 - 2.0$ keV band can be determined directly by using the Xspec[3] spectral fitting code (Arnaud, 1996) together with the appropriate eROSITA response file. In order to save computation time, the countrates are not calculated during the runtime, but rather saved in a big lookup table prior to running the cluster counter program. The exact countrates are linearly interpolated from the support points of the lookup table in the three dimensions z, n_{H}, and L.

---

[3]http://heasarc.nasa.gov/xanadu/xspec/

c_{lim}	N_{allsky}	$N_{\mathrm{extragalactic}}$
30	393 810	293 767
50	236 503	176 946
100	113 227	85 139
500	17 272	13 159
1 000	7 191	5 514

Table 8.1: Resulting total number of expected clusters in the all-sky survey (N_{allsky}) and excluding a region around the galactic plane with $-20° < b < 20°$ ($N_{\mathrm{extragalactic}}$). Five different count limit scenarios for the minimal number of photons required to detect a cluster (c_{lim}) were assumed.

In the next step, the number of photons expected at the current position in the eROSITA all-sky survey is determined by multiplying with the corresponding exposure time:

$$cts(z, L, l, b) = cr(z, L, kT(L), n_{\mathrm{H}}(l, b)) \cdot exp(l, b) \ . \tag{8.3}$$

For each luminosity, the algorithm checks, whether the expected number of photons exceeds the count limit c_{lim}, which has been set by the user. If this is the case, the number of clusters in the current redshift bin is increased by the corresponding number of clusters computed from the luminosity function by multiplying with the solid angle of a sky patch, the thickness of a redshift shell and the width of the current luminosity bin:

$$N_{i+1}(z) := N_i(z) + \mathrm{d}N = N_i(z) + \tilde{\Phi}(L, z) \cdot \Omega(l, b) \cdot \mathrm{d}z \, \mathrm{d}L \ , \tag{8.4}$$

and the cluster number density (in this case clusters per square degree) in the current sky bin l, b is increased by the corresponding cluster number density from the luminosity function:

$$n_{i+1}(l, b) := n_i(l, b) + \tilde{\Phi}(L, z) \cdot \mathrm{d}z \, \mathrm{d}L \ , \tag{8.5}$$

where i is the respective loop variable. The functions $n(l, b)$ and $N(z)$ are written to disk. The total number of clusters found in the simulated survey is reported for the all-sky case and for high galactic latitudes with the additional constraint $|b| > 20°$. The latter number is a more realistic scenario, because cluster detection in the galactic plane (in this case represented by $-20° < b < 20°$) is not only hampered by large ISM column densities, but also due to the high density of other X-ray sources. Apart from that, optical follow-up observations become more challenging, the closer a cluster lies to the galactic plane, both due to source confusion and high extinction.

8.4   Results from the Cluster counter

Cluster detection is a challenging problem with many tunable parameters (see chapter 6). Giving a count limit is therefore a strong simplification and the real count limit will vary with cluster parameters (e.g. temperature, core radius, shape) as well as observational parameters such as the exposure time, the observed energy band and in particular the total X-ray background radiation. Different possibilities for a mean count limit have therefore been tested in this simulation. Table 8.1 shows the resulting total number of clusters to be expected in the eROSITA cluster survey for five cases of count limits for the whole sky as well as restricted to the region out of the galactic plane ("extragalactic").

A typical lower limit required to identify a cluster as an extended source in the ROSAT cluster surveys (REFLEX and NORAS, see section 3.4.1) was 30 photons. Due to the higher background expected in the eROSITA survey, the count limit will be larger than this. 100 photons is a conservative estimate. Approximately 500 photons are needed to obtain a rough estimate of the cluster temperature, while with more than ~ 1000 photons it becomes possible to determine an approximate cluster redshift from the X-ray emission of the iron line of the ICM without additional optical or infrared observations.

8.4.1 An eROSITA All-Sky Map of Cluster Number Density

The function $n(l, b)$ represents the cluster number density depending on galactic coordinates which is expected from the eROSITA cluster survey. A representation of $n(l, b)$ is shown in figure 8.2 in Aitoff projection. Panels **a** and **b** show the all-sky maps for $c_{\mathrm{lim}} = 100$ and $c_{\mathrm{lim}} = 50$, respectively. Note the different color scales. The low cluster yield in the vicinity of the galactic disk due to the large n_{H} values shows up as central black bands. The regions of the deep survey at the ecliptic poles are also clearly visible. Their sensitivity with respect to cluster number density is partly suppressed at low galactic latitudes. From a technical point of view, it is however not possible to move the deep surveys to higher galactic latitudes, due to space flight related constraints of the orbit around L2.

8.4.2 Redshift Distribution of eROSITA Clusters

The expected redshift distribution $N(z)$ of clusters detected by eROSITA is shown in figure 8.3 for the case $c_{\mathrm{lim}} = 100$. The increase at low redshifts shows the effect of increasing observed volume, while the decrease at larger redshifts is due to a combination of the decreasing cluster flux at fixed luminosity on the one hand and the decreasing cluster number density on the other hand.

By integrating $N(z)$, it can be estimated how many clusters are detectable beyond redshift z (where N_{tot} is the total number of clusters found by the cluster counter):

$$N(> z) = N_{\mathrm{tot}} - \int_{0}^{z} N(z') \, \mathrm{d}z' \, . \tag{8.6}$$

This function is shown in figure 8.4. A particularly interesting result is the number of clusters detectable beyond redshift $z = 1$: In the case of $c_{\mathrm{lim}} = 100$, the numbers are 425 clusters at $z > 1$, out of which 383 are "extragalactic", i.e. with $|b| > 20°$.

8.4.3 Discussion

The estimated eROSITA cluster number estimates are based on assumptions on scaling relations, which still bear significant uncertainties, in particular concerning their redshift evolution and the low-mass end. Significant progress in this field is expected prior to cosmological analysis of the eROSITA data from other surveys (e.g. the XDCP) as well as from fitting the parameters of scaling relations together with the cosmological ones to the eROSITA data. This technique is known as *self-calibration* (e.g. Majumdar and Mohr, 2004).

From currently available studies, it can already be deduced, that the L-T relation does probably not evolve (e.g. O'Hara et al., 2007) or even with a trend opposite to self-similar predictions
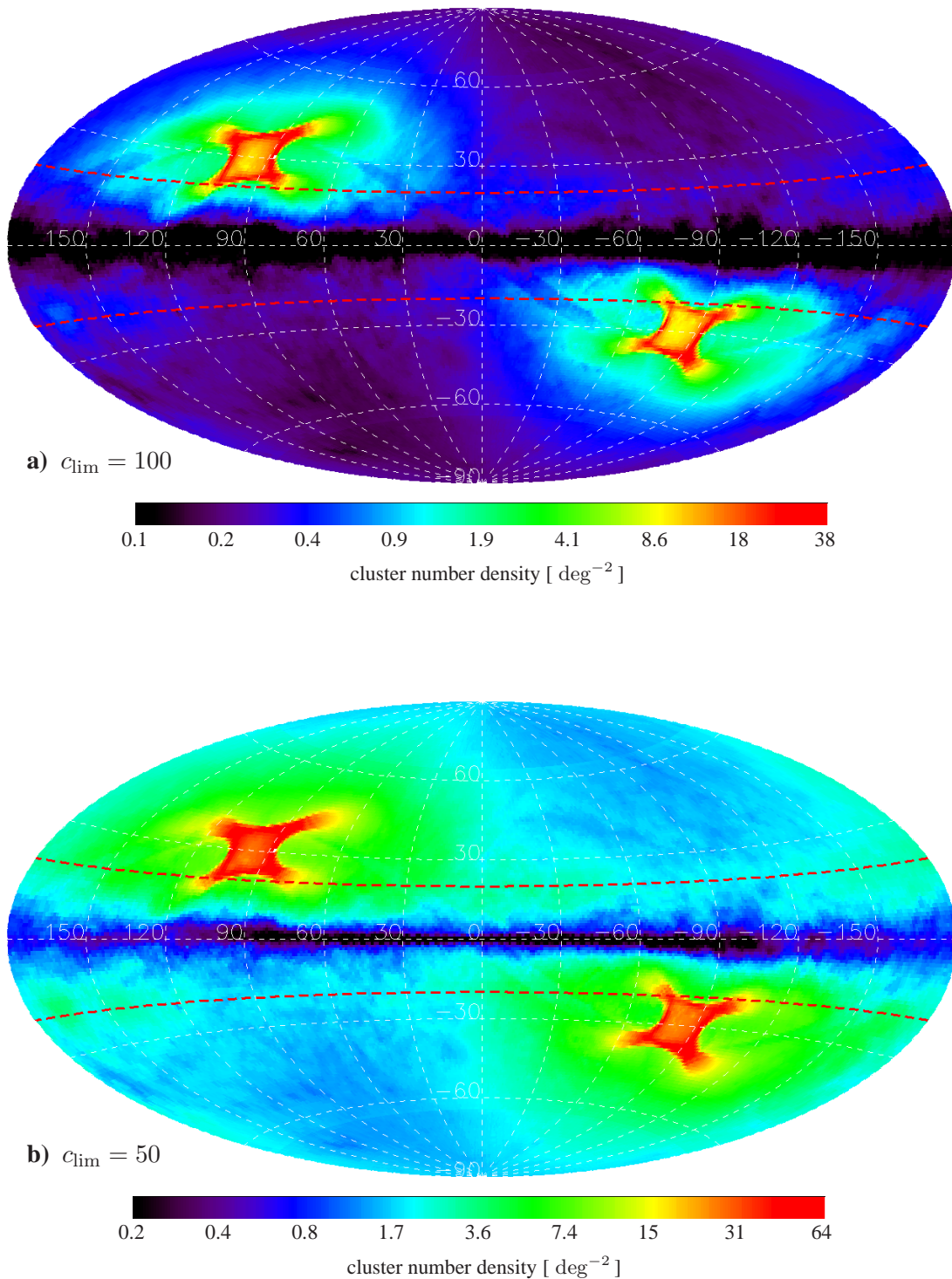
Figure 8.2: All-sky maps (in Aitoff projection) of cluster number density detectable in principle by eROSITA. Panel **a** is for an assumed count limit of 100 counts, panel **b** for 50 counts. Note the different color scales. The red dashed parallels indicate the latitudes $-20°$ and $20°$.
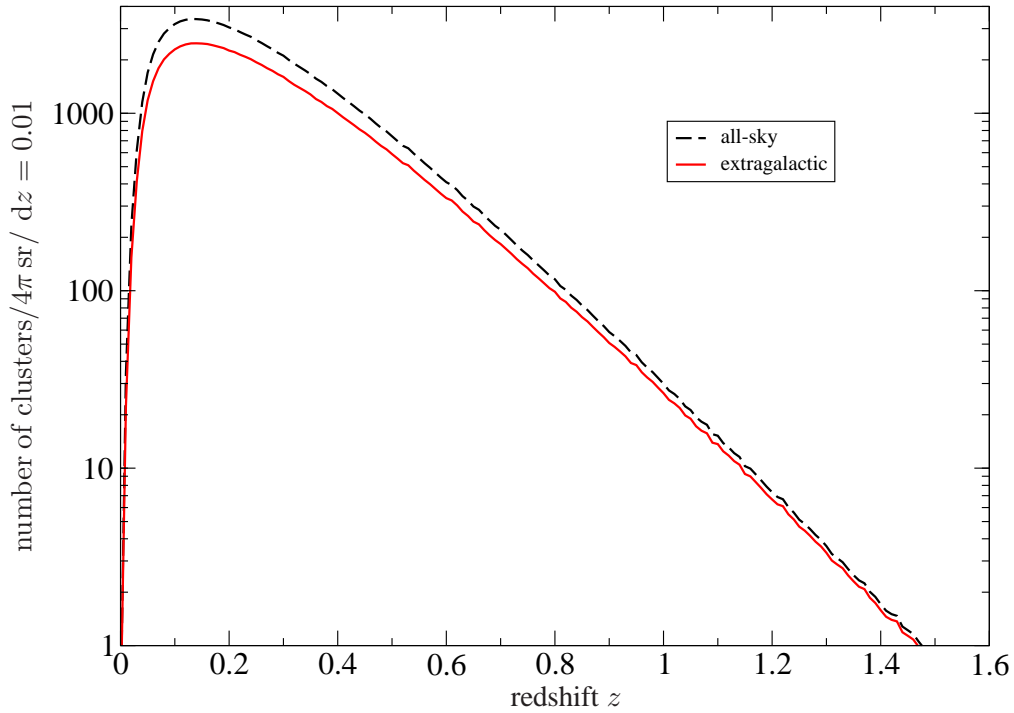
Figure 8.3: Expected redshift distribution of eROSITA clusters for $c_{\lim} = 100$ (all-sky and "extragalactic", i.e. with $|b| > 20°$).
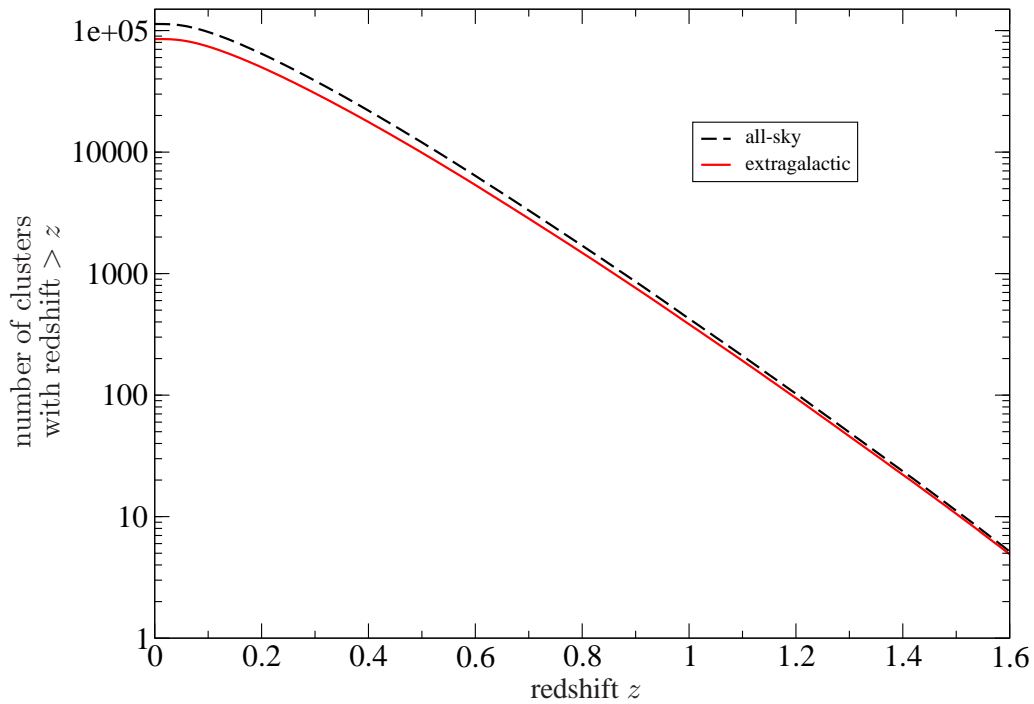

Figure 8.4: Expected number of clusters detectable by eROSITA beyond redshift z for $c_{\lim} = 100$ (all-sky and "extragalactic", i.e. with $|b| > 20°$). In the "extragalactic" survey, ~ 1480 clusters are expected beyond redshift $z > 0.8$, ~ 380 with $z > 1$, ~ 95 with $z > 1.2$ and ~ 20 with $z > 1.4$.

(Ettori et al., 2004). The no-evolution scenario has been implemented in the construction of the luminosity function (section 8.1), but not in the temperature calculation for the Xspec countrate estimation (see section 8.3).

However, as the following consideration shows, this influences the results only marginally: For a given luminosity, the temperature scales with $E^{-1/2}(z)$ (see equation 2.17), i.e.

$$T_{\mathrm{evo}} = E^{-1/2}(z) \cdot T_{\mathrm{non-evo}} \,, \tag{8.7}$$

where T_{evo} is the inferred temperature under the (here employed) assumption of an evolving L-T relation and $T_{\mathrm{non-evo}}$ is the inferred temperature under the (realistic) assumption of a non-evolving L-T relation. For the concordance cosmological model with $\Omega_\Lambda = 0.7$, $\Omega_{\mathrm{m}} = 0.3$ and $w = -1$, the evolution factor at redshift 1.5 is $E(z = 1.5) \approx 2.32$ (see equation B.8). Inserting into equation (8.7) shows, that at this point, the temperatures are underestimated by $\sim 34\%$ at high redshifts. A calculation with Xspec reveals, that this leads to an underestimation of eROSITA countrates (in the $0.5 - 2.0\,\mathrm{keV}$ band) by $\sim 11\%$ for $kT = 7\,\mathrm{keV}$ or $\sim 15\%$ for $kT = 5\,\mathrm{keV}$. Clusters with lower temperature do not contribute much at high redshifts due to their low luminosity. For lower redshifts, the effect is not as pronounced due to the smaller $E(z)$. Judging from this argument, the predictions of this work are slightly conservative.

Nevertheless, there are several reasons why the results bear significant uncertainties. They are listed in the following with increasing importance:

- A mass limit of $M_{\mathrm{min}} = 10^{13}\,\mathrm{h}^{-1}\,\mathrm{M}_\odot$ was used in this study. The scaling relations for these low masses are most probably not simple extrapolations of the power law fits to the relations for more massive clusters. This effect is expected to have significant influence especially at low redshifts. Due to their lower luminosity, the lower mass clusters do not contribute much at high redshifts. The low mass limit is also the reason why the cluster redshift distribution (figure 8.3) peaks at a rather low redshift (as compared to other studies).

- The count limit used in this study is constant over the whole sky. In reality, in the deep survey areas, a larger count limit will be required for cluster detection, due to the higher total X-ray background in longer exposures. This effect can be seen directly in figure 6.1 where the tip of the V-shaped maps of detection probability lies at a larger value in N_{ph} in the LBQS field ($52\,\mathrm{ks}$ exposure time), as compared to the one in the SCSA field ($8.8\,\mathrm{ks}$ exposure time). Thus, the count limit used here should ideally depend on the exposure time and also on the background level depending on location on the sky. The sky position dependent background could for example be estimated from the ROSAT all-sky survey.

- This study considers a range of count limits, spanning various applications from marginal detectability to high quality X-ray spectral information. They are so far only based on experience from former cluster surveys. A (background and exposure time dependent) realistic count limit (or flux limit) should be estimated by simulations in a similar way as it has been done for the XDCP survey (see chapter 6). This is a task, which is well suited for the eROSITA image simulator, which has been developed within the scope of this thesis (chapter 7).

- Cluster detectability depends not only on the cluster's X-ray flux. Many other parameters hidden in the selection function (i.e. completeness and purity/contamination) of a survey play an equally important role. In this respect, section 8.4.4 discusses important aspects learned from the XDCP simulations analyzed in chapter 6.

8.4.4 Lessons for the eROSITA Cluster Survey from the XDCP Simulations

The eROSITA mission will provide the largest sample of galaxy clusters ever. Only $\sim 2\%$ of them will be known already from ROSAT cluster surveys like REFLEX and NORAS.The significance of the mission lies therefore **(i)** in the highly increased statistics, **(ii)** in the low-mass regime at the transition to galaxy groups and **(iii)** in the high redshift regime, where currently projects with XMM-Newton and Chandra do the pioneering work (see section 3.4.3). The experience gained from these projects is of crucial importance for the calibration and understanding of eROSITA data as well as for improving cluster detection algorithms.

Identifying tens of thousands of galaxy clusters from the raw data of four years of all-sky survey is a truly challenging task. The non-detection of a cluster can mainly be caused by three effects: If the cluster core radius (r_c) is too small, it can be mistaken as a point-source. If it is too large, it possibly disappears in the background. Furthermore, a bright point-source in the cluster can prevent the cluster from being classified as an extended source.

Although the analysis of eROSITA cluster simulations is not available yet, from the detection probability maps derived for the XDCP (especially figure 6.6, right panel), some basic conclusions can be drawn at this point.

The position of the probability map with respect to the r_c-axis is mainly governed by the PSF quality of the instrument. Although the on-axis imaging properties of the eROSITA mirrors will be comparable to the ones of XMM-Newton, the *average survey* PSF of eROSITA is approximately a factor of 2–3 larger. This means that the detection probability map scales to larger r_c by the same factor.

The r_c-distribution of galaxy clusters at high redshift is very uncertain. The one used for the construction of the XDCP sky coverage was measured at low to intermediate redshifts with a sample median of $z_{\mathrm{median}} = 0.24$. Depending on the real r_c-distribution and its shape at high redshift, the cluster detectability in the eROSITA survey might be strongly hampered by the PSF quality of the X-ray telescopes. Especially for the realistic scenario **c** with $\mu_{r_c} = 7.03''$ (red/left curve in figure 6.6, right panel), cluster detection with eROSITA becomes extremely difficult. A large fraction of the high redshift clusters would not be distinguishable from point-sources, resulting in a low completeness or a high flux limit, respectively.

One possibility for improving on cluster detection probability would be to analyze photons with low off-axis angle separately from those at large off-axis angle. The better imaging qualities of the X-ray telescopes towards the optical axis can be exploited with this approach. This technique has to be developed and tested thoroughly.

Concluding Statement

A sophisticated data analysis is a very important key for being able to address the challenges described above. The goal of identifying $100\,000$ clusters of galaxies from the raw data of the eROSITA mission, characterizing their properties and making use of the sample for astrophysical and cosmological science application can only be successfully completed with the availability of new and improved cluster detection software and analysis techniques. Generating simulated data is a crucial part of this effort. This thesis is therefore a starting point for further projects concerning the improvement of cluster detection algorithms.

Chapter 9

Summary, Conclusions and Outlook

Within the scope of this thesis, I developed a number of numerical methods, tailored to be applied to studies on the detectability of clusters of galaxies with the X-ray missions XMM-Newton and eROSITA. All of the performed studies are embedded in larger programs beyond the scope of the thesis. This final chapter gives a summary of the thesis and its main conclusions and provides an outlook on possible further developments in future projects.

9.1 Summary and Conclusions

Sub-Pixel Resolution and PSF Measurements

TRoPIC is the Third Röntgen Photon Imaging Camera operated at the PANTER facility. It is a smaller version of the eROSITA CCD. Among the three PANTER cameras, it provides the highest spatial resolution. However, due to the relatively short focal length of the eROSITA mirrors (1600 mm), it is not sufficient to resolve the PSF core. By making use of split events, where the charge of an event is distributed among neighboring pixels, the incident position of a photon can be determined with a precision better than the physical pixel size. I have developed a new analysis algorithm tailored to the data from the TRoPIC CCD, which produces images with Sub-Pixel Resolution (SPR) and optionally determines the Half Energy Width (HEW) of the PSF of the tested mirror shell. As an important calibration measurement, I have suggested to incorporate a flatfield exposure into the standard experimental sequence.

Because the size of the PSF core is on the order of the CCD's physical pixel size, mirror characterization measurements are performed in scanning mode in order to guarantee a fair illumination of each part of a pixel. As an example, I analyzed a recent pixel scan with the new SPR algorithm. The measured HEW could be improved by 18% with respect to the standard analysis.

XMM-Newton Simulations

For the purpose of computing a sky coverage for the XMM-Newton Distant Cluster Project (XDCP), I developed an XMM-Newton image simulator, which can be operated in two modes. Running in the artificial background mode, it simulates the X-ray background from a background model and point-sources from an observed logN-logS distribution. In real background mode, it simulates galaxy clusters on top of a real XMM-Newton observation. Positions where previously

a real cluster had been found are forbidden for placing an artificial cluster. The simulated clusters are realized by β-models with $\beta = 2/3$.

The simulator works on an event by event basis. The Monte Carlo transformation method is used to distribute the photons within a β-model, which is in this case interpreted as a probability distribution. Also PSF convolution is performed by Monte Carlo transformation. A comparison with conventional image convolution revealed a saving in runtime of at least a factor of four.

The simulation pipeline is an adapted version of the XDCP pipeline which was used for the analysis of the real archival data. Both pipelines are based on the sliding box source detection technique. A subsequent maximum likelihood method is employed to distinguish galaxy clusters, i.e. extended sources, from point-sources. For each simulated pointing, a summary file is written to disk containing the parameters of generated versus reconstructed clusters.

First Results from XMM-Simulations

As a first application of the newly designed XMM simulator, I have simulated a subsample of 160 out of the 469 XDCP fields in a computation run of 2.5 months on 20 CPUs in parallel. The 160 fields are selected to have a low galactic hydrogen value, a minimum exposure time of 10 ks, no bright sources in the field and a low particle background. The galaxy clusters found within this subsample are intended for a cosmological project based on follow-up observations with the Chandra observatory: the Chandra extended Cluster Cosmology Sample (CheCCS).

By matching reconstructed clusters with generated ones, a detection probability was calculated depending on core radius, number of photons and off-axis angle. After some adequate interpolation, extrapolation and smoothing steps during the post-processing stage, those datacubes were weighted with an assumed core radius distribution derived from observations. Two extreme cases of the distribution were also generated by scaling the core radii up and down, respectively by a factor of 2. The downscaling can be justified for $z = 1$ with an expected redshift evolution of $r_c \propto 1/(1 + z)$. The up-scaling was considered for completeness but a possible astrophysical reason could be the higher merger rate for higher redshifts.

After a suitable countrate-to-flux conversion, a sky coverage of the 160 CheCCS fields could be computed from considering each pixel in the masks of the fields. Overlapping fields were treated with a special method involving the creation of mosaic images from the masks.

As a result, it turned out that the sky coverage depends only slightly on the applied core radius distribution. Especially the outcome of the realistic case of the $1/(1 + z)$ scaling differs only marginally from using the raw r_c-distribution. The flux limit of the survey could be determined to be $f_{\text{lim}}(0.5 - 2.0 \text{ keV}) = 5.7 \times 10^{-15} \text{ erg cm}^{-2} \text{ s}^{-1}$ at a completeness level of $c = 0.5$ for the case of the raw r_c-distribution and a maximum off-axis angle of $\theta_{\text{max}} = 12'$. The total survey area in this case is 17.679 deg^2. A comparison with the case of $\theta_{\text{max}} = 10'$ showed that this further restriction of the field, which would imply a loss of 30% of the survey area, results in only a marginal improvement of 3.5% in the flux limit.

An Image Simulator for eROSITA

In parallel to the eROSITA event simulator based at the Dr. Remeis-Sternwarte in Bamberg, I developed an eROSITA image simulator which relies on different approximations to speed up the computation process. The celestial sources observed by the image simulator are **(i)** an X-ray background estimated for the expected orbit around L2, **(ii)** an AGN population following a realistic logN-logS distribution and randomly distributed spatially and **(iii)** a population of galaxy

clusters. The latter one is realized through a surface brightness map of large-scale structure which was provided by the collaboration. It is created from a hydrodynamical N-body simulation by putting simulation boxes at various redshifts next to each other to form a light cone. The developed eROSITA simulator is very well suited for projects similar to the one performed for the XDCP. It simulates X-ray images in a certain energy band by taking into account an average survey PSF as well as the effects of sub-pixel resolution. Since at this early stage a dedicated analysis software package for eROSITA data was not available, the processing of simulated eROSITA images is deferred to future projects.

Prospects of the eROSITA Cluster Survey

Without relying on the analysis of simulated images, the prospects of the eROSITA cluster survey were estimated from luminosity arguments only. Based on a redshift dependent cluster luminosity function, I developed a program which estimates the number of clusters to be found in the survey for each $1° \times 1°$ sky patch. Further input data are an all-sky map of the galactic hydrogen column density as well as an all-sky exposure map. Within each sky bin, the algorithm steps through the redshift- and luminosity scale and calculates the expected number of photons to be detected with eROSITA. If the number of photons exceeds a certain (globally constant) count limit, the number of clusters in the current redshift- and luminosity bin of the luminosity function is counted as detected. The resulting function is the number of clusters per redshift bin per sky pixel. This function is presented as an all-sky map and as a redshift distribution. Assuming a conservative count limit of 100 photons, this estimation predicts 1.1×10^5 clusters to be detected in the all-sky survey out of which 8.5×10^4 are "extragalactic", i.e. with galactic latitude $|b| > 20°$.

This estimation relies on scaling relations which are not yet well constrained at high redshifts, but it is based on a realistic scenario in agreement with the current knowledge. This means that the potential to detect 10^5 clusters of galaxies with the eROSITA mission is confirmed, whereas their identification and the scientific use of the data is still a very challenging project. Further significant progress in the development of source detection algorithms and analysis techniques is necessary to achieve the mission's scientific objectives.

9.2 Possible Refinements for Future Projects

This section summarizes the suggestions for possible future projects which were made throughout the thesis:

Next Steps on Sub-Pixel Resolution

- Development of a new version of the SPR code which writes out the reconstructed SPR coordinates back into the input data file for further processing.

- Implementation and testing of the more exact reconstruction of photon positions relying on the ratio of charge distribution among adjacent pixels.

Next Steps on XDCP Simulations

- Calibration of the flux contained in the simulated β-models on a firm basis as mentioned in section 6.6.

- Computation of the point-source contamination of the XDCP survey selection function.

- Optimization of the parameter settings for DET_ML and EXT_ML.

- Test of an implementation of the new in-flight calibrated PSF model and comparison with simulation runs using the ray-tracing simulated PSF model.

- Implementation of a simulation run with hydrodynamically simulated clusters of galaxies and computation of completeness depending on mass and redshift of a cluster.

- Comparison of completeness corrected prospects of the expected redshift distribution of XDCP clusters with a histogram of the 25 spectroscopically confirmed XDCP clusters above redshift $z > 0.8$. This project has the potential to provide constraints on cosmological parameters.

Next Steps on eROSITA Simulations

- Analysis of first simulations from the newly developed eROSITA image simulator once the dedicated Science Analysis Software System (SASS) becomes available.

- Development, improvement and optimization of various source detection and characterization algorithms with β-model simulations as well as with hydrodynamically simulated galaxy clusters.

9.3 Outlook on the Impact of the eROSITA Mission on Dark Energy Studies

More than ten years after the first convincing evidence of Dark Energy (Riess et al., 1998), eROSITA will be the first space mission dedicated to Dark Energy research. The report of the Dark Energy Task Force (Albrecht et al., 2006) recommends "[...] that the dark energy program have multiple techniques at every stage, at least one of which is a probe sensitive to the growth of cosmological structure in the form of galaxies and clusters of galaxies.", where the term "stage" refers to different levels of experimental advancement.

eROSITA is scheduled for launch in late 2012. Taking into account a commissioning phase and travel time to L2 of $\sim 110\,\mathrm{days}$, the four years of all-sky survey are expected to be finished in 2017. Follow-up observations (for measuring cluster redshifts) can only partly be performed in parallel to the X-ray survey and thus additional time is required to complete the full cluster catalogue from the eROSITA mission.

From a sample of 10^5 galaxy clusters, without priors from complementary probes and taking into account self-calibration, one can expect the following constraints on Dark Energy parameters: $\sigma(w_0) = 0.093$, $\sigma(w_a) = 0.490$ and $\sigma(\Omega_\Lambda) = 0.0067$ where w_0 is the present-day equation-of-state parameter, $w_a = \mathrm{d}w/\mathrm{d}a$ is its evolution with the scale factor a and Ω_Λ is the Dark Energy density (Haiman et al., 2005). In this respect, eROSITA can be a major player in the field of Dark Energy research for the next decades. The results of this thesis help to pave the way to this ambitious goal.

Appendix A

Acronyms and Terminology

This is a list of acronyms and technical terms used throughout the thesis. The numbers indicate the pages of their occurrence, page numbers of important text passages are typed in bold.

2XMM: Second XMM-Newton serendipitous source catalogue. 37

AAAC: Astronomy and Astrophysics Advisory Committee. 29

ABRIXAS: A Broad Band Imaging X-ray All-sky Survey. 28

ADC: Analog-to-Digital Converter. 23, 49

ADU: Analog-to-Digital Unit, internal unit used by an ADC. 50

AGN: Active Galactic Nucleus. 7, 28, **32**, **60**, **98**

AIP: Astrophysikalisches Institut Potsdam. **28**, 94

ARF: Ancillary Response File. 24

ART: Astronomical Röntgen Telescope. The second instrument on SRG. 24

Attitude: Current orientation of a spacecraft or the pointing direction in the case of a spaceborne observatory. 31, 46, **96**

AXAF: Advanced X-ray Astrophysics Facility. NASA's major X-ray satellite which is now known as Chandra. 28

BAO: Baryonic Acoustic Oscillations. 1, 13

BCS: Blanco Cosmology Survey. 37

Boresight: Direction of the optical axis of an X-ray telescope. **67**, 75

CAMEX: CMOS Amplifier and MultiplEXer. 23, 49

CCD: Charge Coupled Device. **22**, **49**

CCF: Current Calibration File. These files compose the calibration database of the XMM-SAS. 44

CDF-N, CDF-S: Chandra Deep Field North / South. 32

Chandra: NASA's major X-ray satellite, formerly known as AXAF. 35, 73

CheCCS: Chandra extended Cluster Cosmology Sample. **73**

Cheese image: Source exempted image containing to first order only background radiation. 60, 68

CMB: Cosmic Microwave Background. 1

COSMOS: Cosmic Evolution Survey. **37**, 60, 98

CPU: Central Processing Unit. 73, **78**

CTE: Charge Transfer Efficiency.

CTI: Charge Transfer Inefficiency, $\mathrm{CTI} = 1 - \mathrm{CTE}$. 23

CXB: Cosmic X-ray Background. 98

DETF: Dark Energy Task Force. Advisory panel for DOE, NASA and NSF on the future of Dark Energy research. **29**

DLR: Deutsches Zentrum für Luft- und Raumfahrt (Germany's National Space Agency). 29

DOE: Department of Energy of the United States government. **29**

DSP: Digital Signal Processor. 50

DUO: Dark Universe Observatory. **28**, 48

ECF: Energy Conversion Factor. **24**, 61, 64, 79, 99

Einstein: First X-ray observatory carrying a Wolter telescope on a satellite. It was known initially known as HEAO-2 and renamed to Einstein after launch. 15, 34, 83

EMSS: Extended Medium Sensitivity Survey (by the Einstein Observatory). 34

EPIC: European Photon Imaging Camera (The three cameras of XMM-Newton: EPIC-MOS1, EPIC-MOS2 and EPIC-PN). **26**, 32, 44, 57, 64, 67, 74

eROSITA: extended ROentgen Survey with an Imaging Telescope Array. **29**, and many others

ESA: European Space Agency. 26

ESO: European Southern Observatory. 35

FoV: Field-of-View. 20, 27, 38

FWHM: Full Width at Half Maximum. **42**

FITS: Flexible Image Transport System: file format for all kinds of astronomical data, defined in Hanisch et al. (2001). **44**

Grasp: Product of effective area times field-of-view. The grasp of an instrument is a measure of how efficiently it can survey a specific portion of the sky. 28, **33**

HEAO: High Energy Astronomy Observatory. A series of three missions launched by NASA, beginning in 1977. 15, 34

HEPAP: High Energy Physics Advisory Panel. **29**

HEW: Half Energy Width. **43**, 47, 55

IAAT: Institut für Astronomie und Astrophysik der Universität Tübingen. 28

ICM: Intra Cluster Medium. **6**

IDL: Interactive Data Language, a scripting language widely used in astronomy. It is currently maintained by ITT Visual Information Solutions (http://www.ittvis.com/). **50**

IKI: Институт Космических Исследований
say: "Institut Kosmicheskih Issledovanij", Russian *Institute for Space Research*. 29

ISM: Interstellar Medium. Gas and dust filling interstellar space within galaxies. Massive galaxies can be detected in X-rays through their ISM emission. In the special case of the Milky Way, the ISM is relevant because it absorbs X-rays from extragalactic sources. Its column density is expressed in terms of the galactic neutral hydrogen column density n_{H}. **6**, 61, 97

ISS: International Space Station. 97

IXO: International X-Ray Observatory. 39

L2: Second Lagrangian Point of the Sun-Earth system. 31, 32, **37**, 39, 108

LBQS: Working title of the XMM pointing named LBQS 2212-1759 (see section 6.2.3).
LBQS stands for Large Bright Quasar Survey. 67, 76, 77

LEO: Low Earth Orbit. 28, 31, 39

LH: Lockman Hole. An area in the northern sky with very low absorption by galactic foregrounds. This field is especially suited for deep extragalactic observations. 32

logN-logS: Astronomers' jargon for the function representing the number of sources above a certain flux (cumulative representation) or in certain flux bins (differential representation). 32, **60**, 98

LSS: Large-Scale Structure. The cosmic web with its filaments and galaxy clusters at their knots. 32, 33

MOS: Metal Oxide Semiconductor. A special layout of CCDs and also the name of two of the three EPIC instruments aboard XMM-Newton. 27, 32, 44, 64

MPE: Max-Planck-Institut für extraterrestrische Physik. 2, and many others

NASA: National Aeronautics and Space Administration. The national space agency of the United States of America. 28, 29, 73

NFW: Navarro, Frenk and White. Initials of the authors of a paper about a universal Dark Matter halo density profile (Navarro et al., 1997). 9

NGC: New General Catalog of Nebulae and Clusters of Stars (Dreyer, 1888). 6

NORAS: NOrthern ROSAT All-Sky Survey. 34, 111

NRTA: Near Real Time Analysis. 96

NSF: National Science Foundation of the United States government. 29

OoT: Out-of-Time (events). 23

OBS_ID: Unique identifier of an XMM observation with ten digits. 86

PANTER: X-ray testing facility operated by MPE in Neuried (south of Munich). **47**

PHA: Pulse Height Amplitude. 23, 25

Pile-up: The arrival of two or more photons within one CCD frame in the same pixel. This causes a wrong energy assignment, because the detector always assumes only one photon per pixel per CCD frame. 23, 30, 47

PN: Positive and Negative doped semiconductors. A special layout of CCDs and also the name of one of the three EPIC instruments aboard XMM-Newton. 27, 32, 44, 64

Poissonization: Drawing a random number from a Poisson distribution $p(k)$ with expectation value λ: $p(k) = \frac{\lambda^k}{k!} \cdot e^{-\lambda}$. This is frequently used in simulations to convert an expected number (real value λ) of objects (e.g. photons, AGN) to a really observed number of objects (integer value k). 60

PSF: Point Spread Function. 19, **41**, 43, 45, and many others

PSPC: Position Sensitive Proportional Counter (the X-ray Detector of ROSAT). 21, 48

QE: Quantum Efficiency. 19, 22

RASS: ROSAT All-Sky Survey. 34

REFLEX: ROSAT-ESO Flux-Limited X-ray cluster survey. 34, 111

RGS: Reflection Grating Spectrometer. Two identical ones of the five X-ray instruments aboard XMM-Newton. 27

RMF: Redistribution Matrix File. 24, **25**

ROI: Region Of Interest. 53

ROSAT: ROentgen SATellite (1990-1999). 21, **28**, 34, 38, 109, and many others

ROSITA: ROentgen Survey with an Imaging Telescope Array. One of eROSITA's precursors, which was planned to be operating on the ISS before it was realized that the space station's environment is not suitable for an X-ray telescope. 28

SAA: South Atlantic Anomaly: closest approach of the inner Van Allen radiation belt to the Earth's surface with therefore enhanced flux of energetic particles. The ROSAT PSPC was regularly switched off during the passage of the SAA, in order to protect it from the high radiation level. 38, 39

SAS: Science Analysis System (for XMM-Newton data). **68**

SASS: Science Analysis Software System (for eROSITA data). 95, 97

SCS: Southern Cluster Survey. Working title for the overlap of the XDCP and the planned survey area of the SPT. 125

SCSA: Short identifier for the simulation test field on the background of the XMM pointing named IRAS 23128-59 (see section 6.2.3). "SCS" is a working title for the Southern Cluster Survey, "A" serves as a running letter. 76, 77

SMEX: SMall EXplorer. A funding program by NASA for space missions with a maximum total budget of 120 million US Dollars. 28
http://explorers.gsfc.nasa.gov/missions.html

SNR: Signal-to-Noise Ratio. 78

SPR: Sub-Pixel Resolution. **50**, 103

SPT: South Pole Telescope. A millimeter wave telescope dedicated for a galaxy cluster survey by means of the SZ effect. 125

SRG: Spektrum-Röntgen-Gamma. The Russian-German space platform for eROSITA. 29

SSC: XMM-Newton Survey Science Centre. 37

SWCX: Solar Wind Charge eXchange. 97

SZ: Sunyaev-Zel'dovich (-effect). Compton up-scattering of CMB photons by electrons in the hot ICM of galaxy clusters. This effect is used to detect galaxy clusters in the radio regime as shadows on the CMB. 13, 32

TRoPIC: Third Roentgen Photon Imaging Camera. 49

UHECR: Ultra High Energy Cosmic Rays. 98

XDCP: XMM-Newton Distant Cluster Project. **35**, 57, 73, and many others

XCS: XMM Cluster Survey. 36

XMM: X-ray Multi-Mirror mission (XMM-Newton). **26**, and many others

XMM-LSS : XMM-Newton Large-scale Structure Survey. 37

XRT: X-Ray Telescope. **15**, 26

XSA: XMM-Newton Science Archive. 35, 86

VLT: Very Large Telescope: four individual eight-meter-class telescopes located at the Paranal Observatory in Chile, which is operated by ESO. 35

WCS: World Coordinate System: Celestial coordinates right ascension (RA) and declination (DEC). 86

WMAP: Wilkinson Microwave Anisotropy Probe. 107

Appendix B

Useful Cosmological Equations

Some cosmological equations are given here for reference. They are taken from Dodelson (2003), Schneider (2006) and from the cosmology section of Fassbender (2008).

In an expanding universe, it is convenient to introduce comoving coordinates $\vec{x}$ and physical coordinates $\vec{r}(t)$. During expansion, two points maintaining their comoving distance increase their physical distance. The two coordinate systems are connected through the time dependent scale factor $a(t)$:

$$\vec{r}(t) = a(t) \cdot \vec{x} \tag{B.1}$$

The light waves emitted by a receding object are stretched out so that the observed wavelength λ_{obs} is larger than the emitted one λ_{emit}. The redshift z is defined as the stretching factor:

$$z(t) = \frac{\Delta\lambda}{\lambda_{\mathrm{emit}}} = \frac{\lambda_{\mathrm{obs}} - \lambda_{\mathrm{emit}}}{\lambda_{\mathrm{emit}}} = \frac{\lambda_{\mathrm{obs}}}{\lambda_{\mathrm{emit}}} - 1 = \frac{a_0}{a(t_{\mathrm{emit}})} - 1 \,. \tag{B.2}$$

Defining the scale factor of today ($t = t_0$) as $a_0 = 1$, this leads to the relation

$$a(t) = \frac{1}{1 + z(t)} \,. \tag{B.3}$$

The Hubble parameter is defined as the expansion rate of the universe:

$$H(t) = \frac{\mathrm{d}a(t)/\mathrm{d}t}{a(t)} \,, \tag{B.4}$$

its present value is the Hubble constant $H_0 \approx 70\,\mathrm{km\ s^{-1}\,Mpc^{-1}}$. The Hubble constant is often parameterized by the dimensionless constant

$$h = H_0/100\,\mathrm{km\ s^{-1}\,Mpc^{-1}} \,. \tag{B.5}$$

The critical energy density of the universe is defined as the energy density leading to a flat geometry. It can be expressed in terms of the Hubble parameter $H(z) = H_0 \cdot E(z)$ and Newton's constant G (the evolution parameter $E(z)$ is defined below in equation B.8):

$$\rho_{\mathrm{cr}}(z) = \frac{3H_0^2}{8\pi G} \cdot E^2(z) = 1.879 \times 10^{-29}\,h^2\,\mathrm{g\,cm^{-3}} \cdot E^2(z) \,. \tag{B.6}$$

The energy content of the universe as measured today is usually stated with respect to the critical density of today ($\rho_{cr,0}$), leading to the dimensionless density parameters

$$\Omega_x = \frac{\rho_x}{\rho_{cr,0}} \, , \tag{B.7}$$

where x is a variable for the type of energy component: Ω_m is the matter density, Ω_{DE} the Dark Energy density, Ω_r the radiation density and $\Omega_{tot} = \Omega_m + \Omega_{DE} + \Omega_r$ is the total energy density. $\Omega_{tot} = 1$ means that the total density ρ_{tot} is equal to the critical one (ρ_{cr}) and thus implies a flat universe.

The various energy components show different scaling with redshift (scale factor). The expansion history of the universe can be expressed in terms of the evolution factor $E(z) = H(z)/H_0$ which is related to the cosmological parameters by

$$E^2(z) = \Omega_m(1+z)^3 + \Omega_{DE} \cdot e^{3\int_0^z \frac{1+w(z')}{1+z'}dz'} + \Omega_r(1+z)^4 + (1 - \Omega_{tot})(1+z)^2 \, , \tag{B.8}$$

where $w = p/(\rho c^2)$ is the equation-of-state parameter of Dark Energy.

The comoving distance D of an object at redshift z is given by

$$D(z) = \frac{c}{H_0} \int_0^z \frac{dz'}{E(z')} \, , \tag{B.9}$$

where c is the speed of light. There are two more distance definitions which are observationally motivated: The *luminosity distance* d_{lum} is defined via the relation between luminosity L of an object and the observed flux f by $f = L/(4\pi d_{lum}^2)$, while the *angular diameter distance* d_{ang} relates the physical size l of an object to its apparent size θ via $l = \theta \cdot d_{ang}$. Both are connected to the comoving distance D via

$$d_{lum}(z) = D \cdot (1+z) \tag{B.10}$$

$$d_{ang}(z) = \frac{D}{1+z} \, . \tag{B.11}$$

Bibliography

E. Abbe. *Gesammelte Abhandlungen. I Abhandlungen über die Theorie des Mikroskops*. 1904.

G. O. Abell. *The Distribution of Rich Clusters of Galaxies.* ApJS, 3:211–+, 1958.

A. Albrecht, G. Bernstein, R. Cahn et al. *Report of the Dark Energy Task Force*. ArXiv Astrophysics e-prints, 2006. arXiv:astro-ph/0609591.

S. W. Allen, D. A. Rapetti, R. W. Schmidt et al. *Improved constraints on dark energy from Chandra X-ray observations of the largest relaxed galaxy clusters*. MNRAS, 383:879–896, 2008. arXiv:0706.0033.

R. Angulo, C. M. Baugh, C. S. Frenk et al. *Constraints on the dark energy equation of state from the imprint of baryons on the power spectrum of clusters*. MNRAS, 362:L25–L29, 2005. arXiv:astro-ph/0504456.

R. Antonucci. *Unified models for active galactic nuclei and quasars*. ARA&A, 31:473–521, 1993.

V. Arefiev, M. Pavlinsky, I. Lapshov et al. *ART-XC: a medium-energy x-ray telescope system for the Spectrum-R-Gamma mission*. In *Society of Photo-Optical Instrumentation Engineers (SPIE) Conference Series*, volume 7011. 2008.

K. A. Arnaud. *XSPEC: The First Ten Years*. In G. H. Jacoby and J. Barnes (editors), *Astronomical Data Analysis Software and Systems V*, volume 101 of *Astronomical Society of the Pacific Conference Series*, pages 17–+. 1996.

C. Arviset, M. Guainazzi, J. Hernandez et al. *The XMM-Newton Science Archive*. ArXiv Astrophysics e-prints, 2002. Also available at http://xmm.esac.esa.int/xsa/docs/XSA_paper_hr.pdf, arXiv:astro-ph/0206412.

B. Aschenbach. *X-ray telescopes*. Reports on Progress in Physics, 48:579–629, 1985.

R. Berry and J. Burnell. *The handbook of astronomical image processing*. 2005.

H. Böhringer, C. Mullis, P. Rosati et al. *Galaxy Cluster Archaeology*. The Messenger, 120:33–36, 2005.

H. Böhringer, P. Schuecker, L. Guzzo et al. *The ROSAT-ESO Flux Limited X-ray (RE-FLEX) Galaxy cluster survey. V. The cluster catalogue*. A&A, 425:367–383, 2004. arXiv:astro-ph/0405546.

H. Böhringer, W. Voges, J. P. Huchra et al. *The Northern ROSAT All-Sky (NORAS) Galaxy Cluster Survey. I. X-Ray Properties of Clusters Detected as Extended X-Ray Sources*. ApJS, 129:435–474, 2000. arXiv:astro-ph/0003219.

S. Borgani, G. Murante, V. Springel et al. *X-ray properties of galaxy clusters and groups from a cosmological hydrodynamical simulation*. MNRAS, 348:1078–1096, 2004. arXiv:astro-ph/0310794.

W. N. Brandt and G. Hasinger. *Deep Extragalactic X-Ray Surveys*. ARA&A, 43:827–859, 2005. arXiv:astro-ph/0501058.

U. G. Briel, J. P. Henry, D. H. Lumb et al. *A mosaic of the Coma cluster of galaxies with XMM-Newton*. A&A, 365:L60–L66, 2001. arXiv:astro-ph/0011323.

R. A. Burenin, A. Vikhlinin, A. Hornstrup et al. *The 400 Square Degree ROSAT PSPC Galaxy Cluster Survey: Catalog and Statistical Calibration*. ApJS, 172:561–582, 2007. arXiv:astro-ph/0610739.

C. J. Burrows, R. Burg and R. Giacconi. *Optimal grazing incidence optics and its application to wide-field X-ray imaging*. ApJ, 392:760–765, 1992.

E. T. Byram, T. A. Chubb and H. Friedman. *Cosmic X-Ray Sources-Galactic and Extragalactic*. AJ, 71:379–+, 1966.

N. Cappelluti. *Large scale structures in X-ray surveys*. Ph.D. thesis, 2007. Comments: PhD thesis, Technische Universität München (2007), in English, also available at http://mediatum2.ub.tum.de/doc/628520/628520.pdf.

N. Cappelluti, M. Ajello, P. Rebusco et al. *A candidate tidal disruption event in the Galaxy cluster Abell 3571*. A&A, 495:L9–L12, 2009a. arXiv:0901.3357.

N. Cappelluti, M. Brusa, G. Hasinger et al. *The XMM-Newton wide-field survey in the COSMOS field. The point-like X-ray source catalogue*. A&A, 497:635–648, 2009b. arXiv:0901.2347.

N. Cappelluti, G. Hasinger, M. Brusa et al. *The XMM-Newton Wide-Field Survey in the COSMOS Field. II. X-Ray Data and the logN-logS Relations*. ApJS, 172:341–352, 2007. arXiv:astro-ph/0701196.

A. Cavaliere and R. Fusco-Femiano. *X-rays from hot plasma in clusters of galaxies*. A&A, 49:137–144, 1976.

G. W. Clark. *Balloon Observation of the X-Ray Spectrum of the Crab Nebula Above 15 keV*. Physical Review Letters, 14:91–94, 1965.

T. E. Cravens. *Heliospheric X-ray Emission Associated with Charge Transfer of the Solar Wind with Interstellar Neutrals*. ApJ, 532:L153–L156, 2000.

J. H. Croston, G. W. Pratt, H. Böhringer et al. *Galaxy-cluster gas-density distributions of the representative XMM-Newton cluster structure survey (REXCESS)*. A&A, 487:431–443, 2008. arXiv:0801.3430.

R. G. Cruddace, G. R. Hasinger and J. H. Schmitt. *The application of a maximum likelihood analysis to detection of sources in the ROSAT data base*. In F. Murtagh & A. Heck (editor), *European Southern Observatory Astrophysics Symposia*, volume 28 of *European Southern Observatory Astrophysics Symposia*, pages 177–182. 1988.

J. M. Dickey and F. J. Lockman. *H I in the Galaxy*. ARA&A, 28:215–261, 1990.

S. Dodelson. *Modern cosmology*. 2003.

T. Döhring, B. Aschenbach, H. Bräuninger et al. *Die MPE Testanlage PANTER: Simulation von Sternenlicht zur Charakterisierung von Röntgensatelliten*. Proceedings of the 26th annual meeting of the Gesellschaft für Umweltsimulation, pages 7/1–7/13, 1997.

J. L. E. Dreyer. *A New General Catalogue of Nebulae and Clusters of Stars,being the Catalogue of the late Sir John F.W. Herschel, Bart., revised, corrected, and enlarged.* MmRAS, 49:1–237, 1888.

M. Ehle, M. Breitfellner, M. Díaz Trigo et al. *XMM-Newton Users' Handbook.* 2007.

D. J. Eisenstein and W. Hu. *Baryonic Features in the Matter Transfer Function*. ApJ, 496:605–+, 1998. `arXiv:astro-ph/9709112`.

S. Ettori, P. Tozzi, S. Borgani et al. *Scaling laws in X-ray galaxy clusters at redshift between 0.4 and 1.3*. A&A, 417:13–27, 2004. `arXiv:astro-ph/0312239`.

A. E. Evrard, T. J. MacFarland, H. M. P. Couchman et al. *Galaxy Clusters in Hubble Volume Simulations: Cosmological Constraints from Sky Survey Populations*. ApJ, 573:7–36, 2002. `arXiv:astro-ph/0110246`.

R. Fassbender. *Studying Cosmic Evolution with the XMM-Newton Distant Cluster Project: X-ray Luminous Galaxy Clusters at z≳1 and their Galaxy Populations. oai:cds.cern.ch:1108573.* Ph.D. thesis, 2008. Comments: 284 pages, 84 figures, PhD thesis, Ludwig-Maximilians-Universität Muenchen (2007), in English, also available at http://edoc.ub.uni-muenchen.de/7938.

A. Finoguenov, L. Guzzo, G. Hasinger et al. *The XMM-Newton Wide-Field Survey in the COSMOS Field: Statistical Properties of Clusters of Galaxies*. ApJS, 172:182–195, 2007. `arXiv:astro-ph/0612360`.

P. Friedrich. *Wolter Optics*. In J. Trümper and G. Hasinger (editors), *The Universe in X-Rays*. 2008.

P. Friedrich, H. Bräuninger, B. Budau et al. *Design and development of the eROSITA x-ray mirrors*. In *Society of Photo-Optical Instrumentation Engineers (SPIE) Conference Series*, volume 7011. 2008.

P. Friedrich, P. Predehl, N. Meidinger et al. *Results from a contamination experiment on the ISS*. In O. Citterio and S. L. O'Dell (editors), *Society of Photo-Optical Instrumentation Engineers (SPIE) Conference Series*, volume 5900, pages 172–183. 2005.

G. Fritz, A. Davidsen, J. F. Meekins et al. *Discovery of an X-Ray Source in Perseus*. ApJ, 164:L81+, 1971.

I. George, K. Arnaud, B. Pence et al. *The Calibration Requirements for Spectral Analysis (Definition of RMF and ARF file formats)*. 2007.

R. Giacconi, G. Branduardi, U. Briel et al. *The Einstein /HEAO 2/ X-ray Observatory*. ApJ, 230:540–550, 1979.

R. Giacconi, E. Kellogg, P. Gorenstein et al. *An X-Ray Scan of the Galactic Plane from UHURU*. ApJ, 165:L27+, 1971.

I. M. Gioia, T. Maccacaro, R. E. Schild et al. *The Einstein Observatory Extended Medium-Sensitivity Survey. I - X-ray data and analysis*. ApJS, 72:567–619, 1990.

R. Griffiths, R. Petre, G. Hasinger et al. *DUO: the Dark Universe Observatory*. In G. Hasinger and M. J. L. Turner (editors), *Society of Photo-Optical Instrumentation Engineers (SPIE) Conference Series*, volume 5488, pages 209–221. 2004.

B. Grünecker. *Untersuchung der Röntgenemission rotationsgetriebener Pulsare mit Chandra, XMM-Newton und eROSITA*. Diploma thesis, Ludwig-Maximilians-Universität München, 2008.

F. Guglielmetti, R. Fischer and V. Dose. *Background-source separation in astronomical images with Bayesian probability theory - I. The method*. MNRAS, 396:165–190, 2009. `arXiv:0903.2342`.

H. Gursky, E. Kellogg, S. Murray et al. *A Strong X-Ray Source in the Coma Cluster Observed by UHURU*. ApJ, 167:L81+, 1971.

Z. Haiman, S. Allen, N. Bahcall et al. *An X-ray Galaxy Cluster Survey for Investigations of Dark Energy*. ArXiv Astrophysics e-prints, 2005. `arXiv:astro-ph/0507013`.

R. J. Hanisch, A. Farris, E. W. Greisen et al. *Definition of the Flexible Image Transport System (FITS)*. A&A, 376:359–380, 2001.

D. Hartmann and W. B. Burton. *Atlas of Galactic Neutral Hydrogen*. 1997.

G. Hasinger, J. Trumper and R. Staubert. *Abrixas*. In K. Koyama, S. Kitamoto, & M. Itoh (editor), *The Hot Universe*, volume 188 of *IAU Symposium*, pages 83–+. 1998.

J. P. Henry, C. R. Mullis, W. Voges et al. *The ROSAT North Ecliptic Pole Survey: The X-Ray Catalog*. ApJS, 162:304–328, 2006. `arXiv:astro-ph/0511195`.

M. Henze, W. Pietsch, G. Sala et al. *The very short supersoft X-ray state of the classical nova M31N 2007-11a*. A&A, 498:L13–L16, 2009. `arXiv:0812.4420`.

S. B. Howell. *Handbook of CCD astronomy*. 2006.

A. Jenkins, C. S. Frenk, S. D. M. White et al. *The mass function of dark matter haloes*. MNRAS, 321:372–384, 2001. `arXiv:astro-ph/0005260`.

M. W. Johnson, R. G. Cruddace, K. S. Wood et al. *A survey by HEAO 1 of clusters of galaxies. III - The complete Abell catalog*. ApJ, 266:425–445, 1983.

C. Jones and W. Forman. *Einstein Observatory Images of Clusters of Galaxies*. ApJ, 511:65–83, 1999.

E. Kellogg, H. Gursky, H. Tananbaum et al. *The Extended X-Ray Source at M87*. ApJ, 174:L65+, 1972.

N. Kimmel. *Analysis of the charge collection process in solid state X-ray detectors*. Ph.D. thesis, 2008. Comments: PhD thesis, Universität Siegen, in English, also available at http://dokumentix.ub.uni-siegen.de/opus/volltexte/2009/388/index.html.

N. Kimmel, R. Hartmann, P. Holl et al. *Analysis of the charge collection process in pnCCDs*. In *Society of Photo-Optical Instrumentation Engineers (SPIE) Conference Series*, volume 6276. 2006.

I. R. King. *The structure of star clusters. IV. Photoelectric surface photometry in nine globular clusters*. AJ, 71:276–+, 1966.

G. F. Knoll. *Radiation detection and measurement*. 2000.

E. Komatsu, K. M. Smith, J. Dunkley et al. *Seven-Year Wilkinson Microwave Anisotropy Probe (WMAP) Observations: Cosmological Interpretation*. ArXiv e-prints, 2010. arXiv:1001.4538.

S. Komossa, H. Zhou, A. Rau et al. *NTT, Spitzer, and Chandra Spectroscopy of SDSSJ095209.56+214313.3: The Most Luminous Coronal-line Supernova Ever Observed, or a Stellar Tidal Disruption Event?* ApJ, 701:105–121, 2009. arXiv:0902.3248.

O. Kotov and A. Vikhlinin. *Chandra Sample of Galaxy Clusters at z = 0.4-0.55: Evolution in the Mass-Temperature Relation*. ApJ, 641:752–755, 2006. arXiv:astro-ph/0511044.

I. Kreykenbohm, C. Schmid, J. Wilms et al. *eROSITA Near Real Time Analysis*. In D. A. Bohlender, D. Durand, & P. Dowler (editor), *Astronomical Society of the Pacific Conference Series*, volume 411 of *Astronomical Society of the Pacific Conference Series*, pages 285–+. 2009.

G. Lamer, M. Hoeft, J. Kohnert et al. *2XMM J083026+524133: the most X-ray luminous cluster at redshift 1*. A&A, 487:L33–L36, 2008. arXiv:0805.3817.

S. Majumdar and J. J. Mohr. *Self-Calibration in Cluster Studies of Dark Energy: Combining the Cluster Redshift Distribution, the Power Spectrum, and Mass Measurements*. ApJ, 613:41–50, 2004. arXiv:astro-ph/0305341.

M. Markevitch. *The $L_X - T$ Relation and Temperature Function for Nearby Clusters Revisited*. ApJ, 504:27–+, 1998. arXiv:astro-ph/9802059.

N. Meidinger, R. Andritschke, K. Dennerl et al. *First measurements with DUO/ROSITA pnCCDs*. In O. H. W. Siegmund (editor), *Society of Photo-Optical Instrumentation Engineers (SPIE) Conference Series*, volume 5898, pages 247–255. 2005.

N. Meidinger, R. Andritschke, J. Elbs et al. *eROSITA camera design and first performance measurements with CCDs*. In *Society of Photo-Optical Instrumentation Engineers (SPIE) Conference Series*, volume 7011. 2008.

N. Metropolis. *The Beginning of the Monte Carlo Method*. Los Alamos Science, Special Issue, 15:125–130, 1987. URL http://www.fas.org/sgp/othergov/doe/lanl/pubs/number15.htm.

R. Mewe, E. H. B. M. Gronenschild and G. H. J. van den Oord. *Calculated X-radiation from optically thin plasmas. V*. A&AS, 62:197–254, 1985.

S. M. Molnar, Z. Haiman, M. Birkinshaw et al. *Constraints on the Energy Content of the Universe from a Combination of Galaxy Cluster Observables*. ApJ, 601:22–27, 2004. arXiv:astro-ph/0309807.

C. R. Mullis, P. Rosati, G. Lamer et al. *Discovery of an X-Ray-luminous Galaxy Cluster at z=1.4*. ApJ, 623:L85–L88, 2005. arXiv:astro-ph/0503004.

J. F. Navarro, C. S. Frenk and S. D. M. White. *A Universal Density Profile from Hierarchical Clustering*. ApJ, 490:493–+, 1997. arXiv:astro-ph/9611107.

T. B. O'Hara, J. J. Mohr and A. J. R. Sanderson. *Evolution of the Intracluster Medium Between* $0.2 < z < 1.3$ *in a Chandra Sample of 70 Galaxy Clusters*. ArXiv e-prints, 2007. arXiv:0710.5782.

F. Pacaud, M. Pierre, A. Refregier et al. *The XMM Large-Scale Structure survey: the X-ray pipeline and survey selection function*. MNRAS, 372:578–590, 2006. `arXiv:astro-ph/0607177`.

M. Pavlinsky, G. Hasinger, A. Parmar et al. *Spectrum-RG/eROSITA/Lobster astrophysical mission*. In *Society of Photo-Optical Instrumentation Engineers (SPIE) Conference Series*, volume 6266. 2006.

W. Pence. *CFITSIO, v2.0: A New Full-Featured Data Interface*. In D. M. Mehringer, R. L. Plante, & D. A. Roberts (editor), *Astronomical Data Analysis Software and Systems VIII*, volume 172 of *Astronomical Society of the Pacific Conference Series*, pages 487–+. 1999.

E. Pfeffermann. *Imaging Proportional Counters*. In J. Trümper and G. Hasinger (editors), *The Universe in X-Rays*. 2008a.

E. Pfeffermann. *Proportional Counters*. In J. Trümper and G. Hasinger (editors), *The Universe in X-Rays*. 2008b.

E. Pfeffermann and U. G. Briel. *Performance of the position sensitive proportional counter of the ROSAT telescope*. In J. L. Culhane (editor), *Society of Photo-Optical Instrumentation Engineers (SPIE) Conference Series*, volume 597, pages 208–212. 1986.

M. Pierre, I. Valtchanov, B. Altieri et al. *The XMM-LSS survey. Survey design and first results*. Journal of Cosmology and Astro-Particle Physics, 9:11–+, 2004. `arXiv:astro-ph/0305191`.

W. Pietsch, J. Fliri, M. J. Freyberg et al. *Optical novae: the major class of supersoft X-ray sources in M 31*. A&A, 442:879–894, 2005. `arXiv:astro-ph/0504321`.

M. Popp, R. Hartmann, H. Soltau et al. *Modeling the energy response of pn-CCDs in the 0.2-10 keV band*. Nuclear Instruments and Methods in Physics Research A, 439:567–574, 2000.

G. W. Pratt, J. H. Croston, M. Arnaud et al. *Galaxy cluster X-ray luminosity scaling relations from a representative local sample (REXCESS)*. A&A, 498:361–378, 2009. `arXiv:0809.3784`.

P. Predehl. *ABRIXAS: scientific goal and mission concept*. In O. H. Siegmund and K. A. Flanagan (editors), *Society of Photo-Optical Instrumentation Engineers (SPIE) Conference Series*, volume 3765, pages 172–183. 1999.

P. Predehl, R. Andritschke, H. Böhringer et al. *eROSITA on SRG*. SPIE Astronomical Instrumentation 2010, Conference 7732-29, 2010.

P. Predehl, R. Andritschke, W. Bornemann et al. *eROSITA*. In *Society of Photo-Optical Instrumentation Engineers (SPIE) Conference Series*, volume 6686. 2007.

P. Predehl, P. Friedrich, G. Hasinger et al. *ROSITA*. Astronomische Nachrichten, 324:128–131, 2003.

P. Predehl, G. Hasinger, H. Böhringer et al. *eROSITA*. In *Society of Photo-Optical Instrumentation Engineers (SPIE) Conference Series*, volume 6266. 2006.

W. H. Press. *Numerical recipes in C++ : the art of scientific computing*. 2002.

W. H. Press and P. Schechter. *Formation of Galaxies and Clusters of Galaxies by Self-Similar Gravitational Condensation*. ApJ, 187:425–438, 1974.

J. C. Raymond and B. W. Smith. *Soft X-ray spectrum of a hot plasma*. ApJS, 35:419–439, 1977.

A. Reichert. Diploma thesis, in preparation. Technische Universität München, 2010.

T. H. Reiprich and H. Böhringer. *The Mass Function of an X-Ray Flux-limited Sample of Galaxy Clusters*. ApJ, 567:716–740, 2002. `arXiv:astro-ph/0111285`.

A. G. Riess, A. V. Filippenko, P. Challis et al. *Observational Evidence from Supernovae for an Accelerating Universe and a Cosmological Constant*. AJ, 116:1009–1038, 1998. `arXiv:astro-ph/9805201`.

A. K. Romer, P. T. P. Viana, A. R. Liddle et al. *A Serendipitous Galaxy Cluster Survey with XMM: Expected Catalog Properties and Scientific Applications*. ApJ, 547:594–608, 2001.

M. Roncarelli, L. Moscardini, P. Tozzi et al. *Properties of the diffuse X-ray background in a high-resolution hydrodynamical simulation*. MNRAS, 368:74–84, 2006. `arXiv:astro-ph/0507643`.

P. Rosati, R. della Ceca, C. Norman et al. *The ROSAT Deep Cluster Survey: The X-Ray Luminosity Function Out to z=0.8*. ApJ, 492:L21+, 1998. `arXiv:astro-ph/9710308`.

P. Rosati, C. Lidman, R. Della Ceca et al. *The ROSAT Deep Cluster Survey: probing the galaxy cluster population out to z = 1.3*. The Messenger, 99:26–30, 2000.

J. S. Santos, P. Rosati, P. Tozzi et al. *Searching for cool core clusters at high redshift*. A&A, 483:35–47, 2008. `arXiv:0802.1445`.

C. L. Sarazin. *X-ray emission from clusters of galaxies*. Reviews of Modern Physics, 58:1–115, 1986.

R. D. Saxton, A. M. Read, P. Esquej et al. *The first XMM-Newton slew survey catalogue: XMMSL1*. A&A, 480:611–622, 2008. `arXiv:0801.3732`.

C. Scharf. *Optimal Chandra and XMM-Newton Bandpasses for Detecting Low-Temperature Groups and Clusters of Galaxies*. ApJ, 572:157–159, 2002. `arXiv:astro-ph/0202353`.

C. Schmid. *Simulation of the Imaging and Detection Properties of the eROSITA Experiment on Spectrum-X-Gamma*. Diploma thesis, University of Erlangen-Nuremberg, 2008.

M. Schmidt. *Space Distribution and Luminosity Functions of Quasi-Stellar Radio Sources*. ApJ, 151:393–+, 1968.

P. Schneider. *Extragalactic Astronomy and Cosmology*. 2006.

K. Schwarzschild. *Untersuchungen zur geometrischen Optik I–III,*. Astronomische Mittheilungen der Königlichen Sternwarte zu Göttingen, 1905.

C. E. Shannon. *Communication in the Presence of Noise*. Proceedings of the IRE, 37(1):10–21, 1949.

R. K. Sheth, H. J. Mo and G. Tormen. *Ellipsoidal collapse and an improved model for the number and spatial distribution of dark matter haloes*. MNRAS, 323:1–12, 2001. `arXiv:astro-ph/9907024`.

V. Springel, S. D. M. White, A. Jenkins et al. *Simulations of the formation, evolution and clustering of galaxies and quasars*. Nature, 435:629–636, 2005. `arXiv:astro-ph/0504097`.

L. Strüder. *High-resolution imaging X-ray spectrometers*. Nuclear Instruments and Methods in Physics Research A, 454:73–113, 2000.

L. Strüder, U. Briel, K. Dennerl et al. *The European Photon Imaging Camera on XMM-Newton: The pn-CCD camera*. A&A, 365:L18–L26, 2001.

L. Strüder and N. Meidinger. *CCD Detectors*. In J. Trümper and G. Hasinger (editors), *The Universe in X-Rays*. 2008.

R. Suhada, J. Song, H. Böhringer et al. *XMM-Newton detection of two clusters of galaxies with strong SPT Sunyaev-Zel'dovich effect signatures*. A&A, 514:L3+, 2010. `arXiv:1003.3020`.

R. A. Sunyaev and I. B. Zel'dovich. *Microwave background radiation as a probe of the contemporary structure and history of the universe*. ARA&A, 18:537–560, 1980.

R. A. Sunyaev and Y. B. Zel'dovich. *The Observations of Relic Radiation as a Test of the Nature of X-Ray Radiation from the Clusters of Galaxies*. Comments on Astrophysics and Space Physics, 4:173–+, 1972.

J. Trümper. *The ROSAT mission*. Advances in Space Research, 2:241–249, 1982.

N. Tsoulfanidis. *Measurement and Detection of Radiation*. 1995.

M. J. L. Turner, A. Abbey, M. Arnaud et al. *The European Photon Imaging Camera on XMM-Newton: The MOS cameras*. A&A, 365:L27–L35, 2001. `arXiv:astro-ph/0011498`.

I. Valtchanov, M. Pierre and R. Gastaud. *Comparison of source detection procedures for XMM-Newton images*. A&A, 370:689–706, 2001. `arXiv:astro-ph/0102297`.

A. Vikhlinin, R. Burenin, W. R. Forman et al. *Lack of Cooling Flow Clusters at $z > 0.5$*. In H. Böhringer, G. W. Pratt, A. Finoguenov et al. (editors), *Heating versus Cooling in Galaxies and Clusters of Galaxies*, pages 48–+. 2007.

A. Vikhlinin, R. A. Burenin, H. Ebeling et al. *Chandra Cluster Cosmology Project II: Samples and X-ray Data Reduction*. ArXiv e-prints, 2008. `arXiv:0805.2207`.

A. Vikhlinin, A. V. Kravtsov, R. A. Burenin et al. *Chandra Cluster Cosmology Project III: Cosmological Parameter Constraints*. ApJ, 692:1060–1074, 2009. `arXiv:0812.2720`.

A. Vikhlinin, M. Markevitch, W. Forman et al. *Zooming in on the Coma Cluster with Chandra: Compressed Warm Gas in the Brightest Cluster Galaxies*. ApJ, 555:L87–L90, 2001. `arXiv:astro-ph/0102483`.

A. Vikhlinin, B. R. McNamara, W. Forman et al. *A Catalog of 200 Galaxy Clusters Serendipitously Detected in the ROSAT PSPC Pointed Observations*. ApJ, 502:558–+, 1998. `arXiv:astro-ph/9803099`.

G. M. Voit. *Expectations for evolution of cluster scaling relations*. Advances in Space Research, 36:701–705, 2005a.

G. M. Voit. *Tracing cosmic evolution with clusters of galaxies*. Reviews of Modern Physics, 77:207–258, 2005b. `arXiv:astro-ph/0410173`.

M. G. Watson, J. Auguères, J. Ballet et al. *The XMM-Newton Serendipitous Survey. I. The role of XMM-Newton Survey Science Centre*. A&A, 365:L51–L59, 2001. `arXiv:astro-ph/0011463`.

M. G. Watson, A. C. Schröder, D. Fyfe et al. *The XMM-Newton serendipitous survey. V. The Second XMM-Newton serendipitous source catalogue.* A&A, 493:339–373, 2009. `arXiv:0807.1067`.

M. C. Weisskopf, B. Brinkman, C. Canizares et al. *An Overview of the Performance and Scientific Results from the Chandra X-Ray Observatory.* PASP, 114:1–24, 2002. `arXiv:astro-ph/0110308`.

M. C. Weisskopf, S. L. O'dell and L. P. van Speybroeck. *Advanced X-Ray Astrophysics Facility (AXAF).* In R. B. Hoover and A. B. Walker (editors), *Society of Photo-Optical Instrumentation Engineers (SPIE) Conference Series*, volume 2805, pages 2–7. 1996.

B. Y. Welsh and R. L. Shelton. *The trouble with the Local Bubble.* Ap&SS, 323:1–16, 2009. `arXiv:0906.2827`.

N. E. White and A. E. Hornschemeier. *International X-ray Observatory (IXO).* In *Bulletin of the American Astronomical Society*, volume 41 of *Bulletin of the American Astronomical Society*, pages 388–+. 2009.

S. D. M. White. *Fundamentalist physics: why Dark Energy is bad for astronomy.* Reports on Progress in Physics, 70:883–897, 2007. `arXiv:0704.2291`.

M. Wolleben. *A New Model for the Loop I (North Polar Spur) Region.* ApJ, 664:349–356, 2007. `arXiv:0704.0276`.

H. Wolter. *Spiegelsysteme streifenden Einfalls als abbildende Optiken für Röntgenstrahlen (Grazing Incidence Mirror Systems as Imaging Optics for X-Rays).* Annalen der Physik, 445(1):94–114, 1952.

H. Yang, P. M. Ricker and P. M. Sutter. *The Influence of Concentration and Dynamical State on Scatter in the Galaxy Cluster Mass-Temperature Relation.* ApJ, 699:315–329, 2009. `arXiv:0808.4099`.

Y. Yang, R. F. Mushotzky, A. J. Barger et al. *Spatial Correlation Function of the Chandra-selected Active Galactic Nuclei.* ApJ, 645:68–82, 2006. `arXiv:astro-ph/0601634`.

Acknowledgements